Long-term analysis of ionospheric response during geomagnetic storms in mid, low and equatorial latitudes

A thesis submitted in fulfilment of the
requirements for the degree of

DOCTOR OF PHILOSOPHY

of

RHODES UNIVERSITY

by

Tshimangadzo Merline Matamba

06 December 2017

Abstract

Understanding changes in the ionosphere is important for High Frequency (HF) communications and navigation systems. Ionospheric storms are the disturbances in the Earth's upper atmosphere due to solar activities such as Coronal Mass Ejections (CMEs), Corotating interaction Regions (CIRs) and solar flares. This thesis reports for the first time on an investigation of ionospheric response to great geomagnetic storms (Disturbance storm time, Dst ≤ -350 nT) that occurred during solar cycle 23. The storm periods analysed were 29 March - 02 April 2001, 27 - 31 October 2003, 18 - 23 November 2003 and 06 - 11 November 2004. Global Navigation Satellite System (GNSS), Total Electron Content (TEC) and ionosonde critical frequency of F2 layer (foF2) data over northern hemisphere (European sector) and southern hemisphere (African sector) mid-latitudes were used to study the ionospheric responses within 15°E - 40°E longitude and $\pm 31°$ - $\pm 46°$ geomagnetic latitude. Mid-latitude regions within the same longitude sector in both hemispheres were selected in order to assess the contribution of the low latitude changes especially the expansion of Equatorial Ionization Anomaly (EIA) also known as the dayside ionospheric super-fountain effect during these storms. In all storm periods, both negative and positive ionospheric responses were observed in both hemispheres. Negative ionospheric responses were mainly due to changes in neutral composition, while the expansion of the EIA led to pronounced positive ionospheric storm effect at mid-latitudes for some storm periods. In other cases (e.g 29 October 2003), Prompt Penetration Electric Fields (PPEF), EIA expansion and large scale Traveling Ionospheric Disturbances (TIDs) were found to be present during the positive storm effect at mid-latitudes in both hemispheres. An increase in TEC on the 28 October 2003 was because of the large solar flare with previously determined intensity of X45$\pm$ 5. A further report on statistical analysis of ionospheric storm effects due to Corotating Interaction Region (CIR)- and Coronal Mass Ejection (CME)-driven storms was performed. The storm periods analyzed occurred during the period 2001 - 2015 which covers part of solar cycles 23 and 24. Dst$\leq$ -30 nT and Kp$\geq$ 3 indices were used to identify the storm periods considered. Ionospheric TEC derived from IGS stations that lie within 30°E - 40°E geographic longitude in mid, low and equatorial latitude over the African sector were used. The statistical analysis of ionospheric storm effects were compared over mid, low and equatorial latitudes in the African sector for the first time. Positive ionospheric storm effects were more prevalent during CME-driven and CIR-driven over all stations considered in this study. Negative ionospheric storm effects occurred only during CME-driven storms over mid-latitude stations and were more prevalent in summer. The other interesting finding is that for the stations considered over mid-, low, and equatorial latitudes, negative-positive ionospheric responses were only observed over low and equatorial latitudes. A significant number of cases where the electron density changes remained within the background variability during storm conditions were observed over the low latitude stations compared to other latitude regions.

Acknowledgement

Publications from this thesis

The work submitted for this thesis (Chapter 5 of this thesis) has been published in international peer-reviewed journal.
Matamba, T. M., J. B. Habarulema, and D. Burešová (2016), Midlatitude ionospheric changes to four great geomagnetic storms of solar cycle 23 in Southern and Northern Hemispheres, Space Weather, 14, 1155–1171, doi:10.1002/2016SW001516.

Chapter 6 is based on the work that is under review in Space weather journal:
Matamba, T. M. and Habarulema, J. B. (2017), 'Ionospheric response to CME and CIR- driven geomagnetic storms along 30°E - 40°E over the African sector from 2001 - 2015', Space Weather. Under review.

Dedication

This thesis is dedicated to my husband, Thingahangwi, daughter, Vhugala, mother in Law, Vho-Merina, Mrs Magadze, my late parents, Johannah and Solomon, and my late uncle, Mr Magadze.

Contents

List of Figures

Acronyms

AE	Auroral Electrojet
AIA	Atmospheric Imaging Assembly
ATM	Apollo Telescope Mount
AU	Astronomical Unit
CEJ	Counter-Electrojet
CH	Coronal Hole
CIR	Corotating Interaction Region
CME	Coronal Mass Ejection
DDEF	Disturbance Dynamo Electric Field
Dst	Disturbance storm time
EEJ	Equatorial Electrjet
EIA	Equatorial Ionisation Anomaly
EUV	Extreme Ultraviolet
foF2	Critical Frequency of the F2 layer
GIC	Geomagnetically Induced Currents
GNSS	Global Navigation Satellite System
GPS	Global Positioning System
GLONASS	Globalnaya Navigazionnaya Sputnikovaya Sistema (Global Navigation Satellite System)
GUVI	Global Ultraviolet Imager
HF	High Frequency
hmF2	Maximum peak height of the F2 layer
HMI	Helioseismic and Magnetic Imager
HSSWS	High Speed Solar Wind Stream
ICME	Interplanetary Coronal Mass Ejection
IEF	Interplanetary Electric Field
IMF	Interplanetary Magnetic Field
IONEX	IONosphere EXchange
IPP	Ionospheric Pierce Point
IRI	International Reference Ionosphere
ISR	Incoherent Scatter Radar
LT	Local Time
LSTID	Large Scale Traveling Ionospheric Disturbance
MSTID	Medium Scale Traveling Ionospheric Disturbance
Ne	Electron density
N_{max}	Maximum electron density
NGA	National Geospatial-intelligence Agency
nT	Nanoteslas

PC	Polar Cap
PPEF	Prompt Penetration Electric Field
SAO	Standard Archiving Output
SEP	Solar Energetic Particles
SI	Sudden Impulse
SID	Sudden Ionospheric Disturbances
SSC	Sudden Storm Commencement
SSN	Sunspot number
STEC	Slant Total Electron Content
SYM	Symmetric
TAD	Traveling Atmospheric Disturbance
TEC	Total Electron Content
TECU	Total Electron Content Unit
TID	Traveling Ionospheric Disturbance
TRACE	Transition Region and Coronal Explorer
USDoD	United States Department of Defence
UT	Universal Time
VTEC	Vertical Total Electron Content

Chapter 1

Introduction

The ionosphere is the part of the Earth's atmosphere where electrons and ions are present in quantities sufficient to affect radio waves propagation (Rishbeth and Garriott, 1969; Hargreaves, 1992). It is formed when Extreme Ultraviolet (EUV) radiation from the Sun strips electrons from the neutral atoms of the Earth's atmosphere (McNamara, 1991). The ionosphere responds significantly with the varying solar activities (such as Coronal Mass Ejections (CMEs) and Corotating Interaction Regions (CIRs)), the electric field distribution and particle precipitation from the magnetosphere. The electron density of the ionosphere at a given altitude and location depends on the solar EUV fluxes, the neutral composition and dynamical effects of neutral winds and electric fields. During geomagnetic storms, the Earth's magnetosphere is compressed by disturbed solar wind, and intense electric fields are mapped along geomagnetic field lines to high latitude ionosphere. When electric fields penetrate to low latitudes from high latitudes they produce a rapid convection of plasma which also drives the neutral winds via collision (e.g. Buonsanto, 1999; Yizengaw, 2004; Tsurutani et al., 2008a). Energetic particles precipitate to the lower thermosphere and below expanding the auroral zone, and increasing ionospheric conductivities. Intense electric currents couple the high latitude ionosphere with the magnetosphere and the increased energy input causes considerable heating of the neutral gases (Buonsanto, 1999).

The Sun is a variable star that expels high energy particles in the form of electrodynamic and particle radiation out into space. This radiation can impact and damage technological systems and is one of the major concerns for human space exploration (Moldwin, 2008). Solar activities can not only damage or destroy orbiting satellites, but can also injure or kill astronauts, degrade or blackout certain radio and navigation communications, and cause regional power failures by destroying critical components of electrical power grids (e.g. Viljanen and Pirjola, 1994; Boteler, 1994; Pirjola, 2000; Pulkkinen et al., 2003; Pirjola et al., 2005; Ngwira et al., 2008). With the continued growth of the satellite communications industry and our growing dependence on wireless communication and instant access to global information, we are more likely to be affected by problems caused by space weather (Moldwin, 2008).

The term space weather refers "to the conditions on the Sun and in solar wind, magnetosphere, ionosphere and thermosphere that can influence the performance and reliability of ground-based and space-borne technological systems and can endanger human life or health" (Wright Jr et al., 1995). Most severe ionospheric storms mainly result from space weather events (e.g. Lastovicka, 2002a; Gopalswamy et al., 2005; Tsurutani et al., 2005, 2008a; Howard, 2013; Borries et al., 2015).

This thesis reports on the ionospheric response due to geomagnetic storm events over the mid-, low- and equatorial-latitudes. For the mid-latitudes it presents, ionospheric response to four intense geomagnetic storms (Dst ≤ -350 nT) that occurred during solar cycle 23 in southern (African sector) and northern (European sector) hemispheres respectively. It further presents statistical analysis of ionospheric response to CME and CIR- driven storms using the stations located within 30°E - 40°E geographic longitude over the African, mid-, low and equatorial latitudes during the time interval 2001 - 2015.

The ionospheric storm research dates back to around 1920s when the experiments in one way radio telephone transmissions were conducted from Rocky Point in united States to New south Gate in England (Prölss, 2008). Ionospheric storm effects have been studied using different data sources such as, ionosondes (e.g Appleton and Piggott, 1952; Heisler, 1958; Matsushita, 1959; Prölss and Zahn, 1974; Prölss et al., 1991a; Lei et al., 2005), satellite observations (e.g Wand, 1967; Chapman, 1969; Benkova and Zevakina, 1970; Prölss, 1980), Incoherent Scatter Radar (ISR) (e.g Georges, 1968; Woodman and Hagfors, 1969; Fejer et al., 1979a; Hunsucker, 1980; Nicolls et al., 2004; Kelley et al., 2009), magnetometers (e.g Sastri, 1988; Anderson et al., 2002, 2004; Yizengaw et al., 2014) and etc. Of recent, Global Navigational Satellite Systems (GNSS) such as the American Global Positioning System (GPS), the Russian Globalnaya Navigazionnaya Sputnikovaya Sistema, or Global Navigation Satellite System (GLONASS), and Galileo the European global navigation satellite system have emerged as powerful tools for ionospheric investigations mainly due to their continuous databases and extended spatial coverage (e.g. Hofmann-Wellenhof et al., 1997; Leitinger et al., 1997; Basu et al., 2001; Jakowski et al., 2002; Mannucci et al., 2005; Misra and Enge, 2006). This work was conducted using GNSS Total Electron Content (TEC) data for the northern and southern hemispheres' mid, low and equatorial latitudes to study the ionospheric responses to geomagnetic storms. Ionosonde foF2 data for selected stations located in the southern (African) and northern (European) hemisphere mid-latitudes were used to supplement GNSS TEC. The European and South African GNSS receiver networks are dense enough to map the ionospheric variation of TEC and the ionosonde data were used to confirm the observed ionospheric response of TEC.

1.1 Research motivation

Event(s) analyses of ionospheric storm effects over the African sector have been seperately done during either CME- or CIR- driven storms (e.g., Prölss et al., 1991a; Yizengaw et al., 2011; Ngwira et al., 2012; Habarulema et al., 2013b, 2017). Statistical analyses of ionospheric storm effects due to geomagnetic storms over mid- and low latitude in the African sector have also been done separately in different latitude regions (e.g. Adeniyi, 1986; Adewale et al., 2011a; Adeniyi et al., 2014; Burešová et al., 2014; Matamba et al., 2015). Matamba et al. (2015) did a statistical analysis of ionospheric storm effects over Grahamstown, GR13L (33.3°S, 26.5°E; 41.8°S, geomagnetic), South Africa during solar cycle 23 and part of solar cycle 24 (1996 - 2011). They found that during great or intense geomagnetic storms (Dst $\leq$ -350 nT), only negative ionospheric storm effects were observed and were attributed to neutral composition changes. However, in other studies, the response is not only limited to negative ionospheric storm effects (Matamba et al., 2016; Habarulema et al., 2017) as reported in Matamba et al. (2015) and therefore single station analysis does not necessarily provide a complete picture in what may be happening within the entire mid-latitude region. While previous studies were limited to data period and latitude regions covered

mainly due to sparse instrumentation within the African sector, over the past few years, there has been significant improvement in deployment of GPS receivers that allow for relatively extended analysis to be performed across different latitudes simultaneously. Using TEC derived from GNSS receivers, the presented work in this thesis started with an analysis of ionospheric response to four intense geomagnetic storms that occurred during solar cycle 23. The storm periods considered in this analysis were 29 March - 02 April 2001, 27 - 31 October 2003, 18 - 23 November 2003 and 06 - 11 November 2004. TEC at Ionospheric Pierce Point (IPP) (assumed at an altitude of 350 km) locations in latitude range 20°S - 38°S (31°S - 46°S, geomagnetic) and 38°N - 50°N (31°N - 46°N, geomagnetic) within 15°E - 40°E longitude over the African and European sector mid-latitudes were used to study ionospheric responses. Ionosonde data was used to supplement GNSS TEC data analysis in investigating the physical mechanisms driving ionospheric response over both northern and southern hemisphere mid-latitude regions. Negative and positive ionospheric storm effects were observed which will be discussed later. All the four great storms were induced by CMEs (`http://cdaw.gsfc.nasa.gov/CME_list/`, Echer et al., 2008).

The modern society currently depends heavily on a variety of technologies that are vulnerable to ionospheric storms. Strong auroral currents and Geomagnetically Induced Currents (GIC) due to geomagnetic storms can disrupt and damage modern electric power grids and may contribute to the corrosion of oil and gas pipelines (Campbell, 1978; Pirjola et al., 2003; Moldwin, 2008). Equatorial plasma irregularities and the subsequent scintillation processes are intensified or suppressed depending on some factors during geomagnetic storms. Ionospheric storm effects interfere with High-Frequency (HF) radio communications and navigation signals from GNSS satellites (Baker et al., 2004; Lanzerotti, 2007). Exposure of spacecraft to energetic particles during solar energetic particle events and radiation belt enhancements can cause temporary operational anomalies, damage critical electronics, degrade solar arrays, and blind optical systems such as imagers and star trackers (Buonsanto, 1999; Moldwin, 2008; Borries et al., 2015). Monitoring and forecasts of these space weather-related ionospheric storms are essential for the mitigation of space weather impacts (Moldwin, 2008; Borries et al., 2015).

Understanding different ionospheric responses to CME- or CIR- driven storms over mid, low, and equatorial latitudes in African sector could assist in developing reliable regional and global models for forecasting ionospheric responses during storm conditions. Regional studies are necessary especially since the ionosphere behaves differently at different latitudes during geomagnetic storms.

The statistical analyses of ionospheric storm effects due to CME- and CIR-driven storms in the African sector using stations located within 30° - 40°E longitude over mid, low and equatorial latitude was done. The main aim was to compare the ionospheric responses due to CME and CIR-driven storms over mid, low and equatorial latitudes.

1.2   Thesis overview

This thesis comprises seven Chapters. Chapter 1 is an introduction and research motivation. Chapter 2 details the theoretical background of the Sun, solar wind, magnetosphere and ionosphere. Chapter 3 gives an overview of geomagnetic storms and ionospheric storm effects including some mechanisms leading to ionospheric storms. Chapter 4 describes the ionospheric data sources used, including various geomagnetic indices, Ionosonde and GPS TEC data. Chapter 5 discusses the mid-latitude ionospheric response during intense geomagnetic storms of solar cycle 23. Chapter 6 presents the statistics of the ionospheric storm effects over mid-, low-, and equatorial latitudes

over the African sector and their discussion and Chapter 7 gives the conclusion and suggestions for future work.

Chapter 2

The Sun, Solar Wind, Magnetosphere and Ionosphere

2.1 Introduction

This chapter provides a brief theoretical background starting from the Sun and its activities that lead to geomagnetic and consequently ionospheric storms. A description of the ionosphere and its variation is also provided.

2.2 The Sun

The Sun is our nearest star and controls both space and climate weather. Figure 2.1 shows the Sun as observed by the Helioseismic and Magnetic Imager (HMI) at a wavelength of 6173 angstroms. It consist mainly of Hydrogen and Helium with small amounts of Argon, Calcium, Iron, Neon, Magnesium, Carbon, Silicon, Oxygen and Sulphur. It has a mass of 1.99×10^{30} kg, radius of 6.95×10^5 km, luminosity of 3.84×10^{26} watts, effective black body temperature of 5778 K, and average density of 1.4 g/cm^3. The Sun's energy is generated by the nuclear fusion of hydrogen into helium in the core. The energy is transported through the radiative and convective zones. The convective zone extends from 0.7 solar radius to near the surface of the Sun. The atmosphere of the Sun is composed of three parts, the photosphere, chromosphere, and corona.

The photosphere is the visible surface of the Sun, which is very thin ($\sim$100 km) and cool ($\sim$5778 K) layer from which radiation is emitted. The chromosphere is above the photosphere and is also a relatively thin ($\sim$1500 km) layer in which the temperature increases rapidly from the minimum temperature of 5800 K to about 10 000 K near the base of the outer atmosphere The outer atmosphere is the corona which contains a tenuous, hot ($\sim 10^6$), ionised plasma that typically extends several radii from the Sun. Its density is very low, so it is not very bright. Until the 1930s, when the use of coronagraphs were introduced, the corona could only be seen during total solar eclipses (Bond, 2012). The corona is the source of soft x-rays.

Beyond the corona, there is solar wind which is not strictly part of the Sun, but a stream of particles from the Sun into the interplanetary space (Kutner, 2003; Stix, 2004; Moldwin, 2008; Schunk and Nagy, 2009).
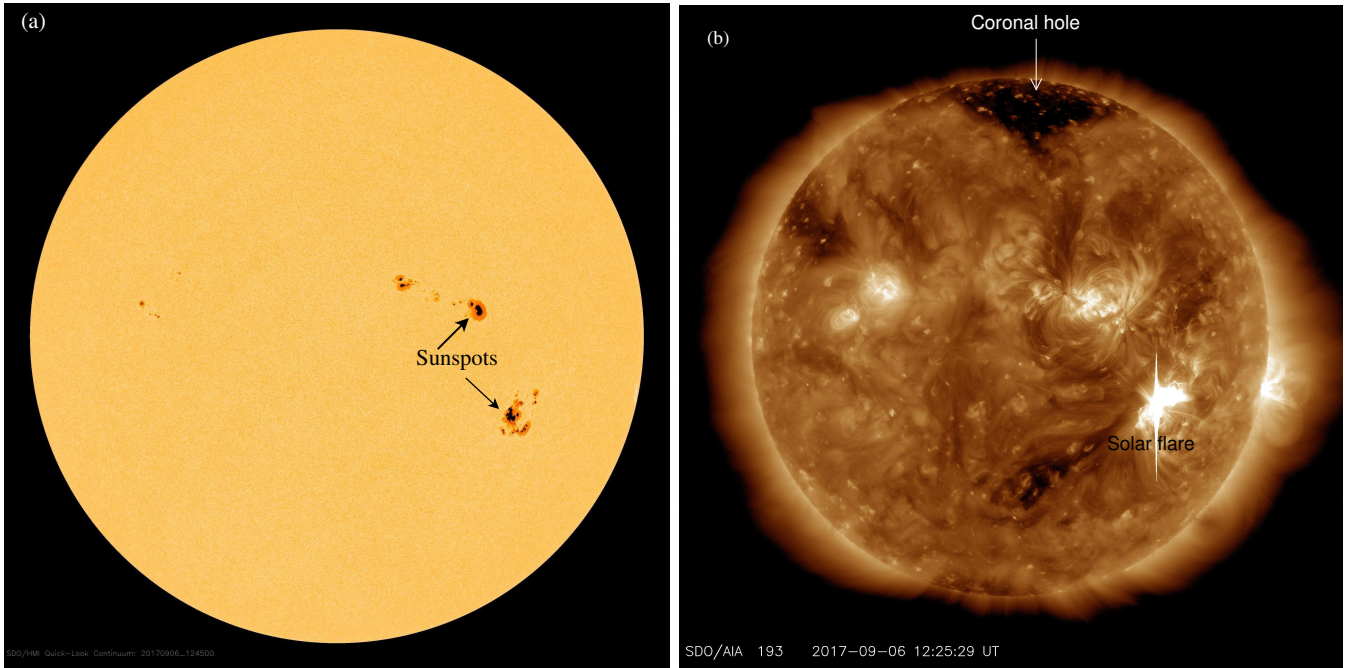
Figure 2.1: The Sun (06 September 2017) as observed by (a) the Helioseismic and Magnetic Imager (HMI) at a wavelength of 6173 angstroms and (b) Atmospheric Imaging Assembly (AIA) at a wavelength of 193 angstroms. Credit: Solar Dynamics Observatory, NASA

2.3 Solar Activity

Sunspots are the manifestation of solar activity related to the Sun's magnetic field (e.g. Davies, 1990; Hasan, 2003; Kutner, 2003; Aarons, 2012). They are dark areas on the Sun's atmosphere. They are dark because they are cooler ($\approx$3000 K) than the area (photosphere) around them (5778 K). The sunspots are indicated in Figure 2.1(a), and can last for several hours to months. In the mid-nineteenth century it was realized that sunspot numbers follow an 11-year cycle. The number of sunspots per peak differs from peak to peak, however they are noticeable (Hanslmeier, 2002; Kutner, 2003; Hanslmeier, 2008). Sunspots tend to form groups. A group may contain a single spot or dozens of spots. The spots rotate with the Sun, that is, from east to west and the Sun rotates in the same direction as the Earth even though the Earth is a rigid body (Davies, 1990). Between 1816 and 1893, R. Wolf studied all available sunspot records and derived an estimate of the sunspot cycle. He introduced the relative Zurich sunspot number RZ in 1948 as a measure of solar activity (Hanslmeier, 2002, 2008), given in the expression below:

$$RZ = k(10g + f) \tag{2.1}$$

where k is a correction which takes into account the different instruments used for the determination of RZ, g is the number of sunspot groups, and f is the number of individual spots (Davies, 1990; Hanslmeier, 2002; Kutner, 2003; Schunk and Nagy, 2009). Sometimes there are powerful explosions in the atmosphere above sunspots, such as solar flares, prominences and coronal mass ejections.

2.3.1 Solar flares

Solar flares are large explosions on the Sun which take place in the solar corona and chromosphere. These bright flashes of light last only a few minutes to a few hours, but the explosions send bursts of energetic particles into space. A solar flare is indicated in Figure 2.1(b). They occur mostly around the sunspots or active regions and are hotter than the corona. Sometimes they become hotter than the centre of the Sun for a short period of time (Lang, 2008). Flares are frequently observed around the peaks of sunspot cycles. They are observed over a wide band of wavelengths from radio to X-rays. Solar flares that are mostly associated with producing geophysical responses are large and characterized by an explosive phase (Davies, 1990). They also trigger many of the short duration ionospheric events called Sudden Ionospheric Disturbances (SID). The flare strength as measured in the X-ray band is most likely to be associated with the ionospheric effects (Goodman, 2006) that will be discussed later. Table 2.1 lists the classification of X-ray flares.

Table 2.1: Classification of X-ray flares (Hanslmeier, 2002)

Class of Flare	X-Ray Energy Output (Φ) at Earth (watt/m^2), 1-8 Å
B	$\Phi < 10^{-6}$
C	$10^{-6} < \Phi < 10^{-5}$
M	$10^{-5} < \Phi < 10^{-4}$
X	$\Phi > 10^{-4}$

The biggest X-class flares are by far the largest explosions in the solar system. Loops tens of times the size of Earth leap up off the Sun's surface when the Sun's magnetic fields cross over each other and reconnect. In the biggest events, this reconnection process may produce as much energy as a billion hydrogen bombs. If they're directed at Earth, such flares can create long-lasting radiation storms that can harm satellites, communications systems, and even ground-based technologies and power grids (e.g. Moldwin, 2008). The flare that occurred on the 06 September 2017 shown in Figure 2.1(b), was a powerful solar flare (an X 9.3) and was followed by Coronal Mass Ejection (CME). It was reported that "the flare was the strongest flare in over a decade. The burst radiation was very intense, it created a strong shortwave radio blackout over Europe, Africa and the Atlantic Ocean"(http://www.sansa.org.za/, https://sdo.gsfc.nasa.gov/gallery/potw/item/838).

2.3.2 Prominences

Prominences are great areas of luminous material extending outwards from the solar atmosphere and were first observed during eclipses. Figure 2.2 shows a prominence erupting from the Sun's surface, with the Earth superimposed for scale purposes. They appear dark over the photosphere and at the limb as bright structures and are called filaments. Some prominences are short-lived eruptive events, while others can be quiescent and survive many rotational periods of the Sun (e.g. Tandberg-Hanssen, 1974; Priest, 1988; Tandberg-Hanssen and Emslie, 1988; Davies, 1990; Hanslmeier, 2002, 2008).

2.3.3 Coronal Mass Ejections (CMEs)

CMEs are large eruption of magnetic field and plasma from the corona, which propagate outward into interplanetary space (Moldwin, 2008; Howard, 2014). They are observed as loops or bubbles
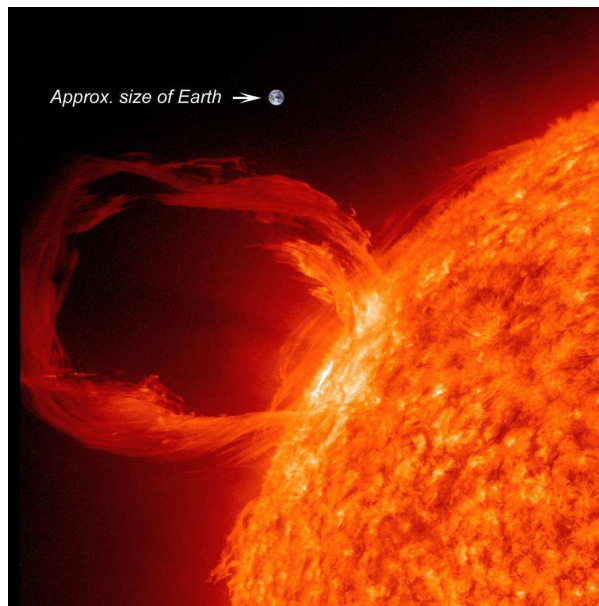
Figure 2.2: A prominence erupting from the Sun's surface as seen in extreme UV light on 30 March 2010 with superimposed Earth for Scale. Credit: NASA/SDO.
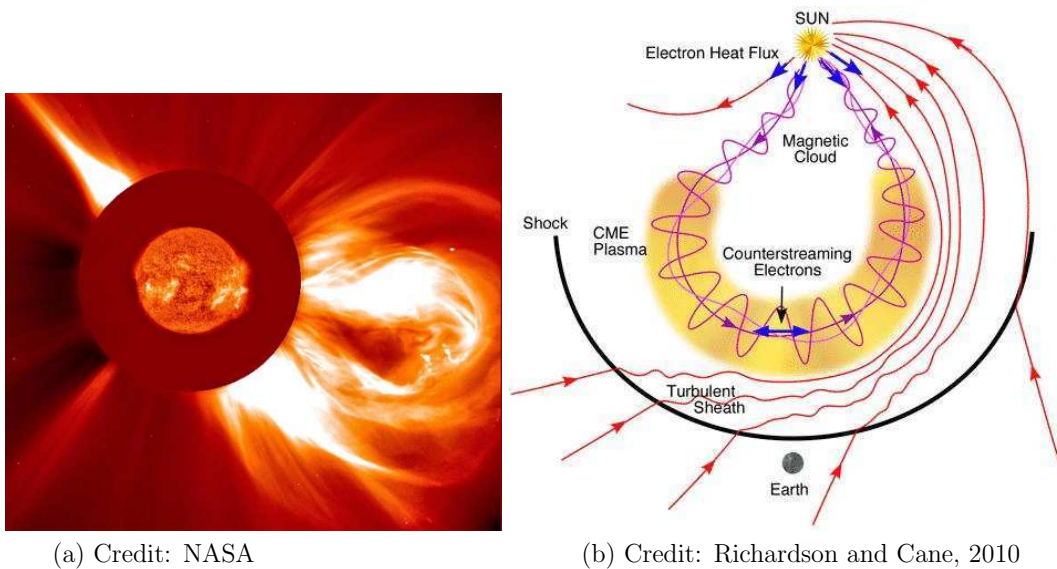
(a) Credit: NASA

(b) Credit: Richardson and Cane, 2010

Figure 2.3: (a) A CME erupting from the Sun. (b) A schematic representation of an ICME and upstream shock indicating magnetic field, plasma and solar wind consisting of electron flows.

of dense plasma that propagate away from the Sun and interact with the surrounding solar wind and interplanetary magnetic field (IMF). They are characterized by twisted magnetic fields that are commonly referred to as magnetic clouds (Moldwin, 2008). They may have a mass larger than 10^{13} kg and may achieve a velocity of over 1000 km/s (Howard, 2014).

CMEs with a linear velocity higher than the solar wind velocity create shocks in the interplanetary medium. These shocks can be identified by observation of a sudden increase in the magnetic field and of plasma velocity, proton temperature and proton density. The area between the shock and the main part of the CME, as illustrated in Figure 2.3(b), is called a sheath. It is possible for a CME to have a sheath without shock. The solar wind is compressed in the sheath resulting in a

increase in magnetic field. These increased magnetic fields often produce high negative values of the IMF Bz component, which cause strong effects on the Earth's magnetosphere (Richardson and Cane, 2010; Paouris and Mavromichalaki, 2017).

2.3.4   Coronal Holes (CHs)

Coronal Holes (CHs) are regions where the Sun's corona is dark, as shown in Figure 2.1(b). They were first observed by measurements made with rocket-borne X-ray telescope, looking at the Sun during the period 1963 - 1969. In 1973 and 1974 CHs were studied in great detail, using the X-ray telescope on the Apollo Telescope Mount (ATM) on the Skylab mission of NASA and their new properties were established (Biswas, 2000). CHs occur when the Sun's magnetic field is open to interplanetary space and are commonly found at the Sun's poles. The open magnetic field lines are the regions where the corona has a low temperature and low density. The open configuration of the magnetic field in CHs allow the solar wind to escape to space, resulting in streams of relatively fast solar wind often referred to as a high speed streams. CHs can develop at any location and time, but are more common during the declining and minimum phase of the 11 years solar activity cycle and they can extend to latitude close to the ecliptic plane. They can last through several solar rotations i.e. 27 days periods. They are more prevalent at the poles of the Sun (South and North poles) but they can grow and expand to the lower latitudes of the Sun. When the particles from these streams hit the Earth they may cause geomagnetic storms. In general, the geomagnetic storms originating from CH have a gradual commencement and are weak to moderate in intensity.

2.3.4.1   Corotating Interaction Regions (CIRs)

Corotating Interaction Regions (CIRs) are the structures formed when the fast solar wind overtakes the slower solar wind as they propagate outward. They produce regions of increased magnetic field strength and density in the solar wind close to the ecliptic plane. During the declining phase of the 11 year solar activity cycle as the Sun rotates, the fast solar wind follows the slow solar wind, and as they propagate away from the Sun, the fast solar wind catches up with the slower wind. During the interaction of the fast and slower solar wind, the plasma at the boundary is compressed and the density in the slow solar wind region is enhanced. The kinetic energy of the plasma in the fast solar wind is converted into thermal energy, resulting in plasma heating and density decreasing. The contact between the fast and slow solar wind is called the stream interface (Kallenrode, 2004; Alves, 2006; Balogh et al., 2013).

The formation of CIRs

CIRs form at the leading edges of corotating high-speed streams as they collide with the preceding solar wind (Richardson, 2006; Tsurutani et al., 2006a). The solar wind flow steamlines, and the magnetic field lines are carried out with the solar wind plasma and are twisted into Archimedian spirals, of the form:

$$r - r_o = -V(\phi - \phi_o)/(\Omega cos\theta) \tag{2.2}$$

where r and ϕ are the heliocentric distance and heliolongitude of the observer respectively, r_o and ϕ_o are the heliocentric distance and heliolongitude of the initial plasma position at the Sun. V is the solar wind speed, Ω is the solar angular velocity (Richardson, 2006). At low latitudes, the

streamlines are inclined at an angle to the outward radial direction as follows:

$$\psi = tan^{-1}\frac{r\Omega}{V} \qquad (2.3)$$

"The streamlines in faster solar wind follow spirals that are less tightly wound" (Richardson, 2006). The collision following from the leading edge of fast solar wind stream with the slower solar wind ahead of it forms a region of enhanced pressure, the CIR that lies approximately along the Archimedian spiral (Richardson, 2006, and references therein). At 1 Astronomical Unit (AU), $r\Omega \approx 400$ km/s and $V \sim 400$ km/s, the IMF, the flow streamlines and CIR are typically inclined at $\psi \sim 45°$ to the radial direction.
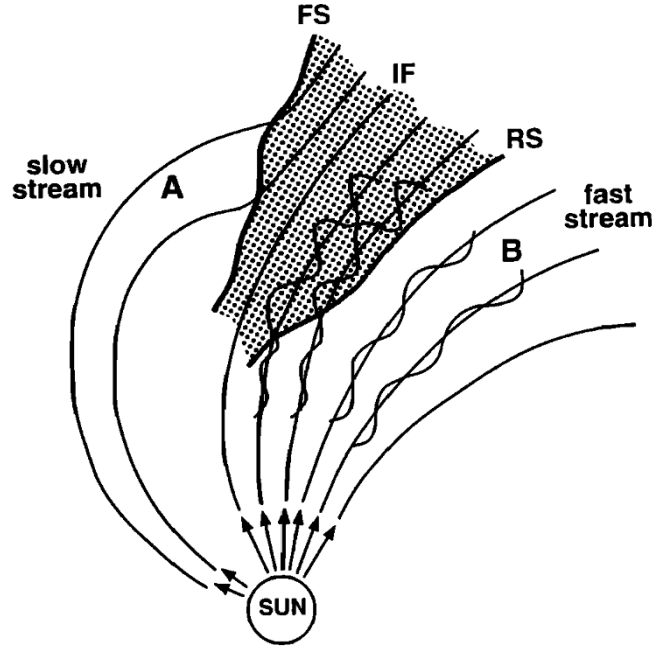
Figure 2.4: Schematic representation of the formation of CIRs due to a fast stream-slow stream interaction. A forward (fast) shock (FS), interface discontinuity (IF), and reverse (fast) shock (RS) are indicated. Shocks typically do not form until a distance of ~1.5 AU to 2.0 AU from the Sun. Figure adapted from Kamide et al. (1998).

Figure 2.4 is a schematic representation of the formation of the CIRs as viewed from the north pole of the Sun; the cut is in the ecliptic plane (Tsurutani et al., 2006a). The shaded region represents the CIR. The boundaries are fast reverse (RS), and fast forward (FS) shocks. Shocks typically form at ~1.5 to 2.0 AU distance from the Sun. The fields and plasma within CIRs are not from the same solar wind source. The outermost of the CIR is compressed, accelerated slow solar wind plasma and fields. The innermost portion is compressed, decelerated fast solar wind plasma and fields (Tsurutani et al., 2006a). The interface discontinuity (IF) separates the FS and RS regions, and is an important feature in a CIR. It is typically characterized by a relatively abrupt fall in plasma density, increase in plasma proton temperature and solar wind speed. The temperature and density changes lead to an increase in the specific entropy (Richardson, 2004, 2006). The azimuthal solar wind flow angle also reverses because the interaction tends to deflect solar wind to the west ahead of the interface and to the east following the interface (Richardson, 2004, 2006, and references therein). The solar activity and associated phenomena such as solar flares, CMEs and CIRs influence changes in the ionospheric electron density.

2.4 The solar wind and Earth's magnetosphere

2.4.1 Solar Wind

The Sun loses mass in three ways, namely, CMEs, the solar wind and Solar Energetic Particles (SEPs) (Gopalswamy et al., 2006). These phenomena are signatures of solar variability. The major variability is represented by electromagnetic radiation in the form of quiescent and flare emissions. The mass emission from the Sun signal the fundamental physical processes like magnetic field reconnection, acceleration of plasmas and interaction between structures of large scale plasmas (Gopalswamy et al., 2006; Heikkila, 2011). There are two main types of solar coronal magnetic field structures, namely, closed and open magnetic field lines where coronal plasma expands into the interplanetary medium and forms solar wind (Davies, 1990; Mullan, 2009; Lang, 2008). The closed field regions such as filament and active regions on the Sun are the origin of the CMEs. On the other hand, the open field regions are known as coronal holes from which the fast solar wind originates. The solar wind is a mixture of electrons and ions of solar origin, mostly protons and a few percent of helium doubly charged ions (Lang, 2008; Heikkila, 2011). The typical solar wind speed is 400 km/s during quiet periods and increase to ∼1000 km/s during disturbed periods. It can take 3 to 4 days for the non-disturbed solar wind to reach the Earth (Davies, 1990; Heikkila, 2011). The rotation of the Sun causes the largest scale structures of the solar wind in the interplanetary medium. A typical density of the solar wind is 5×10^6 protons m^{-3} with an equal density of electrons (Davies, 1990). There are irregularities of ∼105 km and larger within the solar wind which could be noticed by fluctuations of density of an order of magnitude occurring over times of minutes to hours. The mean electron energy is ∼0-25 eV and mean proton energy is ∼ 0-5 keV (Davies, 1990, and references therein). Near the Sun the solar wind speed is small, however, it increases with radial distance and becomes supersonic at a critical distance of about 5 solar radii above the photosphere.

2.4.2 Earth's Magnetosphere

The magnetosphere is the region above the ionosphere in which the magnetic field of the Earth has dominant control over the motions of gas and fast charged particles. It is formed by the interaction of the solar wind with Earth's magnetic field.
Figure 2.5 is a schematic illustration of a cross-section of the Earth's magnetosphere. The sunward and opposite sides of the magnetosphere are referred to as dayside and nightside magnetosphere respectively. The characteristic feature of the nightside magnetosphere is the tail that is elongated over a great distance, namely the magnetotail (Gombosi, 1998; Obara, 2002). The solar wind flows around the Earth's magnetic field creating a geomagnetic cavity (Davies, 1990; Kivelson and Russell, 1995; Gombosi, 1998; Moldwin, 2008). The supersonic flow of the solar wind first encounters the magnetosphere and creates a shock wave. This interaction compresses the magnetosphere on the dayside and drags it out into space at the nightside, creating the magnetotail. The shock wave is called the bow shock, which is a jump in plasma density, magnetic field, and temperature associated with the transition from supersonic to subsonic flow. The bow shock separates free streaming solar wind from the region where the presence of the Earth's magnetic field significantly modifies the space environment (Gombosi, 1998). It slows the solar wind so that the flow can be diverted around the dipole. Over 90% of the solar wind flow is diverted around the magnetosphere while the rest encounters the magnetopause and the smaller fraction gets into the low-latitude boundary layer. Less than 1% of the solar wind gets into the plasma sheet which is responsible for
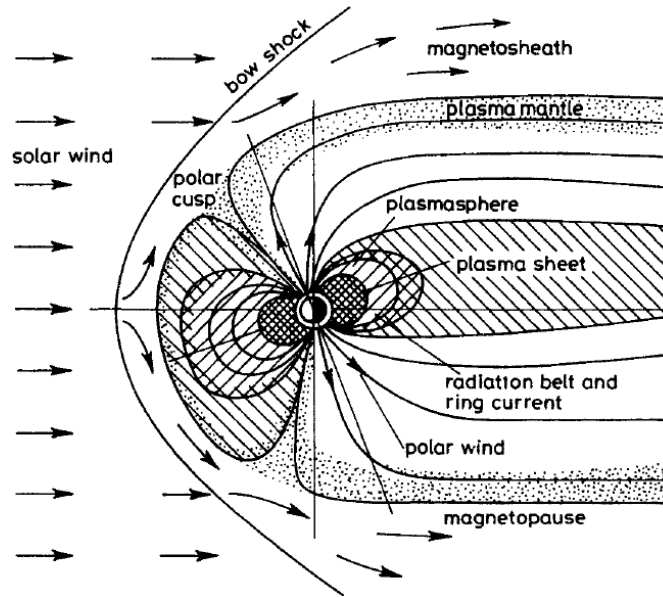
Figure 2.5: The Earth's magnetosphere is formed by the interaction of the solar wind with the magnetic field of the Earth (Davies, 1990).

auroral phenomena (Gombosi, 1998; Heikkila, 2011).

Within the magnetosphere the charged particles are dominated by forces due to the Earth's magnetic and electric fields (Davies, 1990). The region between the magnetosphere and bow shock is the magnetosheath. The magnetosheath is filled with shocked solar wind plasma, which flows around the magnetopause (boundary of the magnetosphere). The magnetic field lines are arranged loosely around the magnetopause. The level of magnetic field turbulence in the magnetopause is higher than in the solar wind and depends on the strength of solar wind pressure (Gombosi, 1998). As solar wind pressure increases the magnetopause is moved earthward and when it decreases the magnetosphere expands (Gombosi, 1998; Moldwin, 2008). The region where the magnetosheath particles have access to the ionosphere is called the polar cusp and is found between the dayside and nightside magnetic field lines (Davies, 1990; Gombosi, 1998).

2.5 Ionosphere

The ionosphere is the part of the Earth's upper atmosphere where electrons and ions are present in quantities sufficient to affect radio wave propagation (Rishbeth and Garriott, 1969). The ionosphere consists of free electrons and ions that are formed during the interaction of solar extreme ultraviolet (EUV) radiation with atoms and molecules in the Earth's upper atmosphere. The term ionosphere was first proposed by R. A. Wattson Watt, in a letter to the United Kingdom Radio Research Board dated 8 November 1926 (Rishbeth and Garriott, 1969) and has been used since about 1932. The ionosphere has a tendency to separate into layers at all latitudes, despite the fact that different processes dominate in different latitudinal domains (Rishbeth and Garriott, 1969; Kelley, 1989; McNamara, 1991; Goodman, 2006; Schunk and Nagy, 2009). The ionosphere is divided into regions namely, the D, E and F regions.
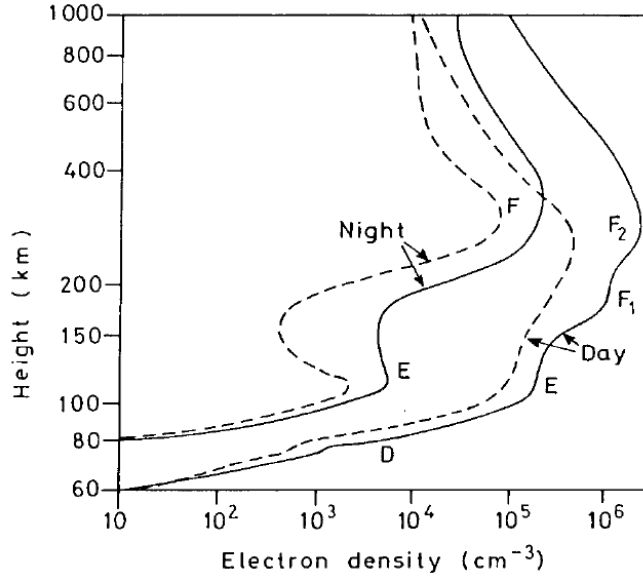
Figure 2.6: The structures and typical vertical profiles of electron density in the mid-latitude ionosphere. Solid and broken lines represent electron density profiles during sunspot maximum and sunspot minimum respectively (Hunsucker and Hargreaves, 2003).

Figure 2.6 illustrates the day and night electron density profiles of the ionospheric layers during sunspot maximum (solid line) and sunspot minimum (broken lines). During the daytime, the ionosphere consists of the D, E, F1 and F2 regions, while in the nighttime only the E and F regions are present. The ionosphere shows high electron densities in the daytime compared to the nighttime. The D layer extends from an altitude of ~50 km to the base of the E-layer. The electron density peaks for the various layers are as follows: D-layer (~ 60) km, E-layer (~ 100) km, F1 -layer ~ 200 km) and F2-layer (~ 300 km) (Rishbeth and Garriott, 1969; McNamara, 1991; Goodman, 2006; Schunk and Nagy, 2009).

There are two important processes that occur in the ionosphere, namely, photoionisation and recombination. Photoionisation is a process by which a photon strips an electron from a neutral atom creating a positively charged ion. On the other hand, recombination is a process by which negatively charged electrons combine with positively charged ions to produce a neutral atom. It is the main process by which electrons are lost in the higher parts of the ionosphere (Vanzandt, 1967; Rishbeth and Garriott, 1969; McNamara, 1991). In the lower ionosphere, the electrons are lost by the process of attachment, in which electrons are attached to neutral molecules and thus become negatively charged ions (Rishbeth and Garriott, 1969; McNamara, 1991). There are two types of recombination namely, radiative and dissociative recombinations. Radiative recombination is a process in which the electrons combine directly with the positively charged ions, converting them into neutral atoms:

$$X^+ + e \rightarrow X + h\nu, \tag{2.4}$$

where X denotes either an atom or molecule. On the the other hand, dissociative recombination is a two-stage process whereby in the first stage, the positive ions are formed by photoionisation interact with the neutral atom or molecules such as nitrogen or oxygen given in the following equation:

$$X^+ + Z_2 \rightarrow ZX^+ + Z, \tag{2.5}$$

where Z_2 is either oxygen or nitrogen molecule. In the second stage, electrons combine with the

13

positively charged molecules ZX^+ giving two neutral atoms as follows:

$$ZX^+ + e \rightarrow Z + X. \tag{2.6}$$

The dissociative recombination has a reaction rate much higher than that of radiative recombination which results in a much shorter lifetime for molecular ions than for atomic ions (Kelley, 1989). Because the molecular ions has a shorter lifetime, when their production is restricted at night, recombination quickly reduces the plasma concentration. The O^+ ions at higher altitudes often survives the night at concentrations between 10^4 and 10^5 cm^{-3}. They are lost through the two step process below the F peak by charge exchange reaction and then dissociative recombination takes place (Rishbeth and Garriott, 1969; Kelley, 1989) as follows:

$$O^+ + O_2 \rightarrow O + O_2^+$$
$$O^+ + NO \rightarrow NO^+ + O \tag{2.7}$$

The ionosphere is dominated by photoionisation during the day and at night recombination takes over (McNamara, 1991). The structure of the ionosphere at any particular location is not simple, because the intensity of the EUV radiation from the Sun is not constant at all wavelengths but is much stronger at some wavelengths depending on the type of atom which is emitting it. The ionosphere height varies with time of day, season, geographic/ geomagnetic latitude, and solar activity. The variation of the ionosphere will be discussed later in this chapter.

2.5.1   Composition of the ionosphere

The atmosphere near the surface of the Earth consists primarily of oxygen molecules (O_2) and nitrogen molecules (N_2). At greater altitudes the atmospheric constituents change significantly. At altitudes of $\sim$100 km and above, molecular oxygen dissociates to atomic oxygen by ultra-violet radiation between 102.7 and 175.9 nm (McNamara, 1991; Hunsucker and Hargreaves, 2003). This is because the atmospheric constituents above 100 km directly absorb solar radiation and can be expressed by the reaction:

$$O_2 + h\nu \rightarrow O + O$$
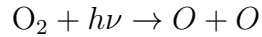
where $h\nu$ is a quantum of radiation. The nitrogen molecule does not dissociate directly to the atomic form in the atmosphere. At night, there is very small amount of radiation input resulting from the high altitude scattering of the solar radiation into the shadow of the planet and other minor sources. The incoming solar X-ray and EUV radiation penetrate the upper atmosphere with sufficient energy to detach an electron from a neutral atom to create an ion and electron pair (Pfaff, 2012),

$$O + h\nu \rightarrow O^+ + e^-$$
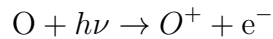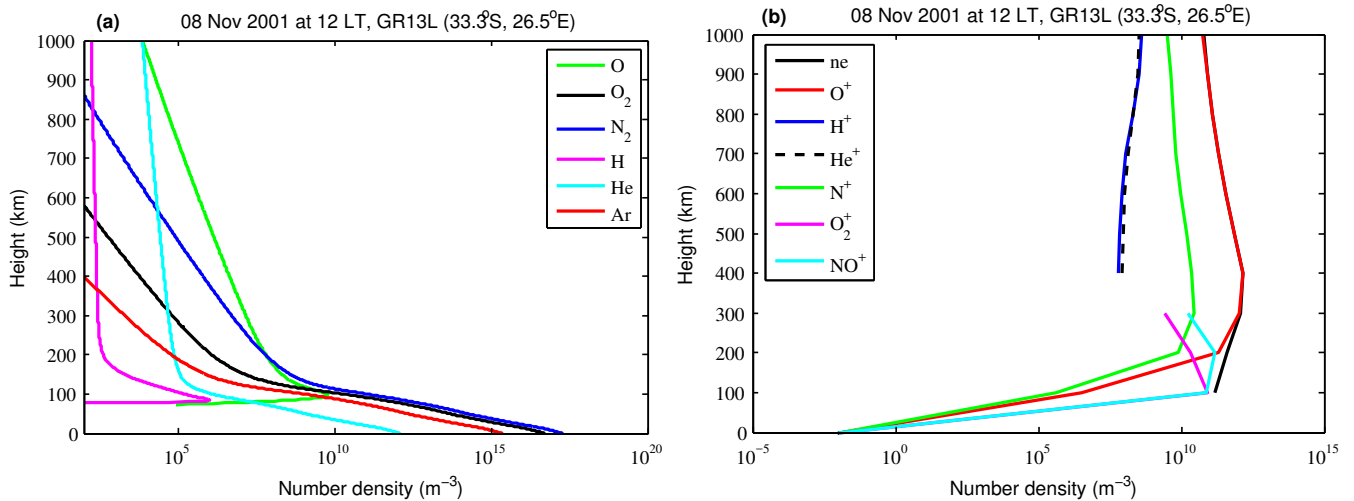
Figure 2.7: (a) Neutral constituents distribution based on NRLMSISE-2000 empirical model of the atmosphere (Picone et al., 2002) and (b) Ionic constituents distribution based on the International Reference Ionosphere (IRI) 2012 empirical model (Bilitza et al., 2011, 2014). The neutral and ionic constituents shown are modeled for Grahamstown, GR13L (33.3°S, 26.5°E; 41.95°S, geomagnetic), mid latitude location at 12 LT.

Figure 2.7 shows (a) neutral constituents obtained using NRLMSISE 2000 empirical model (Picone et al., 2002) and (b) ionic constituents found using International Reference Ionosphere (IRI) 2012 model (Bilitza et al., 2011, 2014) for the mid-latitude location, Grahamstown (33.3°S, 26.5°E) at 12 LT. The molecular constituents (O_2 and N_2) dominate at lower heights and the neutrals (O, H, and He) dominate at higher heights (Schunk and Nagy, 2009). The NO^+ and O_2^+ number densities dominate the lower heights (regions below 300 km) while the N^+ and O^+ ions are more abundant constituents at higher heights (above 300 km).

2.5.2   Mid-latitude ionosphere

The mid-latitude ionosphere is within $60° > \lambda > 20°$ geomagnetic latitude (λ) on each side of the magnetic equator (Wanninger, 1995; Bruno, 2014). It is a buffer between the high and low latitudes phenomena (Kelley, 1989). At mid-latitudes, the production process for the creation of ion-electron pairs is mainly by absorption of solar EUV and X-rays (Rishbeth and Garriott, 1969). The electric field and neutral winds penetrate the mid-latitude ionospheric plasma from the high-latitude sources whereas, the equatorial streams in through the magnetic field lines. The gravity waves continually whirl in from the high-latitude up from the stratospheric and tropospheric sources (Kelley, 1989; Schunk and Nagy, 2009). The neutral winds are significant in transporting ionospheric plasma structures to lower or higher altitudes. The neutral winds are presented in zonal (east - west), meridional (north - south) and vertical components. The neutral wind blows away from the sub-solar point poleward and it drives the ionisation down the magnetic field lines on the dayside. However, on the night side, meridional wind blows from the poles toward the equator, and the ionisation is driven up the field lines (Rishbeth and Garriott, 1969; Rees, 1989; Buonsanto et al., 1990; Schunk and Nagy, 2009).

2.5.3   Low / equatorial latitude ionosphere

The low latitude ionospheric region is within $0° < \lambda < 20°$ geomagnetic latitudes on each side of the magnetic equator (Wanninger, 1995; Bruno, 2014). The ionosphere at the equator varies from the mid and high latitudes ionosphere. At low latitudes, the geomagnetic field lines are nearly horizontal, and initiate some unique transport effects. The first is the equatorial anomaly, also known as the Appleton anomaly, which was first identified by Appleton (1946). He reported that for noon equinox conditions the F2 layer critical frequency exhibits an equatorial trough in its latitudinal distribution. The equatorial anomaly is associated with a significant departure in the latitudinal distribution of the maximum ionisation concentration within 20° to 30° on either side of the equator. A single peak of ionisation is observed in the early morning over the magnetic equator. Nevertheless, after a few hours the equatorial F-region is characterised by two distinct crests of ionisation that increase in electron density as they move poleward. The result is called the fountain effect initiated by an $\mathbf{E} \times \mathbf{B}$ plasma drift, where $\mathbf{E}$ is the equatorial electrojet electric field and $\mathbf{B}$ is geomagnetic field vector. The equatorial electric field is eastward during the day and hence the drift is upwards. As the electrojet decays, the displaced plasma is subjected to downward diffusion which is constrained along paths parallel to the geomagnetic field, which maps to either side of the geomagnetic equator. The poleward extent of the anomaly crest is increased if the initial plasma drift amplitude is large (Hanson and Moffett, 1966; Kelley, 1989; Davies, 1990; Brekke, 1997; Goodman, 2006; Schunk and Nagy, 2009).

Second, the meridional neutral wind, which can induce inter-hemispheric plasma flow along the geomagnetic field lines, is downward during the day and upward at night. The meridional neutral wind blows across the equator from the southern (summer) to the northern (winter) hemisphere at solstice. It acts to transport ionospheric plasma up the field line in the summer hemisphere and down the field line in the winter hemisphere (Schunk and Nagy, 2009).

2.5.4   High latitude ionosphere

The high latitude ionosphere region is within $90° > \lambda > 60°$ geomagnetic latitudes on each side of the magnetic equator (Wanninger, 1995; Bruno, 2014). It is subject to the highest variability of all regions because of its connection via the Earth's magnetic field to the magnetosphere and the interplanetary medium. It is controlled mainly by solar wind which is also variable. The main contributors to ion production at high latitudes are the energetic charged particles from the Sun (Hunsucker and Hargreaves, 2003; Bruno, 2014). The main feature of the high latitudes is the "trough" of lesser ionisation which is formed between the auroral and mid-latitude ionospheres. The fundamental cause of the trough is the difference in circulation patterns between the inner and outer parts of the magnetosphere (Hunsucker and Hargreaves, 2003; Bruno, 2014). It is affected by sporadic events, which can seriously degrade polar radio propagation (Hunsucker and Hargreaves, 2003). The auroral zones occur within the high latitude region and their location depends on the linkage with the magnetosphere. Electrojets, which cause magnetic disturbances, form part of the auroral phenomena in which the rate of ionisation is greatly increased (Hunsucker and Hargreaves, 2003). In summer and winter, the high latitude ionosphere may be in continuous daylight and darkness respectively. During these periods the ionosphere will be typical of daylight or nighttime conditions respectively (Davies, 1990).

2.5.5 Ionospheric variation

Ionospheric variations can be broadly categorised as periodic and random on a relatively short time scale. Periodic variability includes diurnal and seasonal variations while the random aspects are related to solar and geomagnetic activities. The ionosphere also varies with geographic/geomagnetic location.

2.5.5.1 Diurnal variation

The ionosphere varies with time of day, which is due to the Earth's rotation into and out of the sunlight. Diurnal variation occurs mostly in the lower altitude of the ionosphere, reaching its maximum values near noon when the solar zenith angle is smallest (Schunk and Nagy, 2009). The daytime ionosphere has peak electron density at ∼300 km altitude and at high altitude it decays steadily.
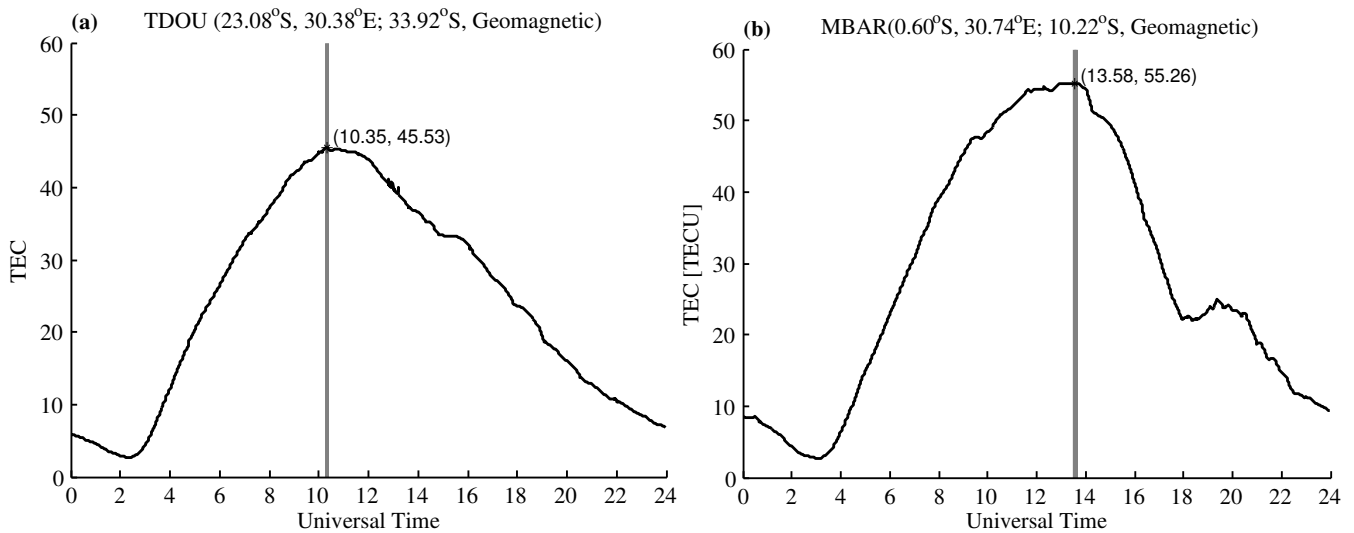
Figure 2.8: Variation of monthly median values of Total Electron Content (TEC) for (a) mid-latitude station Thohoyandou, TDOU (23.08°S, 30.38°E; 33.92°S, geomagnetic), South Africa and (b) low-latitude Mbarara, MBAR (0.60°S, 30.74°E; 10.22°S, geomagnetic), Uganda for November 2013. The grey vertical lines indicates the time (in hours) of maximum TEC.

Figure 2.8 shows the diurnal variation of monthly median Total Electron Content (TEC) values for the mid-latitude, Thohoyandou, TDOU (23.08°S, 30.38°E; 33.92°S, geomagnetic), South Africa and low-latitude, Mbarara, MBAR (0.60°S, 30.74°E; 10.22°S, geomagnetic), Uganda stations in November 2003. The grey horizontal line in the figure indicates the time of the maximum of the monthly medians of TEC during November 2013. The physical processes that control the diurnal variation of the electron density changes with time of day and geomagnetic latitude. The TEC values vary throughout the day, with low TEC values in the morning and night times over both mid and low latitude stations. The TEC values peak at 10.35 UT and 13.58 UT over TDOU and MBAR stations respectively.

2.5.5.2 Seasonal variation

The seasonal variation of the ionosphere is partly due to the zenith angle of the Sun which varies with time of day and season. Every time the solar zenith angle changes, the ionosphere also changes.

In summer, the solar zenith angle at noon is always smaller compared to the corresponding angle in winter.
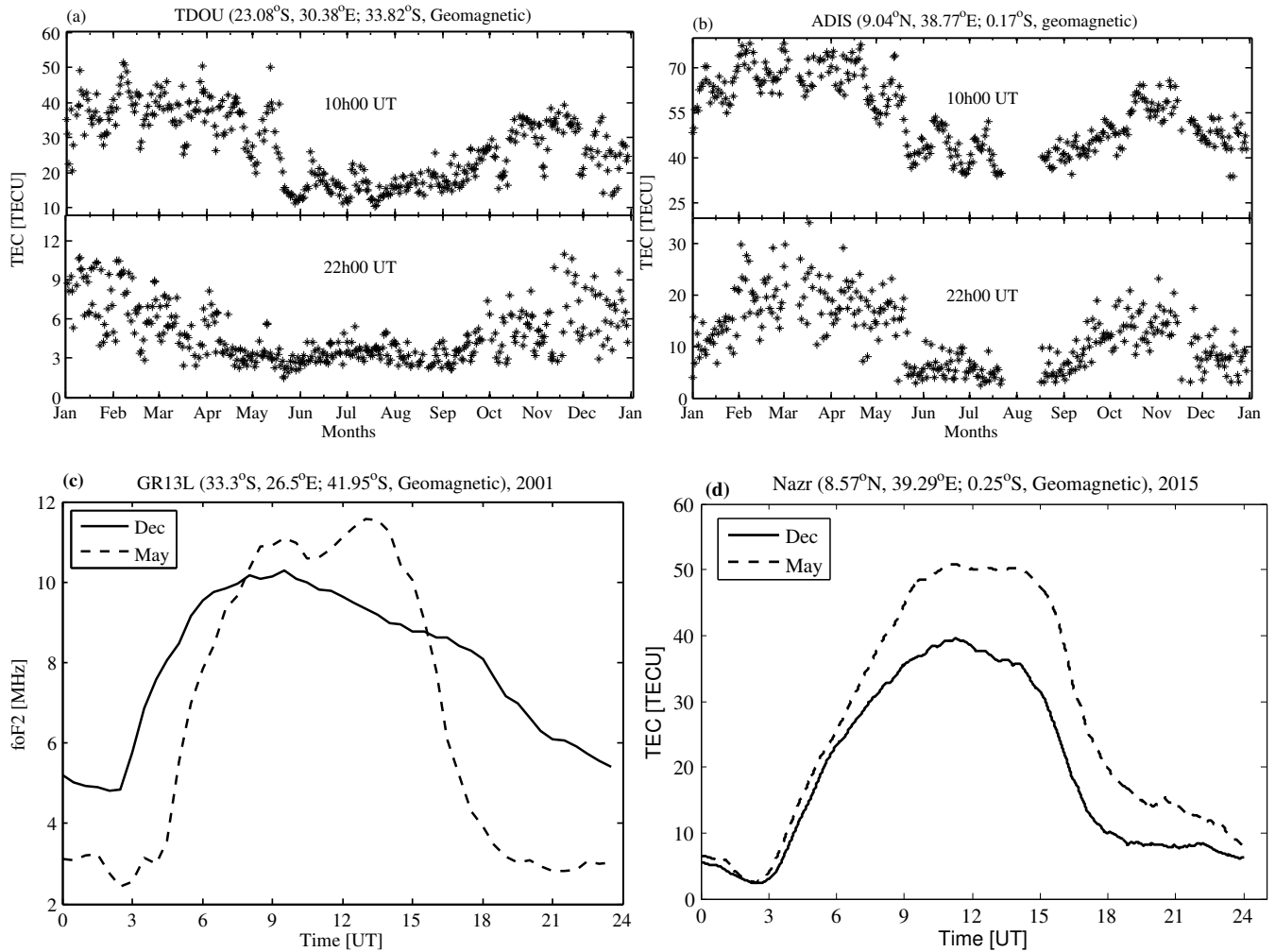
Figure 2.9: Seasonal variation of TEC over (a) mid-latitude Thohoyandou, TDOU (23.08°S, 30.38°E; 33.92°S, geomagnetic), South Africa and (b) equatorial latitude, Addis Ababa University, ADIS (9.04°N, 38.77°E; 0.17°S, geomagnetic), Ethiopia at 10h00 UT and 22h00 UT for 2013. (c) The monthly median of the critical frequency of the F2 layer (foF2) over mid-latitude Grahamstown, GR13L (33.3°S, 26.5°E; 41.95°S, geomagnetic), South Africa station during May (winter) and December (summer) 2001. (d) is the monthly median of TEC over the equatorial latitude at Nazret, NAZR (8.57°N, 39.29°E; 0.25°S, geomagnetic), Ethiopia during May and December months for 2015.

Figure 2.9(a) and (b) illustrate the seasonal variation of TEC values at 10h00 UT and 22h00 UT over mid-latitude Thohoyandou, TDOU (23.08°S, 30.38°E; 33.92°S, geomagnetic), South Africa and equatorial latitude Addis Ababa University, ADIS (9.04°N, 38.77°E; 0.17°S, geomagnetic), Ethiopia for 2013. Figure 2.9(c) shows monthly median values of critical frequency of F2 layer (foF2) for December (summer) and May (winter) for 2001 over mid-latitude, Grahamstown, GR13L (33.3°S, 26.5°E; 41.95°S, geomagnetic), South Africa. The TEC values are higher in summer than in winter at 10h00 and 22h00 over both mid- and equatorial latitude stations (Figure 2.9(a) and (b)). In general the nighttime foF2 values are greater in summer than in winter (Rishbeth and

18

Garriott, 1969; Davies, 1990) as shown in Figure 2.9(c). Moreover, the foF2 values during the daytime are greater in winter (May) than in summer (December). This process is called the seasonal or winter anomaly. This process is a daytime phenomenon and vanishes at night. The seasonal anomaly is more apparent during high solar activities (Rishbeth and Garriott, 1969) and occurs because of the seasonal changes in the neutral atmosphere. To be more precise, the summer to winter neutral circulation results in a decrease in the O/N_2 ratio in the summer hemisphere and an increase in the winter hemisphere. The enhanced O and depleted N_2 densities in winter act to increase the O^+ densities, due to the relative increase in the production rate and decrease in the loss rate. Overall, the O^+ densities in winter are larger than those in summer at F-region altitudes (Rishbeth and Garriott, 1969; Davies, 1990; McNamara, 1991; Schunk and Nagy, 2009).

2.5.5.3   Solar activity variation

The solar cycle variation is related to change in the solar EUV and X-ray radiation fluxes. Various parameters indicate solar activity, for example, sunspot numbers (SSN), solar radio flux with wavelength of 10.7 cm, grouped solar flares, solar flare index, coronal index, and tilt angle (Rishbeth and Garriott, 1969; McNamara, 1991; Schunk and Nagy, 2009). In general, the SSN shows a high correlation with solar activity (Gupta et al., 2007).
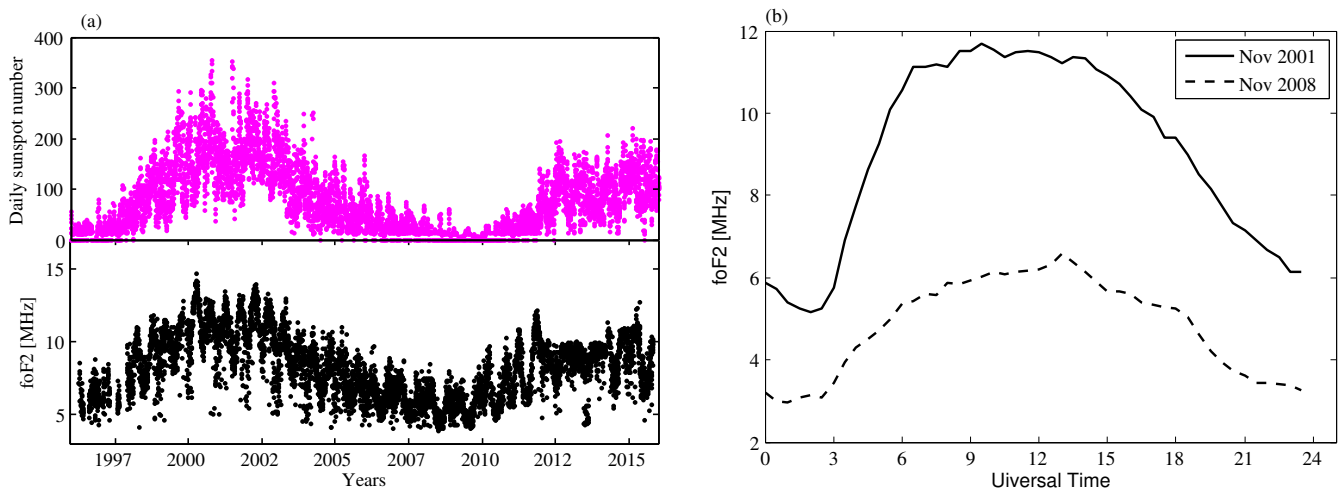
Figure 2.10: (a) The variation of foF2 values (bottom panel, black) over Grahamstown, GR13L (33.3°S, 26.5°E; 41.95° geomagnetic) for the period 1996 - 2015 at 10:00 UT and the daily sunspot numbers (top panel, magenta). (b) The diurnal variation of foF2 during November 2001 (solar maximum) and November 2008 (solar minimum) over Grahamstown station.

Figure 2.10(a) shows the variation of foF2 (bottom panel) over the mid-latitude station, Grahamstown (33.3°S, 26.5°E; 41.95°S, geomagnetic) with SSN (top panel) during solar cycles 23 and 24. Figure 2.10(b) shows the diurnal variation of average foF2 values during solar maximum (November 2001) and solar minimum (November 2008) over Grahamstown. Figures 2.10(a) and (b) show that higher foF2 values were observed during solar maximum than during solar minimum. This could be, because during solar maximum, the solar EUV fluxes and the atomic oxygen densities are greater than those at solar minimum, and these conditions lead to higher ionisation densities (Schunk and Nagy, 2009). Over the low latitudes, high electron densities are also observed during solar maximum.

2.5.5.4 Geographic and geomagnetic variation

Ionospheric parameters such as electron density, critical frequency, height and TEC can be used to study ionospheric variation (Rishbeth and Garriott, 1969; Davies, 1990; McNamara, 1991). In this work, global TEC maps were used to show the geographic/geomagnetic variation of the ionosphere.
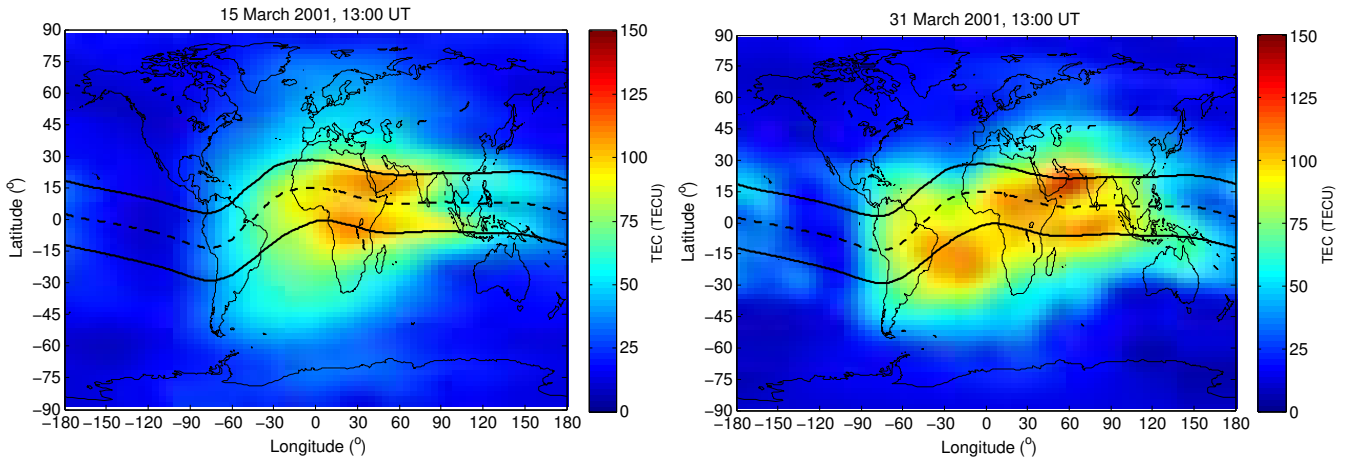
Figure 2.11: Global TEC maps of 15 March 2001 (geomagnetic quiet day) and 31 March 2001 (geomagnetic disturbed day) at 13:00 UT. The IONosphere Exchange (IONEX) data was obtained from ftp://cddis.gsfc.nasa.gov/pub/gps/products/ionex/2001/.

Figure 2.11 shows global IONosphere Exchange (IONEX) TEC maps at 12:00 UT on 15 March 2001 (geomagnetic quiet day) and 31 March 2001 (geomagnetic disturbed day). The geomagnetic equator is represented by a black dashed line whereas, the two solid lines below and above it represent the equatorial ionisation anomaly crests at $\pm 15°$. Maximum TEC occur at about $15°$ to $20°$ from the geographic equator in both hemispheres on 15 March 2001 (geomagnetic quiet day). During disturbed conditions on 31 March 2001, the enhanced TEC expanded to the mid-latitude regions. This could be due to electrodynamic lifting at the magnetic equator. When the plasma is lifted up due to horizontal electric field produced by dynamic action in the E region, the plasma will drift due to combination of thermal diffusion and electrodynamic drift along the magnetic field lines to higher latitudes. This phenomena is called the fountain effect or the Equatorial Ionisation Anomaly (EIA) (Rishbeth and Garriott, 1969; Kelley, 1989; Davies, 1990; Brekke, 1997). Intense geomagnetic storms (disturbances in the Earth' magnetosphere) are often characterized by drastic long-term changes in the ionosphere i.e. the dayside ionospheric uplift and development of the dayside ionospheric super-fountain effect. The dayside TEC within the crests of EIA can exceed $\sim 25\%$ of the background levels. The EIA descends poleward for more than $10°$ - $15°$ latitude from the regular position, spreading towards mid-latitudes (Tsurutani et al., 2004; Astafyeva et al., 2014).

2.6 Summary

Important aspects on the Sun and its activities namely, solar flares, prominences, CMEs, CH, CIRs were discussed. Furthermore a description of solar wind and Earth's magnetosphere was provided. A brief background of the mid-, low or equatorial and high latitude ionosphere was also given. This chapter ends by discussing how the ionosphere varies with time of the day (diurnal), season, solar activities and geographic/ geomagnetic latitude.

Chapter 3

Geomagnetic and ionospheric storms

3.1 Introduction

This chapter briefly discusses geomagnetic storms and their effect on the ionosphere. During geomagnetic storms, the ionosphere may sometimes be affected severely and could result in what is called ionospheric storm effects. This chapter will also describe some of the mechanisms responsible for ionospheric storm effects.

3.2 Geomagnetic storms

A geomagnetic storm is a temporary disturbance of the Earth's magnetosphere which results from solar flares, high stream solar wind and Coronal Mass Ejections (CMEs). The term geomagnetic/magnetic storms was coined by Alexander von Humboldt in 1800s (Gonzalez et al., 1994; Akasofu, 2007). The changes of geomagnetic field are produced by various electric currents that develop around the Earth when solar disturbances reach this planet (Akasofu, 2007). The principal feature of a geomagnetic storm is a decrease of the horizontal (H) component intensity and its subsequent recovery (Gonzalez et al., 1994). This decrease in H component is due to an increase of the trapped magnetospheric particle population and can be monitored by Disturbance storm time (Dst) index (Gonzalez et al., 1994). It is now commonly assumed that the magnitude of the geomagnetic storm can be defined by the minimum Dst value (Gonzalez et al., 1994).
Figure 3.1 shows a typical profiles of magnetic storms caused by a CME and a Corotating Interaction Region (CIR) during 17 - 20 March 2015 and 02 - 12 January 2008 respectively. The two types of geomagnetic storms both have initial, main and recovery phases. However, their scale sizes, both in terms of duration and amplitude, are quite different, because their interplanetary causes are distinct from each other (Tsurutani et al., 2006a).

3.2.1 Initial phase

The initial phase of a geomagnetic storm is characterised by a positive increase in the Dst index. The initial phases of the interplanetary CME-driven storms typical start abruptly. The increases in the H component of near-equatorial magnetic fields at Earth can occur in time scales of seconds. The abrupt jumps are caused by sudden enhancement of ram pressure impinging upon the magnetosphere. The enhancement of ram pressure is due to immediate increase of solar wind plasma density and velocity following fast forward shocks upstream of interplanetary CMEs (Kamide et al.,
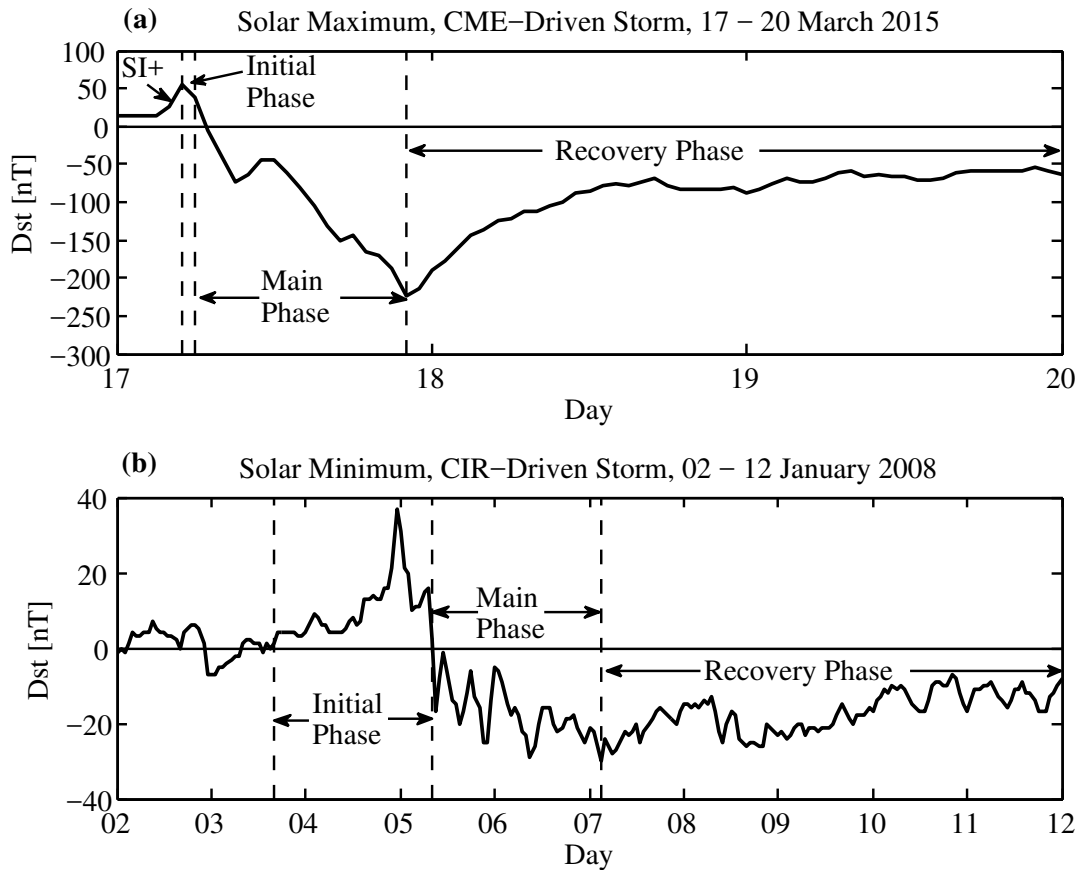
Figure 3.1: An example of (a) solar maximum, CME-driven storm during 17 - 20 March 2015 and (b) solar minimum, CIR-driven storm from 02 - 12 January 2008 measured by Dst index. The CME and CIR-driven storms are both characterised by initial, main and recovery phases. The CME-driven storm is also characterised by a short-duration positive spike (SI+) in the Dst data.

1998; Tsurutani et al., 2006a). The sudden increases in the Earth's near-equatorial magnetic field have been called sudden impulses (SIs) or a sudden storm commencement, which has been replaced by a short duration positive (SI+) spike in the Dst index (Joselyn and Tsurutani, 1990; Tsurutani et al., 2006a). The term SI+ is used only when the SI is followed by magnetic storm (Joselyn and Tsurutani, 1990; Tsurutani et al., 2006a). The SI+ is caused by the impact of the shock wave on the magnetosphere and is generated by a solar plasma or magnetic cloud advancing in the solar wind after being ejected during solar activities (Akasofu, 2007). The negative SI (SI$^-$) is due to fast reverse shock which is characterised by a negative jump in the interplanetary magnetic field and interplanetary plasma parameters (such as temperature and density). Matsushita (1962) noted that SI$^-$ is characterised by a small negative impulse preceding the positive impulse. SI$^-$ is observed as a decrease in horizontal geomagnetic field strength and occurs because of the expansion of the magnetosphere due to a decrease in solar wind pressure (Nishida and Cahill, 1964; Joselyn and Tsurutani, 1990; Andrioli et al., 2007).

On the other hand, the initial phases of the CIR-driven storms typically have gradual onsets. At the beginning of an event there are no SI+, which is due to lack of shocks preceding corotating stream at 1 AU, as discussed before. The H-component of the Earth's magnetic field is highly variable, indicating variable interplanetary ram pressure (Tsurutani et al., 2006a).

3.2.2 Main phase

The main phase of a storm is due to the formation of a ring current belt of energetic particles that surrounds the Earth (Hargreaves, 1992; Kamide et al., 1998; Akasofu, 2007). The diamagnetic effect of the ring current particles associated with gradient and curvature drifts of electrons, protons and oxygen causes decreases in the H-component of the near-equatorial magnetic field (Tsurutani et al., 2006a, and references therein).

CME-driven storm main phases generally develop smoothly. They are caused by a step-like decrease in the southward component of the magnetic field across the shocks antisunward of the ICME, or by the southward magnetic field within magnetic clouds (Tsurutani et al., 2006a, and references therein). The magnetic clouds are the most geoeffective parts of the ICMEs. The two-step main phases results when there are southward sheath fields followed by magnetic clouds with southward component magnetic fields (Tsurutani et al., 2006a). The intensity of CME-driven storm main phase can be from as little as Dst = -25 nT to as large as hundreds of nT. The duration can be as short as a few hours and in exceptional cases, can be as long as a day. Almost all major geomagnetic storms of Dst < -100 nT are due to magnetic clouds within the ICMEs (Gonzalez et al., 1999; Tsurutani et al., 2006a,b).

In contrast, the CIR-driven storm main phases are irregular in profile. They typically last about a day and are weak to moderate (-25 nT > Dst >-75 nT) in intensity. The cause of the main phase is the southward component of the IMF Bz within the CIRs (Tsurutani et al., 2006a).

3.2.3 Recovery phase

The recovery phase of a geomagnetic storm starts at the interval when the depressed horizontal fields return to normal levels (Tsurutani et al., 2006a,b; Akasofu, 2007). For CME-driven storms, after the main phase, the losses of the electrons, energetic protons and oxygen ions forming the ring current cause the decrease of the diamagnetic current and thus the increase in the Dst index to quiet time values (Tsurutani et al., 2006a). However, the recovery phases of CIR-driven geomagnetic storms are long compared to CME-driven storms. They can last for days to many weeks (Tsurutani et al., 2006a,b).

3.2.4 Classification of geomagnetic storms

As already discussed, the principal defining property of geomagnetic storm is the enhancement of the ring current which leads to a significant depression of the Dst index (Loewe and Prölss, 1997). The geomagnetic storm intensities may be classified as follows:

Table 3.1: Geomagnetic storms classification

Storm class	Dst [nT]	Classification
1	-25 to -50	weak
2	-50 to -100	moderate
3	-100 to -200	strong
4	-200 to -350	very strong
5	-350 to -400	great
6	< -400	extreme

Table 3.1 shows the geomagnetic storm classification based on previous studies (e.g. Gonzalez and Tsurutani, 1987; Gosling et al., 1991; Gonzalez et al., 1994; Tsurutani et al., 1995b; Loewe and Prölss, 1997; Gonzalez et al., 1999; Tsurutani et al., 2006b; Echer et al., 2008; Gonzalez et al., 2011).

3.3   CIR- and CME-driven storms

The sources of geomagnetic storms may be divided into two categories based on their solar wind drivers, namely CME and CIR. The CME-driven storms may cause problems for the Earth-based electrical systems such as power grids (Borovsky and Denton, 2006; Moldwin, 2008) while CIR-driven storms, on the other hand, pose more problems for space-based assets (Borovsky and Denton, 2006). Borovsky and Denton (2006) compiled a summary of differences between CME- and CIR-driven storms.

3.3.1   CME-driven storms

CMEs originate from the Interplanetary Magnetic Field (IMF) southward component in the CME flux ropes and in the sheath between the CME-driven shock and flux rope (Echer et al., 2008; Gopalswamy, 2009). The CME-driven storms are more frequent during solar maximum even though they occur throughout the cycle (Gopalswamy, 2004; Borovsky and Denton, 2006; Tsurutani et al., 2006a, and references therein). Solar Energetic Particles (SEP) events such as strong interplanetary shocks and solar flares are phenomena associated with CMEs, hence they sometimes accompany CME-driven storms. The intensity of SEP is correlated with the velocity of the coronal ejecta driving the shocks. The SEP events can be large enough to pose a hazard to aircraft passengers and electronics and to astronauts in high latitude orbit (Borovsky and Denton, 2006). The ion and electron temperature for CME-driven storms are substantially elevated over typical values. A CME drives a plasma sheet that is more dense than that of CIR and the high-density values persist longer (Borovsky and Denton, 2006, and references therein).

3.3.2   CIR-driven storms

CIR-driven storms include storms driven by High-Speed Solar Wind Streams (HSSWSs) that follow the CIR. The HSSWSs are produced by solar flare activity or by coronal holes. A corotating coronal hole is a low-temperature and low-density area in the Sun's atmosphere. As the Sun rotates, coronal holes pass across the Sun-Earth line, and the HSSWSs catch up with the previously emitted solar wind and form an interface in the interplanetary medium called CIR (Mavromichalaki et al., 1988; Xystouris et al., 2014). CIR-driven storms occur mainly during the declining phase and solar minimum years of the solar activity. During descending and minimum solar activity, the recurrent of coronal holes High Speed Stream (HSS) have a high possibility of occurrence (Tsurutani et al., 1995b). Thus, their recurring effects can be observed on Earth for several days or weeks, lasting up to an entire solar rotation (~ 27 days) (Tsurutani et al., 1995b). Most recurring CIRs have an extended interval (1–2 days) of extreme geomagnetic calm (Kp $\geq 1^+$) within 24 hours before storm onset (Borovsky and Denton, 2006, and references therein). The electron and ion temperature for CIR-driven storms are beyond typical values. The temperature for CIR-driven storms remains elevated for longer period (days) (Borovsky and Denton, 2006, and references therein).

3.4   Thermospheric storms

Thermospheric storms are severe perturbations of the neutral upper atmosphere (mainly at altitudes between 100 and 1000 km) caused by solar wind energy (Prölss and Roemer, 1987). Solar wind energy continuously affects the electron density of the polar upper atmosphere, even during geomagnetically quiet conditions. The energy addition is sufficient to generate a permanent disturbance zone which is characterised by a significant increase in the molecular nitrogen (N_2) density and simultaneous depletion in Oxygen (O) density (Mayr and Trinks, 1977; Prölss, 1980; Prölss and Roemer, 1987; Prölss, 1995). The composition zone/bulge can expand towards the mid-latitude regions following geomagnetic disturbances (Prölss, 1995). The composition zone responds to both storm-induced and background horizontal winds and does not rotate with the Earth. During the storm the disturbance wind modulates the location of the composition zone (Fuller-Rowell et al., 1994).

During geomagnetic storms, enhanced energy deposition from the magnetosphere in the form of Joule and particle heating causes a strong upwelling of the atmosphere around the auroral zone. The strong upwelling of the atmosphere transports nitrogen-rich or oxygen-depleted air up from much lower in the thermosphere into the F-region (Mayr and Volland, 1972; Mayr and Trinks, 1977; Prölss, 1980; Prölss and Roemer, 1987; Rishbeth et al., 1987; Prölss, 1995; Zhang et al., 2004; Liou et al., 2005). The horizontal neutral winds will then redistribute the nitrogen-rich/oxygen-depleted (N_2/O) air over the high-latitude and part of the mid-latitude regions. The N_2/O air causes a reduction in the ionisation density of the F-region heights (Prölss, 1995; Zhang et al., 2004).

3.4.1   Ionospheric storm effects

Ionospheric storms are the perturbations of the Earth's upper atmosphere caused by geomagnetic storms. The ionosphere responds noticeably to varying solar and magnetospheric energy inputs. Dynamic electric field effects, neutral winds, and composition changes following a geomagnetic storm have a major impact on electron density of the ionospheric F-region. The electron density in the ionosphere may either decrease or increase during geomagnetic storms (Appleton and Piggott, 1952; Matsushita, 1959, 1963; Prölss, 1995; Buonsanto, 1999; Mendillo, 2006), and sometimes alteration of both. The increase or decrease in electron density are termed positive or negative ionospheric storm effects respectively (e.g. Prölss, 1995; Buonsanto, 1999; Moldwin, 2008). The ionospheric storm effects depend on the onset time of the geomagnetic storm, geomagnetic/geographic location, season and solar activity (e.g. Prölss, 1977, 1980, 1993b, 1995; Mendillo, 2006; Vijaya Lekshmi et al., 2011; Bagiya et al., 2011; Habarulema et al., 2013b).

In determining the nature of the ionospheric storm as a result of geomagnetic storm occurrence, parameters such as ionospheric total electron content (TEC) and critical frequency of the F2 layer (foF2) are used. In these cases, the measure of disturbance is determined by using the deviations calculated by

$$\Delta X = \frac{X - X_{mm}}{X_{mm}} \times 100\% \tag{3.1}$$

where X represents time series foF2 or TEC during the storm period and X_{mm} is the monthly median of TEC or foF2 when a storm occurred (e.g Danilov and Lastovicka, 2001; Burešová and Laštovička, 2007; Matamba et al., 2015). Ionospheric storm effects are classified based on the nature of the dominant deviation values of ΔX during quiet periods prior to the geomagnetic storm. The consideration of quiet periods before and after the storm leads to five classes of ionospheric storms, namely positive (P), negative (N), positive-negative (PN), negative-positive

(NP) and not significant (NS) ionospheric storm effects. The P and N correspond to increase and decrease in ΔX respectively. For PN and NP, an increase followed by a decrease in ΔX and vice versa is observed, while NS indicates a no significant effect on ΔX (e.g. Adeniyi, 1986; Gao et al., 2008; Vijaya Lekshmi et al., 2011; Matamba et al., 2015).

3.4.2   Negative ionospheric storm effects

Figure 3.2 illustrates an example of N ionospheric storm effects over MBAR ($0.60°$S, $30.74°$E; $10.22°$S, geomagnetic), Uganda, southern hemisphere during 11 - 14 January 2005. Figure 3.2 presents (I) Dst index (nT), (II) Kp index and (III) deviations of TEC (ΔTEC (%). The shaded region on the figure highlights the part where the negative ionospheric storm effect occurred. Dst index was at its minimum on 12 January 2005. There was a decrease in ΔTEC ($\sim 70\%$) on 12 January 2005.
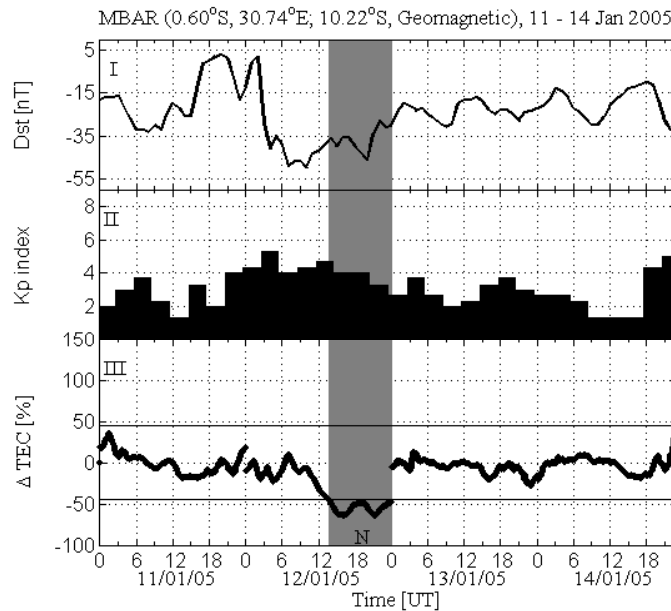
Figure 3.2: An example of a negative ionospheric storm effect.

The decrease in electron density in the F-region during a geomagnetic storm was first suggested by Seaton (1956) and it was believed that the negative ionospheric storm effect was due to changes of atmospheric constituents, especially an increase in number of molecular oxygen (Matsushita, 1959). It is accepted that negative ionospheric storm effects over the mid-latitudes are due to neutral composition changes (e.g Prölss, 1976; Prölss and Fricke, 1976; Prölss, 1977, 1980; Titheridge and Buonsanto, 1988; Fuller-Rowell et al., 1994; Prölss, 1995; Fuller-Rowell et al., 1996; Prölss, 2004; Mendillo, 2006). During geomagnetic storms, a large amount of energy is deposited in the high-latitude region of the upper atmosphere, and leads to the development of disturbance zones in the neutral composition (Prölss, 1980; Prölss et al., 1988). Figure 3.3 illustrates the schematic representation of neutral disturbance zone as well as the energy injection in the high latitude regions (Prölss, 1980, 1995).

During geomagnetic storms, intense Joule and particle heating causes strong upwelling of the atmosphere around the auroral oval, which leads to a variety of dynamic and chemical changes in

the atmosphere. The strong upwelling of the atmosphere transports oxygen-depleted or nitrogen-rich air from lower down in the thermosphere into the F-region (e.g. Prölss, 1980, 1995; Zhang et al., 2004).

Neutral winds then redistribute this nitrogen-rich/oxygen-depleted air over much of the high-latitude region and part of the mid-latitude region. The nitrogen-rich/oxygen-depleted air causes a reduction in the ionospheric electron density. The transport is strongest during postmidnight hours owing to wind surges arising from ion convection and the associated momentum transfer to neutrals. With a sufficiently strong wind surge, the disturbed region extends to low latitude and co-rotates with the Earth (Prölss, 1980, 1995; Prölss et al., 1988). The negative ionospheric storm effects are caused by enhanced molecular nitrogen in regions of sunlight (Fuller-Rowell et al., 1994).
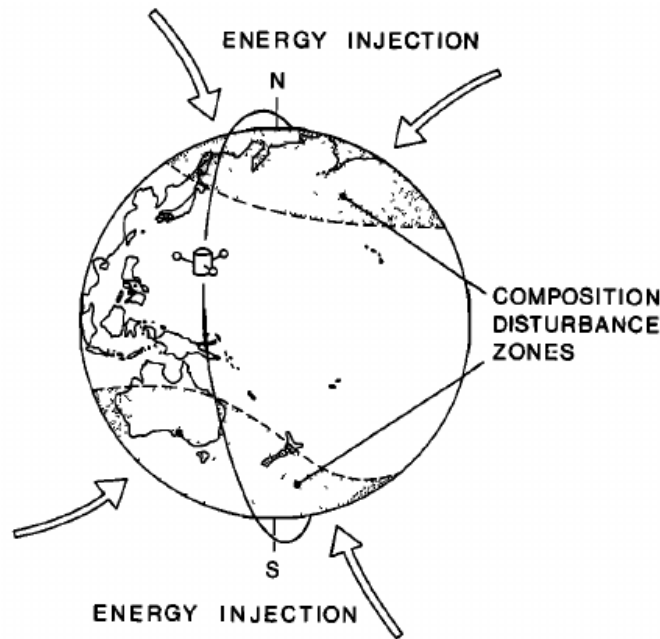
Figure 3.3: A schematic representation of energy injection and the formation of neutral disturbance zones during a geomagnetic storm (Prölss, 1980).

Figure 3.4 shows a direct correlation between the maximum electron density (N_{max}) of the F region and O/N_2 ratio densities over the southern and northern hemisphere mid-latitude stations for the time interval 17 - 25 February 1973 and 25 - 31 October 1973 respectively (Prölss, 1980). The coordinates of the stations are also indicated in the figures. The quiet time periods are days 17 - 20 February 1973 (Figure 3.4(a)). The storm occurred on 21 February 1973. Over the northern hemisphere, 26 - 27 October 1973 were quiet days, while 29 and 30 October 1973 were disturbed days. Note that the selected stations are under the disturbance zone. It is evident from Figures 3.4(a) and (b) that the variations of O/N_2 ratio and N_{max} shows a high degree of correlation. During the geomagnetic storm on 21 February 1973 (Figure 3.4(a)), over the southern hemisphere, a significant decrease in O/N_2 ratio caused a decrease in N_{max}. Over the northern hemisphere (Figure 3.4(b)) a geomagnetic storm which occurred on 29 and 30 October 1973, the decrease in O/N_2 ratios lead to a decrease in N_{max}. In general, composition changes and electron density are well correlated (Prölss, 1980). Habarulema et al. (2013b) did a comparative study of ionospheric storms over the African mid- and equatorial latitudes during geomagnetic storm of 07 - 12 Novem-
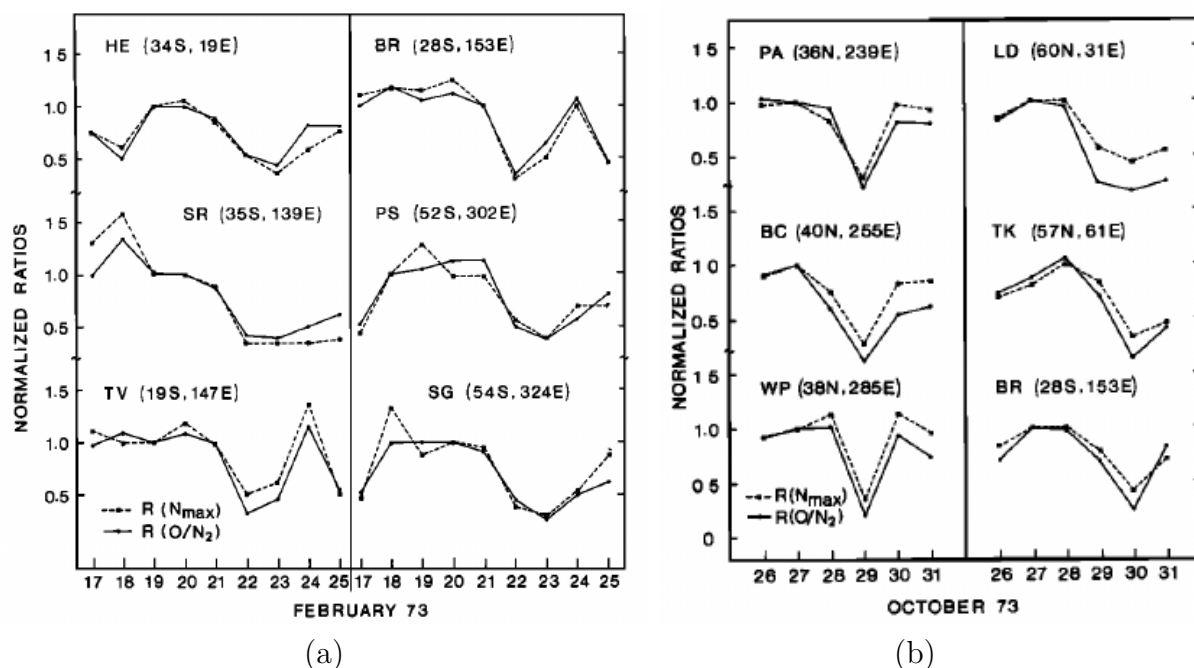
Figure 3.4: Relationship of negative ionospheric storm effects with neutral composition changes. Variations of the maximum electron density (Nmax) of the F region and in the atomic Oxygen to molecular Nitrogen (O/N_2) density ratio are shown as observed above (a) six southern hemisphere mid-latitude stations for the period 17 to 25 February 1973 at 11:00 local solar time and (b) six northern hemisphere stations from 26 - 31 October 1973 at 09:00 local solar time (Prölss, 1980).

ber 2004. There was a significant GPS TEC decrease with a corresponding depletion in foF2 over the mid-latitude stations that were due to the reduction in Global Ultraviolet Imager (GUVI) O/N_2 ratio as observed from the global maps. Matamba et al. (2016) studied the response of mid-latitude ionosphere to four great geomagnetic storms of solar cycle 23 in southern and northern hemispheres. They observed negative ionospheric storm effects which were attributed to neutral composition changes.

Negative ionospheric storms in the mid-latitudes vary with both local time and seasons. They usually follow the geomagnetic storms that occur during the night. Observations show that negative ionospheric storm effects commence most frequently in the morning and very rarely in the noon and afternoon sectors (e.g. Prölss, 1993b; Fuller-Rowell et al., 1994; Prölss, 1995). Negative ionospheric storm effects are in response to the composition disturbance zone and its movement through the day. The magnitude of the storm effects are directly proportional to the strength of the composition disturbance in a particular region (Prölss, 1993b; Fuller-Rowell et al., 1994). The local time on the negative ionospheric storm effects can be explained by changes in neutral composition (Prölss, 1993b, 1995). The explanation by Prölss (1993b) of the impact of local time on the nature ionospheric storms in the mid-latitudes forms the basis of our description.

Figure 3.5 is a schematic illustration of the view of thermospheric-ionospheric storm effects from above onto the northern hemisphere. The three concentric circles indicate the locations 40°, 60° and 80° magnetic latitude with a fixed local time frame, with midnight at the bottom and morning to the right. The circled 1 and boxed 2 represent the two ionosonde stations as indicated in the

28

figure. The dotted area indicates the regions where neutral composition is disturbed and where high values of N_2/O density ratio are observed (Prölss, 1993b, 1995).

Figure 3.5(a) illustrates a moderately quiet geomagnetic condition before the onset time of the geomagnetic storm. The composition changes due to Joule heating and particle precipitation are restricted to the high latitude sector, except in the midnight/early morning sector. Winds of moderate magnitude labeled "midnight surge" in Figure 3.5, transport composition disturbance towards the sub-auroral latitude. Nevertheless, these composition changes are relatively small and dissolve quickly as they rotate with the Earth in the morning sector (Prölss, 1981, 1993b, 1995, and references therein).
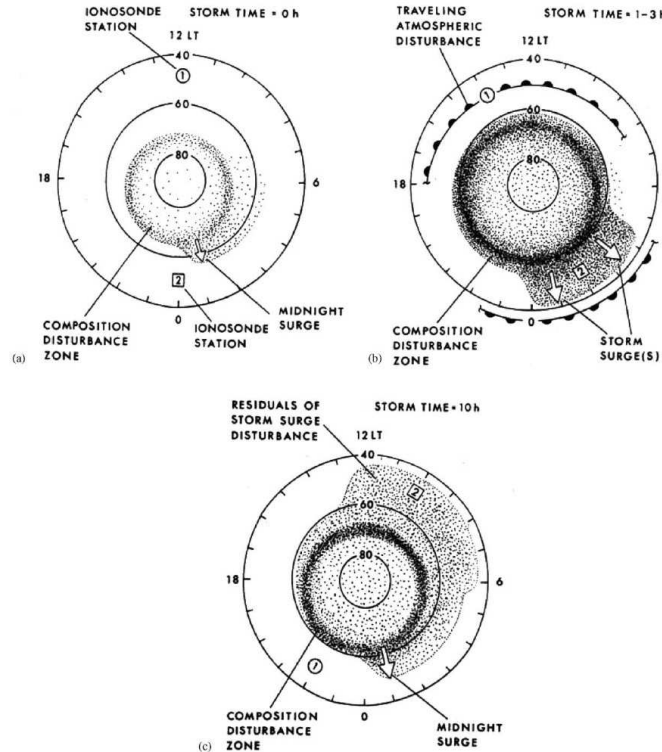
Figure 3.5: Time sequence of thermospheric–ionospheric storm effects. The diagrams show a view from above onto the northern hemisphere. Circles indicate magnetic latitudes 40°, 60° and 80° and local time is given on the outer latitudinal circle. The dotted areas indicate regions of anomalous high N_2/O ratio. (1) and (2) indicate locations of two ionosonde stations in mid-latitudes. (a) shows pre-storm conditions, (b) the expansion phase and (c) the late phase of the storm (Prölss, 1993b).

The next phase is shown in Figure 3.5(b), the expansion phase or initial phase. Now ionosonde station number 2 is located in the morning sector. The strong winds designated by storm surges carry air of disturbed composition out of the heating region (high latitudes) towards the mid-latitudes. Therefore this region is swamped with air of strongly enhanced molecular content and ionosonde station number 2 will observe a negative ionospheric storm effect (Prölss, 1993b, 1995, and references therein).

Now, consider the later phase of the storm, when geomagnetic activity has already subsided (Figure 3.5(c)). Ionosonde stations number 1 and 2 are now located in the pre-midnight and pre-noon

sectors respectively. The distinguishing feature is that the composition disturbance which was generated in the early morning sector has rotated to the forenoon sector. Despite a partial recovery that has taken place, the perturbations are large enough to produce a substantial negative ionospheric storm effect which will dominate ionospheric behavior observed at ionosonde station 2. Nevertheless, ionosonde station number 1 has yet to encounter a region of disturbed composition. It will happen when it is passing through the night sector, presuming that geomagnetic activity continues. In this case, Ionosonde station 1 will only observe a delayed daytime negative ionospheric storm effect the next morning (Prölss, 1993b, 1995).

In general, it was found that during disturbances, maximum ionisation density increases at low magnetic latitudes and decreases at high magnetic latitudes in all seasons, while at mid-latitude stations, maximum ionisation density shows a seasonal change with increases in winter and decreases in summer (Matsushita, 1959; Prölss, 1977; Titheridge and Buonsanto, 1988). The negative ionospheric storm effects mostly occur in the summer hemisphere. During summer, negative ionospheric storm effects are observed all the way from high latitude to low latitude, whereas during winter they are restricted to high latitude. It is now believed that the seasonal variations arise from the interaction between seasonal and storm-induced winds. In summer both types of winds support each other while they are out of phase in winter (Prölss, 1977, 1995; Fuller-Rowell et al., 1996, and references there in).

Figures 3.6 (a) and (b) illustrate the latitudinal asymmetric distribution of foF2 and the extension of the atmospheric-ionospheric disturbance zone for summer and winter conditions at the southern and northern hemisphere ionosonde stations. Figure 3.6 (a) shows the event that occurred on 26 - 27 July 1973, which is summer and winter in the northern and southern hemisphere respectively. In contrast, Figure 3.6 (b) shows the event that occurred on 4 - 6 December 1973, which is winter and summer in northern and southern hemisphere respectively.

The upper and lower panels of Figure 3.6 show the local time variation of the observed critical frequency of the F2 layer (foF2) (heavy dotted line), superimposed are the monthly median of foF2 (thin line) at some stations located in the northern and southern hemispheres. The hatched areas in second and third panels give a rough estimate of the extension of the neutral atmospheric disturbance zone as inferred from the distribution of negative storm effects. Solid and open circles in panels 2 and 3 of Figure 3.6 indicate regions where significant negative and no negative ionospheric responses were observed respectively at that location. Figures 3.6 (a) and (b) clearly show remarkable changes in the seasonal behaviour of ionospheric storm effects. In the summer hemisphere, even moderate geomagnetic activity could lead to significant negative ionospheric storm effects. Neutral composition disturbance zone cover all latitudes from the high latitude down to the lower latitude region, where pre-storm electron densities are not so much depressed by seasonal changes in the neutral composition. In the winter hemisphere, negative ionospheric storm effects are observed to be restricted to high latitude regions, while the mid-latitudes exhibit an increase in foF2 (positive ionospheric storm effects) rather than a decrease in foF2. Therefore, the increased N_2/O ratio indicated by the hatched area may extend to much lower latitude on a disturbed summer day than on a disturbed winter day (Prölss, 1977, 1995). It is generally believed that global thermospheric winds may play an important role in transporting the composition zone out of the heated auroral zone. Results from general circulation models indicate that the superposition of the storm-induced equatorward wind with the global neutral wind circulation, diurnal wind, and ion drag associated with ionospheric plasma convection, produces complex local time and seasonal effects (Fuller-Rowell et al., 1996, 1997; Liou et al., 2005).
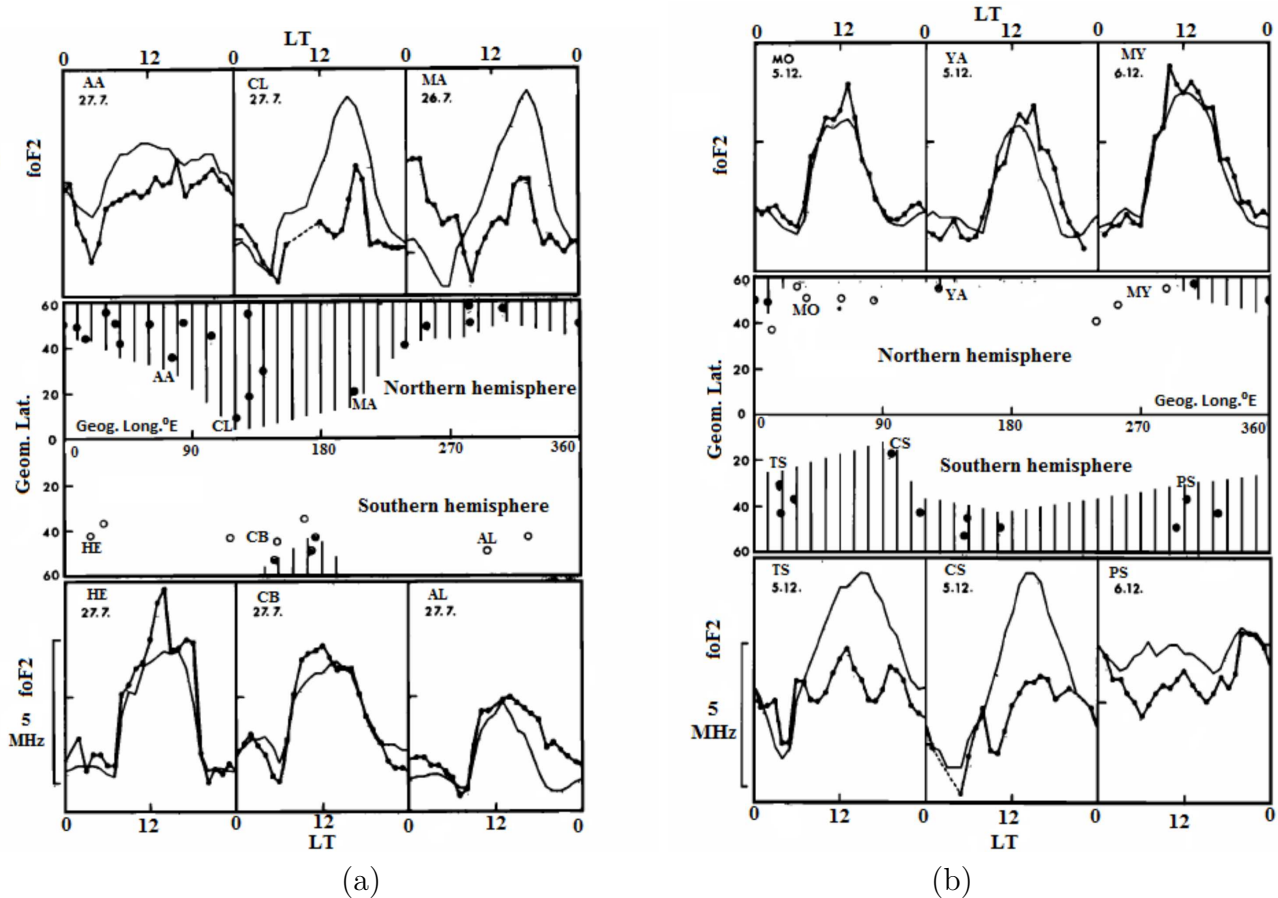
Figure 3.6: Extension of the atmospheric-ionospheric disturbance zone in geographic longitude/invariant geomagnetic latitude coordinate system during the (a) northern summer and southern winter event of 26 - 27 July 1973 and (b) the northern winter and southern summer event of 4-6 December 1973 (Prölss, 1977).

Significant reductions in the strength of the Equatorial Electrojet (EEJ) which are accompanied by poor development of the EIA occur simultaneously with negative ionospheric storm effects at mid-latitude (Tanaka, 1981; Sastri, 1988). The decrease in EEJ strength follows geomagnetic disturbances with delays of 13 - 22 hours which are interpreted as signatures of equatorial Disturbance Dynamo Electric Fields (DDEF) produced by the storm time modifications in the global circulation due to energy inputs at high latitude (Sastri, 1988). The simultaneous electron density data at mid-latitude at the same longitude, which provide the information on the thermospheric composition neutral changes, can be used for the identification of DDEF (Sastri, 1988).

3.4.3   Positive ionospheric storm effects

Figure 3.7 shows an example of a positive ionospheric storm effect for 07 - 10 May 2005 over Halat Ammar, HALY (29.14°N, 36.10°E; 21.83°N, geomagnetic), Saudi Arabia, in the northern hemisphere. Figure 3.7 illustrates (I) Dst index, (II) Kp index and (III) deviations of TEC (ΔTEC). The shaded region on the figure highlights the type of ionospheric response observed. The Dst

index shows the double peak Dst index on 08 May 2005 with a minimum intensity of ~ -80 nT and ~ -116 nT. The 06 May 2005 (quiet day) was compared with the disturbed day (07 May 2005) to check the variation of TEC during geomagnetic storm. Positive ionospheric storm effects were observed for both minimum Dst index. The deviations of TEC clearly show a significant increase in ΔTEC of about 80% and 130%.
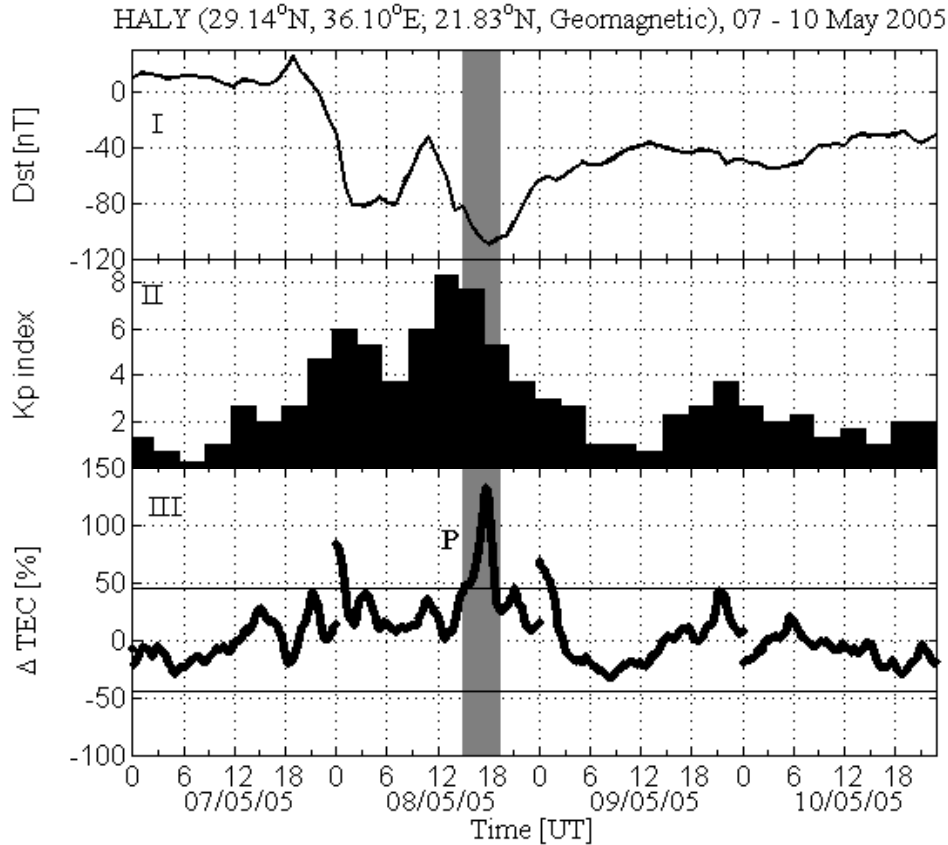
Figure 3.7: An example of a positive ionospheric storm effect.

The origin of positive ionospheric storms is not yet well understood, with several mechanisms having been proposed to explain them without arriving at a generally accepted explanation (e.g. Prölss, 1995, 2008; Ngwira, 2011; Kuai et al., 2015). Positive ionospheric storm effects may be categorized into several classes, depending on the duration, local time and latitude. The most observed class of positive storm is the daytime short-duration enhancement of the mid-latitude ionospheric electron density. These are usually attributed to Prompt Penetration Electric Field (PPEF) and Traveling Atmospheric Disturbances (TADs).

The daytime positive ionospheric storm effect is believed to be due to Prompt Penetration Electric Field (PPEF). PPEF is the electric field of magnetospheric origin observed equatorward of the shielding layer. It generally occurs during the period of large and rapid changes in magnetospheric convection and at the time of preliminary magnetic sudden commencement and the sudden changes in the dynamic solar wind pressure (Fejer et al., 1979b; Tsurutani et al., 2004, 2008a; Bagiya et al., 2011). The PPEF is generally composed of a convection electric field and an over-shielding electric field (Fejer et al., 1979b) which are active during the main phase and recovery phase of the storm respectively (Kikuchi et al., 2008; Bagiya et al., 2011). The plasma sheet moves earthward because

of the enhanced convection field and drives a partial ring current (Bagiya et al., 2011). During this process the shielding electric fields are built up towards the equator of the auroral latitude. After the shielding electric field grows, the electric fields at mid- and low latitudes are often reversed when the convection electric field is decreased suddenly, because of the northward turning of the IMF Bz (e.g. Kelley et al., 1979; Kikuchi et al., 2000, 2008). The reversal of the penetrated electric field is known as the over-shielding electric field. The daytime PPEF is eastward to the dusk sector and westward in the midnight to dawn sector (Tsurutani et al., 2008a). An eastward PPEF in the dayside ionosphere during the southward IMF Bz will move the plasma particles to high altitude at mid-latitude, resulting in the formation of positive ionospheric storm effects (Tsurutani et al., 2008a). The time of the SI+ plays an important role in understanding the PPEF. The changes in TEC due to PPEF occur within 2 - 3 hours (Tsurutani et al., 2004, 2008a).

The TADs result from atmospheric gravity waves, which are launched in the high latitudes during storms and travel to mid-latitudes (e.g. Prölss and Jung, 1978; Prölss, 1993a,b, 1995; Tsagouri et al., 2000; Prölss, 2004; Ngwira et al., 2012a).

The TADs are pulse-like perturbations formed by a superposition of atmospheric gravity waves which propagate at high speed (500 - 1000 m/s) from the polar to equatorial latitudes, carrying along equatorward-directed meridional winds. These winds drag the ionisation along the inclined magnetic field lines, thus changing the altitude of the ionisation layer. At mid-latitudes these winds cause an enhancement in height of the F2 region, which in turn will lead to an increase in electron density. At F region heights the loss rate of ionisation is proportional to the molecular nitrogen and molecular oxygen densities. The loss rate decreases much faster with height than the production rate, which is proportional to the atomic oxygen density. An upward displacement will therefore lead to an overall increase in ionisation density (e.g. Prölss, 1993a, 1995, 2004, 2008). During geomagnetic storms, increased atmospheric heating in the polar region can set up large amplitude atmospheric gravity waves (AGWs) that manifest in the ionosphere as Traveling Ionospheric Disturbances (TIDs) (Hines, 1960; Buonsanto, 1999; Nicolls et al., 2004; Nicolls and Heinselman, 2007; Ngwira et al., 2012a; Habarulema et al., 2015). TIDs are wavelike fluctuations of the electron density induced by gravity waves in the neutral atmosphere. There are two basic types or classes of quasi-periodic TIDs, namely, Large-Scale TIDs (LSTIDs) and Medium-Scale TIDs (MSTIDs).

MSTIDs are assumed to propagate in the lower atmosphere before being detected in the ionosphere and have horizontal speeds between 100 and 250 m/s that is less than the velocity of sound in the lower atmosphere (Hocke and Schlegel, 1996). They have shorter periods between 15 and 60 min (Francis, 1974; Hunsucker, 1982; Davies, 1990; Hocke and Schlegel, 1996). MSTIDs may be excited by sources at any altitude/height (Hunsucker, 1982). MSTIDs are believed to be ionospheric manifestation of the AGWs caused by magnetic activity at auroral region or launched from lower atmosphere (Francis, 1974). Possible mechanism for MSTIDs are Joule heating, particle precipitation and the Lorentz forces (Francis, 1974).

On the other hand, LSTIDs propagate equatorward in the thermosphere and are characterised by horizontal speeds of between 400 and 1000 m/s which is comparable with the speed of sound in the thermosphere. Their periods are in a range of 30 minutes to 3 hours and horizontal wavelength is greater than 1000 km. LSTIDs can be excited by sources at heights of 100 km and above (Hunsucker, 1982).

It is generally accepted that the main source of LSTIDs are the acoustic gravity waves generated from the auroral regions of the southern or northern hemisphere (e.g. Hocke and Schlegel, 1996; Afraimovich et al., 2000; Habarulema et al., 2013a, 2015). The gravity waves in the mid-latitudes can be observed as typical LSTIDs propagating equatorwards (Hunsucker, 1982). During geomagnetic storms, the LSTIDS are excited from the auroral zone and can propagate from the auroral and high-latitudes equatorward towards mid-latitudes. They may sometimes even propagate across the equator leading to poleward propagation of these disturbances (e.g. Bruinsma and Forbes, 2009; Ding et al., 2013; Habarulema et al., 2015, and references therein). Habarulema et al. (2015) presented the first observations of poleward propagation of LSTIDs over the African sector during a strong geomagnetic storm of 9 March 2012 using data from a number of Global Positioning System (GPS) receiver networks.

Figure 3.8 illustrates the LSTIDs observed during the main phase of geomagnetic storm of 24 April 2012. Figure 3.8 illustrates two-dimensional diurnal ΔTEC maps on days when each storm was in the main phase. ΔTEC variability was within the longitude sector of 10°E - 40°E on all storm days. The method for computing ΔTEC involves fourth-order polynomial fitting of each satellite's TEC values (Ding et al., 2007; Valladares and Hei, 2012) at 30 s resolution, and subtracting fitted TEC from actual TEC to give detrended TEC (TEC perturbations denoted by ΔTEC). Figure 3.8 was generated by binning ΔTEC data into 3 min × 0.5° time and latitude grids. For example, the velocity values of the TIDs in Figure 3.8 were determined as 611 $\pm$ 37 m/s, 306 $\pm$ 18 m/s, and 244 $\pm$ 15 m/s between 05:00 to 06:00 UT, 09:00 to 10:00 UT, and 10:00 to 11:00 UT respectively, with periods of at least 1 hour. Equatorward large-scale TIDs are basically identified by observation of enhanced ΔTEC (with reference to the background values) in an equatorward direction, as indicated by arrows in Figure 3.8 from 05:00 to 06:00 UT, 09:00 to 10:00 UT, 10:00 to 11:00 UT, and 14:00 to 15:00 UT (Habarulema et al., 2017).
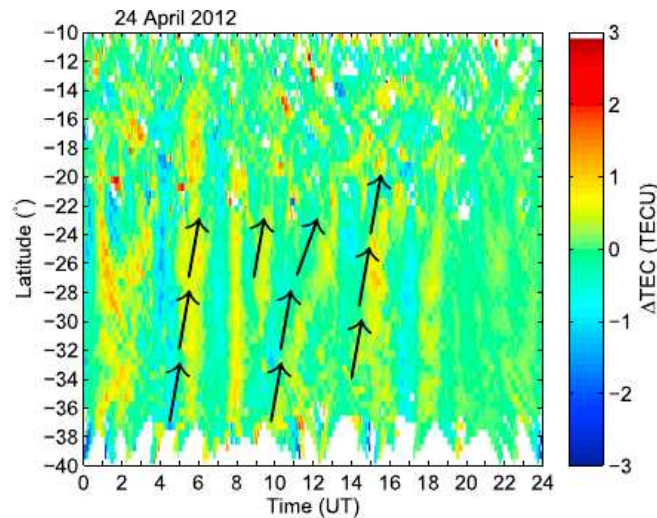
Figure 3.8: Changes in ΔTEC (TECU) for 24 April 2012 during main phase of geomagnetic storm. The black arrows indicate the equatorward direction of large-scale TIDs (Habarulema et al., 2017).

A second class of positive ionospheric storm effects comprises the long-duration positive ionospheric

storm effects, which is attributed to downwelling of neutral atomic oxygen and uplifting of the F layer due to winds. Both mechanisms rely on the large-scale changes in thermospheric circulation caused by heating in the auroral zone. Buonsanto (1999) reviewed these two mechanisms. According to the mechanism of the downwelling of neutral atomic oxygen, the altered thermospheric circulation causes downwelling of the neutral species through constant pressure surfaces at low mid-latitude equatorwards of the composition disturbance zone, increasing the density of the oxygen relative to molecular nitrogen (N_2) and molecular oxygen (O_2). This results in an increase of the electron density of the F-region (Buonsanto, 1999, and references therein). The uplifting of the F-region due to winds is explained by, the long-duration positive ionospheric storm effects which occur when the enhanced equatorward winds lift the ionisation to greater altitudes at a time when production is still occurring. This mechanism works best during the daytime, while the increase in oxygen density causes positive storms at night (Buonsanto, 1999, and references therein).

Positive ionospheric storm effects over the mid-latitude could also be attributed to the expansion of the Equatorial Ionization Anomaly (EIA) (e.g. Yizengaw et al., 2005; Huang et al., 2005a,b; Ngwira, 2011; Ngwira et al., 2012b; Katamzi and Habarulema, 2014b; Matamba et al., 2016). An enhanced EIA can lead to increase in the electron density of the F region at lower mid-latitudes (Huang et al., 2005a,b; Ngwira et al., 2012b). Ngwira et al. (2012b) reported on the positive ionospheric storm effect that occurred on 25 July 2004 during the main phase of the storm.

The Interplanetary Magnetic Field (IMF) Bz component was southward for an extended time period for more than 15 hours. The extended IMF Bz southward orientation on 25 July 2004 could have caused thermospheric and ionospheric disturbance for longer time periods, thus resulting in long-duration positive ionospheric storm effects. For sustained high-level magnetic disturbances, the continuing high energy input may lead to prolonged changes in the global wind circulation (Ngwira et al., 2012b).

Positive ionospheric storm effects over the mid-latitude vary with local time and seasons (Titheridge and Buonsanto, 1988; Prölss, 1993b, 1995). Positive ionospheric storm effects are generally associated with the magnetic storm beginning in the local daytime sector. Figure 3.5(b) illustrates the time sequence of a thermospheric-ionospheric storm effect during geomagnetic storm conditions. The energy addition in the polar atmosphere launches TADs which move in the form of global and circumpolar disturbance front toward lower latitude. As it passes ionosonde station number 1 (indicated in Figure 3.5(b)), it produces a positive ionospheric storm effect. This disturbance propagates with storm-induced meridional wind pushing ionisation upward along geomagnetic field lines. This results in an increase in electron density due to lower electron loss rate at higher altitudes. The ionospheric response to a TAD will critically depend on local time (Prölss, 1993b). Therefore at night, a lack of ionisation production will prevent the formation of positive ionospheric storm effects. Thus, the positive phase is predominantly a daytime phenomenon according to this mechanism. The additional storm-induced equatorward circulation seems to be the most important factor for creating the positive phase at mid-latitudes (Prölss, 1995, 1993b; Lastovicka, 2002b, and references therein).

The positive ionospheric storm effects at mid-latitude are mainly observed during winter (Matsushita, 1959; Prölss, 1977, 1980; Titheridge and Buonsanto, 1988; Prölss, 1995; Fuller-Rowell et al., 1996). This could be explained by the limited extent of the composition disturbance zone in this season. Therefore, a much larger proportion of the mid-latitude region will be exposed only to wind perturbations (Prölss, 1995). For example, Figure 3.6 shows an increase in foF2 for the

stations located over the mid-latitude in the winter hemisphere, while the negative ionospheric storm effects were observed at stations located in high latitudes even during winter season (Prölss, 1977).

3.4.4 Double disturbance ionospheric storm effects

The double disturbance ionospheric storm effects are positive-negative (PN) and negative-positive (NP) ionospheric storm effects. Matsushita (1959) noted that the maximum electron density in higher and mid-latitudes are characterised by short increase followed by a much larger decrease (PN ionospheric storm effects) while in the equatorial region there was generally a short decrease followed by an increase in maximum electron density (NP ionospheric storm effects). PN ionospheric storm effects over mid-latitudes could be explained by local time dependence, as illustrated in Figure 3.5 (c) during the later phase of the storm, where ionosonde number 1 was located in the pre-midnight sector where it observed positive ionospheric storm effect due to traveling atmospheric disturbance which moves in the form of global disturbance front towards low latitudes. Later, when ionosonde number 1 encounters the composition disturbance zone, it observes a delayed negative storm effects the next morning (Prölss, 1993*b*, 1995; Lastovicka, 2002*b*). Figures 3.9 illustrate examples of PN and NP ionospheric storm effects over the mid- and equatorial latitude stations, Thohoyandou, TDOU (23.08°S, 30.38°E; 33.92°S, geomagnetic), South Africa, southern hemisphere and Nazret, NAZR (8.57°N, 39.29°E; 0.25°S, geomagnetic), Ethiopia, northern hemisphere respectively. Figure 3.9 shows the variation of (I) Dst index (nT), (II) Kp index and ΔTEC (%) during the storm periods 06 -09 January 2005 and 23 - 27 October 2011. P and N on the figure indicate Positive and Negative ionospheric storm effects. The shaded region on the figure indicates the time when either P or N ionospheric storm effects were observed and the stage of the storm.
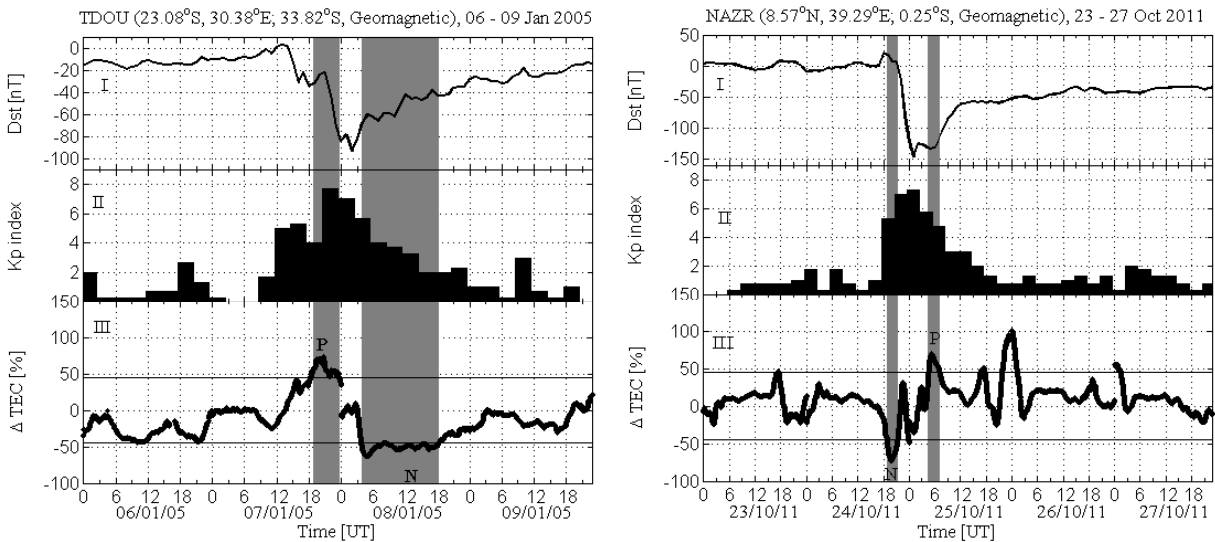
Figure 3.9: Examples of PN and NP ionospheric storm effects over Thohoyandou, TDOU (23.08°S, 30.38°E; 33.92°S, geomagnetic), South Africa, southern hemisphere and Nazret, NAZR (8.57°N, 39.29°E; 0.25°S, geomagnetic), Ethiopia, northern hemisphere respectively.

At TDOU, positive and negative storm effects occurred during 17:47 - 23:36 UT and 03:58 - 18:11 UT on 07 January and 08 January 2005 respectively. The positive and negative ionospheric storm effects occurred during the main and recovery phases of the geomagnetic storm respectively, as

indicated by Dst. At NAZR, negative and positive ionospheric storm effects occurred during 18:50 - 21:20 UT and 04:32 - 07:07 UT on 24 October and 08 October 2011 respectively. Negative and positive ionospheric storm effects occurred during the initial and recovery phases of the geomagnetic storm respectively.

3.4.5   Not-significant ionospheric storm effects

Figure 3.10 shows an example of a not-significant ionospheric storm effect for the period 06 to 10 March 2005 over Halat Ammar, HALY (29.14°N, 36.10°E; 21.83°N, geomagnetic), Saudi Arabia, northern hemisphere. The main phase occurred on 06 March 2005 with a minimum Dst of -54 nT. There was no significant increase or decrease in ΔTEC values during storm. ΔTEC values were observed to be within the quiet time variability ranges.
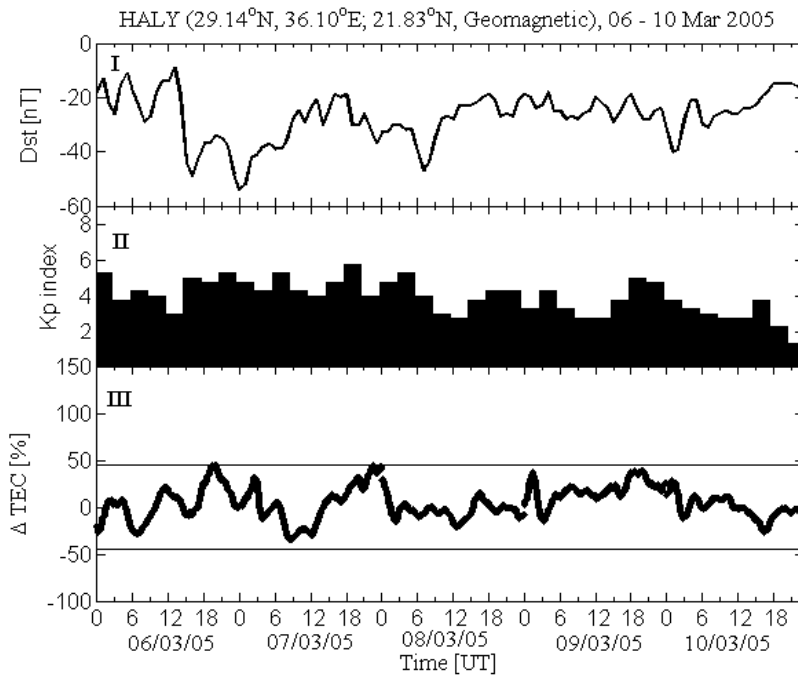
Figure 3.10: An example of a not-significant ionospheric storm effect.

The NS ionospheric storm effects could be due to competing mechanisms such as, the one arising from EIA expansion and neutral composition changes. The equatorward neutral winds carry atmospheric composition changes from the high latitudes to lower latitudes causing a decrease in electron density (Fuller-Rowell et al., 1994; Prölss, 1995; Maruyama and Nakamura, 2007), while an enhanced EIA may cause an increase in F-region electron density at lower mid-latitudes (Ngwira et al., 2012b).

3.5   Summary

This chapter gave background information on geomagnetic storms, thermospheric storms and ionospheric storm effects. CME- and CIR-driven geomagnetic storms were briefly discussed. Positive, negative, double disturbance and not-significant ionospheric storms were explained. Some mechanisms such as TIDs, expansion of EIA, PPEF, changes in neutral composition and DDEF were

highlighted. Ionospheric storm effects, in particular over the mid-latitudes depend on local time and season which is due to the limited extent of the composition disturbance zone during winter; hence the increased observation of positive ionospheric storm effects (Prölss, 1995; Fuller-Rowell et al., 1996).

Chapter 4

Data sources

4.1 Introduction

This chapter discusses the data sources used in this study. This includes various geomagnetic indices with focus on Dst and Kp indices, which are used to study the magnetic activity. The ionosonde foF2 and GPS TEC observations provide the necessary information to understand the various processes occurring in the ionosphere and they are discussed here.

4.2 Geomagnetic indices

Geomagnetic indices are a measure of magnetic activity which is a signature of the response of the Earth's ionosphere and magnetosphere to solar activity. They are the key indicators used to detect and describe space weather events. An index is a number representing an event or set of events. Geomagnetic indices are recorded by ground-based magnetometers. This section summarises the geomagnetic indices used in this study (Mayaud, 1980; Mandea and Korte, 2010).

4.2.1 Dst index

The Disturbance storm time (Dst) index describes geomagnetic activity. It is derived from measurements recorded at near-equator observatories, and thus monitors the Earth's ring current. When the ring current is enhanced, the Dst index which is expressed in nT shows a decrease. The decrease in Dst index measurement is an indication that the equatorial geomagnetic field is reduced (suppressed). A sudden large reduction in the Dst index is an indicator of a geomagnetic storm (Gubbins and Herrero-Bervera, 2007; Howard, 2014). The World Data Center for Geomagnetism, Kyoto (`http://wdc.kugi.kyoto-u.ac.jp/`) offers three classes of Dst index, namely the Quick look, Provisional and Final Dst indices. They are defined by the stage of data processing provided by the observatories. The Alibag (18.64°N, 72.87°E; 10.19°N, magnetic) observatory provides the Quick look and provisional Dst data. However, for the final Dst index data from four magnetic observatories (Hermanus, Honolulu, Kakioka, and San Juan) are used. The coordinates of the stations are given in Table 4.1, and their locations are shown in Figure 4.1. These observatories were originally chosen because of their data quality, their location (distant from the equatorial and auroral electrojets) and, their even distribution longitudinally (Sugiura, 1963; Gubbins and Herrero-Bervera, 2007; Mandea and Korte, 2010).
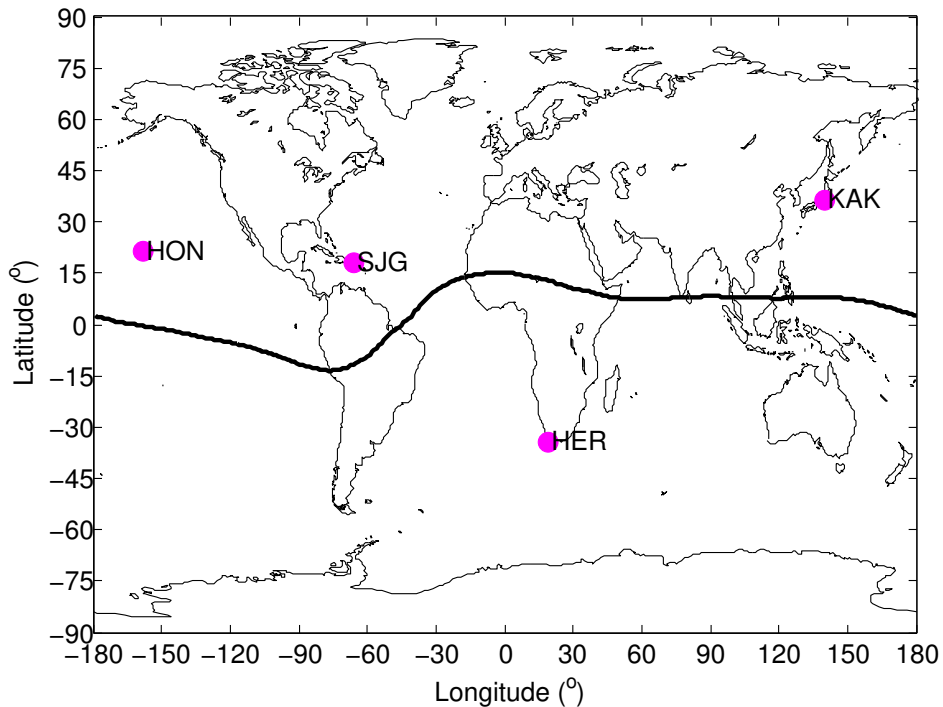
Figure 4.1: A map showing the magnetometers network which provides data for the derivation of the Dst index.

Table 4.1: Coordinates of the geomagnetic stations used to derive Dst index (Sugiura and Kamei, 1991).

Observatory	Observatory code	Geographic Longitude	Geographic Latitude	Geomagnetic latitude
Hermanus	HER	19.22°	-34.40°	-42.33°
Kakioka	KAK	140.18°	36.23°	29.04°
Honolulu	HON	201.98°	21.32°	21.66°
San Juan	SJG	293.85°	18.01°	28.69°

4.2.2   K and Kp indices

The 3-hour range K index was introduced by Bartels et al. (1939) to characterize the variation in the degree of irregular magnetic activity throughout the day. The K index quantifies disturbances in the horizontal component of the Earth's magnetic field with an integer ranging from 0 (quiet) to 9 (active). The K index is calculated separately for each observatory (Gubbins and Herrero-Bervera, 2007; Mandea and Korte, 2010).

The planetary K (Kp) index was introduced as a magnetic index by Bartels in 1949. The Kp index is designed to give a global measure of geomagnetic activity, while the K index is an indicator of disturbances in the Earth's magnetic field at a particular observatory. The Kp index is created by first standardising the observatories K indices to Ks (standardised K index) values. This is done by tables that create equal distributions of Ks values for each observatory for every 3-hour interval of every season. The tables for each observatory translate the integral (0-9) K values into

28 fractional Ks values quantized to units of $\frac{1}{3}$ i.e., $(0, \frac{1}{3}, \frac{2}{3}, 1, ..., 9)$. The Kp index is defined as the arithmetic average of Ks values at 13 standard observatories (Kivelson and Russell, 1995; Gubbins and Herrero-Bervera, 2007; Mandea and Korte, 2010), shown in Figure 4.2.
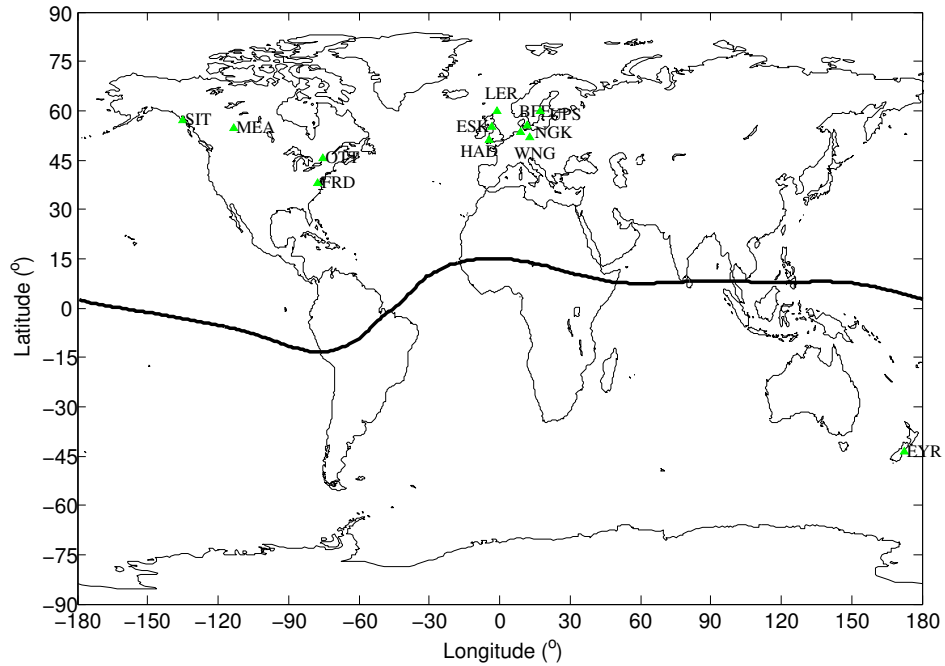
Figure 4.2: A map illustrating the network of magnetometers used for the derivation of the Kp index. The green triangles represent station locations.
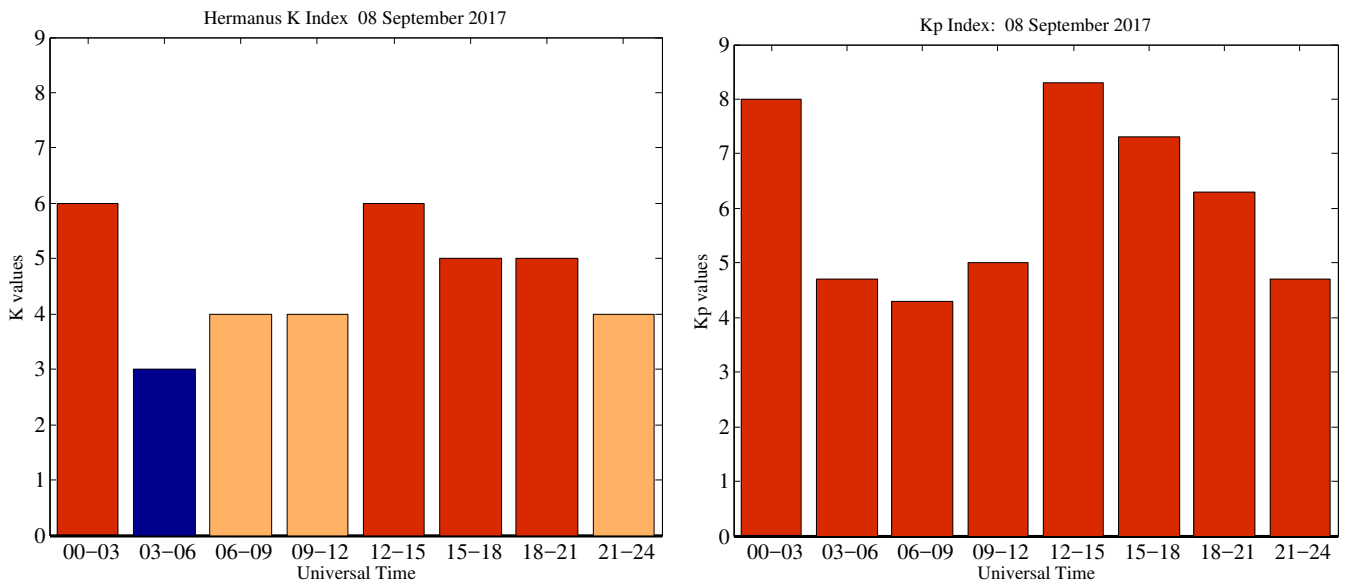
Figure 4.3: K index and Kp index for 08 September 2017.

Figure 4.3 shows the local Hermanus K index and Kp index for 08 September 2017. The blue, yellow and red bars represent K < 4, K = 4 and K > 4 respectively. Figure 4.3 illustrates the difference between local K index and the planetary K index well, in that the latter values are generally higher. It is generally agreed that K = 0–2, K = 3–5 and K = 6–9 correspond to

41

geomagnetic quiet, moderate and intense to very intense geomagnetic activity periods respectively (Mandea and Korte, 2010; Data Solar Geophysical, 2012). There are a number of other indices related to K and Kp. Ak and Ap are linear and equivalent to K and Kp indices. Kn, An, Ks and As are similar to Kp and Ap indices, apart from using northern and southern hemisphere observatories respectively, and their global indices are Km and Am. The aa index utilizes only two observatories each in southern and northern hemispheres. The aa index is one of the longest historical time series in geophysics, and has been continuously calculated since 1868 (Gubbins and Herrero-Bervera, 2007; Mandea and Korte, 2010).

4.2.3 Auroral Electrojet (AE) index

The Auroral Electrojet (AE) index measures the current which flows in the auroral zone, and is derived from horizontal (H) component observed at the stations located in latitude near the auroral zone in the northern hemisphere (Davies, 1990; Gubbins and Herrero-Bervera, 2007; Mandea and Korte, 2010). It was originally introduced by Davis and Sugiura in 1966, and is widely used today for research in terrestrial physics, geomagnetism and aeronomy. A list of papers on the use of the AE index (since 2002) are published on `http://wdc.kugi.kyoto-u.ac.jp/wdc/aedstcited.html`.
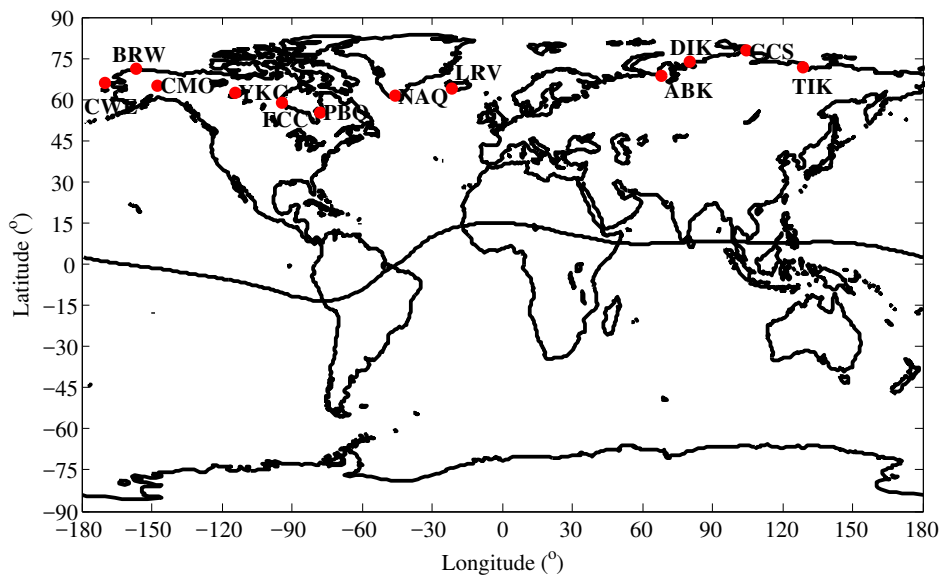
Figure 4.4: A map showing the locations of the observatories which provide data for the calculation of the AE index.

The calculation of the AE index is based on one-minute resolution data from 12 observatories along the auroral zone in the northern hemisphere, as shown in Figure 4.4. To normalise the data, a base value for each station is first calculated for each month, by averaging all the data from the station on the internationally selected five quietest days. The calculated base value is then subtracted from each one-minute data value obtained at the station during that month. Then the largest (defined as AU) and smallest (AL) values are selected from all the stations for a given time. The daily H from the stations is superimposed, and the upper and lower envelopes define AU and AL respectively. The AL and AU indices are intended to express the strongest current intensity of the westward and eastward auroral electrojets respectively (Mayaud, 1980; Davies, 1990; Gubbins

and Herrero-Bervera, 2007; Mandea and Korte, 2010). The AE index is defined as:

$$AE = AU - AL, \tag{4.1}$$

and the AO is defined as the average of AU and AL, that is,

$$AO = \frac{AU + AL}{2} \tag{4.2}$$

The AO index provides a measure of the equivalent zonal current. The term "AE index" is usually used to represent these four indices, namely, AU, AL, AE and AO (Davies, 1990; Mandea and Korte, 2010).

Figure 4.5 illustrates the AE, AU, AL and AO indices during the geomagnetic activity on 03 - 07 July 2011.
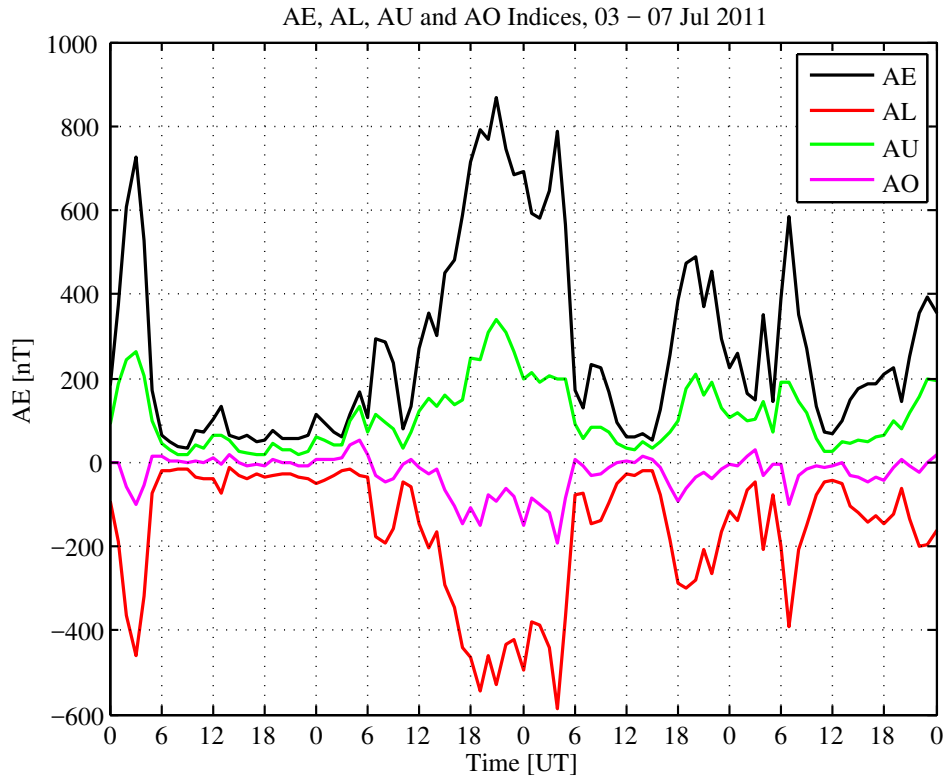
Figure 4.5: An example of AE, AL, AU and AO indices for 03 - 07 July 2011.

4.2.4 Polar Cap (PC) Index

The Polar Cap (PC) index aims at characterising the magnetic activity generated by the geoeffective solar wind acting on the magnetosphere. It is a measure of magnetic disturbance caused by the transpolar portion of ionospheric currents associated with global convection (Lukianova, 2003). The PC index is derived from an assumed linear relation between the geoeffective electric field in the solar wind encountering the Earth, and the polar cap magnetic variation projected in the direction perpendicular to the average Disturbance Polar of type 2 (DP2) transpolar equivalent current (Stauning, 2013). Troshichev et al. (1979) proposed an idea to introduce into practice PC index, defined as the 15 minutes sum of values of the PC magnetic disturbances, concerned with southward interplanetary magnetic field (Bz component), with an account of variability of these

disturbances.

The index is derived from two stations, namely Thule (86.5° geomagnetic latitude), Greenland (PCN) and Vostok (83.3° geomagnetic latitude) (PCS), located respectively in the northern and southern hemispheres near the pole regions. In 2013, the International Association of Geomagnetism and Aeronomy (IAGA) recommended that the international scientific community use the PC index as a proxy for energy that enters the magnetosphere during solar wind – magnetosphere coupling.

This thesis used Dst and Kp indices to identify the geomagnetic disturbed days. The Kyoto World Data Center calculates AE and Dst (`http://wdc.kugi.kyoto-u.ac.jp/dstae/index.html`). The GeoForschungs Zentrum in Potsdam calculates Kp (`http://www.gfz-potsdam.de/~kp_index/`). Onother agency that supports and archives the distribution of these indices is the Goddard Space Flight Center (`https://omniweb.gsfc.nasa.gov/form/dx1.html`).

4.3 Solar wind data

The interplanetary magnetic field (IMF) Bz component and the solar wind velocity were used to characterize variations of the solar wind **in this thesis**. The analysis used solar wind data shifted to the Earth's bow shock to account for the propagation delays towards the Earth's magnetosphere (Case and Wild, 2012). The data was obtained from Goddard Space Flight Center (GSFC) OMNIWeb Plus (`http://omniweb.gsfc.nasa.gov/form/sc_merge_min1.htm`).

The primary reason for the development of OMNIweb (`http://omniweb.gsfc.nasa.gov/form/sc_merge_min1.htm`) is the challenge to accurately predict the delay time of the solar wind. The OMNIweb combines data from several spacecrafts namely, Advanced Composition Explorer (ACE), Wind, IMP 8 and GEOTAIL to produce a high-resolution database of solar wind conditions lagged to the nose of the Earth's bow shock. It calculates the appropriate lag time applicable to data using the time shift equation,

$$\Delta t = \frac{n.(R_d - R_o)}{n.V} \tag{4.3}$$

where R_o and R_d represent the location of observing spacecraft and displaced location of the spacecraft respectively, V denotes the solar wind velocity and n is the variation phase front normal (Case and Wild, 2012, `https://omniweb.gsfc.nasa.gov/html/omni_min_data.html#3`)

Figure 4.6 shows the variation of the symetrical-H component (SYM-H) (nT), shifted V_{sw} (km/s) to bow shock obtained from OMNI (b) and unshifted V_{sw} (km/s) from ACE for 30 September - 02 October 2012. The red and green vertical broken lines represent the sudden storm commencement which has been replaced by a short duration positive (SI+) spike on SYM-H and the shock (Lugaz et al., 2015; Habarulema et al., 2017). During the SI+ ($\sim$ 11:32 UT) and shock ($\sim$23:15 UT), the OMNI solar wind speed (Figure 4.6(b)) shows a sudden increase simultaneously with the SI+ and the shock. In contrast, Figure 4.6(c) shows an increase $\sim$ 60 minutes before the SI+ and the occurrence of the shock. The solar wind data were downloaded from `http://omniweb.gsfc.nasa.gov/form/sc_merge_min1.htm`.

30 September − 02 October 2012
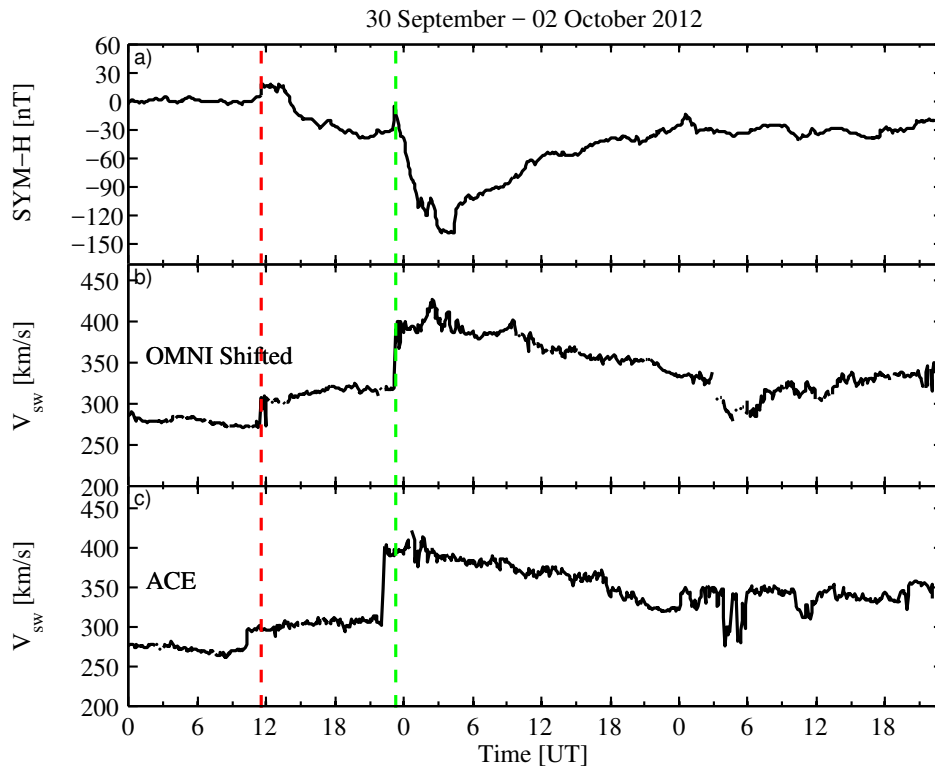
Figure 4.6: Variation of (a) SYM-H (Dst), (b) Shifted solar wind speed (km/s) (OMNI), (c) unshifted solar wind speed (km/s) for 30 September - 02 October 2012. The vertical red and green broken lines show the sudden storm commencement (SI+) (30 September 2012 at 11:32) and a shock (30 September 2012 at 23:15) that occurred inside a CME respectively.

4.4 Ionosonde data

The first measurements of the ionospheric height were done by Appleton and Barnett (1926) with a continuous wave transmitter and a receiver located 65 to 130 km distant from the transmitter. A sounder is a type of radar that is capable of obtaining echoes from the ionosphere over a wide range of operating frequencies (Rishbeth and Garriott, 1969). An ionosonde is a High Frequency (HF) radar that operates in the frequency band of 0.5 to 30 MHZ, and sounds the bottomside (up to the maximum electron density altitude) ionosphere. Ionosondes have been used extensively in remote sensing for monitoring long-term temporal and spatial variations of the ionosphere and also for ionospheric physics research (Rishbeth and Garriott, 1969; Davies, 1990; Hunsucker, 1991). There are two possible modulation methods for use in an ionosonde, i.e. the sweep frequency pulsed method and the chirp method. Each method has its own pros and cons. The principle of the Chirp technique differs from the pulse-amplitude technique in that the radio signals in the Chirp technique are continuous waves in which the frequency is modulated (Rishbeth and Garriott, 1969; Davies, 1990; Hunsucker, 1991, and reference therein).

"Modern digital ionosondes are highly flexible HF radar systems tasked to reliably describe the status of the ionospheric density distribution on a continuous basis. Robust automated operation is necessary for the monitoring function of the ionosonde. Measuring flexibility and precision are required for research application". The modern Digisonde-4D uses one simple crossed delta or rhombic antenna for transmission, and an array of four small crossed loops for reception (LDI,

2015). The analysis done in this project utilised digisonde measurements.

4.4.1 Ionospheric sounding measurements

Ionospheric sounding experiments determine the electron density profile between the transmitter and the point of highest density, by varying the probing frequency and measuring the time it takes a radio signal wave to travel from the transmitter to the reflection point and back.
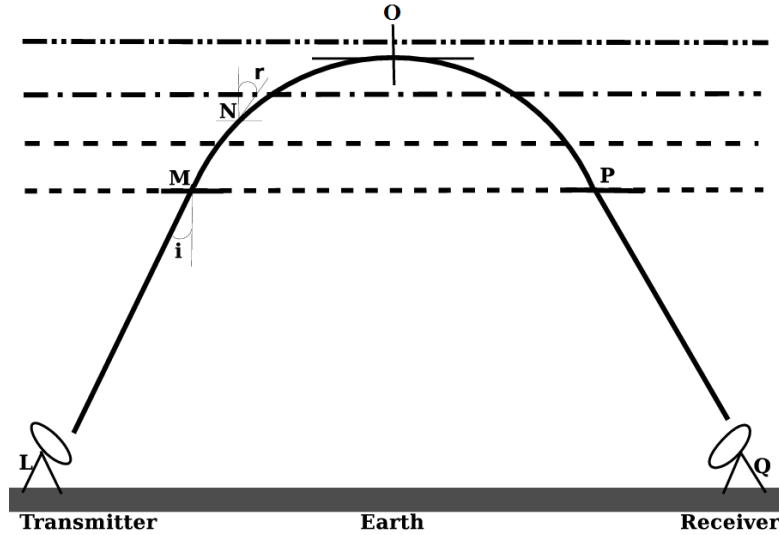
Figure 4.7: A schematic representation of the propagation of radio waves through the ionosphere along the path LMNPQ (adopted from White, 1970).

Figure 4.7 demonstrates the propagation of radio signal waves through the ionosphere. A radio signal wave transmitted by the transmitter L on the Earth surface enters the ionosphere at point M and is refracted by the electron density at a higher altitude. In the figure, i is the angle of incidence at point M and r is the angle of refraction at point N. The refraction angle at point O is 90°. The beam exits the ionosphere at P and goes back to the Earth surface to a receiver at Q. At higher frequencies, the refraction may not be sufficient to return the wave to the Earth, and it passes through the ionosphere (White, 1970).

When radio waves travel through the ionosphere, their phase velocity increases and the refractive index is greater than one in the lower ionosphere, while below the ionosphere is equal to one. For a radio signal wave of frequency f, propagating through the ionosphere, the refractive index can be derived from the Appleton-Hartree equation (Rishbeth and Garriott, 1969; White, 1970; Davies, 1990; Sizun and de Fornel, 2005) which is given by:

$$\mu^2 = 1 - \frac{4\pi N_e e^2}{m_e \omega^2},\tag{4.4}$$

where N_e is the electron density measured in electrons/m^3, e is the electron charge ($e = -1.602 \times 10^{-19}$ C), m_e is mass of electron ($m_e = 9.11 \times 10^{-30} kg$) and ω is angular frequency ($\omega = 2\pi f$), and f is radio signal wave frequency (Hz).

The refractive index outside the ionosphere is μ_M and within the ionosphere it is μ_N at N, as illustrated in Figure 4.7. As the wave penetrates the layers, the electron density increases and the wave normal changes according to Snell's law:

$$\mu_M \sin i = \mu_N \sin r. \tag{4.5}$$

At point O at the top of the trajectory in Figure 4.7, the angle r = 90°. At point M the refractive index (μ_M) is equal to 1 (Jahoda and Sawyer, 1971; Davies, 1990). Therefore,

$$\mu_M \sin i = \mu_O \sin r \tag{4.6}$$
$$\sin i = \mu_O$$

and therefore,

$$\mu_O = \sin i$$

For the case where the wave rises nearly vertically under the ionosphere, the angle i = 0 therefore $\mu_O = \sin 0 = 0$. Setting $\mu^2 = 0$ in Equation 4.4 and letting $\omega_o = 2\pi f_o$ gives

$$f_o = \sqrt{\frac{N_e e^2}{\pi m_e}} \tag{4.7}$$

which is the cutoff frequency or critical frequency. Every frequency less than f_o is reflected and will eventually return to Earth; however, the higher frequencies penetrate the ionosphere and go out into space. Therefore, the maximum electron density at the maximum height is

$$N_e(max) = \frac{\pi m_e f_o^2}{e^2} \tag{4.8}$$
$$= 1.24 \times 10^{-10} f_o^2 \text{ electrons/m}^{-3}$$

This implies that electron density N_e is directly proportional to the square of the critical frequency f_o.

The virtual height (h') of the ionospheric reflection is the height at which impulse propagated at the speed of light would be reflected. It can be found when the flight time t from the transmitter to the receiver via the ionosphere is considered. As the frequency increases, the pulse penetrates to higher altitudes in the ionosphere and the virtual height continues to increase until the signal penetrates the ionosphere (Davies, 1990; Sizun and de Fornel, 2005). The virtual height is related to the time of flight t and the refractive index as follows:

$$h' = \frac{1}{2}ct = \int_0^{h_r} \frac{dh}{u} = \int_0^{h_r} \mu' dh \tag{4.9}$$

where c is the speed of light, u is the group speed and h_r is the real height of reflection (Davies, 1990). The simultaneous measurements of observable parameters of the reflected signals received from the ionosphere include, height for vertical incidence measurements, phase, angle of arrival, frequency, wave polarisation, doppler shift & spread and amplitude. Since the physical parameters of the ionospheric plasma affect the way radio waves reflect or pass through the ionosphere, it
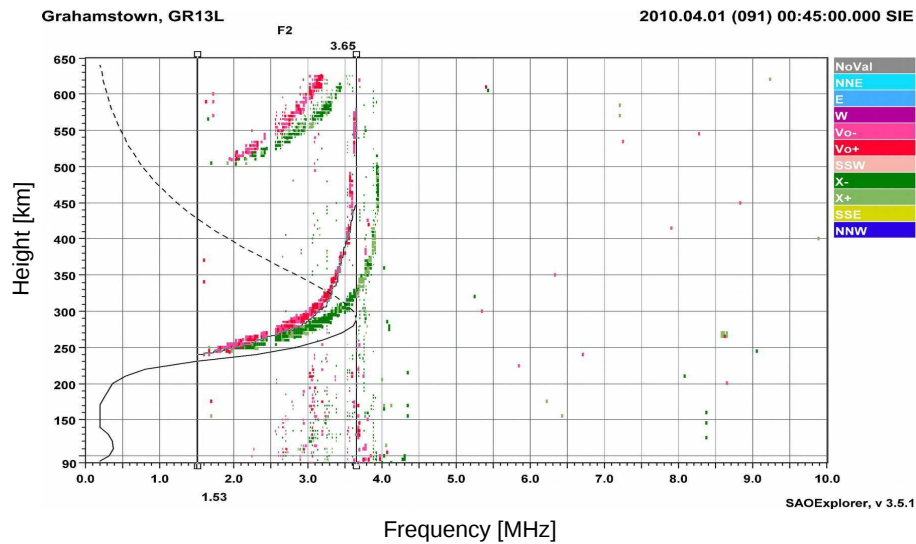
(a) Nighttime Ionogram at 00:45 UT
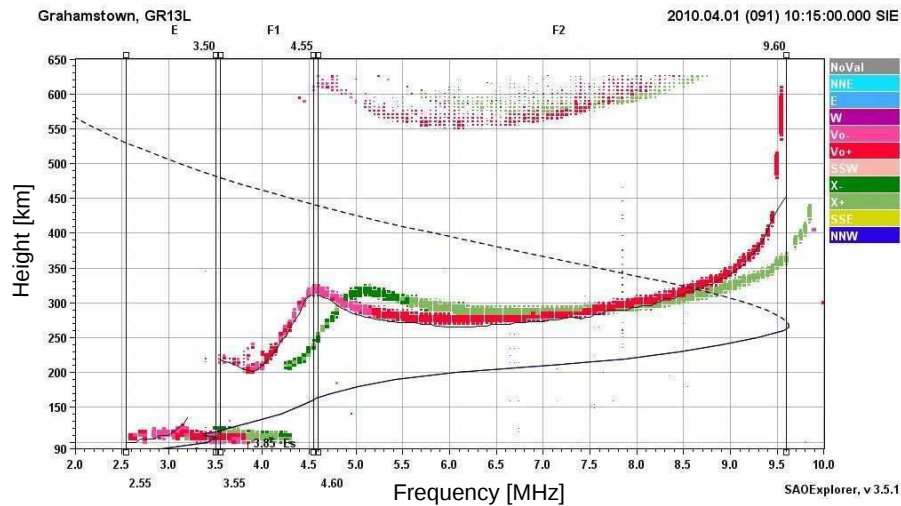
(b) Daytime Ionogram at 10:15 UT

Figure 4.8: Example of (a) a nighttime and (b) a daytime ionogram for Grahamstown (33.3° S, 26.5°E) ionosonde station on 01 April 2010.

is possible to measure the seven observable parameters at a number of discrete frequencies and heights to map out and characterise the structure of the ionosphere. Both the height and frequency dimensions of these measurements require hundreds of individual measurements to approximate the underlying continuous functions. The resulting measurements are called an ionogram which is a graph of virtual height plotted against frequency as shown in Figure 4.8 (LDI, 2015). Figure 4.8 gives samples of a nighttime (a) and daytime (b) ionograms observed at the mid-latitude, Grahamstown (33.3°S, 26.5°E), South African ionosonde station. The ionograms display two traces of the radio signal waves for each layer of the ionosphere, the ordinary (O) and extraordinary (X) waves which are shown in red and green respectively. The overplotted black curves are the generated electron density profiles with real height. The dotted and solid black curves represent the derived topside and the bottomside ionospheric density profiles respectively. The vertical asymptotes for O and X traces represent the critical frequencies foF2 and fxF2 respectively, and

48

are separated by approximately half the gyrofrequency, f$_{ce}$ (McNamara, 1991). In the nighttime ionogram, (Figure 4.8(a)) only the echoes of the F2 layer are present. The daytime ionogram, Figure 4.8(b) shows the wave traces with reflections from the E, F1, and F2 layers. The virtual height appears to increase steadily with frequency until the signal penetrates the ionosphere at a higher frequency than the critical frequency of the F2 layer (foF2). The foF2 values for nighttime and daytime are different, which suggests the ionisation levels in the ionosphere (Davies, 1990; Ngwira, 2011).

4.4.2 Ionogram interpretation

In order to understand and interpret radio signals propagating through and reflected by the ionosphere to the receiver on Earth, it is important to first understand the radio refractive index of the ionosphere. Neglecting the influence of positive and negative ions on wave propagation, two frequencies can be defined:

$$\text{Plasma frequency: } (2\pi f_{be})^2 = \omega_{be}^2 = N_e e^2 / m_e \epsilon_0 \tag{4.10}$$

$$\text{Gyro frequency: } 2\pi f_{ce} = \omega_{ce} = \mathbf{B}e/m_e \tag{4.11}$$

where f_{be} and f_{ce} are plasma and gyro-frequencies respectively, ϵ_0 is the electric permitivity of free space and $\mathbf{B}$ is the geomagnetic field flux density (Rishbeth and Garriott, 1969; Davies, 1990). Consider a uniform external magnetic field $\mathbf{B}$ which makes an angle θ with the direction of propagation of a plane wave in the x-direction as shown in Figure 4.9.
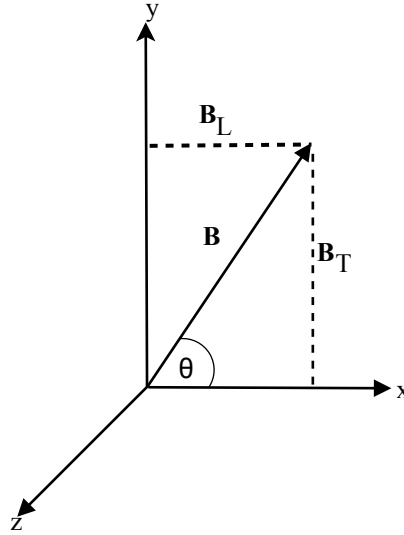
Figure 4.9: A schematic representation of the system of orthogonal axes (Davies, 1990)

X, Y and Z are dimensionless quantities defined by the following expressions:

$$X = \omega_p^2/\omega^2$$
$$Y = \omega_{\mathbf{B}}/\omega$$
$$Z = \omega_e/\omega$$

49

and

$$Y_L = \omega_L/\omega = \frac{\omega_{\mathbf{B}} cos\theta}{\omega}$$

$$Y_T = \omega_T/\omega = \frac{\omega_{\mathbf{B}} sin\theta}{\omega}$$

where $\omega_{\mathbf{B}}$ is gyro frequency, ω_L and ω_T are longitudinal and transverse components respectively and ω_e is angular collision frequency between electrons and heavier particles. Hence, the magnetoionic parameters can be expressed as:

$$X = N_e e^2/\epsilon_0 m_e \omega^2, \; Y_L = e\mathbf{B}_L/m_e\omega, \; Y_T = e\mathbf{B}_T/m_e\omega \text{ and } Z = \nu/\omega \tag{4.12}$$

The expression for the complex refractive index μ can be expressed in terms of the Appleton-Hatree formula (Davies, 1990) as:

$$\mu^2 = 1 - \frac{X}{1 - jZ - \left(\frac{Y_T^2}{2(1-X-jZ)}\right) \pm \left(\frac{Y_T^4}{4(1-X-jZ)^2} + Y_L^2\right)^{\frac{1}{2}}} \tag{4.13}$$

For the negligible collision frequency in the F region, the case $Z \approx 0$ (Rishbeth and Garriott, 1969; Davies, 1990), the refractive index μ becomes:

$$\mu^2 = 1 - \frac{X}{1 - \frac{Y_T^2}{2(1-X)} \pm \left[\frac{Y_T^4}{4(1-X)^2} + Y_L^2\right]^{\frac{1}{2}}} \tag{4.14}$$

$$= 1 - \frac{2X(1-X)}{2(1-X) - Y_T^2 \pm [Y_T^4 + 4(1-X)^2 Y_L^2]^{\frac{1}{2}}},$$

$$= 1 - \frac{X(1-X)}{(1-X) - \frac{1}{2}Y_T^2 \pm \left[\frac{1}{4}Y_T^4 + (1-X)^2 Y_L^2\right]^{\frac{1}{2}}}$$

The positive (+) and negative (-) signs refer to the ordinary and extraordinary waves respectively. For the horizontally stratified ionosphere, a vertical incident wave is reflected at a level of $\mu^2 = 0$. This occurs at $X = 1$ for the ordinary wave, which is the same as having no magnetic field. The reflections occur at the level where $X = 1 - Y$ if $Y < 1(f > f_{ce})$ and where $X = 1 + Y$ if $Y > 1(f < f_{ce})$ for the extraordinary wave (Rishbeth and Garriott, 1969).

For a normal wave propagating parallel to the magnetic field $\theta = 0$, then $Y_L = Y$ and $Y_T = 0$ and the refractive index μ can be easily simplified from Equation 4.14. Again for a normal wave propagating perpendicularly to the magnetic field, the quasi-transverse approximation ($Y_T^4 \gg 4(1-X)^2 Y_L^2$) holds both for $\theta = 90$ with nearly all values of X and the ordinary wave with $X \approx 1$, when $Y << 1$, at nearly all values of θ. Therefore, at $X = 1$ and $\theta = 90$ and at very high frequency

the quasi-longitudinal approximation ($Y_T^4 \ll 4(1-X)^2 Y_L^2$) is useful and the refractive index is now expressed as

$$\mu^2 = 1 - \frac{X}{1 \pm Y_L} \tag{4.15}$$

The ordinary and extraordinary wave modes are elliptically polarized. Hence, any plane polarized wave propagating through the ionosphere may be considered as the sum of the extraordinary and ordinary components. The plane of polarization continues to rotate along the wave path because the ordinary and extraordinary waves have different phase velocities (Rishbeth and Garriott, 1969; Davies, 1990).

The relationship between the ordinary (O) and extraordinary (X) wave critical frequencies are found from the reflection conditions, $X = 1 + Y$, $X = 1$, and $X = 1 - Y$ (Davies, 1990). As already mentioned, the vertical asymptotes for foF2 and fxF2 are separated by approximately half the gyrofrequency f_{ce} (McNamara, 1991). The O and X waves are reflected at the same height and they are related by the following expression:

$$f_o^2 = f_x(f_x - f_{ce}) \tag{4.16}$$

$$f_o^2 = f_x\left[f_x\left(1 - \frac{f_{ce}}{f_x}\right)\right]$$

$$f_o^2 = f_x^2\left(1 - \frac{f_{ce}}{f_x}\right)$$

Taking the square root on both sides of the equation we have,

$$f_o = f_x\left(1 - \frac{f_{ce}}{f_x}\right)^{\frac{1}{2}} \tag{4.17}$$

Using the Taylor expansion formula (Ho and Lee, 2004):

$$(1 + x)^\alpha = 1 + \alpha x + \frac{\alpha(\alpha - 1)}{2!}x^2 + \frac{\alpha(\alpha - 1)(\alpha - 2)}{3!}x^3 + ... \tag{4.18}$$

with, $\alpha = \frac{1}{2}$ and $x = -\frac{f_{ce}}{f_x}$ in our case, we have

$$\tag{4.19}$$

$$\left(1 - \frac{f_{ce}}{f_x}\right)^{\frac{1}{2}} = 1 + \frac{1}{2}\left(-\frac{f_{ce}}{f_x}\right) + \frac{\frac{1}{2}(\frac{1}{2} - 1)}{2!}\left(-\frac{f_{ce}}{f_x}\right)^2 + ...$$

$$= 1 - \frac{f_{ce}}{2f_x} - \frac{1}{8}\left(\frac{f_{ce}}{f_x}\right)^2 + ...$$

Hence, if $f_x \gg f_{ce}$ it means that $1 >> \frac{f_{ce}}{f_x}$ and all the high orders $\left(\frac{f_{ce}}{f_x}\right)^2$; $\left(\frac{f_{ce}}{f_x}\right)^3$; ... are close to zero and can be neglected. Neglecting all the high order terms of the Taylor expansion represented by Equation 3.19, we have

$$\left(1 - \frac{f_{ce}}{f_x}\right)^{\frac{1}{2}} = 1 - \frac{f_{ce}}{2f_x}, \tag{4.20}$$

and then Equation 4.17 becomes:

$$(4.21)$$

$$f_o = f_x \left(1 - \frac{f_{ce}}{2f_x} \right)$$

$$f_o = f_x - \frac{f_{ce}}{2}$$

$$\therefore f_x \cong \frac{f_{ce} + 2f_o}{2} \cong f_o + \frac{f_{ce}}{2}$$

The above formula is important for the interpretation of an ionogram. It differentiates the critical frequency of the O and X ray penetration of a particular layer and vice versa (McNamara, 1991).

The ionosonde foF2 data for southern and northern hemispheres over African and European sectors respectively were used to analyse the ionospheric responses. The southern hemisphere was represented by Madimbo, MU12K (22.4°S, 30.9°E; 32.7°S, geomagnetic) and Grahamstown, GR13L (33.3°S, 26.5°E; 41.8°S, geomagnetic) stations while Juliusruh, JR055 (54.6°N, 13.4°E; 50.9°N, geomagnetic) and Rome, RM041 (41.9°N, 12.5°E; 35.6°N, geomagnetic) stations were considered for the northern hemisphere mid-latitudes. The foF2 values were extracted using Standard Archiving Output (SAO) explorer software.

4.5 Global Positioning System data

The Global Navigation Satellite System (GNSS) is the constellation of satellites providing signals from space and transmit timing and positioning data to GNSS receivers. It is of significant use to ionospheric TEC studies both regionally and globally (Misra and Enge, 2006). GNSS constellations such as the American Global Positioning System (GPS), the Russian Global Navigation Satellite System (GLONASS), Galileo (European GNSS) and the Chinese COMPASS Navigation are either fully operational or are being developed. The discussion here will only focus on GPS satellites, since the data used in this study is from GPS.

The GPS is an all-weather, space-based navigation system developed by the United State (US) Department of Defense (DoD) to meet the requirements for military forces to precisely determine their velocity, position and time in a common reference system, anywhere on or near the Earth on a continuous basis (Hofmann-Wellenhof et al., 1994; Misra and Enge, 2006). The satellites emit coded radio signals that a GPS receiver decodes to determine important system parameters. The satellites are operated and maintained by the US DoD. GPS was initially intended for military applications, but in the 1980s the government made the system available for civilian applications, such as rail transport, road, shipping, aviation, Geophysics, mapping, science, surveying, telecommunication, security, etc (Farrell and Barth, 1998; Misra and Enge, 2006).

GPS consists of three main segments, namely the space segment which comprises the satellite, the control segment that deals with the management of the satellite operations and the user segment which covers the activities related to the development of military and civil GPS user equipment (Misra and Enge, 2006).

4.5.1 Space segment
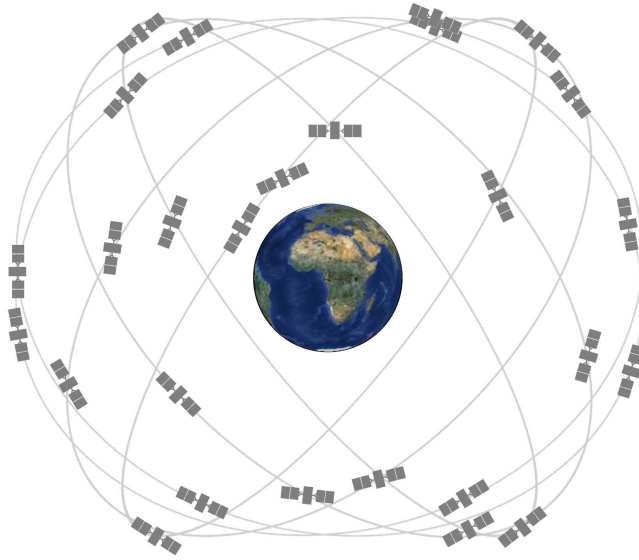
Figure 4.10: The constellation of GPS satellites (Gps.gov, 2017).

The space segment comprises a baseline constellation of 24 satellites in near circular orbits with an altitude of about 20,200 km above the Earth, and a period of ≈12 hours. The constellation of satellites is shown in Figure 4.10. Each satellite circles the Earth twice a day. The satellites are distributed into six equally-spaced orbital planes with an inclination angle of 55° relative to the equatorial plane, with four slots distributed unevenly in each orbit. The satellites are located such that a user anywhere in the world has a direct line of sight to at least four satellites at any time (Misra and Enge, 2006).

4.5.2 Control segment

The control segment consists of a global network of ground facilities that track and monitor satellite transmission, perform analysis and send commands and data to the GPS operational constellation. Figure 4.11 shows the GPS control segment locations. The current operational control segment includes the master control station, ground-based antennas, and monitor stations.

Monitor stations track the GPS satellites as they pass overhead and channel their observations back to the master control station. They also collect atmospheric data, range/carrier measurements, and navigation signals. There are sixteen monitor stations throughout the world, namely 10 stations of the National Geospatial-intelligence Agency (NGA) and six of the United States Air Force (Hofmann-Wellenhof et al., 1994; Misra and Enge, 2006; Gps.gov, 2017).

The master control station generates and uploads navigation messages and ensures the health and accuracy of the satellite constellation. The master control station receives the navigation information from the monitor station and uses it to compute the precise locations of the GPS satellites in space, and then uploads this data to the satellites (Gps.gov, 2017).

The ground antennas communicate with the GPS satellites for control and command purposes. The antennas support the S-band communication protocol. This links or sends navigation data

GPS Control Segment
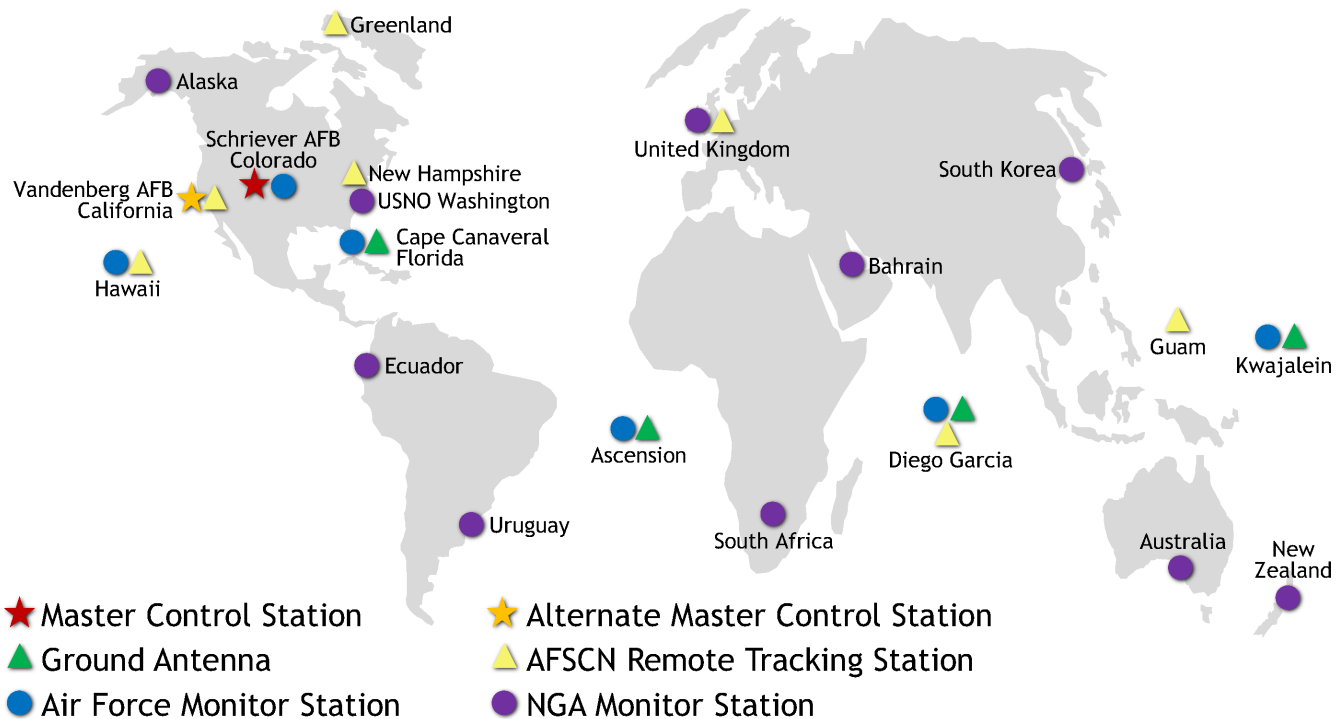
Figure 4.11: The Operational Control segment includes a master control station, an alternate master control station, 11 command and control antennas, and 16 monitoring sites (Gps.gov, 2017).

uploads and processor programme loads, and collects telemetry. The ground antennas are also responsible for normal command transmissions to the satellites (Hofmann-Wellenhof et al., 1994; Gps.gov, 2017).

The user segments has two primary user groups, that is the military and the civilian. It consists of antennas and receiver processors that measure and decode the satellite transmissions to provide positioning, velocity and precise timing information to the user (Farrell and Barth, 1998; Misra and Enge, 2006).

4.5.3 GPS signal

Each GPS satellite continuously broadcasts radio signals using two L-band frequencies which are referred to as L1 (Link 1) and L2 (Link 2). The L-band covers frequencies between 1 GHz and 2 GHz. Therefore the centre frequency between L1 and L2 is

$$\text{L1: } f_{L1} = 1575.42 \text{ MHz and L2: } f_{L2} = 1227.60 \text{ MHz.}$$

54

There are other L bands on GPS such as L5 signal allocated frequency band centered at $f_{L5} = 1176.45$ MHz. The Coarse/Acquisition (C/A) code is modulated on the L1 carrier phase. Each satellite has different C/A pseudorandom noise (PRN) codes and each PRN code is nearly orthogonal to all other C/A PRN codes. The Precision-code (P-code) modulates both L1 and L2. The P-code is a long PRN code. The P-code is encrypted into the Y-code in the Anti-Spoofing (AS) mode of operation. Only authorized users with the cryptographic keys can use the encrypted Y-code which requires a classified AS module for each receiver channel (Farrell and Barth, 1998; Misra and Enge, 2006).

4.6   GPS observables

The GPS observables are ranges which are inferred from measured time or phase differences based on a comparison between a received signal and a receiver-generated signal. There are two fundamental observables, namely the pseudorange and carrier phase (Hofmann-Wellenhof et al., 1994; Strang and Borre, 1997; El-Rabbany, 2002; Xu and Xu, 2016).

4.6.1   Pseudorange measurements

The pseudorange is a measure of the distance between the GPS receiver' and the GPS satellite's antenna. The P-code or C/A code can be used to measure the pseudorange. The distance can be measured by determining the time lapse from GPS signal transmission by the satellite to signal reception at the GPS receiver antenna. On the other hand, the transmitting time can be measured through maximum correlation analysis of the receiver code and the GPS signal.

Let the reading of satellite clock at emmission time and receiver clock at signal reception time be indicated by t^S and t_R respectively. The clocks delay with respect to the GPS system time are designated as δ^S and δ_R. The difference between the clock readings is equivalent to the time shift Δt, which aligns the satellite and reference signal during the code correlation procedure in the receiver (Hofmann-Wellenhof et al., 1994; Xu and Xu, 2016). Therefore,

$$\Delta t = t_R - t^S = [t_R(GPS) - \delta_R] - [t^S(GPS) - \delta^S] \qquad (4.22)$$
$$= t_R(GPS) - t^S(GPS) + \delta^S - \delta_R$$
$$= \Delta t(GPS) + \Delta \delta,$$

where $\Delta \delta = \delta^S - \delta_R$ and $\Delta t(GPS) = t_R(GPS) - t^S(GPS)$. The bias δ^S of the satellite clock can be modeled by polynomial with the coefficients being transmitted in the first sub-frame of the navigation message (Hofmann-Wellenhof et al., 1994). If the δ^S correction is applied, $\Delta \delta$ equals the negative receiver clock delay. The time interval Δt multiplied by the speed of light c (3.0×10^8 m/s) gives the pseudorange R,

$$R = c\Delta t, \qquad (4.23)$$

then substitute Equation 4.22 into Equation 4.23, the pseudorange becomes,

$$R = c\Delta t(GPS) + c\Delta \delta. \qquad (4.24)$$

The pseudorange measurements, P_1 and P_2 at L_1 and L_2 are given by:

$$P_1 = \rho + c(dt - dT) + d\rho + d_T + I_1 + b_{P_1}^S + b_{P_1}^R + \varepsilon(P_1) \tag{4.25}$$
$$P_2 = \rho + c(dt - dT) + d\rho + d_T + I_2 + b_{P_2}^S + b_{P_2}^R + \varepsilon(P_2) \tag{4.26}$$

where

ρ: True geometric range (m) between the satellite and the receiver,

$d\rho$: Orbital error (m),

dt: Satellite clock error with respect to GPS time (s),

dT: Receiver clock error with respect to GPS time (s),

d_T: Tropospheric error (m),

I_1, I_2: Pseudo-range ionospheric delays (m) at L_1 and L_2 respectively,

$b_{P_1}^S, b_{P_2}^S$: Pseudo-range satellite delays (m) at L_1 and L_2,

$b_{P_1}^R, b_{P_2}^R$: Pseudo-range receiver delays (m) at L_1 and L_2,

$\varepsilon(P_1), \varepsilon(P_2)$: Pseudo-range measurement noises which include multipath errors (m).

If thermal noise and multipath errors are ignored, subtracting Equation 4.25 from Equation4.26, the pseudorange measurements elliminates $d\rho$, ρ, dt, dT and d_T and gives the geometry free linear combination, i.e.

$$P_2 - P_1 = I + b_P^S + b_P^S \tag{4.27}$$

where $I = I_2 - I_1$

Defining ionospheric delay as

$$I = \frac{40.30}{f^2}\text{TEC}, \tag{4.28}$$

Where 40.30 is the proportionality that can be obtained from the expression of the ionosphere's index in subsection 4.6.3. The difference between the pseudorange measurements becomes

$$P_2 - P_1 = 40.30\left(\frac{1}{f_2^2} - \frac{1}{f_2^2}\right)\text{TEC} + b_p^S + b_p^R \tag{4.29}$$

Solving for TEC in terms of pseudorange measurements at the two frequencies gives

$$\text{TEC} = \frac{1}{40.30}\left(\frac{(f_1 f_2)^2}{f_1^2 - f_2^2}\right)\{(P_2 - P_1) - (b_p^S + b_p^R)\} \tag{4.30}$$

When the bias terms are ignored, in Equation 4.30 and the respective values of f_1 and f_2 are substituted, then TEC can be expressed in its units (TECU) as

$$\text{TEC} = 9.52(P_2 - P_1)\text{TECU} \tag{4.31}$$

where 1 TECU is equivalent to 10^{16} electrons/m^2.

4.6.2 Carrier phases

The carrier phase measures the phase of the received satellite signal relative to the receiver-generated carrier phase at reception time. The measurements are done by shifting the receiver-generated phase to track the received phase. The carrier phase measurements are more precise than those of code phase, but they cannot provide explicit pseudorange due to integer ambiguity. The combination of code and carrier phase measurements can improve the precision of the pseudorange and the positioning performance of the receivers (Hofmann-Wellenhof et al., 1994; Misra and Enge, 2006; Xu and Xu, 2016). The carrier phase at L_1 and L_2 frequencies, are given by

$$\phi_1 = \rho + c(dt - dT) + d\rho + d_T + \lambda_1 N_1 - I_1 + b^S_{\phi_1} + b^R_{\phi_1} + \varepsilon(\phi_1) \tag{4.32}$$
$$\phi_2 = \rho + c(dt - dT) + d\rho + d_T + \lambda_2 N_2 - I_2 + b^S_{\phi_2} + b^R_{\phi_2} + \varepsilon(\phi_2) \tag{4.33}$$

where

λ_1, λ_2: Carrier signal wavelengths at L_1 and L_2 frequencies respectively,

N_1, N_2: Carrier phase integer ambiguities,

I_1, I_2: Carrier phase ionospheric delays (m),

$b^S_{\phi_1}, b^S_{\phi_2}$: Carrier phase satellite delays or inter-frequency biases (m),

$b^R_{\phi_1}, b^R_{\phi_2}$: Carrier phase receiver delays (m),

$\varepsilon(\phi_1), \varepsilon(\phi_2)$: Carrier phase measurement noises with multipath errors included (m).

Especially the carrier phase polarisation term corresponding to the product of the wavelength and the transmitter-receiver antenna relative rotating angle (which accounts for less than 0.5 TECU for ionospheric carrier phase combination L_1-L_2) is not included in Equations 4.32 and 4.33.

As the pseudorange case, ignoring other errors, including multipath and thermal noise, the difference between the carrier-phase measurements eliminates the orbital error, geometric range, clock errors and tropospheric delay, i.e.

$$\phi_1 - \phi_2 = \lambda N - I + b^S_\phi + b^R_\phi \tag{4.34}$$

where $\lambda N = \lambda_1 N_1 - \lambda_2 N_2$, $I - I_2 - I_1$, $b^S_\phi = b^S_{\phi_1} - b^S_{\phi_2}$, $b^R_\phi = b^R_{\phi_2} - b^R_{\phi_1}$
By definition the ionospheric phase advance is similar to the ionospheric delay (in magnitude) defined in Equation 4.28 Using this result in Equation 4.34 provides,

$$\phi_1 - \phi_2 = 40.30 \left(\frac{1}{f_2^2} - \frac{1}{f_1^2} \right) \text{TEC} + (\lambda_1 N_1 - \lambda_2 N_2) + (b^R_\phi - b^S_\phi) \tag{4.35}$$

Solving for a TEC value independent of ambiguities and biases gives

$$\text{TEC} = 9.52(\phi_2 - \phi_1) \tag{4.36}$$

This is a precise but ambiguous measurement due to the presence of the integer ambiguities, while Equation 4.31 provides an unambiguous but imprecise observable due to the presence of noise (Misra and Enge, 2006; Xu and Xu, 2016). These two sets of observables are combined while using the pseudo-ranges to estimate the biases and ambiguities in the carrier phase measurements (Misra and Enge, 2006).

4.6.3 Total electron content derived from GPS

The GPS network provides an opportunity to derive the TEC for global and regional ionospheric studies. TEC is the key parameter for describing the ionosphere and is also used to correct ionospheric effects which degrade GNSS positioning accuracy (Misra and Enge, 2006). The influence of the ionosphere on GNSS measurements depends on GNSS signal frequency and TEC.

TEC is the total number of electrons integrated between two points along a tube of one meter squared cross section. It is measured in TEC units (TECU) which is equivalent to 10^{16} electrons per m^2. The electron content does not depend on the assumptions related to the Earth's magnetic field and reaches up to a height of 20,000 km (Davies and Hartmann, 1997). Neglecting the assumptions of the magnetic field, where $Y = 0$, Equation (4.14) reduces to:

$$\mu^2 = 1 - X \tag{4.37}$$

Expanding Equation 4.37 we get:

$$\mu = 1 - \frac{1}{2}X + \frac{\frac{1}{2}(\frac{1}{2}-1)}{2!}X^2 + ... \tag{4.38}$$

At GPS frequencies, the higher order terms may be neglected and the refractive index may be approximated (Parkinson et al., 1996) as:

$$\mu \approx 1 - \frac{1}{2}X \tag{4.39}$$

where

$$X = N_e e^2 / \epsilon_0 m_e \omega^2 = \omega_{be}^2 / \omega^2 \tag{4.40}$$

$$= \left(\frac{2\pi f_{be}}{2\pi f}\right)^2 = \frac{f_{be}^2}{f^2}$$

therefore,

$$\mu \approx 1 - \frac{1}{2}\frac{f_{be}^2}{f^2} \tag{4.41}$$

but from Equation (4.10) plasma frequency $f_{be}^2 = \frac{N_e e^2}{4\pi^2 m_e \epsilon_0}$, where $\epsilon_0 = 8.854 \times 10^{-12}$ Fm^{-1}. Therefore, plasma frequency becomes:

$$f_{be}^2 = \frac{N_e(-1.602 \times 10^{-19}C)^2}{4\pi^2(9.11 \times 10^{-31} \text{ kg})(8.854 \times 10^{-12} \text{ Fm}^{-1})}$$
$$= 80.594 N_e$$

then substitute f_{be}^2 into Equation (4.41) and the phase refractive index reduces to,

$$\mu_p = 1 - \frac{80.594 N_e}{2f^2} = 1 - \frac{40.30 N_e}{f^2} \tag{4.42}$$

The assumptions under which the Appleton-Hartree magnetoionic theory is applicable (Davies, 1990):

- Ionospheric electrons oscillate at angular plasma frequency.

- The number of ions in the ionosphere is equal and there is no resultant space charge.

- Since the mass of an electron is less than mass of an ion, electrons are more mobile and thus the positive ions have a negligible effect on radio waves.

The group refractive index may be written in terms of the phase refractive index (Kaplan and Hegarty, 2006) as

$$\mu_g = \mu_p + f\frac{d\mu_p}{df} \tag{4.43}$$

Differentiating phase refractive index we have:

$$d\mu_p = \frac{80.594 N_e}{f^3} df \tag{4.44}$$

To get the group refractive index, substitute Equations (4.42) and (4.44) into Equation (4.43) we get,

$$\mu_g = 1 + \frac{40.30 N_e}{f^2} \tag{4.45}$$

Thus the phase and group velocity of wave can be expressed as

$$\nu_p = \frac{c}{1 - \frac{40.30 N_e}{f^2}} \tag{4.46}$$

$$\nu_g = \frac{c}{1 + \frac{40.30 N_e}{f^2}} \tag{4.47}$$

where c is the speed of light, ν_p and ν_g are phase and group velocity respectively. Thus, conventionally, the phase and group refractive indices can be written as

$$\mu_p = 1 - \frac{40.30 N_e}{f^2} \tag{4.48}$$

$$\mu_g = 1 + \frac{40.30 N_e}{f^2} \tag{4.49}$$

4.6.4 TEC derived from ionospheric refraction

The ionospheric free electrons influence electromagnetic wave propagation, for example the GPS satellite signal. As the GPS signal propagates through the ionosphere, it is bent as a result of Fermat's principle which states that, "of all the paths that can be taken by an electromagnetic wave e.g. a GPS signal, a radio wave or a light wave travelling from one point to another, it will take the path which requires the least amount of time" (Hofmann-Wellenhof et al., 1994).
The measured range (s) between the receiver (R) and satellite (S) along the signal path, according to Fermat's principle (Hofmann-Wellenhof et al., 1997; Kaplan and Hegarty, 2006) is defined by:

$$s = \int n\,ds \tag{4.50}$$

where n is the refractive index. The geometric range s_0 along the straight line between the satellite and the receiver can be found by setting n = 1

$$s_0 = \int ds_0 \tag{4.51}$$

The ionospheric delay (Δ^{Iono}) is the difference between the geometric range and the measured range and follows from:

$$\Delta^{Iono} = \int nds - \int ds_0 \tag{4.52}$$

For a phase refractive index n_p, and for a group refractive index (n_g) obtained from Equations 4.48 and 4.49 respectively, the ionospheric delay may be written as follows:

$$\Delta_p^{Iono} = \int \left(1 + \frac{40.30N_e}{f^2}\right)ds - \int ds_0 \tag{4.53}$$

$$\Delta_g^{Iono} = \int \left(1 - \frac{40.30N_e}{f^2}\right)ds - \int ds_0 \tag{4.54}$$

Rewriting the above equations we have,

$$\Delta_p^{Iono} = \int ds + \frac{40.30}{f^2} \int N_e ds - \int ds_0 \tag{4.55}$$

$$\Delta_g^{Iono} = \int ds - \frac{40.30}{f^2} \int N_e ds - \int ds_0 \tag{4.56}$$

By considering the integration along the path, ds becomes ds_0 and the two equations can be simplified:

$$\Delta_p^{Iono} = -\frac{40.3}{f^2} \int N_e ds_0 \tag{4.57}$$

$$\Delta_g^{Iono} = \frac{40.3}{f^2} \int N_e ds_0$$

The electron density along the signal path is referred to as TEC. TEC is defined as:

$$\text{TEC} = \int N_e ds_0 \tag{4.58}$$

substitution of TEC into Equation 4.57 gives

$$\Delta_p^{Iono} = -\frac{40.3}{f^2}\text{TEC} \tag{4.59}$$

$$\Delta_g^{Iono} = \frac{40.3}{f^2}\text{TEC}$$
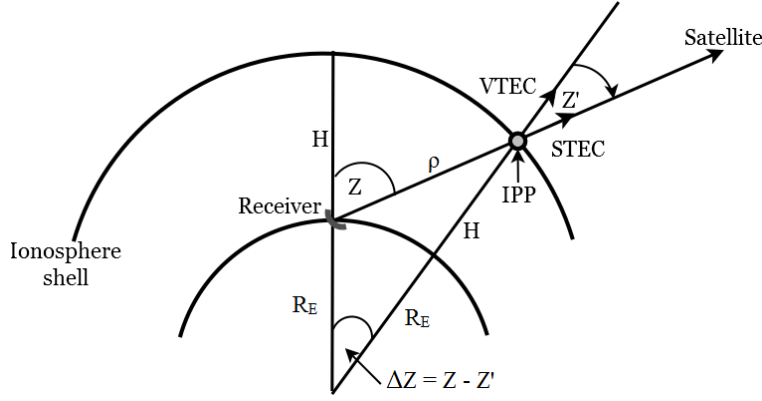
Figure 4.12: Geometry of the Vertical Total Electron Content (VTEC) and Slant Total Electron Content (STEC) mapping function. Ionospheric shell height (H) corresponds to typical F2 peak height, $hmF2 \sim 300 - 500$ km. VTEC is mapped at geographic location of the Ionospheric Pierce Point (IPP), distinct from the receiver location (Adopted from Hofmann-Wellenhof et al., 1994).

4.7 Ionospheric shell model

The ionospheric mapping function is one of the approximations to be taken into account when ionospheric delay of radio signals is estimated from GPS data. For the mapping function, the ionosphere is assumed to be located in a shell at altitude (H) which is taken as the F2 peak height hmF2 (see Figure 4.12).
Slant TEC measurements can be converted using the geometry of Figure 4.12, that is,

$$STEC = \frac{VTEC}{cosZ'} \tag{4.60}$$

$$sinZ' = \frac{R_E}{R_E + H}sinZ$$

where, Z' and Z are the zenith angles at the Ionospheric Pierce Point (IPP) and at the receiver respectively, R_E is the radius of the Earth and H is the assumed ionospheric shell height as illustrated in Figure 4.12. STEC is an ionospheric delay at the IPP as observed from the receiver's position. The aim of the mapping function is to allow a geographic conversion of STEC ionospheric delay to VTEC ionospheric delay at the same geographic point. Equation 4.60 is used to convert STEC to VTEC.

4.8 TEC data

GNSS TEC data for the northern and southern hemispheres' mid, low and equatorial latitudes was used to study the ionospheric responses to geomagnetic storms. GNSS data (in RINEX format) was downloaded from International GNSS Service (IGS) network (`ftp://garner.ucsd.edu`), the South African Chief Directorate: National Geo-spatial information TrigNet GPS receiver network (`ftp://ftp.trignet.co.za`), and the University NAVSTAR Consortium (UNAVCO) `ftp://data-out.unavco.org`. The IONEX data used to plot Global TEC maps were obtained from `ftp://cddis.gsfc.nasa.gov/pub/gps/products/ionex`.
The TEC data was derived at 30 s resolution using the software developed by the researchers from Boston College (Seemala and Valladares, 2011; Seemala, 2011). Only TEC data for satellites with

elevation angles greater than 30° was considered in order to eliminate/minimise multipath errors.

The GPS TEC variability during storm conditions from the stations over the southern and northern hemispheres in the mid, low and equatorial latitudes African sector were studied. The outliers in the TEC data were removed using 2 times the standard deviation of TEC (i.e. values that are greater than 2 times the standard deviation were eliminated) over all satellites' derived TEC by applying the expression,

$$| \, TEC - \overline{TEC} \, | > 2\sigma TEC, \tag{4.61}$$

$\overline{TEC}$ is TEC average and σ is standard deviation. This was done for all satellites. Figure 4.13 is an illustration of how the outliers were removed in the TEC data. Figures 4.13(a), (b) and (c) show TEC with outliers, TEC without outliers and TEC with outliers superimposed on TEC without outliers respectively.
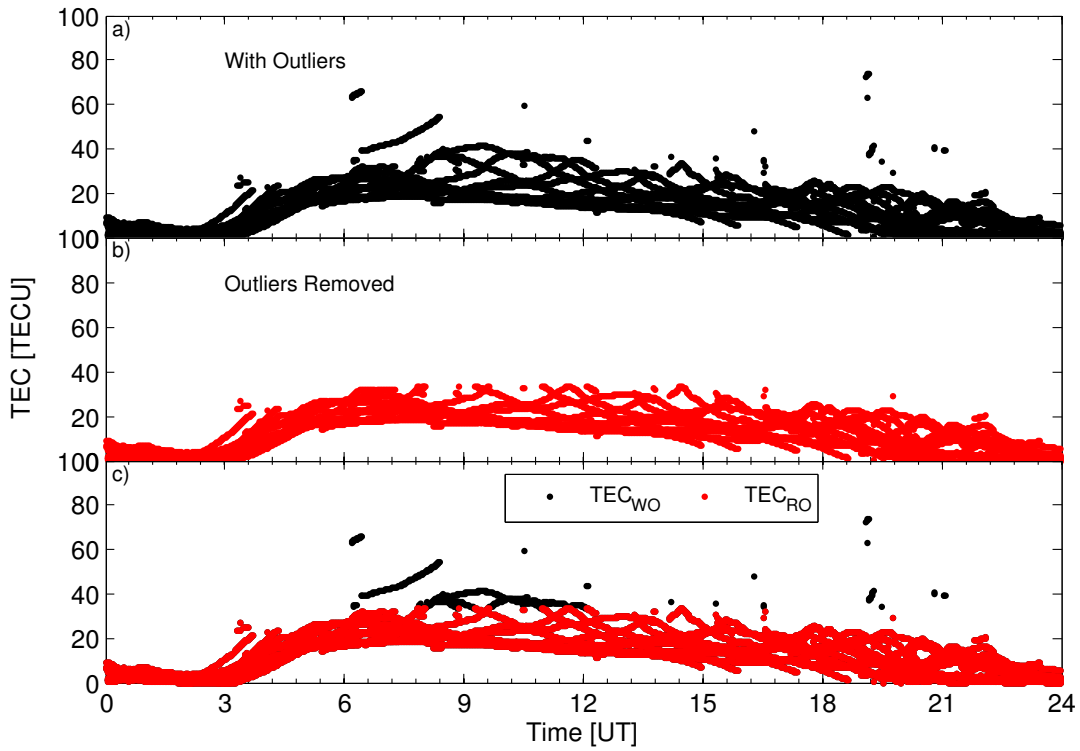
Figure 4.13: An illustration of the difference in data representation when outliers are removed from the observed TEC data. The diurnal variation of TEC (a) the observed TEC with outliers, (b) observed TEC without outliers and (c) TEC with outliers (TEC$_{\mathrm{WO}}$) superimposed on TEC without outliers (TEC$_{\mathrm{RO}}$).

The TEC values were computed by averaging TEC for individual satellites in view for a specific station. The monthly median of TEC values were determined and the percentage deviation of TEC was calculated to determine the degree of disturbance of TEC during CME- or CIR-driven storms as explained in Chapter 3. This method was used for TEC analyses in Chapter 6.

4.9   Summary

This chapter gave a brief discussion to the data sources used for this thesis. The various geomagnetic indices were highlighted. Both ground-based (ionosonde) and space-based (GPS) observations can be used to study the effects of space weather events on electron density of the ionosphere and TEC. The equation that differentiates the critical frequency of the ordinary and extraordinary rays of a particular layer was derived. The phase and group refractive indices were fully derived for the case when the effects of the magnetic field are negligible and for the case based on the electromagnetic wave propagation. The derivation of ionospheric delay which contains TEC was covered in this chapter. The method followed to remove outliers in TEC data was shown. Chapter 5 discusses ionospheric storm effects using GPS TEC and ionosonde foF2 data for the African and European mid-latitudes.

Chapter 5

Mid-latitude ionospheric response during intense geomagnetic storms of solar cycle 23

5.1 Introduction

This chapter describes an investigation of ionospheric response to four great geomagnetic storms (Dst $\leq$ -350 nT) that occurred during solar cycle 23. The storm periods considered in this analysis were 29 March - 02 April 2001, 27 - 31 October 2003, 18 - 23 November 2003 and 06 - 11 November 2004. The Global Navigation Satellite System (GNSS) Total Electron Content (TEC) at Ionospheric Pierce Point (IPP) (assumed at an altitude of 350 km) locations in latitude range 20°S - 38°S (31°S - 46°S, geomagnetic) and 38°N - 50°N (31°N - 46°N, geomagnetic) within 15°E - 40°E longitude over the African and European sector mid-latitudes were used to study ionospheric responses. The mid-latitude regions within the same longitude in both hemispheres were chosen in order to assess the contribution of low latitude changes, especially the Equatorial Ionization Anomaly (EIA) also called super-fountain effect during intense geomagnetic storms.

The ionosonde foF2 data from selected stations within the 15°E - 40°E geographic longitude were also used to study ionospheric responses to supplement TEC data. The local time within this longitude sector lies between approximately UT + 2 hours. The northern hemisphere stations used are Juliusruh, JR055 (54.6°N, 13.4°E; 50.9°N, geomagnetic) and Rome, RM041 (41.9°N, 12.5°E; 35.6°N, geomagnetic) while Madimbo, MU12K (22.4°S, 30.9°E; 32.7°S, geomagnetic) and Grahamstown, GR13L (33.3°S, 26.5°E; 41.8°S, geomagnetic) stations provided data for the southern hemisphere mid-latitudes. The stations considered are shown in a map (Figure 5.1).

Most results from this chapter were published in a paper by Matamba et al. (2016).

5.2 Magnetometer data

The magnetometer data (Horizontal, H component) from the equatorial station Addis Ababa, AAE (9.02° N, 38.77° E, geographic) was used to investigate the possible role of electric fields that penetrate to low latitudes. A change in H due to ionospheric currents was calculated by using the average value of H from 23:00 LT - 03:00 LT as baseline. Direct subtraction of the baseline H value from the time series H component measurements gives dH, which was used to examine equatorial electric field behaviour during storm periods. A positive dH is proportional to the
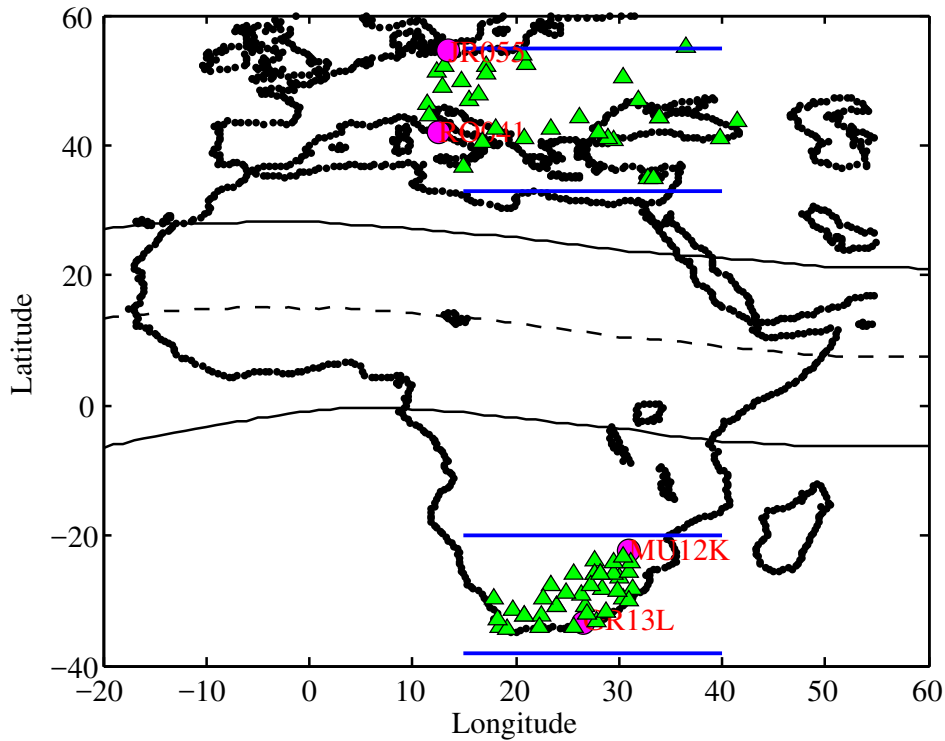
Figure 5.1: A map showing the GNSS (green triangles) and ionosonde (magenta circles) stations considered.

eastward electrojet or electric field (Rastogi, 1975; Ngwira et al., 2013). Strong daytime Equatorial Electrjets (EEJs) during geomagnetic storms are associated with an eastward penetration electric field, due to the southward Bz which occurs either in the Interplanetary Coronal Mass Ejection (ICME) sheath or magnetic cloud (Tsurutani et al., 1988). On the other hand a negative dH is proportional to the equatorial Counter-Electrojet (CEJ) which is due to a westward current (Rastogi et al., 2012; Ngwira et al., 2013). The daytime CEJ seems to be due to Disturbance Dynamo Electric Field (DDEF) caused by the joule heating of the auroral ionosphere (Blanc and Richmond, 1980; Rastogi et al., 2012). The magnetometer data was downloaded from Intermagnet (www.intermagnet.org).

5.3 Storm period : 29 March to 2 April 2001

Figure 5.2 shows the SYM-H (nT) index, IMF Bz (nT) and TEC (TECU) for the southern and northern hemispheres for 29 March - 02 April 2001. The dashed vertical lines in these figures represent the respective times of the sudden storm commencement, as represented by the short-duration positive spike (SI+) (Echer et al., 2009, 2010) in SYM-H or Dst data. During the analyzed event, SI+ occurred at 00:52 UT on 31 March 2001 and the minimum SYM-H index reached −435 nT at 08:10 UT on the same day. During the SI+, IMF Bz abruptly increased to about 50 nT and later turned strongly southward with the minimum reaching about -46 nT at 06:15 UT, as shown in panel 1. Panels 2 and 3 illustrate TEC maps over northern (NH) and southern (SH) hemispheres mid-latitude. Vertical TEC was plotted at Ionospheric Pierce Points (IPPs) to increase the data coverage on a regional scale and not averaged TEC over individual stations. The diurnal TEC maps were generated using TEC at IPP locations. In order to generate the TEC maps, TEC data

were binned within 0.05 h time interval and 0.4° latitude grid range. This procedure was also employed for other 3 storm periods analysed. For all analysed events two days before and after the storm period were considered to represent the state of the ionosphere during the event. Days 29 and 30 March 2001 happened to come after a moderate storm (minimum Dst = -87 nT), so they did not necessarily show quiet time ionospheric variability. These two days were considered to be under storm conditions and hence were not used as quiet days reference for this storm period, when analysing the storm effects on TEC. For this reason days 15 and 16 March 2001 (the quietest days of March 2001) were used as quiet time reference for this storm period and the variation of TEC are shown in Figure 5.3 for both northern (NH) and southern (SH) hemispheres. The discussion of this figure will follow after the description of Figure 5.4.

Figure 5.2: Variations in the interplanetary magnetic field (IMF) Bz (nT) component (black curve) and a symmetric SYM-H (nT), TEC (TECU) in latitude range 20°S - 38°S (31°S - 46°S, geomagnetic) and 38°N - 50°N (31°N - 46°N, geomagnetic) within 15°E - 40°E longitude sector for the period 29 March to 02 April 2001.
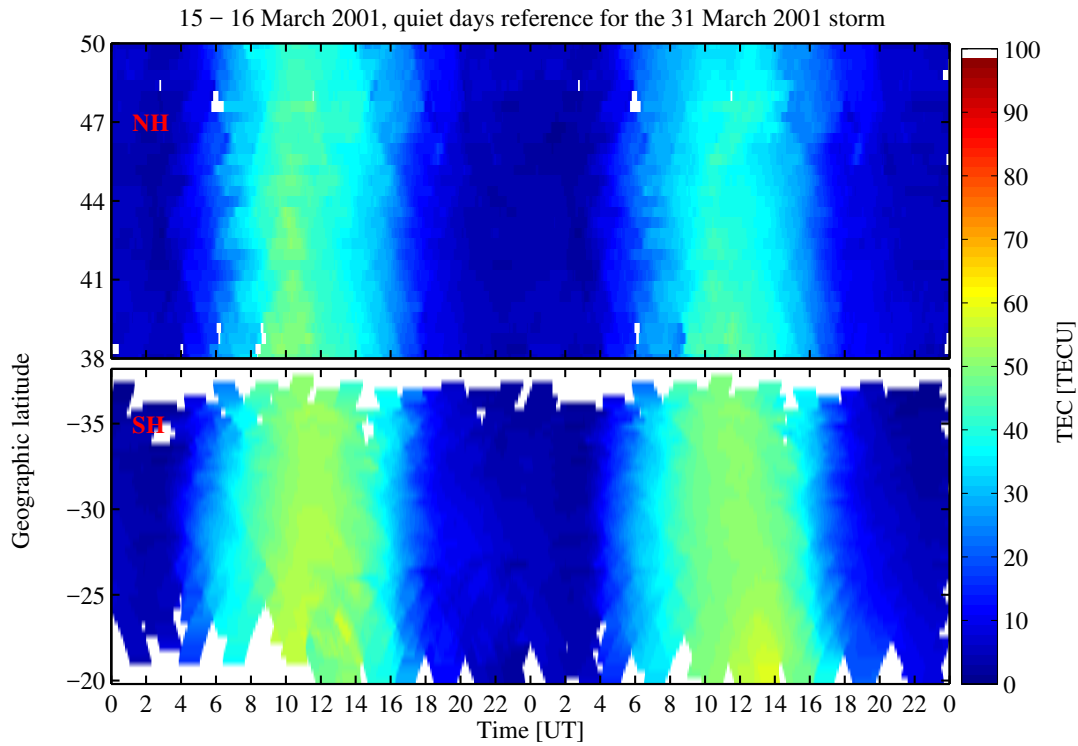
Figure 5.3: TEC (TECU) variation on 15 and 16 March 2001 (the quietest days of March 2001) (Matamba et al., 2016).

Figure 5.4 shows variation of (a) solar wind velocity, V (km/s) and Interplanetary Electric Field, IEF = -V × B, (b) the horizontal component, dH (nT) over AAE, (c) ΔfoF2 over JR055 and RO041, northern hemisphere stations, and (d) ΔfoF2 over GR13L and MU12K, southern hemisphere stations. Figure 5.4(a) shows that V increased significantly from ~424 km/s to about 600 km/s at 00:52 UT, the IEF showed a decrease during SI+ and later increased reaching ~31 mV/m at 06:15 UT. Equatorial magnetometer H measurements (dH in Figure 5.4(b)) exhibited irregular variations consisting of both EEJ and CEJ on 31 March 2001. Figure 5.4(c)-(d) it is seen that the period 29 - 30 March 2001 did not necessarily show quiet time ionospheric variability which has been determined to be within ±20% of ΔfoF2 changes (Vijaya Lekshmi et al., 2011; Matamba et al., 2015).

Figure 5.4: The variation of (a) solar wind speed V (km/s) and Interplanetary Electric Field (IEF) (mV/m), (b) dH (nT) over equatorial magnetometer station AAE (9.02°, 38.77°, geographic), and (c and d) ΔfoF2 over northern hemisphere (Juliusruh, JR055 (54.6°N, 13.4°E; 50.9°N, geomagnetic) and Rome, RM041 (41.9°N, 12.5°E; 35.6°N, geomagnetic)), and southern hemisphere (Madimbo, MU12K (22.4°S, 30.9°E; 32.7°S, geomagnetic) and Grahamstown, GR13L (33.3°S, 26.5°E; 41.8°S, geomagnetic)) stations.

Figure 5.5 shows the variation of the Dst index (first panel) and ΔfoF2 with O/N_2 ratio over-plotted for JRO55 and GR13L for the storm period 29 March - 02 April 2001. The broken lines are showing the SI+.
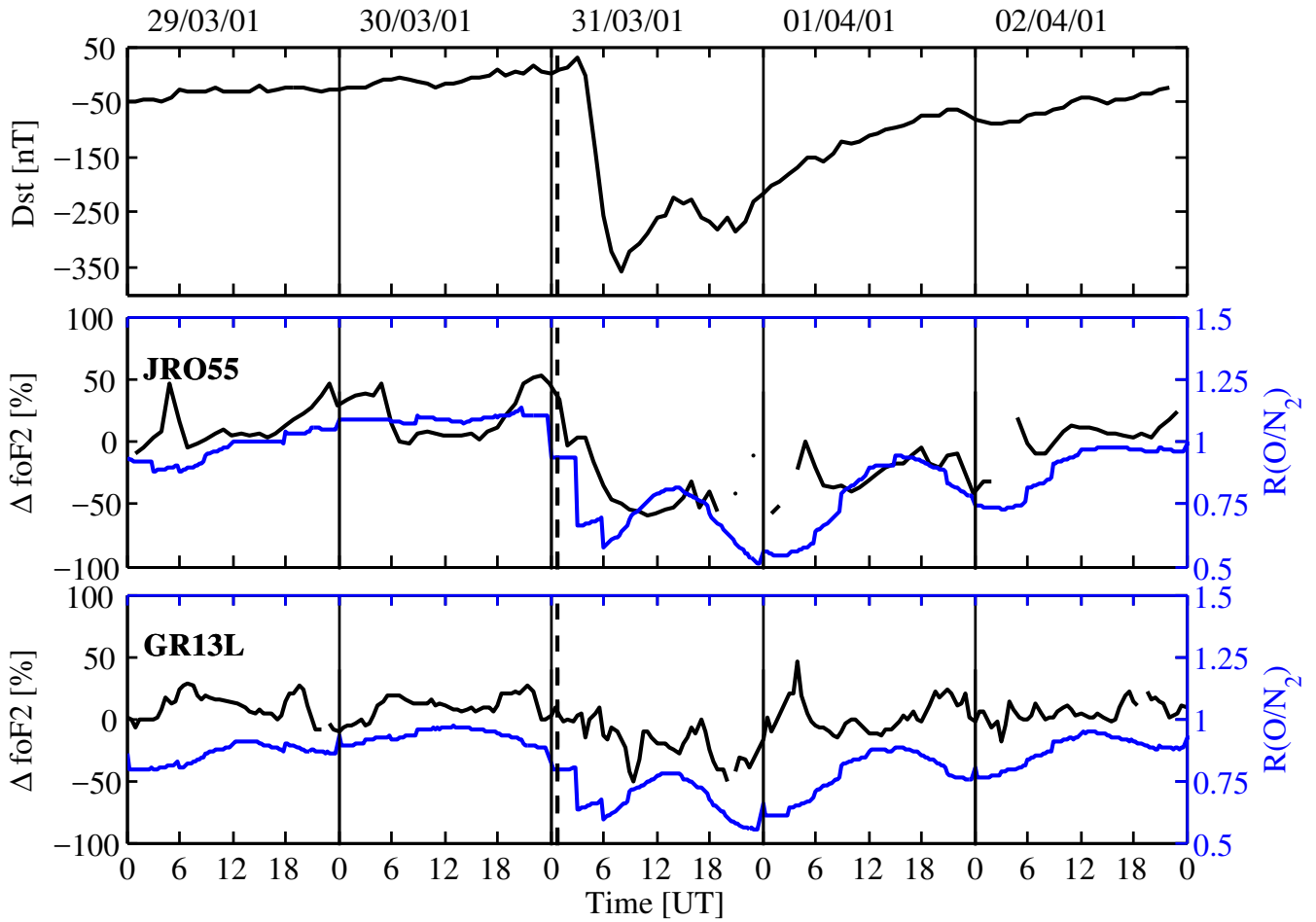
Figure 5.5: Variation of Dst (nT) (first panel), second and third panels show ΔfoF2 [%] and over-plotted is the O/N_2 ratio over JRO55 and GR13L. The O/N_2 ratio data were obtained from NRLMSISE-00 empirical model of the atmosphere (Picone et al., 2002) at a height of 300 km.

A decrease in ΔfoF2 and O/N_2 ratio were observed on 31 March 2001. The O/N_2 ratio can be used to indicate the variation in neutral composition changes. The production and loss of ionisation at F2 region altitudes are very sensitive to changes in O/N_2 ratio. The modeled O/N_2 ratio values to the quiet time O/N_2 ratio values (Prölss and Zahn, 1974) were obtained using,

$$R(O/N_2) = \frac{(O/N_2)_{modeled}}{(O/N_2)_{quiet}}. \tag{5.1}$$

The 29 March - 02 April 2001 storm period occurred during the equinox season. Negative and positive ionospheric storm effects were simultaneously observed over both southern and northern hemispheres mid-latitudes. Regional GPS TEC (Figure 5.2, panels 2 and 3) shows that over both hemispheres, a negative storm effect is seen between ~06:00 UT - 12:00 UT on 31 March 2001 at latitudes from about 47°N - 50°N and 33°S - 38°S in reference to quiet time variability shown in Figure 5.3. The ionosonde data in Figure 5.4(c)-(d) are in agreement with TEC observations and show a negative ionospheric storm effect almost 5 hours after the SI+ in the northern (JR055 and RO041) and southern (GR13L) hemispheres for about 10 hours (06:00 UT - 16:00 UT) and 9 hours (06:00 UT - 15:00 UT) respectively. Similar results over South Africa have been reported for 31 March - 02 April 2001 (Amabayo and Pierre, 2013). The negative ionospheric response

is usually associated with neutral composition changes. Joule and particle heating in the high latitudes cause an expansion of the neutral atmosphere (Buonsanto, 1999). During geomagnetic storms this expansion is rapid and may cause upwelling of plasma around the auroral oval (Prölss, 1995; Buonsanto, 1999). This may result in chemical changes in the atmosphere due to the plasma upwelling which transport depleted oxygen or nitrogen-rich air up from lower thermosphere to F layer (Prölss, 1980; Buonsanto, 1999). The increased loss of O^+ due to charge exchange with N_2 and O_2 and occurring after dissociative recombination of the molecular ions O_2^+ and NO_2^+ results in a depletion of electron density (Prölss, 1995; Daniell and Strickland, 2001). Therefore changes in atomic oxygen to nitrogen molecule (O/N_2) have been used as a proxy to infer TEC or foF2 behavior during storm conditions (Chandra and Herman, 1969; Prölss and Zahn, 1974; Prölss et al., 1975; Prölss, 1980). However, there is no available O/N_2 ratio data in both mid-latitude regions to investigate the thermospheric composition changes during this period. Due to this, we used data obtained from NRLMSISE-00 empirical model of the atmosphere (Picone et al., 2002) shown in Figure 5.5 to see the O/N_2 ratio over GR13L and JRO55 for this storm period at a height of 300 km. It was found that the decrease in O/N_2 density ratio on 31 March 2001 corresponds to the decrease in foF2 as well as TEC. Hence, observed negative ionospheric storm effect from ~06:00 UT - 18:00 UT could be due to composition changes.

Over MU12K, foF2 remained within the quiet time variability range (~19:30 UT - 23:00 UT) and only showed negative ionospheric response during evening and nighttime hours of 31 March 2001. On the other hand, positive ionospheric storm effect was observed at latitudes from about 38°N - 47°N and 20°S - 33°S) as shown in Figure 5.2. There are several mechanisms suggested to explain storm-time electron density increase. Changes in the low latitudes that could influence mid-latitude TEC variability have been considered. Figure 5.4(b) shows the dH changes computed by subtracting average magnetometer H values within 23:00-03:00 LT from the time series 1 minute data over an equatorial location, AAE. A sudden increase in dH is observed after the SI+. However, magnetometer data is only an appropriate indicator during daytime (Sastri, 1988; Anderson et al., 2004) and may not be used to infer local electrodynamics during nighttime when the SI+ occurred. A significant dH fluctuations during the main phase on 31 March 2001 comprising periods of enhanced EEJ (e.g. ~06:25 UT - 06:53 UT) and CEJ (e.g. ~08:07 UT - 09:10 UT) was observed. During periods of increased/decreased dH, a corresponding observation is seen in IEF (Figure 5.4(a)). Increased EEJ is an indicator of increased vertical drifts due to enhanced electric fields. When this happens, plasma is transported to higher altitudes and aids the expansion of EIA towards the mid-latitudes.

To illustrate this, Figure 5.6 shows the global TEC maps (`ftp://cddis.gsfc.nasa.gov/pub/gps/products/ionex/`) on 31 March 2001 at 11:00 UT and 13:00 UT. The expansion of the EIA reached northern and southern hemisphere mid-latitudes contributing to the observed positive ionospheric response on 31 March 2001. For this storm day, related fluctuations of vertical E×B drifts were also observed in two other longitude sectors (Longitude = 127°E and 289°E) over the Asian & Australian and North American sectors (Fuller-Rowell et al., 2007). These authors concluded that both PPEF and DDEF were important in influencing both mid- and low latitude electron density changes during this storm. Positive ionospheric storm effects have also been associated to the manifestation of large-scale Traveling Ionospheric Disturbances (LSTIDs). Borries et al. (2009) reported LSTIDs in Europe (at latitude 30°N - 70°N and longitude 10°W - 30°E) on 31 March 2001 at 07:00 UT with the phase speed of 497±39 m/s. LSTIDs have also been reported over Southern Africa mid-latitude using TEC and ionosonde data on 31 March 2001 (Amabayo and Pierre, 2013). TIDs lead to increased electron densities resulting from plasma motion to F-region heights (Prölss
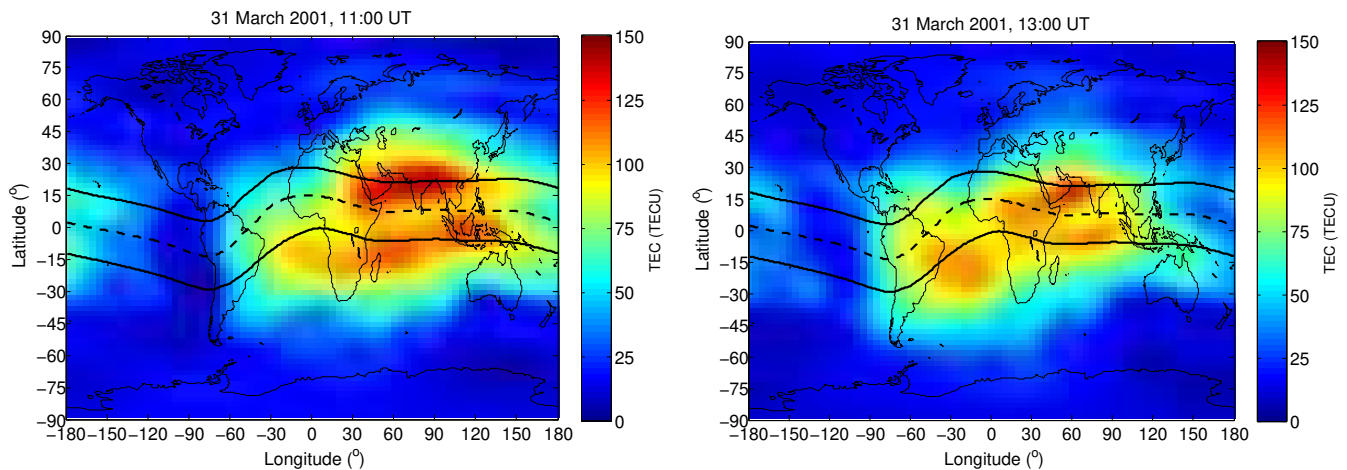
Figure 5.6: Global TEC maps (`ftp://cddis.gsfc.nasa.gov/pub/gps/products/ionex/`) on 31 March 2001 at 11:00 UT and 13:00 UT.

and Jung, 1978; Prölss, 1995). A positive ionospheric storm effect was also observed for the next two days (01 - 02 April 2001) during the recovery phase of the storm which could be attributed to the expansion of the EIA. An interesting observation during this storm period was the ionospheric changes that remained in quiet time variability over MU12K (33.2°S, geomagnetic) during the storm main phase when other mid-latitude stations reported a largely negative storm effect. This could be due to the competing mechanisms arising from EIA expansion and neutral composition changes. It should be noted that MU12K is the closest station to the geomagnetic equator than other considered ionosonde stations and hence will be influenced more by EIA expansion. The second closest ionosonde station to the geomagnetic equator is R0041 (35.6°N, geomagnetic).

5.4 Storm period : 27 - 31 October 2003

Figure 5.7 shows the SYM-H (nT) index, IMF Bz (nT) and TEC (TECU) over southern and northern hemisphere mid-latitudes for 27 - 31 October 2003 storm period. Two successive great geomagnetic storms occurred on 29 and 30 October 2003 with SI+ times occurring at 06:11 UT and 16:38 UT respectively, as shown by the dashed black lines in Figure 5.7. The minimum SYM-H values were recorded on 30 October 2003 with the intensity of SYM-H = -391 nT (at 01:48 UT) and SYM-H = -432 nT (at 22:55 UT). Immediately after the first SI+ on 29 October 2003, the IMF Bz turned northward reaching a maximum of ∼16 nT at 12:00 UT and later turned southward attaining a minimum of ∼-27 nT at 19:00 UT. Before the end of recovery for the 29 October storm, a SI+ occurred and the IMF Bz turned further southward reaching a minimum value of ∼-27 nT at ∼20:00 UT on 30 October 2003. Starting from the 28 October 2003 at 12:00 UT to 31 October 2003 at 12:00 UT there was no high resolution IMF Bz data available, and hourly values have been used for this storm period. It is observed that TEC values on the 28 October 2003 (Figure 5.7) were elevated above the background values starting from ∼10:00 UT - ∼13:00 UT and this was due to the solar flare occurrence (Tsurutani et al., 2005). Following the first SI+ (∼ after 2-3 hours) on 29 October 2003, there was a TEC enhancement in both hemispheres.

The end of October tends to winter and summer in northern and southern hemispheres respectively. The storm period of 27 - 31 October 2003 included a very strong flare ever observed on
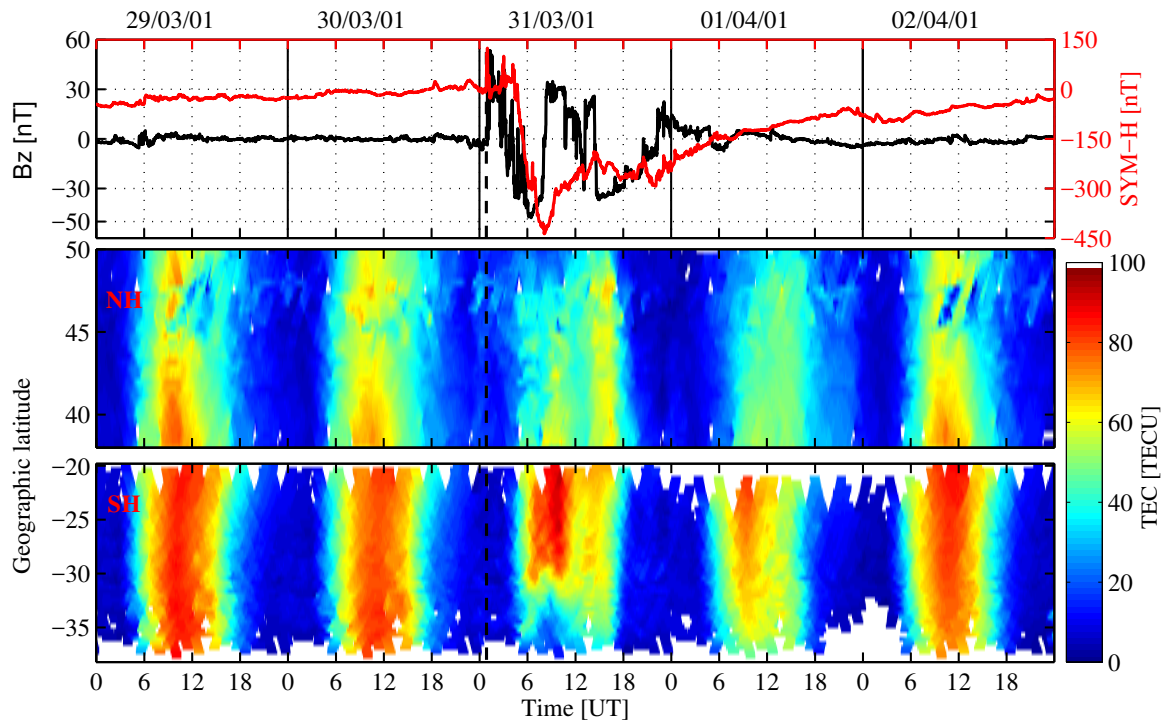
Figure 5.7: Variations in Interplanetary Magnetic Field (IMF) Bz (nT) component (black curve) and Symmetric SYM-H (nT) (red curve), TEC (TECU) in latitude range 38°N - 50°N (31°N - 46°N, geomagnetic) and 20°S - 38°S (31°S - 46°S, geomagnetic) within 15°E - 40°E longitude sector for 27 - 31 October 2003. NH and SH refer to northern and southern hemispheres respectively. The dashed vertical black line represent the Sudden Storm Commencement (SI+) which occurred at 06:11 UT and 16:38 UT on 29 and 30 October 2003 respectively.

28 October 2003. In response to this, both TEC and ionosonde foF2 increased above their quiet time values with more pronounced effect seen in TEC (Figure 5.7, panels 2 and 3). This increase in TEC which was observed on 28 October 2003 (a day before the start of the storm) and which lasted about 3 hours (10:00 UT - 13:00 UT) was due to the most intense EUV flare on record (Tsurutani et al., 2005). The TEC increase is due to high altitude photoionisation, a region where the recombination time scale is hours. Although NOAA has rated the flare as ∼X17, this is only an approximation since the detectors were saturated. Thomson et al. (2004) has approximated the flare intensity using a radio wave technique as X45 ± 5.

Figure 5.8 shows the variations of (a) V (km/s) and IEFy (mV/m), (b) dH (nT), (c) foF2 over JRO55 and RO041, northern hemisphere and (d) ΔfoF2 over GR13L and MU12K, southern hemisphere stations. During SI+, the dH increased to about 464 nT on 29 October 2003 at ∼06:00 UT. A negative ionospheric response on foF2 was observed over all ionosonde stations considered in this study except on 29 October 2003 when positive ionospheric response was observed at RO041.
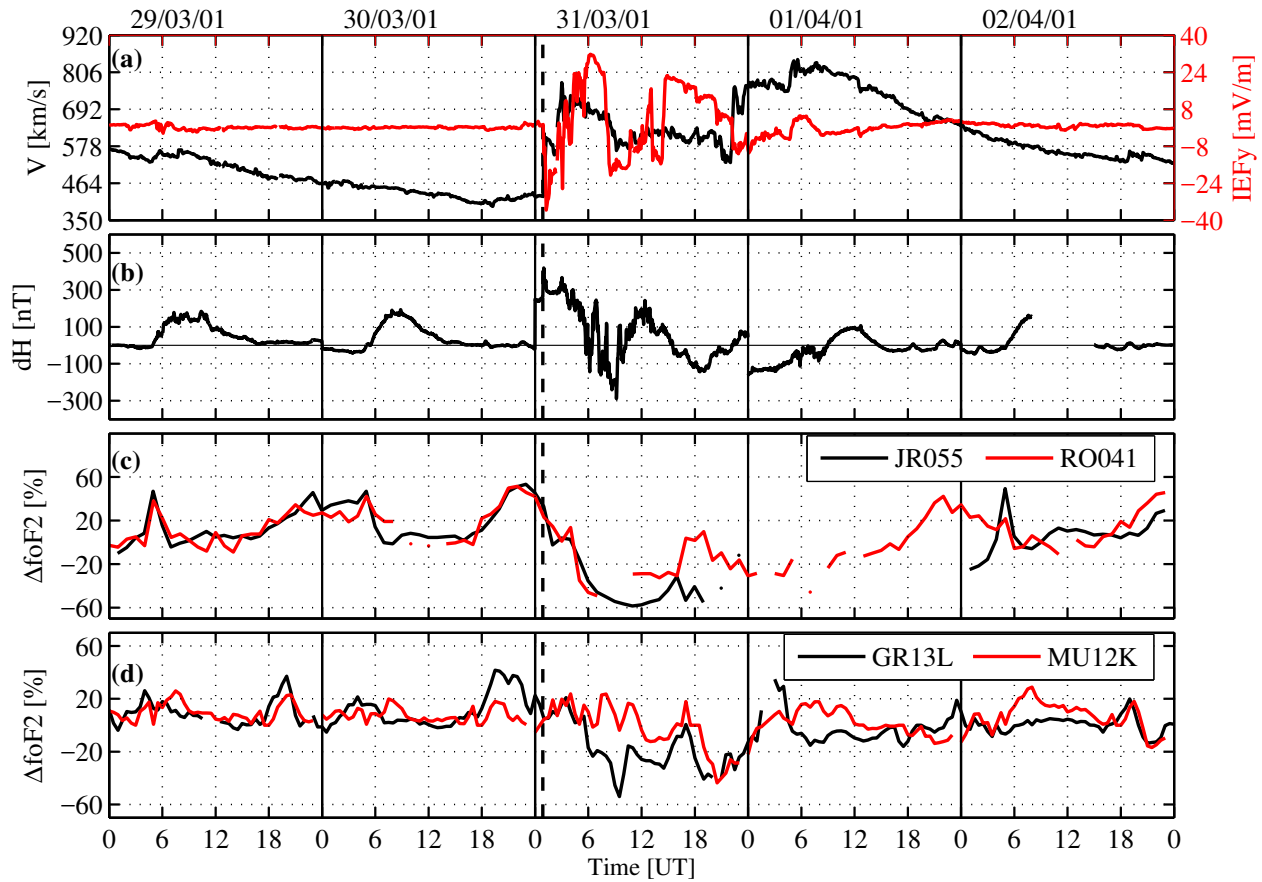
Figure 5.8: Changes of (a) solar wind speed V (km/s) and Interplanetary Electric Field IEFy (mV/m), (b) dH (nT) over equatorial magnetometer station AAE (9.02° N, 38.77° E, geographic), (c) and (d) ΔfoF2 over JRO55 and RO041; and MU12K and GR13L. The SI+ occurred at 06:11 UT and 16:38 UT on 29 and 30 October 2003 respectively as indicated by black vertical dashed line.

During the solar flare event, an increase in foF2 was also observed over JR055 (peaking at ∼12:00 UT) while RO041, MU12K and GR13L data (Figure 5.8(c)-(d)) remained within the quiet time variability range. The response of the ionosphere to the solar flare over southern and northern hemispheres is different with larger TEC enhancement over the northern hemisphere. The ionospheric electron density response to solar flare depends on the number of factors including local time, solar zenith angle and hemispheric differences (Zhang and Xiao, 2003, 2005; Tsurutani et al., 2005; Tsugawa et al., 2007; Zhang et al., 2011). For example Zhang et al. (2002) reported more increased ionospheric TEC in the southern hemisphere during the 14 July 2000 solar flare compared to the northern hemisphere changes, for similar zenith angles. Our analysis show more pronounced increase in TEC for the northern hemisphere mid-latitude than corresponding changes in southern hemisphere during the solar flare event of the 28 October 2003. Our results agree with the study of Zhang et al. (2002) in indicating that the more enhanced TEC to solar flare occurrence is found in the winter hemisphere emphasizing the importance of seasonal effects. In general, summer and winter TEC changes to solar flare are explained by the sunlit hemispherical exposure to the solar photons.

During the main phase on 29 October 2003, an increase in TEC was observed over northern hemisphere and southern hemisphere, mid-latitudes within $\sim$2-3 hours after the SI+ as shown in panels 2 and 3 of Figure 5.7. The TEC increase that occurs almost simultaneously is due to the PPEF contribution (Tsurutani et al., 2004, 2008a). The dH over equatorial station AAE showed an increase on 29 October 2003 immediately after the SI+ as shown in Figure 5.8(b). Daytime dH is directly proportional to vertical drift (E$\times$B) which is responsible for upward/downward plasma movements. PPEF enhances daytime E$\times$B and leads to its decrease during nighttime (Tsurutani et al., 2004, 2008a; Gonzalez et al., 2005; Balan et al., 2013; Habarulema et al., 2015). Increased E$\times$B vertical drifts transport plasma to higher altitudes where recombination rate is lower and hence contributes to increased electron density or TEC in low latitudes. Additionally, plasma diffuses along magnetic field lines and can reach mid-latitude through the expansion of EIA (Abdu, 1997; Lin et al., 2005; Habarulema et al., 2015). Figure 5.9 illustrates the global TEC maps (`ftp://cddis.gsfc.nasa.gov/pub/gps/products/ionex/`) on 28 - 31 October 2003 at 10:00 UT. The EIA on 29 October 2003 at 10:00 UT expanded to the northern and southern hemisphere mid-latitude regions. During the time when an increase in TEC was observed on 29 October 2003 over northern hemisphere (Figure 5.7), the global maps also indicated the expansion of the EIA.
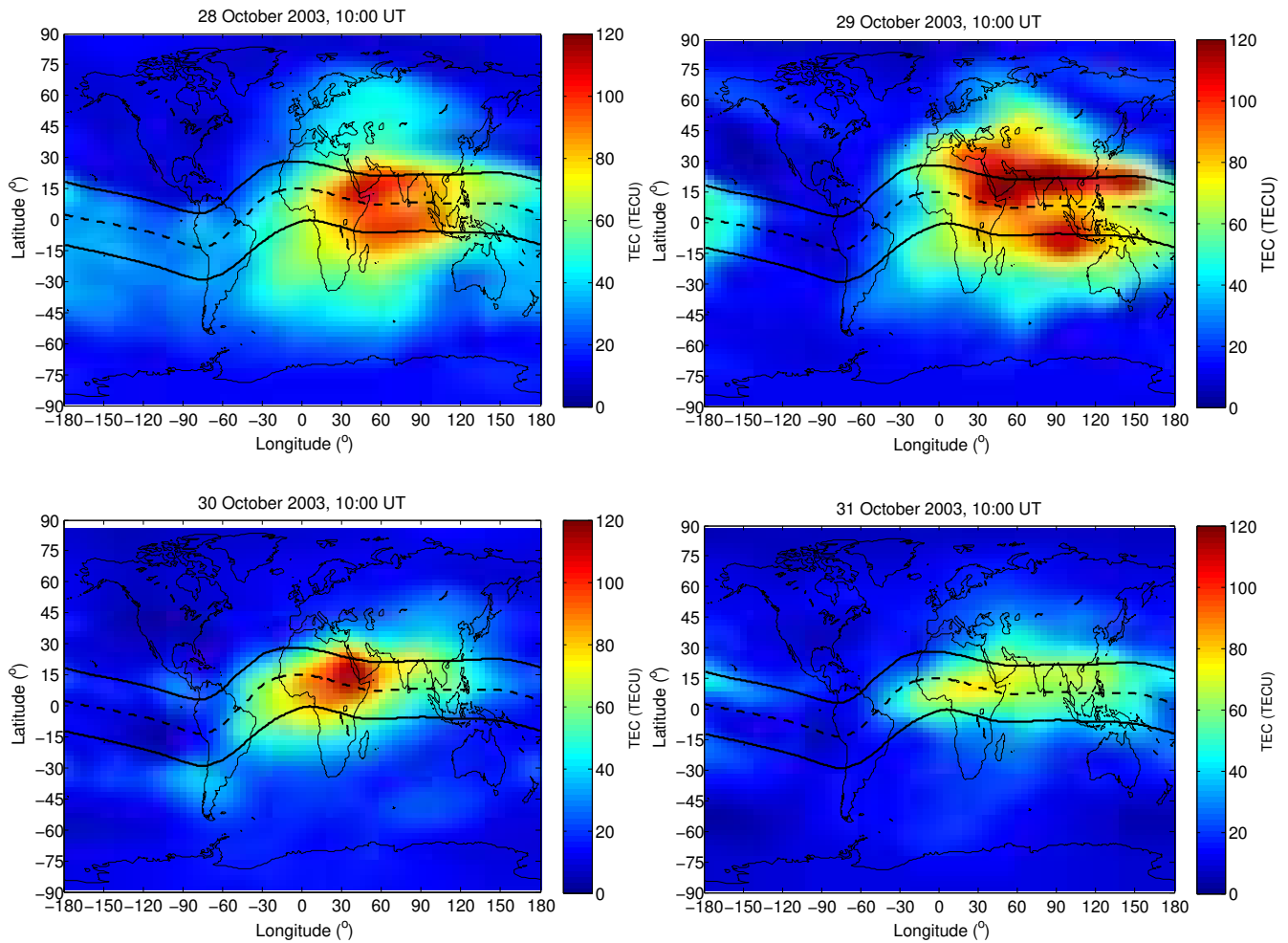
Figure 5.9: Global TEC maps (`ftp://cddis.gsfc.nasa.gov/pub/gps/products/ionex/`) on 28 - 31 October 2003 at 10:00 UT

Northern hemisphere ionosonde foF2 data (Figure 5.8(c)) shows that RO041 (35.6°N, geomagnetic) observed traces of the positive storm effects while available data over JR055 (50.9°N, geomagnetic) shows negative storm effects on 29 October 2003. Observed positive storm effects over RO041 could be due to its proximity to EIA region. Over Europe, Borries et al. (2009) reported LSTIDs on 29 - 30 October 2003 at 06:00 UT, 13:00 UT and 17:00 UT on 30 October 2003 with phase speeds of 976 ± 201 m/s, 681 ± 27 m/s and 910 ± 195 m/s respectively. Over southern hemisphere, using two receiver arrays along the longitudinal sectors 18°E - 20°E and 27°E - 28°E in South Africa, Katamzi and Habarulema (2014a) observed LSTIDs on 29 and 31 October 2003 which propagated towards the equator with velocities between 587 m/s and 1635 m/s. These LSTIDs observed were associated with the geomagnetic storms and are thought to originate from the auroral region due to Joule and particle heating that causes a strong upwelling of the thermosphere (Ding et al., 2008; Katamzi and Habarulema, 2014a). Positive ionospheric storm effects observed in European mid-latitudes on 29 October 2003 are therefore due to a combination of electric field penetration to mid and low latitudes, expansion of EIA and LSTIDs. Southern hemisphere ionosonde data (Figure 5.8(d)) showed predominantly negative storm effects. On 30 - 31 October 2003 over both hemispheres a negative ionospheric response was observed from both ionosonde and TEC data. The decrease in TEC could be due to neutral composition changes. Figure 5.10 illustrates Global Ultraviolet Imager (GUVI) thermospheric O/N_2 ratio maps (`http://guvitimed.jhuapl.edu/guvi-galleryl3on2,`

75

Accessed: December 2016) for 11 October (geomagnetic quietest day of the month), and 29 - 31 October 2003 (geomagnetic disturbed period).
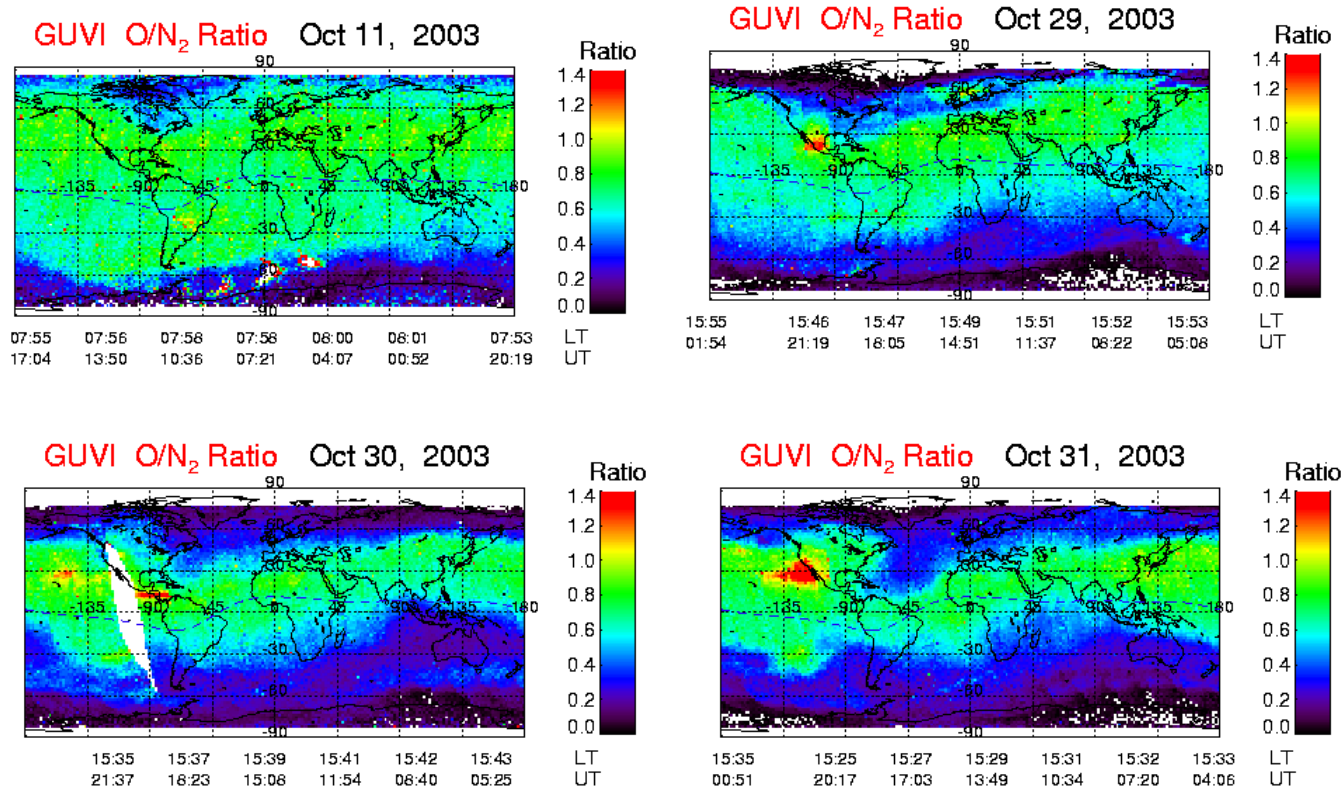
Figure 5.10: Global Ultraviolet Imager (GUVI) thermospheric O/N_2 ratio maps (`http://guvitimed.jhuapl.edu/guvi-galleryl3on2`, Accessed on: December 2016) for the quietest day of October, 11 October, and days 29 - 31 October 2003 during disturbed period.

The O/N_2 ratio observed from GUVI thermospheric maps (`http://guvitimed.jhuapl.edu/guvi-galleryl3on2`, Accessed on: December 2016) shown in Figure 5.10 illustrates a decrease of O/N_2 ratio between $\sim$0.2 - 0.4 over southern and northern hemisphere mid-latitude on 30 and 31 October 2003 at $\sim$15:08 UT and $\sim$13:49 UT respectively as compared to the quietest day of the month (11 October 2003) where the O/N_2 ratio ranges from $\sim$0.6 - 0.8 ($\sim$07:21 UT). Although the O/N_2 ratio data is taken at different times, they are comparable since O/N_2 ratio corotates with the Earth (Burns et al., 1995; Zhang et al., 2004; Habarulema et al., 2013b). In general, it is noticed (panels 2 and 3, Figure 5.7) that TEC over northern hemisphere is more enhanced than in the southern hemisphere most likely due to seasonal dependence. The end of October tends to winter and summer in northern and southern hemispheres respectively. It is known that the background composition O/N_2 density ratio is greater in winter than in summer. This is due to the fact that in summer the composition disturbance zone extends much further equatorward by about 20° on the average than in winter (Prölss, 1995). The summer time background wind circulation is equatorward and therefore in the same direction as the induced wind circulation during the great geomagnetic storm. For the winter time, the background is poleward and therefore opposes the storm induced wind circulation (Buonsanto, 1999). This therefore means that the depleted O/N_2 (proxy to thermospheric composition) have higher chance of moving to mid/low latitudes in the summer hemisphere than the winter hemisphere (Yizengaw et al., 2005), accounting for the observed positive and negative responses in southern and northern hemispheres respectively.

Detailed multi-instrumental analyses of this storm period are presented in Yizengaw et al. (2005).

5.5 Storm period : 18 - 23 November 2003

Figure 5.11 illustrates the IMF Bz (nT), SYM-H (nT) and TEC (TECU) over southern (SH) and northern (NH) hemispheres for 18 - 23 November 2003 storm period. The SI+ occurred on 20 November 2003 at about 08:03 UT as indicated by vertical black dashed line and the SYM-H index reached a value of -488 nT at 18:16 UT. After the SI+, the IMF Bz turned southward for $\sim$1.5 hours and later became northward reaching $\sim$34 nT at 11:15 UT on 20 November 2003. Later the IMF Bz turned southwards at about 11:26 UT reaching a value of $\sim$-52 nT at 15:29 UT and remained southward for the rest of the day. TEC response for this storm period on 20 November 2003 is relatively similar to that of 29 October 2003 event, in relation to enhanced TEC 2-3 hours in both hemispheres after the SI+. This was mainly due to PPEF as observed from the equatorial magnetometer response during this storm period. Figure 5.12 shows the variation of (a) V (km/s) and the IEF (mV/m), (b) dH, (c) ΔfoF2 over JRO55 and RO041, northern hemisphere and (d) ΔfoF2 over GR13L and MU12K, southern hemisphere stations. From Figure 5.12, the shock as identified by an increase in solar wind speed occurred with V starting from $\sim$ 451 km/s ($\sim$ 08:00 UT) to $\sim$727 km/s ($\sim$08:45 UT) on 20 November 2003. On this note, it should be mentioned that identification of shock is not only based on solar wind speed, but also considers other parameters such as density and magnetic field (Tsurutani et al., 2011).
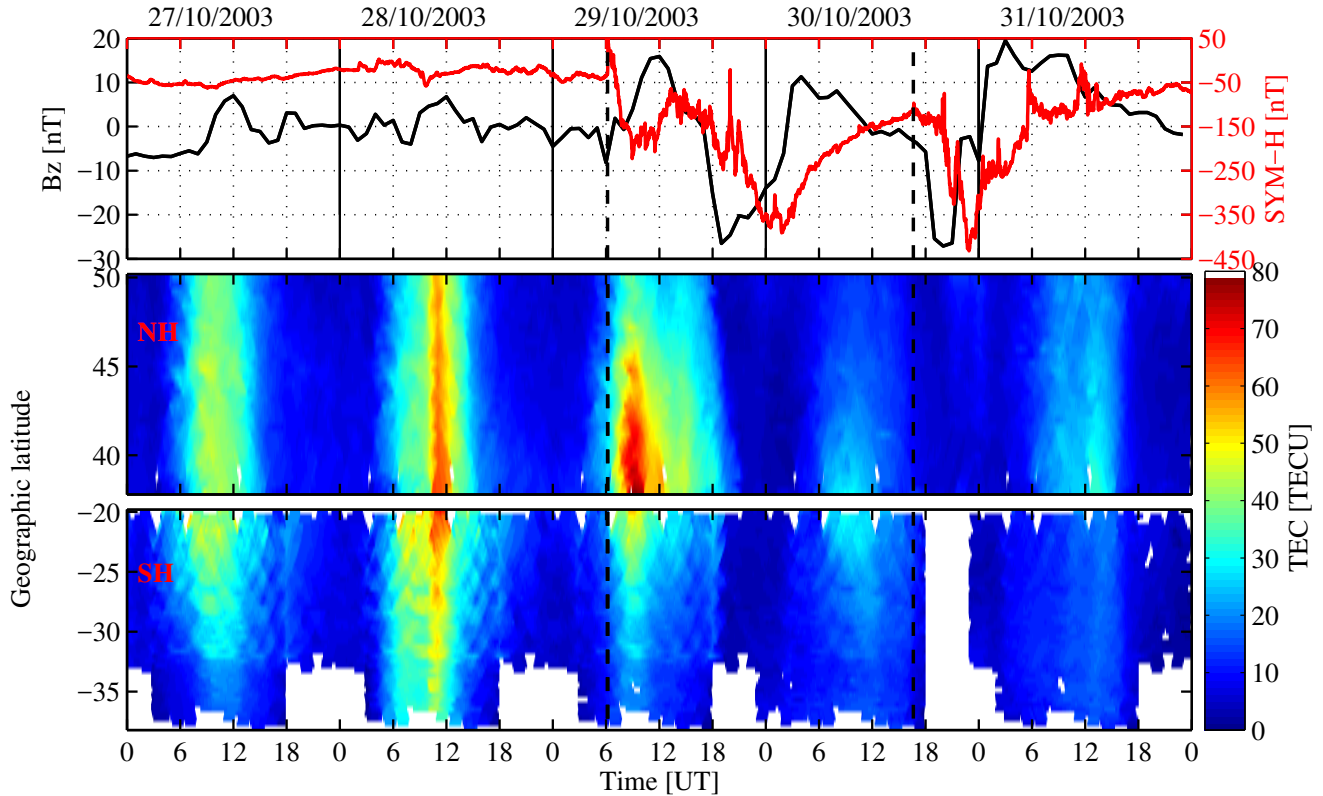
Figure 5.11: Variations in Interplanetary Magnetic Field (IMF) Bz (nT) component (black curve) and Symmetric SYM-H (nT) (red curve), TEC (TECU) in latitude range 38°N - 50°N (31°N - 46°N, geomagnetic) and 20°S - 38°S (31°S - 46°S, geomagnetic) within 15°E - 40°E longitude sector for 18 - 23 November 2003. NH and SH refer to northern and southern hemispheres respectively. The dashed vertical black line represents the Sudden Storm Commencement (SI+) which occurred at 08:03 UT on 20 November 2003.

The IEFy showed a small increase immediately after the SI+ to about 10 mV/m at 09:45 UT and later decreased to ∼-20 mV/m at 11:15 UT on 20 November 2003. The maximum value reached by IEFy was ∼32 mV/m at 15:10 UT. The dH increase exactly corresponded with the SI+ and lasted for about 2 hours. The maximum dH value obtained was 319 nT at 08:06 UT on 20 November 2003. After about 12:00 UT, the dH decreased (a manifestation of CEJ with a minimum value of -722 nT at 19:11 UT) for over 12 hours. Figure 5.12(c) and (d) show that foF2 did not immediately respond in the same way as TEC, but the increase in foF2 was seen after ∼ 4 hours of SI+ occurrence. For the rest of the storm duration, foF2 showed a negative response apart from the northern hemisphere station, JR055 that indicated a positive response during the recovery phase on 21 November 2003.

For 18 - 23 November 2003 storm period, an increase in TEC occurred ∼2.5 hours after the SI+ was observed and is more prominent over southern hemisphere than northern hemisphere as illustrated in Figure 5.11 panels 2 and 3. The presence of the PPEF was investigated using dH over equatorial magnetometer station AAE. An increase in dH (reaching a maximum of 252 nT) at ∼08:19 UT in Figure 5.12(b) almost coincided with a simultaneous increase in TEC from Figure 5.11 on 20 November 2003, pointing to the role of PPEF in influencing ionospheric electron density response which led to the first increase in TEC for the first few hours. Following the SI+,

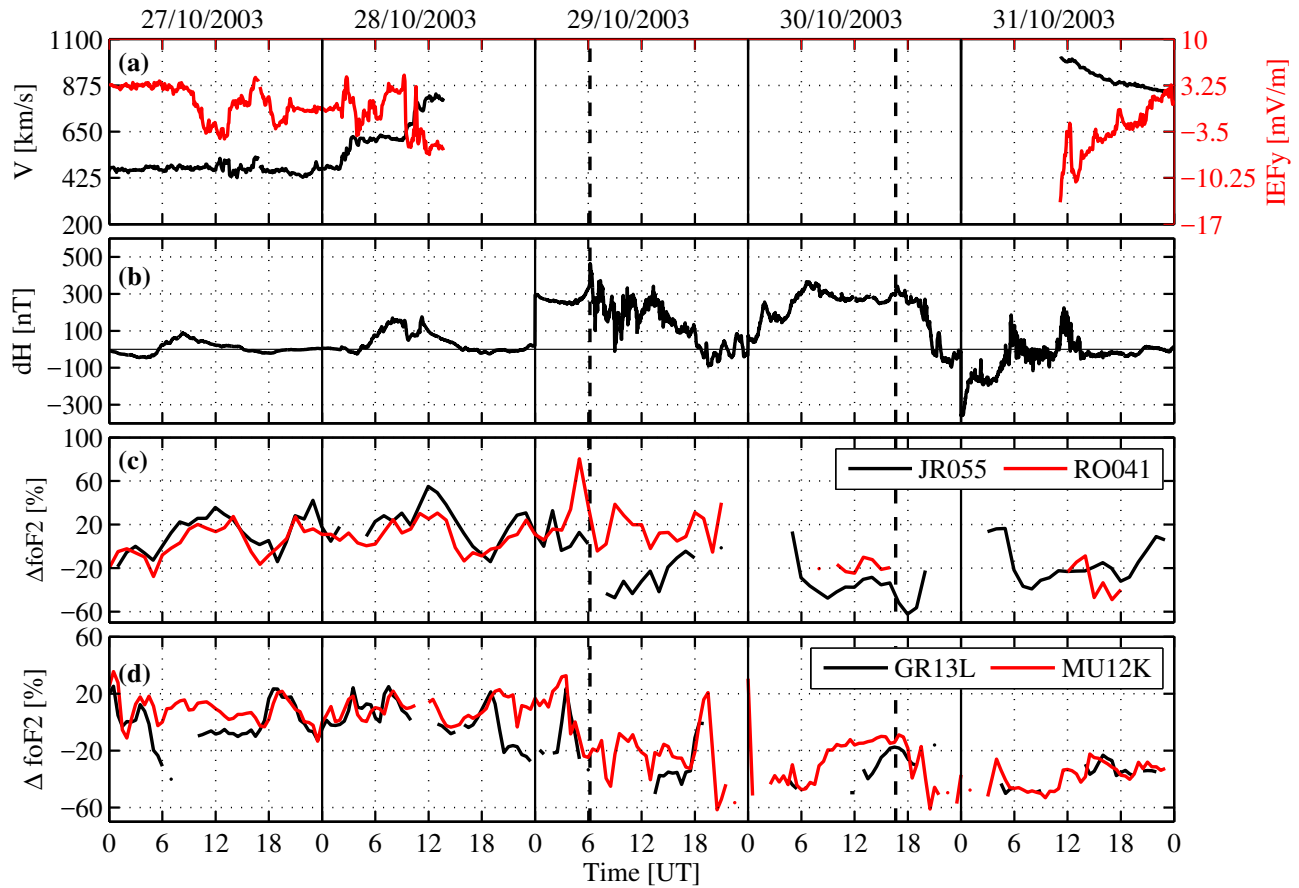Figure 5.12: The variation of (a) solar wind speed V (km/s) and Interplanetary Electric Field IEFy (mV/m), (b) dH (nT) over equatorial magnetometer station AAE (9.02° N, 38.77° E, geographic), (c) and (d) ΔfoF2 over JRO55 and RO041; and MU12K and GR13L. The SI+ occurred at 08:03 UT on 20 November 2003 as indicated by black vertical dashed line.

ionosonde data shows enhanced foF2 almost four hours later. It is noticed that dH increase lasted for 2 hours (08:05 UT - 10:16 UT) and during this time IMF Bz was mostly southward. The foF2 increase at JR055 ($\sim$41% at 12:00 UT), RO041 ($\sim$41% at 13:00 UT) and GR13L (24% at 12:30 UT) could therefore have been due to the PPEF. A decrease in dH on 20 November 2003 starting from $\sim$08:19 UT to $\sim$19:11 UT with minimum of -722 nT ($\sim$19:11 UT) could be due to DDEF and a similar result has been reported over South American sector (Yizengaw et al., 2006). On 21 November 2003, positive and negative storm effects were observed in the northern and southern hemispheres respectively (see Figure 5.11, panels 2-3).

Figure 5.13 shows GUVI O/N$_2$ ratio global maps for 20 - 21 November 2003. GUVI O/N$_2$ ratio showed increased and decreased values on 20 and 21 November 2003 respectively in the African (southern hemisphere) mid-latitude. The increased GUVI O/N$_2$ ratio values were observed over the European (northern hemisphere) mid-latitude on 20 and 21 November 2003. The above agrees with the observed increase and decrease in TEC values in the southern and northern hemispheres (Figure 5.12). This highlights the importance of neutral composition changes to electron density variations during the recovery phase.
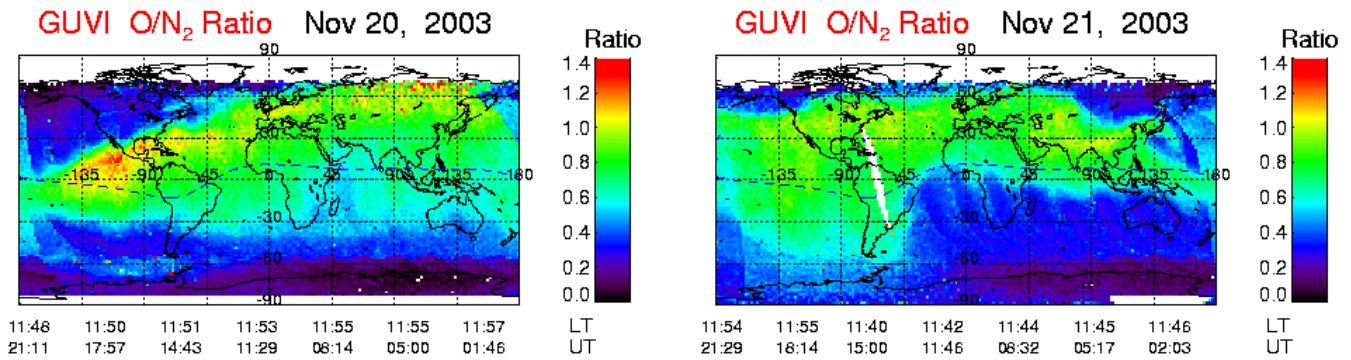
Figure 5.13: Global Ultraviolet Imager (GUVI) thermospheric O/N$_2$ ratio maps (`http://guvitimed.jhuapl.edu/guvi-galleryl3on2`, Accessed on: December 2016) for the period 20 - 21 November 2003

The observed decrease in TEC (as shown in Figure 5.11 panel 3) agrees with a decrease in foF2 over GR13L and MU12K southern hemisphere stations on 21 November 2003. Similarly, for the northern hemisphere, an observed TEC increase corresponds to an increase in foF2 over JR055 from 01:00 UT- 05:00 UT, although a non significant response was largely observed over RO041 apart from few instances at 04:00 UT and 18:00 UT when foF2 deviations were either below or above the quiet time variability. The positive and negative ionospheric response over northern and southern hemisphere respectively during the recovery phase (21 November 2003) could be due to seasonal dependence. During geomagnetic storm, negative ionospheric storm effects are most likely to happen in summer than in winter at mid-latitude (e.g. Prölss, 1976, 1977, 1980, 1995; Fuller-Rowell et al., 1996) mainly due to the role of wind circulation in redistributing oxygen depleted air from high latitude regions. Blanch et al. (2005) studied this storm period using ionosonde data and GPS data over European mid-latitude where negative and positive effect were observed at 55°N - 45°N and 45°N - 30°N latitudes respectively. Both positive and negative effects were explained by composition changes or the equatorward expansion of the main ionospheric trough. For this storm period, the presence of TIDs has been investigated by analysing TEC changes at selected latitudes in both northern and southern hemisphere on 20-21 November 2003. Figure 5.14 shows variation of TEC at different latitudes in the northern (50°N, 45°N, 40°N) and the southern (35°S, 30°S, 25°S) hemispheres.

Figure 5.14 is generated from panels 2 and 3 of Figure 5.11 where diurnal TEC values are extracted for 20 - 21 November 2003 at above selected latitudes with 5° separation in both northern and southern hemispheres. This allows for observation of equatorward TIDs (if available) from appearance of consecutive peaks at different times which also assists in estimating the apparent propagation velocities. The propagation velocity of LSTIDs is simply calculated from the time delay between the peak occurrences. A large scale TID was observed on 20 November 2003 with a propagating speed of about 930 m/s (during 11:08 UT - 11:37 UT) in the northern hemisphere. This velocity is higher than the findings in a study by Borries et al. (2009) which reported LSTIDs using ionospheric perturbation TEC maps over Europe on same day with a speed of 629±48 m/s at 08:00 UT. Higher velocity values in our study are partly due to assumption that the TID is in a perfect equatorward direction. Such approach usually yields higher velocity values compared to actual velocities of the TIDs (e.g. Habarulema et al., 2015, and references therein). Indeed Borries et al. (2009) showed that the observed large scale TID on 20 November 2003 at 08:00 UT was not propagating exactly equatorward. Over southern hemisphere, existence of equatorward TIDs is evident although there was no enough data (see Figure 5.14) to accurately determine the

80

Figure 5.14: Variation of TEC at (a) 50°N, 45°N and 40°N (northern hemisphere) and (b) 35°S, 30°S and 25°S (southern hemisphere). TEC data was averaged in 1 hour bins. Note that there were significant data gaps for the southern hemisphere data.

TIDs velocities. Thus it is feasible to conclude that LSTIDs existed in both northern and southern hemispheres on 20 November 2003 and also played a role in generating the observed positive storm effects.

5.6 Storm period : 06 - 11 November 2004

Figure 5.15 shows the SYM-H (nT) index, IMF Bz (nT) and TEC (TECU) over southern and northern hemisphere for 07 - 11 November 2004 storm period. The interplanetary features of this storm period have been described in great detail by Tsurutani et al. (2008b); Echer et al. (2009, 2010). Figure 5.15 shows that the SI+ which occurred on 07 November 2004 at 19:30 UT led to the great geomagnetic storm on 08 November 2004 with a minimum SYM-H = -394 nT at 05:55 UT. The IMF Bz turned southward after the SI+ reaching a minimum value of ∼-50 nT at 23:29 UT on 07 November 2004. During the recovery phase of the 07 - 08 November 2004 storm, another storm developed starting with the SI+ at about 18:50 UT on 09 November and its main phase reached a minimum SYM-H of -282 nT on 10 November 2004. After the second SI+, the IMF Bz turned southward reaching ∼-30 nT at 19:50 UT and later turned northward reaching ∼ 40 nT
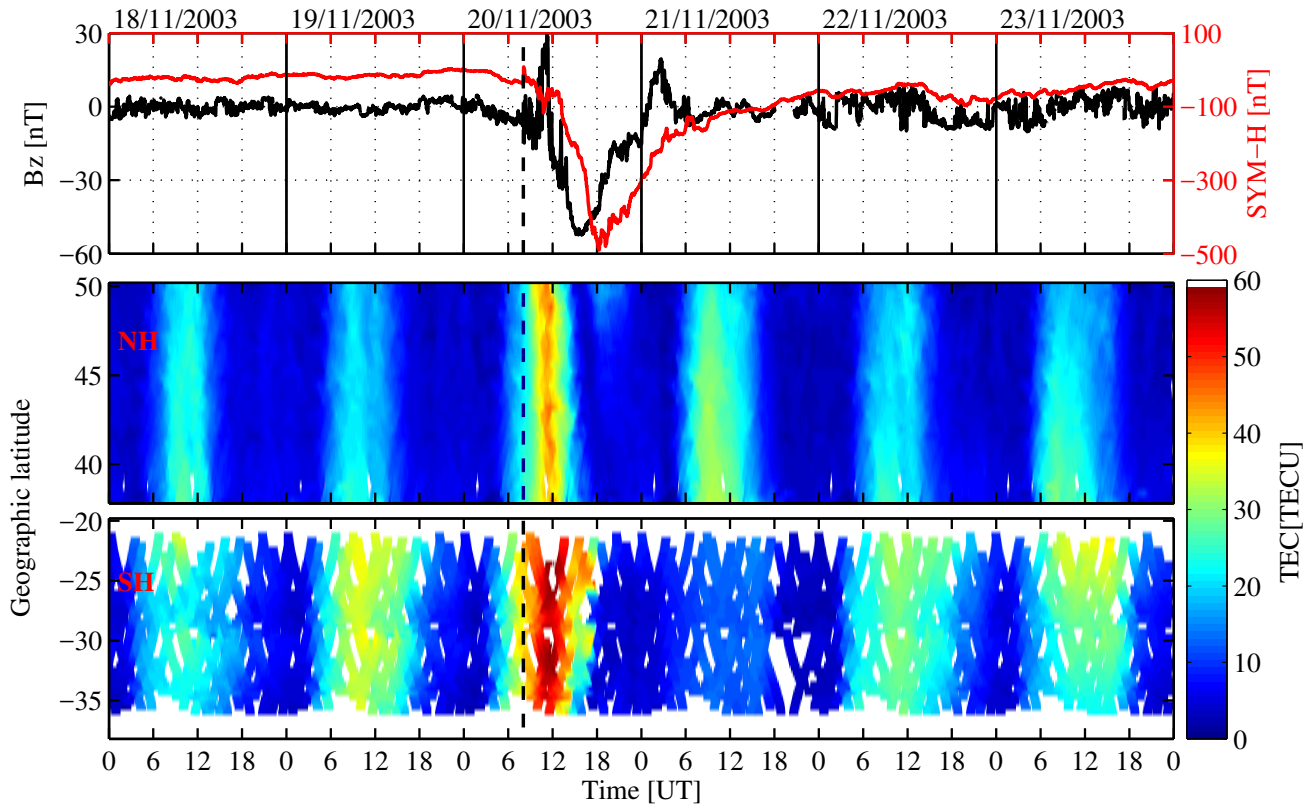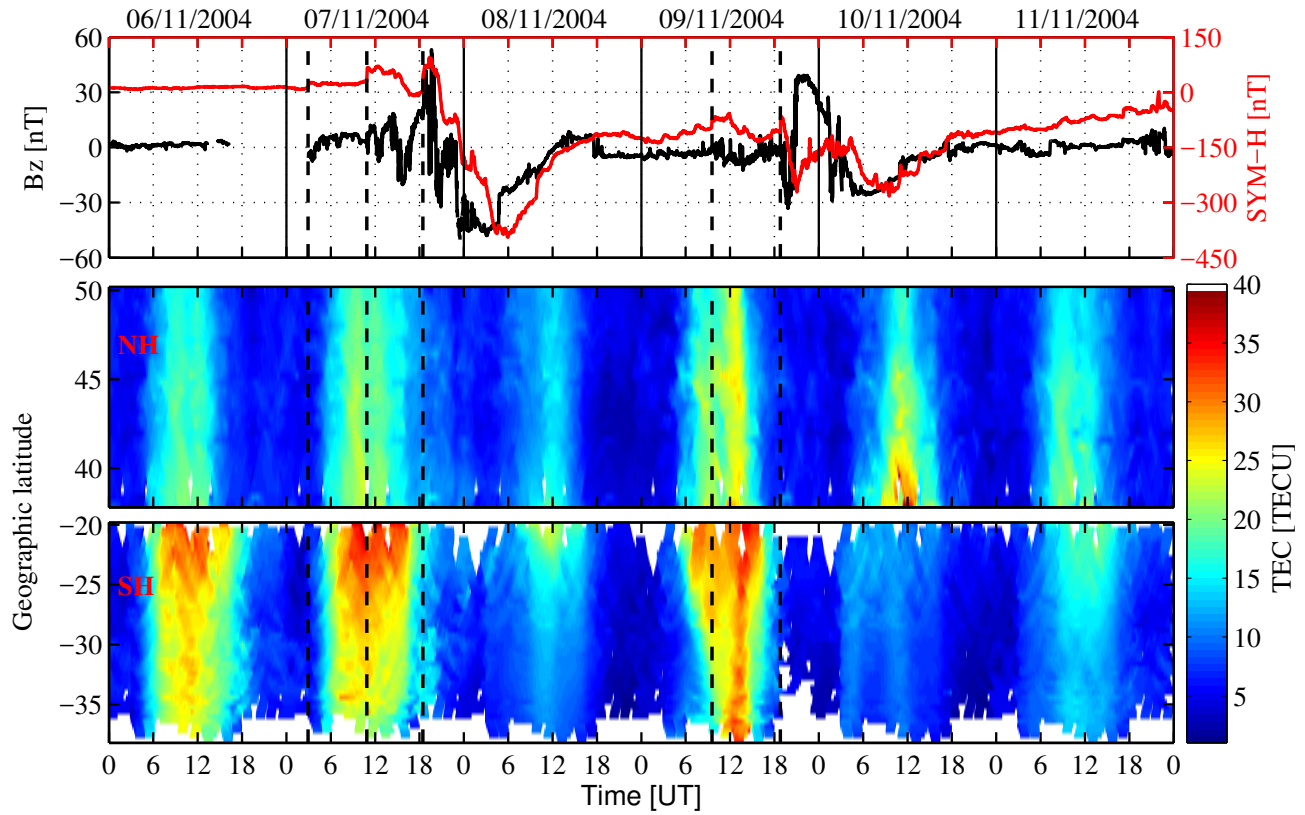
Figure 5.15: Changes in (a) Interplanetary Magnetic Field (IMF) Bz (nT) component (black curve) and Symmetric SYM-H (nT) (red curve), TEC (TECU) in latitude range 38°N - 50°N (31°N - 46°N, geomagnetic) and 20°S - 38°S (31°S - 46°S, geomagnetic) within 15°E - 40°E longitude sector for 06 - 11 November 2004. NH and SH refer to northern and southern hemispheres respectively. The dashed vertical black lines represent the Sudden Storm Commencement (SI+) which occurred at 02:55 UT, 10:52 UT and 18:27 UT on 07 November and at 09:33 UT and 18:48 UT on 09 November 2004.

at 22:24 UT on 09 November 2004. When IMF Bz turned southward again, it reached a value of -26 nT at 06:24 UT on 10 November 2004. In response to the interplanetary changes, ionospheric TEC in both hemispheres showed negative storm effect during the first main phase of 08 November 2004, positive storm effect during the recovery phase on 09 November, and different responses for the main phase of 10 November 2004.

Figure 5.16 shows variation of (a) V (km/s) and IEFy (mV/m), (b) dH (nT), (c) ΔfoF2 over JR055 and RO041, northern hemisphere and (d) ΔfoF2 over GR13L and MU12K, southern hemisphere stations. The vertical dashed black lines on all figures represent the SI+ occurrence time. During the first SI+ (19:30 UT), V increased to about 650 km/s while the IEFy showed a decrease to about -32 mV/m at 19:40 UT on 07 November 2004. The dH decreased to -354 nT at 05:55 UT on 08 November 2004. Generally, V remained high and further increased to $\sim$800 km/s after the SI+ that occurred at 18:50 UT on 09 November 2004. Around 20:45 UT on the same day, IEF dropped to $\sim$ 22 mV/m at 20:45 UT.

The increase in ΔfoF2 was observed on 07 November 2004 over JR055 (up to $\sim$ 116%, 103%, 110% at 07:00 UT, 20:00 UT, 23:00 UT respectively) and RO041 (79% at 20:00 UT) following the SI+ occurrences at 02:55 UT, 10:52 UT and 18:27 UT on 07 November 2004. As earlier
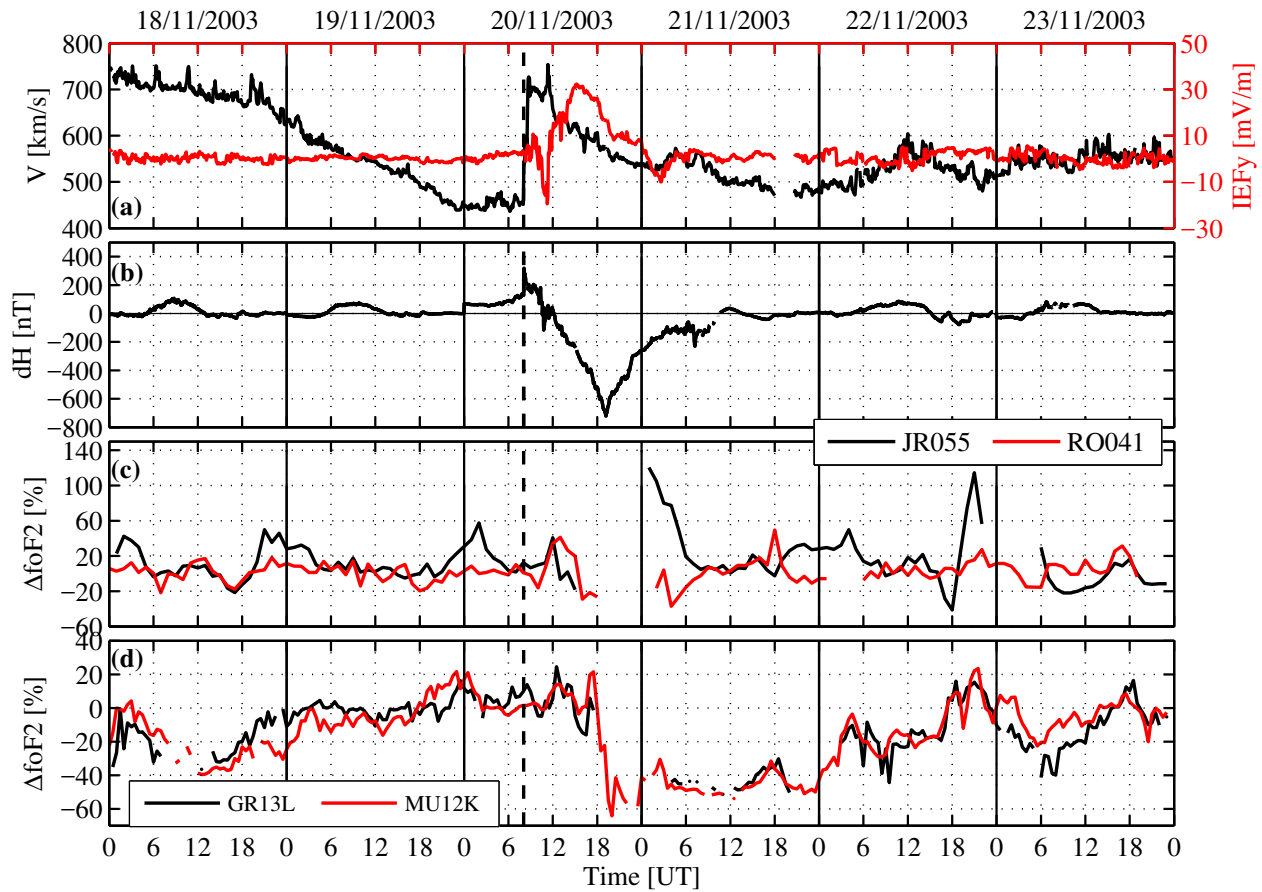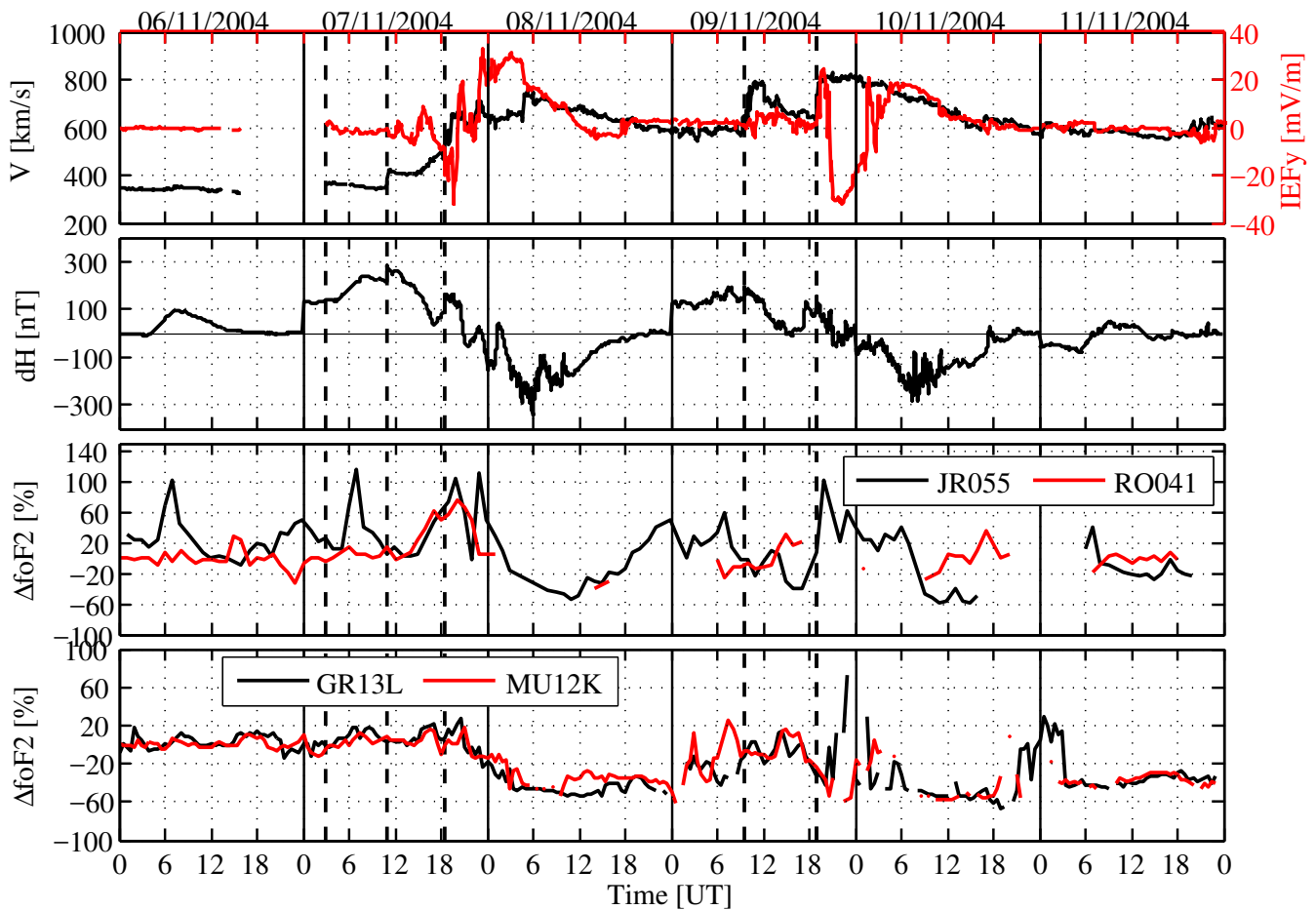
Figure 5.16: The variation of (a) solar wind speed V (km/s) and Interplanetary Electric Field IEFy (mV/m), (b) dH (nT) over equatorial magnetometer station AAE (9.02° N, 38.77° E, geographic), (c) and (d) ΔfoF2 over JRO55 and RO041; and MU12K and GR13L. The SI+ occurred at 02:55 UT, 10:52 UT and 18:27 UT on 07 November and at 09:33 UT and 18:48 UT on 09 November 2004 (Echer et al., 2010) as indicated by black vertical dashed line.

mentioned, details of this storm can be found in Tsurutani et al. (2008b); Echer et al. (2009, 2010). Southern hemisphere foF2 did not show considerable changes during the 07 November 2004. The decrease in ΔfoF2 was observed on 08 and 10 November 2004 over both hemispheres. On 09 November 2004 an increase (up to over 100%) in ΔfoF2 was observed after SI+ at 20:00 UT over JRO55. GR13L data also shows significant increase during the 09 November storm main phase for the first few hours and later negative storm effects dominated.

The 06 - 11 November 2004 storm occurred in summer and winter over southern and northern hemispheres mid-latitudes respectively. During the great geomagnetic storm of 08 November 2004 a decrease in TEC was observed in both southern and northern hemisphere. Available ionosonde data showed depleted foF2 (Figure 5.16(c) and (d)). From ionosonde data, the negative ionospheric response was observed ∼08 hours in JR055 and ∼ 6 hours in GR13L and MU12K after the SI+ (19:30 UT) on 08 November 2004 as shown in Figure 5.16 while there was no data for RO041 to make conclusions. On 09 November during the recovery phase, an increase in TEC was observed over both hemispheres and it was more prominent over southern hemisphere due to seasonal effects. On 10 November 2004 in both hemispheres, a negative ionospheric response was

observed from TEC which agreed with a decrease in foF2 as observed over JR055 and GR13L (Figure 5.16(c) and (d)). Over RO041 and MU12K there was no enough data to conclude about the ionospheric response. This storm period has been studied by different research groups and TEC/foF2 changes were mainly attributed to changes in neutral composition (e.g. Sahai et al., 2009; Wang et al., 2010; Habarulema et al., 2013b).
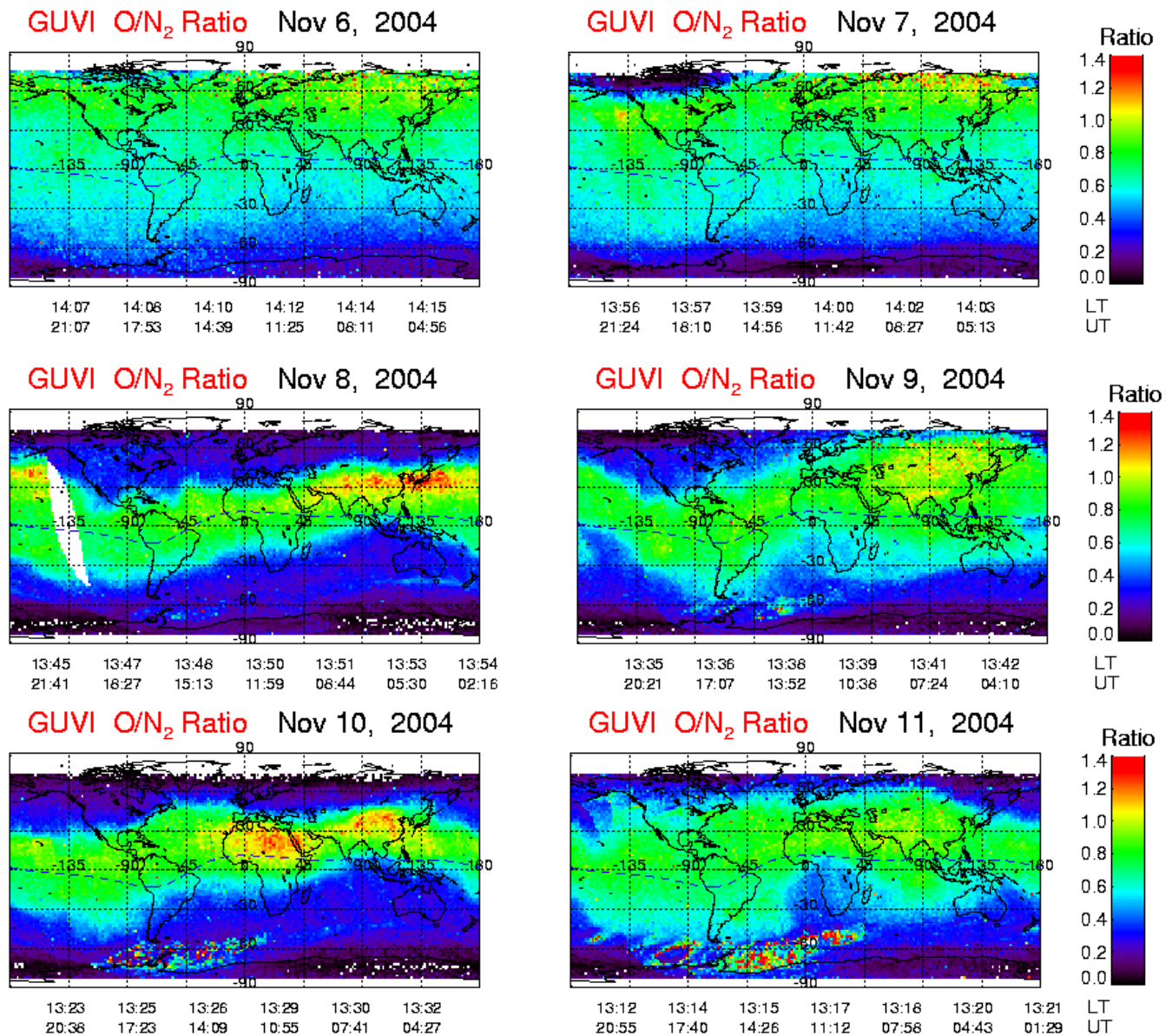
Figure 5.17: Global Ultraviolet Imager (GUVI) thermospheric O/N_2 ratio maps (`http://guvitimed.jhuapl.edu/guvi-galleryl3on2` Accessed: December 2016) for 06 - 11 November 2004 storm period.

Figure 5.17 illustrates the global O/N2 ratio maps obtained from GUVI (`http://guvitimed.jhuapl.edu/guvi-galleryl3on2`) for 06 - 11 November 2004 storm period. Days 06 and 07 November 2004 are the geomagnetically quiet, while 8 - 11 November are disturbed days. On 08 November 2004 a decrease in O/N_2 ratio was observed over both southern

84

and northern hemispheres in the African and European mid-latitude regions. On 10 and 11 November 2004, a decrease in O/N$_2$ ratio was observed over the southern hemisphere mid-latitude in the African sector while an increase is seen over northern hemisphere (European sector). The O/N$_2$ as observed from GUVI thermospheric maps and its behavior is in agreement with TEC and foF2 data. The study by Habarulema et al. (2013b) using TEC and ionosonde data over African equatorial and mid-latitude also reported that the changes in electron density corresponded to the behavior in GUVI O/N$_2$ ratio over mid-latitude, and that TEC was generally depleted on 08 and 10 November 2004. The increase in TEC on 9 November 2004 could be due to an increase in O/N$_2$ ratio due to changes in large scale wind circulation (Prölss, 1997; Sahai et al., 2009).

Figure 5.16(b) shows that the dH (nT) depicted a CEJ on 08 and 10 November 2004 during local daytime. This implies plasma descent to lower altitude where loss rate is higher. Consequently it is an indication of absent or not well developed EIA (Dashora and Pandey, 2007; Tesema et al., 2015; Joseph et al., 2015) suggesting that the changes in mid-latitude electron density may not have significant contribution from the EIA regions. Thus we have not observed clear evidence of PPEF as it is difficult to make a conclusion from the magnetometer data during night time. Nevertheless, if PPEFs were present, they would be westward during nighttime, while the DDEF would be eastward. Similar to the previous storm period, the presence of LSTIDs were investigated from 08 - 10 November 2004 using TEC at different latitudes 50°N, 45°N, 40°N (northern) and 35°S, 30°S, 25°S (southern) hemispheres respectively as shown in Figure 5.18.
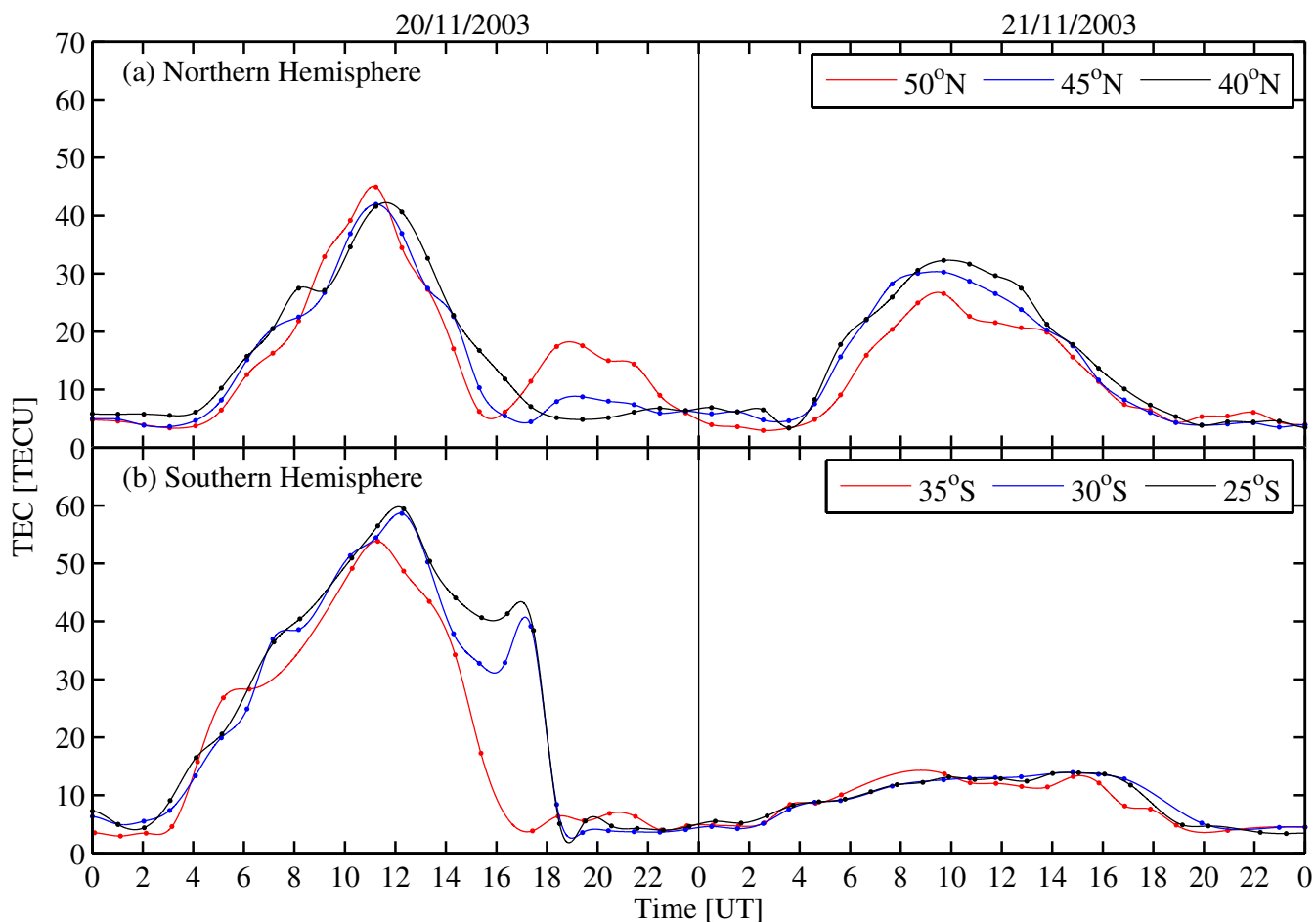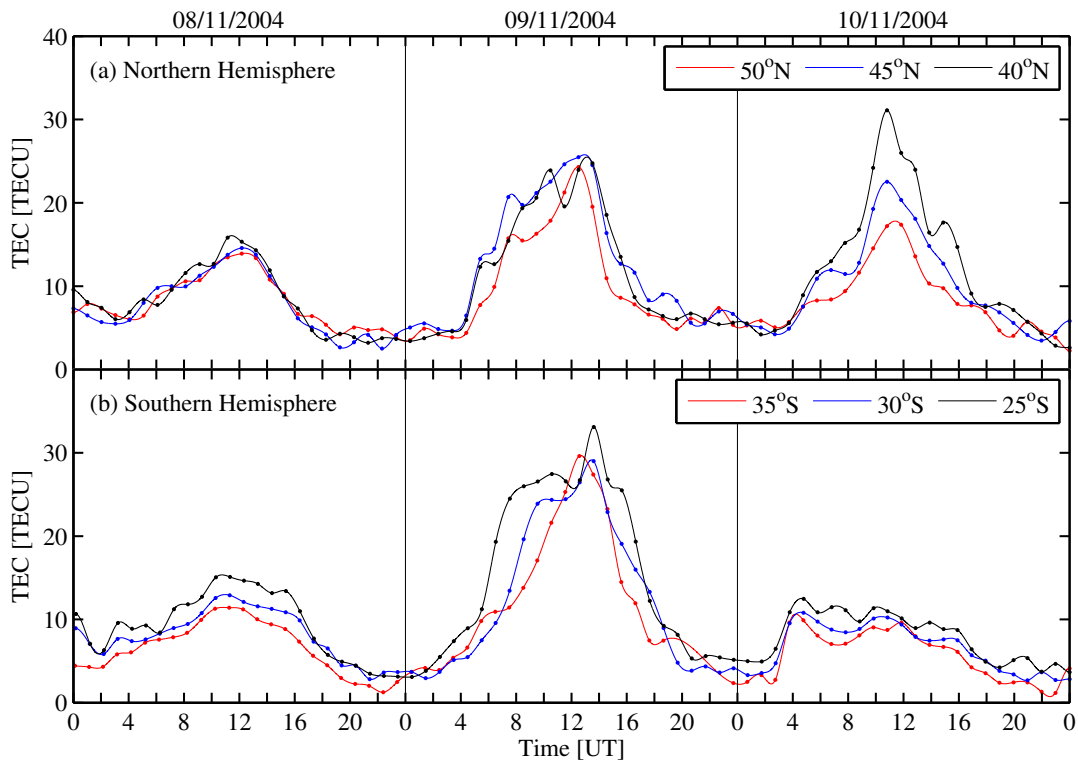

Figure 5.18: Variation of TEC at (a) 50°N , 45°N and 40°N (northern hemisphere) and (b) 35°S, 30°S and 25°S (southern hemisphere). TEC data was averaged in 1 hour bins. Note that there were significant data gaps for the southern hemisphere data (Matamba et al., 2016).

In both hemispheres, there are signatures of LSTIDs propagating equatorwards on 09 November

2004 with a speed of 646 m/s (12:29 UT - 13:07 UT) and 664 m/s (12:40 UT - 13:27 UT) respectively, which could have contributed to the observed positive storm effect. However on 10 November 2004, when there were opposite storm effects in northern (positive) and southern (negative) hemispheres, LSTIDs were only observed in the southern hemisphere. For example, a large scale TID with a speed of 407 m/s (04:13 UT - 04:37 UT) in the southern hemisphere which is not clearly visible in northern hemisphere. A notable result is that although LSTIDs have been associated with positive storm effects, this particular case here is reported during the negative storm phase clearly visible in Figure 5.15, 5.16(d) and 5.18(b) on 10 November 2004.

5.7   Summary

In this chapter analyses of four great geomagnetic storms of solar cycle 23 were presented by examining ionospheric response in southern and northern hemisphere mid-latitude regions. Within both mid-latitude regions, all storm periods were associated with both positive and negative ionospheric storm effects either during the main or recovery phases. Apart from the equinox 29 March - 02 April 2001 storm, the other three storm periods (27 - 31 October 2003, 18 - 23 November 2003 and 06 - 11 November 2004) occurred during winter and summer over northern and southern hemisphere mid-latitudes respectively. Seasonal effects were therefore predominant in determining the observed ionospheric storm effects in both hemispheres. On 31 March 2001 both decrease and increase in TEC were observed simultaneously between ∼06:00 UT - 12:00 UT over both hemispheres. The decrease was observed at latitude from about 47°N - 50°N and 33°S - 38°S and increase was observed in other latitudes. Negative ionospheric effects were largely associated with neutral composition changes while positive ionospheric storm effects were linked to low latitude changes related to the expansion of EIA (day-side super-fountain effect).

A sudden increase in TEC that occurred on 28 October 2003 was due to intense solar flare. It was the EUV portion of the flare spectrum that caused high altitude photoionisation, thus the TEC increase for ∼3 hours (Tsurutani et al., 2005). PPEF effects on mid-latitude ionospheric response have been clearly seen on 29 October 2003 and 20 November 2003 and contributed to the profound increases observed in TEC. In some cases such as on 29 October 2003, PPEF, EIA and LSTIDs were all present during the period of positive storm effect. The negative and positive ionospheric storm effects on November 2004 were both believed to be due to neutral composition changes and LSTIDs. An interesting result on 10 November 2004 was the observation of LSTIDs during the negative storm effect over the southern hemisphere. Usually, LSTIDs are thought to be responsible for positive storm effects.

Chapter 6

Statistical analysis of ionospheric storm effects over the African sector from 2001 - 2015

6.1   Introduction

This chapter discusses a statistical analysis of ionospheric response to Coronal Mass Ejection (CME)- and Corotating Interaction Region (CIR)- driven storms using the stations located within 30°E - 40°E geographic longitude. The storm periods analysed occurred during the period 2001 - 2015, which covered part of solar cycles 23 and 24. Global Positioning System (GPS) Total Electron Content (TEC) derived from the Global Navigation Satellite System (GNSS) observations was used in this analysis. This chapter will discuss comparison of the ionospheric storm effects over the southern and northern hemispheres in the mid, low, and equatorial latitudes over the African sector. The stations which were used are indicated in Figure 6.1 and the geographic and geomagnetic latitudes are shown in Table 6.1. The seasonal and local time dependence of the ionospheric storm effects will also be considered. Most of results discussed on this chapter appear in a paper by Matamba and Habarulema (2017).

Table 6.1: Geographic and geomagnetic coordinates of GPS receiver stations.

Name, country	Code	Geog. lat.	Geog. long.	Geom. lat.	Geom. long.
Thohoyandou, South Africa	TDOU	-23.08	30.38	-33.82	98.48
Halat Ammar, Saudi Arabia	HALY	29.14	36.10	21.83	107.56
Nazret, Ethiopia	NAZR	8.57	39.29	-0.25	111.01
Mbarara, Uganda	MBAR	-0.60	30.74	-10.22	102.36
Sheba, Eritrea	SHEB	15.85	39.05	7.36	110.60

6.2   Data and method

Corotating Interaction Regions (CIRs)- and Coronal Mass Ejections (CMEs)- related storms can be classified based on the features of proton temperature, solar wind speed, magnetic field and proton density (e.g., Richardson and Cane, 2010). CME-driven storms can be identified by sharp increase in solar wind speed, temperature, densities and magnetic field (Gonzalez et al.,
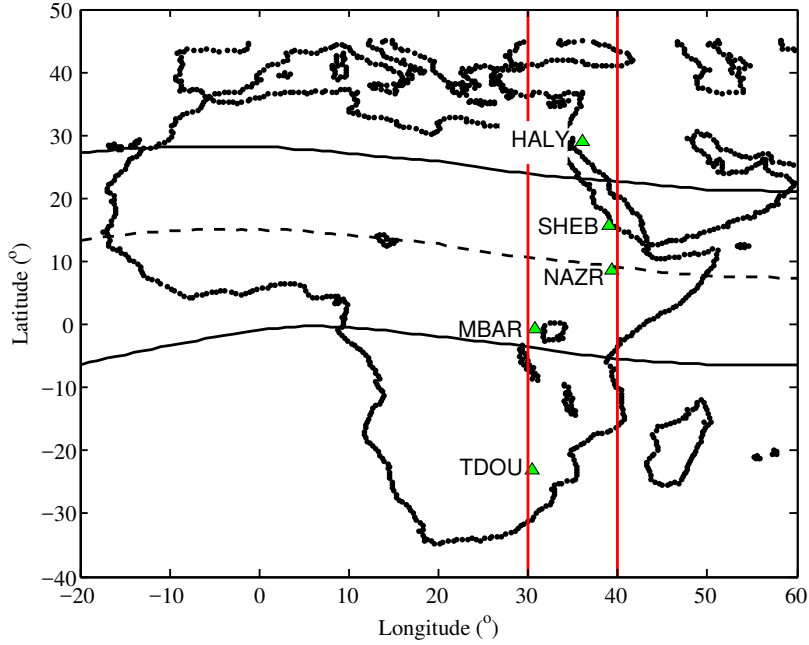
Figure 6.1: Map showing stations used in this study.

1999; Huttunen et al., 2002; Elliott et al., 2005; Chen et al., 2014). On the other hand, the main features of CIR-driven storm, are an enhancement of proton temperature, an increase of solar wind speed, a compression of magnetic field and proton density increases to unusually high values (Mavromichalaki et al., 1988). Figures 6.2 and 6.3 show the geomagnetic indices and solar wind parameters for CME- and CIR-driven storms that occurred on 17 - 20 March 2015 and 02 - 12 January 2008 respectively. The figures show Dst index (nT), Kp index, temperature (10^{-4} K), solar wind speed V (km/s), interplanetary magnetic field Bz component (nT), magnetic field B (nT), density (ρ)(cm^-3) and flow pressure (nPa).

In response to CME-driven storm (Figure 6.2), an intense geomagnetic storm occurred on 17 March 2015 and reached a minimum Dst index of ~ -223 nT at 22:00 UT and Kp index of 8. The temperature increased from $\sim 43 \times 10^{-4}$ K to $\sim 913 \times 10^{-4}$ K after the short duration positive spike (SI+) on Dst index. The solar wind speed, V abruptly increased to ~ 600 km/s from ~ 410 km/s. The Bz component turned southward, from ~ 20 nT (05:00 UT) to ~ -16 nT (07:59 UT) during geomagnetic storm. B, density and flow pressure increased to about 30 nT (14:00 UT), ~ 40 cm^{-3} (05:00 UT) and $\sim$18 nPa (05:00 UT) respectively.

Figure 6.3 illustrates an example of CIR-driven storm for the period 02 - 12 January 2008. A weak geomagnetic storm occurred on 07 January 2008 with a minimum Dst index of -30 nT at 03:00 UT and Kp index of 4. The vertical dashed lines on Figure 6.3 indicate the initial phase of geomagnetic storm. Immediately after the initial phase, an increase in temperature ($\sim 10 \times 10^{-4}$ K to $\sim 450 \times 10^{-4}$ K), solar wind (~ 330 to $\sim$670 km/s), B (~ 2.5 to 16 nT), density (~ 11.9 to 40 cm^{-3}), flow pressure (~ 1.9 to 8 nPa) and Bz showed fluctuation with a minimum Bz of -9 nT.
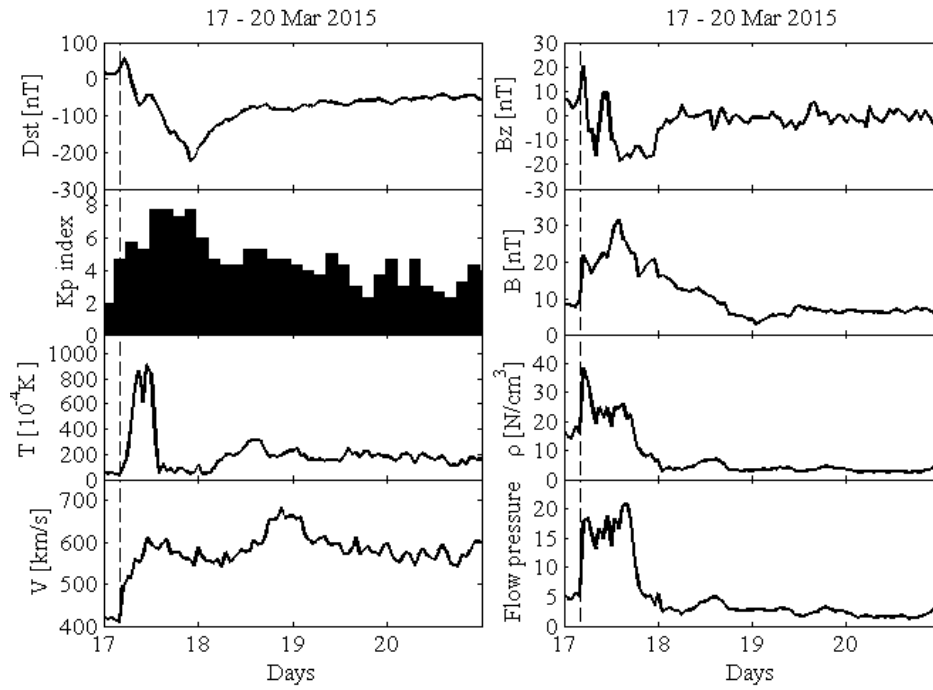
Figure 6.2: Variation of Dst and Kp indices, temperature, solar wind speed, magnetic field (B) and the Bz magnetic field component, density and flow pressure for 17 - 20 March 2015. The vertical line on the figures indicates the sudden storm commencement for CME-driven storm.
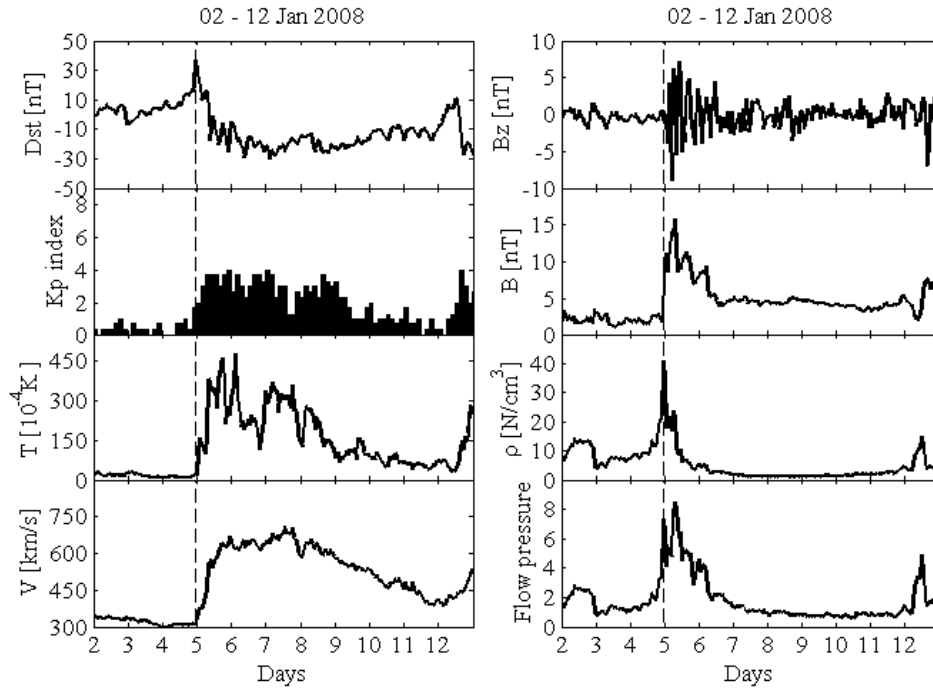
Figure 6.3: Variation of Dst and Kp indices, temperature, solar wind speed, magnetic field (B) and the Bz magnetic field component, density and flow pressure for 02 - 12 January 2008. The vertical line on the figures indicates the sudden storm commencement for CIR-driven storms.

CME and CIR events used in this work were based on previous studies (Richardson and Cane, 2010; Xystouris et al., 2014; Benacquista et al., 2017) and CME and CIRs' cata-

logues within the period 2001 - 2015 found on `http://www.srl.caltech.edu/ACE/ASC/DATA/level3/icmetable2.htm`; `https://umbra.nascom.nasa.gov/lasco/observations/halo/` and `https://www.helcats-fp7.eu/catalogues/wp5\_cat.html`. The Dst≤ -30 nT or/and Kp ≥ 3 were used to determine the geomagnetic storm periods (Huttunen et al., 2002). Kp and Dst indices, were downloaded from `http://www.gfz-potsdam.de/~kp_index/` and `http://wdc.kugi.kyoto-u.ac.jp/dstae/index.html` respectively and used to select the storm periods. For the storm caused by two successive CMEs, two CME-driven storms were classified within one storm period. For example, Figure 6.4 shows the Dst index for 06 - 11 November 2004 storm period. The first and second CME occurred starting on 07 November at 22:00 UT and 09 November 2004 at 20:00 UT respectively (Richardson and Cane, 2010, `http://www.srl.caltech.edu/ACE/ASC/DATA/level3/icmetable2.htm`). The red vertical line indicates where the storm is separated on 09 November 2004. The storm onset time for the first and second geomagnetic storm occurred at 19:00 UT on 07 November 2004 and 11:00 UT on 09 November 2004 respectively.
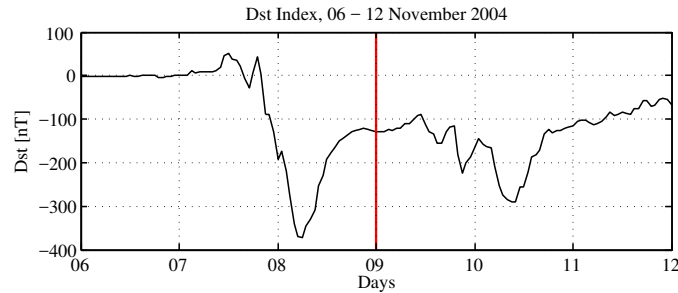
Figure 6.4: Diurnal variation of Dst index for 06 - 11 November 2004

The total number of CME storms and CIR-driven storms identified in this study were 153 and 173 respectively during the period 2001 - 2015. Figure 6.5 shows the number of CIR-(blue bars), CME- (green bars) driven storms per year and total geomagnetic storms (red bars) from 2001 to 2015. The blak solid line in Figure 6.5 indicates the daily sunspot number. Most CIR-driven storms were observed during the declining phase of solar cycle 23 (i.e. 2003 - 2008) as shown in Figure 6.5. However, during the solar maxima (eg. in 2001 and 2012), most CME-driven storms were observed. It is known that CME- and CIR-driven storms generally occur during solar maximum and the declining phase of the solar cycle respectively (e.g., Gonzalez et al., 1999; Borovsky and Denton, 2006; Tsurutani et al., 2006a,b; Balogh et al., 2013; Burešová et al., 2014) and follow the trend of solar activity (Vijaya Lekshmi et al., 2011). A significant number of geomagnetic storms were observed during the declining phases of solar cycles 23 and 24 in 2003 and 2015. The interplanetary causes of intense geomagnetic storms (Dst < -100 nT) during the rising, maximum phase of the solar cycle 23 were studied by Tsurutani et al. (2006a); Gonzalez et al. (2007); Echer et al. (2008).

Figure 6.6 illustrates the seasonal distribution of CME- (green) and CIR- (blue) driven geomagnetic storms for the interval 2001-2015. Most CME- and CIR-driven storms were observed during the March and September equinoxes respectively. Our results are consistent with previous literature (e.g Maris, 1932; Russell and McPherron, 1973; McNamara, 1991; Gonzalez and Tsurutani, 1992;
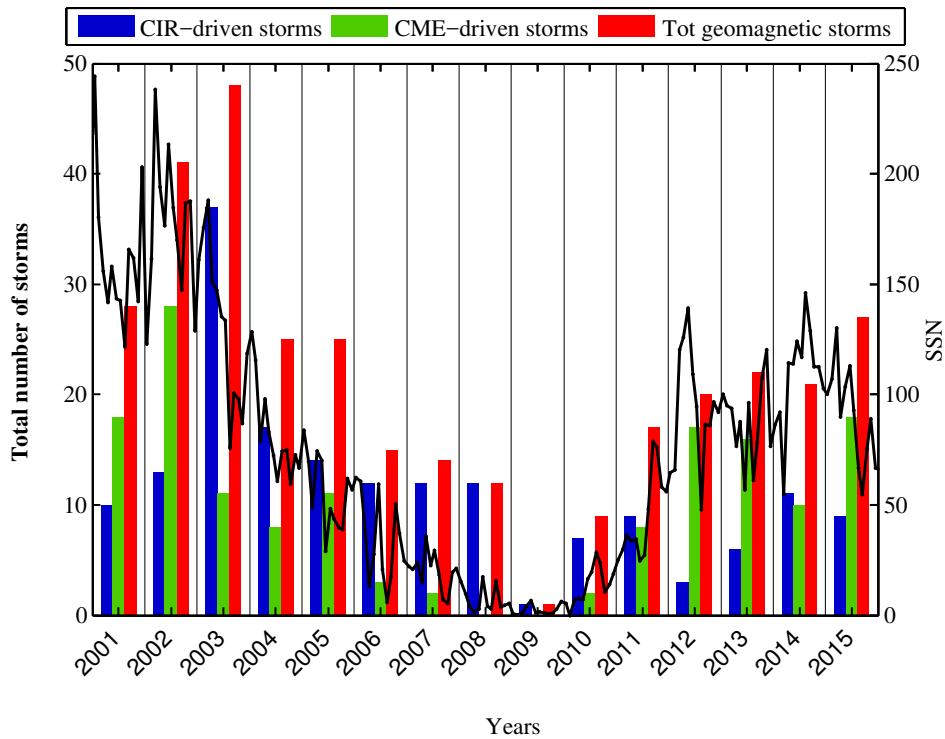
Figure 6.5: Distribution of CIR- (blue bars), CME-driven storms (green bars) and total number of geomagnetic storms (red bars) from 2001 - 2015. Over-plotted is the daily sunspot numbers for the time period 2001 - 2015.
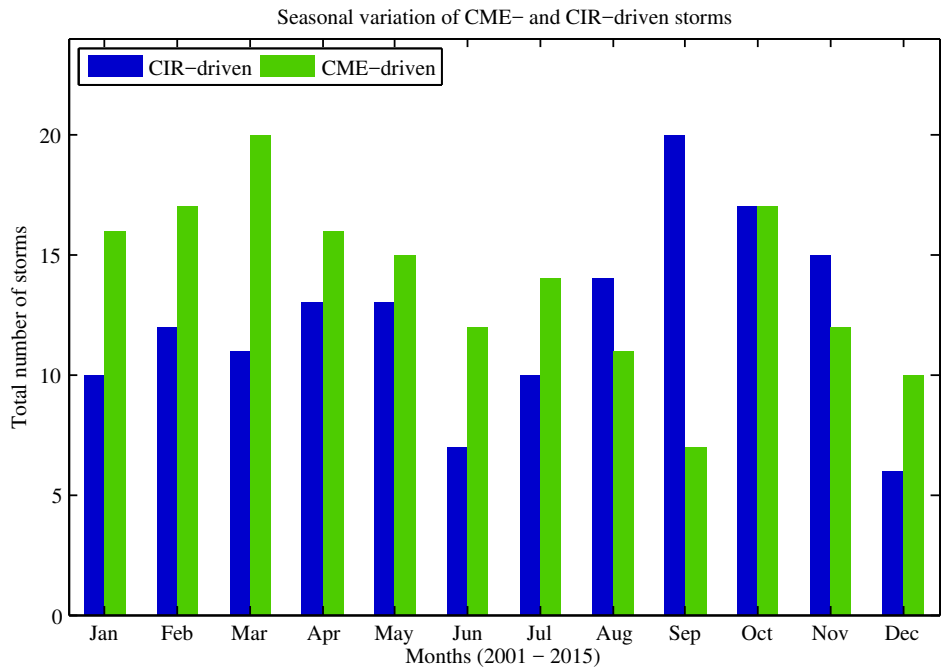
Figure 6.6: Monthly distribution of the CME- and CIR-driven storms during the time period 2001 - 2015.

Gonzalez et al., 1994). Russell and McPherron (1973) attributed the seasonal variation of the geomagnetic activity with the polarity of Interplanetary Magnetic Field (IMF) which emerges

from the changing orientation of the solar equatorial coordinate system. During the equinoxes, the Earth's magnetic field is more likely to be disturbed by solar events, because the direction of the axis of the Earth's magnetic field is more nearly at right angles to the flow of solar wind (McNamara, 1991; Häkkinen et al., 2003).
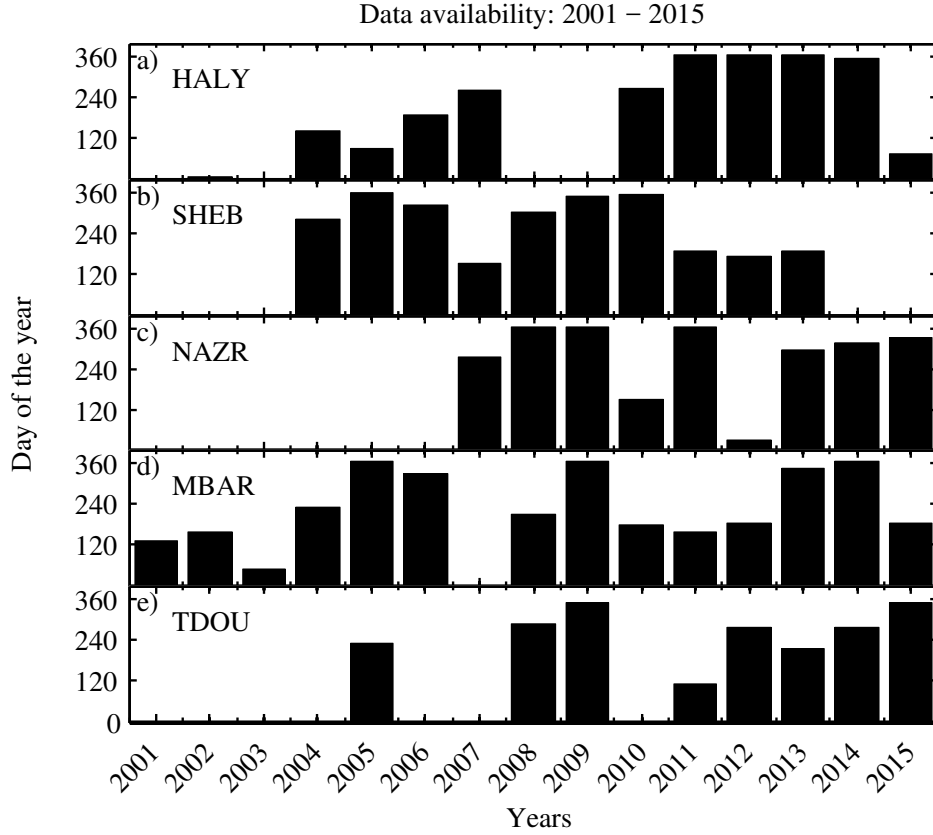
Figure 6.7: Availability of TEC data over (a) Halat Ammar, HALY (29.14°N, 36.10°E; 21.83°N, geomagnetic), Saudi Arabia, (b) Sheba, SHEB (15.85°N, 39.05°E; 7.36°N, geomagnetic), Eritrea, (c) Nazret, NAZR (8.57°N, 39.29°E; 0.25°S, geomagnetic), Ethiopia (d) Mbarara, MBAR (0.60°S, 30.74°E; 10.22°S, geomagnetic), Uganda, and (e) Thohoyandou, TDOU (23.08°S, 30.38°E; 33.92°S, geomagnetic), South Africa during the time interval 2001 - 2015.

Figure 6.7 shows the days when TEC data was available at 30-second time resolution over (a) Halat Ammar, HALY (29.14°N, 36.10°E; 21.83°N, geomagnetic), Saudi Arabia, (b) Sheba, SHEB (15.85°N, 39.05°E; 7.36°N, geomagnetic), Eritrea, (c) Nazret, NAZR (8.57°N, 39.29°E; 0.25°S, geomagnetic), Ethiopia (d) Mbarara, MBAR (0.60°S, 30.74°E; 10.22°S, geomagnetic), Uganda, and (e) Thohoyandou, TDOU (23.08°S, 30.38°E; 33.92°S, geomagnetic), South Africa for the time interval 2001 - 2015. MBAR and NAZR have most and least TEC data respectively. The method used to derive TEC and identify responses of TEC to geomagnetic storms was explained in Chapter 4. The examples of positive (P), negative (N), positive-negative (PN), negative-positive (NP) and not-significant (NS) were also shown in chapter 3. The ionospheric storm effects were presented in terms of percentages in order to capture the behavioural trend of ionospheric response during CME- and CIR-driven storms. The following expression was considered for overall statistics:

$$X = \frac{X_{tot}}{T_{cs}} \times 100\%,$$

(6.1)

92

where X represents either P, N, PN, NP or NS ionospheric storm effects, that occurred during either CME- or CIR-driven storms, X_{tot} is the total number of observed P, N, PN, NP or NS ionospheric storm effects and T_{cs} is total number of CME- or CIR-driven storms for a specific year. For seasonal and local time variation, the ionospheric response (P, N, PN, NP or NS ionospheric storm effects) were divided by either total number of CIR- or CME-driven storms multiplied by 100%.

6.2.1 Mid-latitude ionospheric responses

In order to investigate the mid-latitude ionospheric responses, GNSS TEC data over Thohoyandou, TDOU (23.08°S, 30.38°E; 33.92°S, geomagnetic), South Africa, in the southern hemisphere; and Halat Ammar, HALY (29.14°N, 36.10°E; 21.83°N, geomagnetic), Saudi Arabia, in the northern hemisphere were considered. HALY station is closer to the low-latitude region than TDOU and the two stations are not conjugated.

Figures 6.8(a) and (b) illustrate the overall variation of ionospheric storm effects over TDOU (2005 - 2015) and HALY (2004 - 2015) during CME- and CIR-driven storms. At TDOU and HALY stations, 86 and 71 storm periods had TEC data respectively. Over TDOU station, 35 and 51 storm periods were driven by CIRs and CME respectively. Over HALY, 27 and 44 storm periods were CIR- and CME-driven storms respectively.

Table 6.2 shows the statistics of the mid-latitude ionospheric responses. More P ionospheric storm effects were observed over HALY (21.83°N, geomagnetic) than in TDOU (33.82°S, geomagnetic) stations during both CME- and CIR-driven storms. During geomagnetic storms, the neutral composition changes due to particle precipitation and Joule heating maximizes at polar latitudes, and they expand towards the low latitude (Prölss, 1995; Mendillo, 2006; Buonsanto, 1999). The neutral circulation from high to low latitude results in enriching the mid-latitudes with molecular Nitrogen (N_2) and atomic Oxygen (O) densities at the low latitudes. The stations located closer to the equatorial latitude will observe pro-longed positive storm effects (Prölss, 1995; Mendillo, 2006) as seems to be the case with our statistical results. Another reason why HALY observed more P ionospheric storm effects could be the expansion of the EIA during geomagnetic storm (Batista et al., 1991; Mendillo, 2006; Matamba et al., 2016). The probability that the EIA could reach the low-mid-latitude station HALYis greater than reaching the typical mid-latitude location of TDOU.

Figure 6.8: The annual distribution of positive (P), negative (N), positive-negative (PN), negative-positive (NP) and not-significant (NS) ionospheric storm effects occurrence over the (a) southern hemisphere, TDOU (23.08°S, 30.38°E; 33.92°S, geomagnetic), South Africa and (b) northern hemisphere, HALY (29.14°N, 36.10°E; 21.83°N, geomagnetic), Saudi Arabia.

Table 6.2: Mid-latitude ionospheric responses.

GNNS Location	Geom. Lat	Ionospheric storm effects (%)									
		CME-driven storms					CIR-driven storms				
		P	N	PN	NP	NS	P	N	PN	NP	NS
TDOU, South Africa	33.82°S	35.3	7.8	5.9	0	51.0	57.1	0	0	0	42.9
HALY, Saudi Arabia	21.83°N	52.3	2.3	4.5	0	40.9	63.0	0	3.7	0	33.3

The P ionospheric storm effects are also attributed to Large-Scale Traveling Ionospheric Disturbances (LSTIDs) (e.g. Prölss and Jung, 1978; Prölss, 1993a, 1995, 2004; Ding et al., 2007; Borries et al., 2009; Habarulema et al., 2015). Borries et al. (2009) did a statistical analysis of LSTIDs over Europe using TEC data derived from GNSS measurements for the time interval 2001 - 2007. For some storm periods where Borries et al. (2009) observed TIDs, P ionospheric storm effects were observed over the northern hemisphere station, HALY for the periods where data was available. However, there was no TEC data over TDOU to check the response during the time when TIDs where observed over Europe. TIDs are ionospheric manifestations of the passage of atmospheric gravity waves generated at polar regions by the energy input from the magnetosphere to the auroral ionosphere (Hunsucker, 1982; Tsugawa et al., 2004). LSTIDs propagate equatorward from polar latitudes to mid-latitudes causing an enhancement in the height of the F-region which results in an increase in electron density (Bauske and Prölss, 1997; Ding et al., 2008). The two TIDs propagating equatorward from the southern and northern hemispheres interfere and cross over to the opposite hemisphere without a change in velocity (e.g. Hajkowicz and Hunsucker, 1987; Habarulema et al., 2015). LSTIDs related to geomagnetic storm processes are more likely to be seen over TDOU than HALY station since the LSTIDs normaly originate at high latitude regions and propagate to mid-latitude, low latitude or even to the opposite hemisphere during geomagnetic storm (e.g. Prölss and Jung, 1978; Borries et al., 2009; Cai et al., 2012). A significant number of NS ionospheric storm effects were observed over TDOU and HALY stations during the solar maximum of solar cycle 24 (2012 and 2013).

N ionospheric storm effects were observed only during CME-driven storms over both mid-latitude stations (TDOU and HALY) and were seen during solar maximum of solar cycle 24 (i.e. 2012, 2013, 2014 and 2015) according to the available data. N ionospheric storm effects are widely believed to be due to neutral composition changes (e.g., Prölss, 1977, 1980, 1995; Fuller-Rowell et al., 1996). N ionospheric storm effects seems to follow the solar cycle variation with more N ionospheric storm effects occurring during solar maximum (Titheridge and Buonsanto, 1988; Vijaya Lekshmi et al., 2011; Matamba et al., 2015), which can be understood by neutral composition changes (Fuller-Rowell et al., 1994; Prölss, 1995). N ionospheric storm effects are due to increases in N_2 in regions of sunlight, their strengths depends on local time and the longitude of the sector during storm input (Fuller-Rowell et al., 1994). This may also indicate that larger geomagnetic storms carry composition changes to lower latitudes (Titheridge and Buonsanto, 1988). N ionospheric storm effects were more frequently observed over TDOU than over HALY, which could be due to the neutral composition zone that extends to the mid-latitude (to about $\pm 40°$ geomagnetic latitude) during moderate storms. During strong storms, the composition zone may reach the low-latitude region and N ionospheric storm effects can be observed at mid-latitude region (Prölss, 1995; Lastovicka, 2002b). Thus, TDOU station will observe more N ionospheric storm effects than HALY station.

A few PN ionospheric storm effects were also observed over TDOU (5.9%) and HALY (4.5%) stations during CME-driven storms. The occurrence of PN ionospheric storm effects could be due to local time dependence of ionospheric storm (Prölss, 1993b, 1995; Mendillo, 2006). For example, Figure 6.9 illustrates an example of PN ionospheric storm effect for the storm period 06 - 09 January 2005 over TDOU station. It shows a diurnal variation of the (a) Dst index (nT), (b) Kp index and (c) ΔTEC (%). The shaded region indicate the time when an increase (P) and a decrease (N) in ΔTEC occurred and the strength of geomagnetic storm (based on Dst and Kp indices). P ionospheric storm effect occurred during the initial phase of the storm and during nighttime (18:00 UT-~23:30 UT) and the N ionospheric storm effects were observed from the morning of the next day during recovery phase (05:00 UT-~18:00 UT). N ionospheric storm effects are considered delayed when compared to P ionospheric storm effects and are due to neutral composition changes that rotate into the daytime sector (Prölss, 1995). Mendillo (2006) observed both strongly P and daytime N ionospheric storm effects at northern mid-latitude stations and were thought to be due to the neutral composition changes, which act quickly if a geomagnetic storm starts early in the local day-time and intensifies rapidly, and by the time it rotates to the afternoon sector, P ionospheric storm effect mechanism is ineffective. There were no NP ionospheric storm effects observed over both stations during CME- and CIR- driven storms.
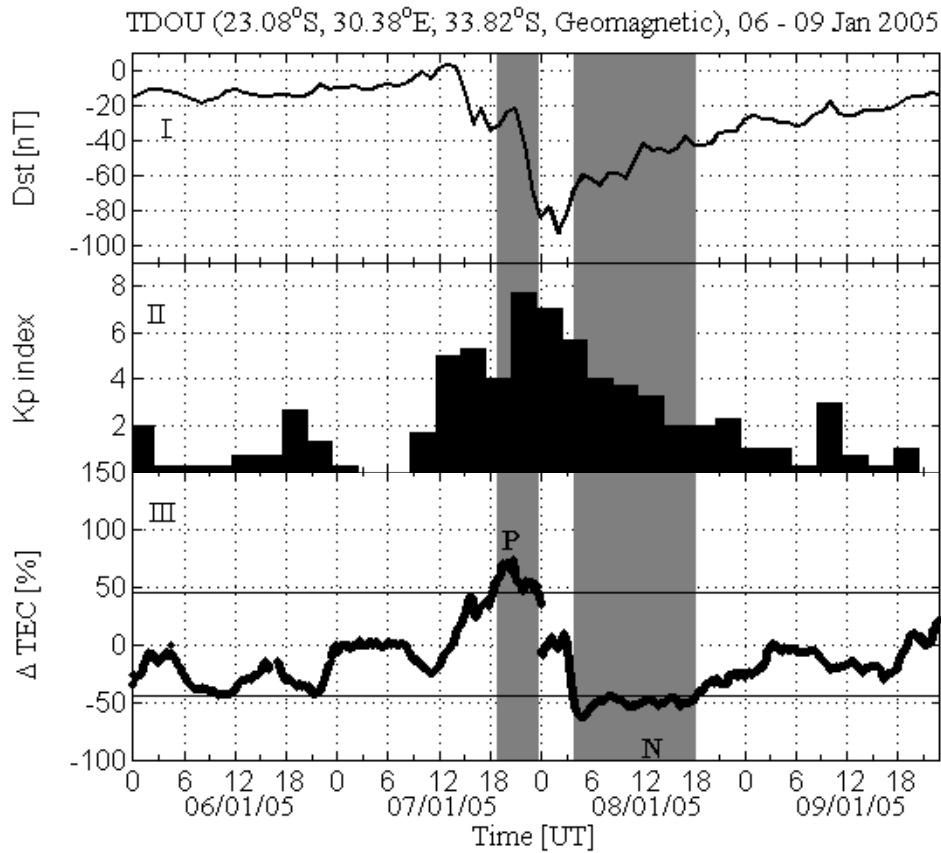
Figure 6.9: An example of positive-negative (PN) ionospheric storm effect over TDOU (23.08°S, 30.38°E; 33.92°S, geomagnetic), South Africa.

Figures 6.10 (a) and (b) show the seasonal variation of ionospheric storm effects over southern (TDOU) and northern (HALY) hemispheres mid-latitude stations respectively during CME- and CIR-driven storms. The ionospheric storm effects were grouped into 4 seasons, namely, December solstice (November, December and January), March equinox (February, March and April), June solstice (May, June and July), and September equinox (August, September and October) during the time interval 2005 - 2015 (TDOU) and 2004 - 2015 (HALY). December and June solstices are close to the summer and winter seasons respectively in the southern hemisphere and vice versa in the northern hemisphere.

The N ionospheric storm effects mostly occur in the summer hemisphere. During summer N ionospheric storm effects are observed all the way from high to low latitudes whereas during winter they are restricted to high latitude (e.g. Prölss, 1977; Titheridge and Buonsanto, 1988; Prölss, 1995; Fuller-Rowell et al., 1996). It is now believed that the seasonal variations arise from the interaction between seasonal and storm induced winds. In summer both types of winds support each other while they are out of phase in winter (Prölss, 1977, 1995; Fuller-Rowell et al., 1996, and references therein). On the other hand, P ionospheric storm effects over the mid-latitude are mainly observed during winter. This could be explained by the limited extent of composition bulge in this season. Therefore, a larger proportion of the mid-latitude region will only be exposed to wind perturbations (Prölss, 1995; Fuller-Rowell et al., 1996).

N and P ionospheric storms were mainly observed on December solstice (summer) and June solstice (winter) respectively during CME-driven storms over southern hemisphere (TDOU)
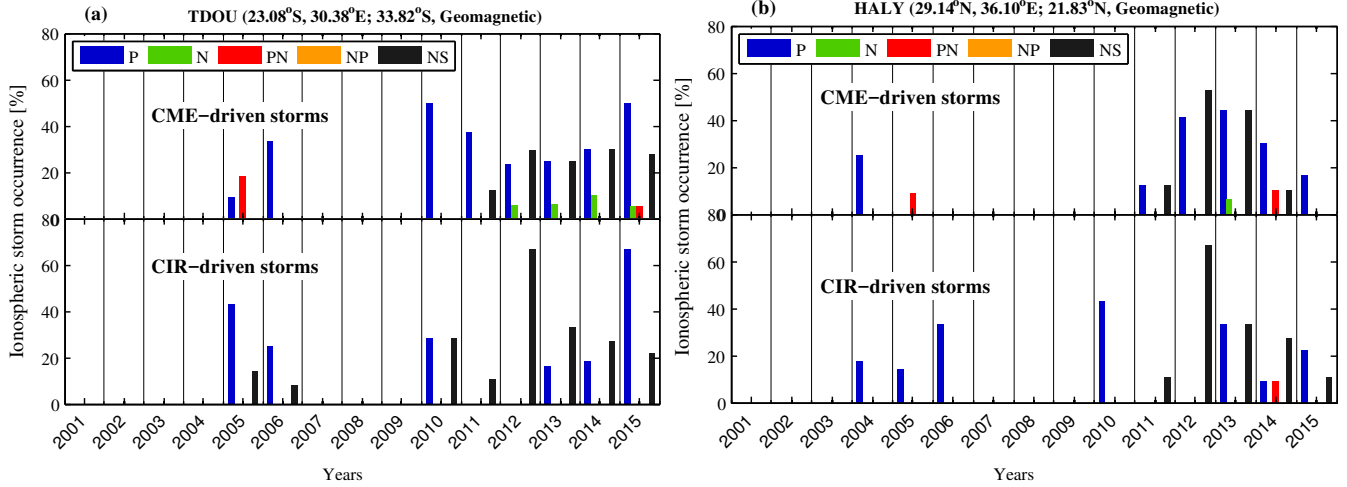
96

Figure 6.10: The seasonal distribution of positive (P), negative (N), positive-negative (PN), negative-positive (NP) and not-significant (NS) ionospheric storm effects occurrence over the (c) southern hemisphere, TDOU (23.08°S, 30.38°E; 33.92°S, geomagnetic), South Africa and (d) northern hemisphere, HALY (29.14°N, 36.10°E; 21.83°N, geomagnetic), Saudi Arabia.

mid-latitude station. Similarly, N and P ionospheric storm effects were only seen on June solstice (summer) and December (winter) during CME-driven storms over the northern hemisphere (HALY) mid-latitude station. These finding are consistent with previous results (e.g. Appleton and Piggott, 1952; Matsushita, 1959, 1963; Prölss, 1977, 1980; Titheridge and Buonsanto, 1988; Prölss, 1993b, 1995; Buonsanto, 1999; Mendillo, 2006; Vijaya Lekshmi et al., 2011; Matamba et al., 2015). However in this study, N ionospheric storm effects were only observed during CME-driven storms over the mid-latitude stations (TDOU and HALY).

Few PN ($\sim 4\%$) ionospheric storm effects were observed on December solstice (summer) over the southern hemisphere (TDOU) mid-latitude station during CME-driven storms. PN ($\sim 3\%$) ionospheric storm effects were equally distributed to March equinox and June solstice (Summer) at HALY station during CME-driven storms. Matsushita (1959) noted that the PN ionospheric storm effects were observed mostly at the mid-latitudes and occurred mainly in summer which could be due to changes in atmospheric constituents, particularly an increase in the number of oxygen molecules in the F2 region. At mid-latitudes, the P ionospheric storm effects are restricted to the early phase of a geomagnetic storm (Titheridge and Buonsanto, 1988).

Most NS ionospheric storm effects occurred during the equinoxes for both CME- and CIR-driven storms over both TDOU and HALY stations, which could be to the competing mechanisms arising from Equatorial Ionization Anomalies (EIA) with neutral composition changes (e.g. Yizengaw et al., 2005; Ngwira, 2011; Ngwira et al., 2012b; Katamzi and Habarulema, 2014b; Matamba et al., 2016). Zhao et al. (2009) studied the characteristics of TEC at the EIA in the Asian-Australian sector and found that the magnitude of the most developed EIA crest is larger at equinox than at solstice.

During CIR-driven storms, most P ionospheric storm effects were observed in equinoxes and June solstice (winter) over southern hemisphere station. On the other hand, over HALY, P ionospheric storm effects were mainly observed during equinox and June solstice (summer). P ionospheric storm

effects could also be due to enhancement of a low background electron density during geomagnetic storms (Mendillo et al., 2013). The PN (3%) ionospheric storm effects were observed in summer (June solstice) in the northern hemisphere (HALY) station during CIR-driven storms, this could also be attributed to the local time of geomagnetic storm onset time (Prölss, 1993b). The P and N ionospheric storm effects could be due to TADs and neutral composition changes respectively. The seasonal variation analyses at mid-latitudes, showed N and P ionospheric storm effects occurring during summer and winter respectively (e.g., Matsushita, 1959; Prölss, 1977, 1980; Titheridge and Buonsanto, 1988; Prölss, 1995; Fuller-Rowell et al., 1994, 1996; Vijaya Lekshmi et al., 2011) during CME-driven storms. This could be due to the prevailing summer to winter circulation, where the poleward winds restrain the equatorward propagation of the composition disturbance zone in the winter hemisphere which leads to a decrease of molecular gases (such as, N_2 and O_2) and produces positive ionospheric storm effects (Fuller-Rowell et al., 1996). However, the modified neutral-chemical distribution in the summer hemisphere leads to an increase of molecular gases which subsequently reduces the F-region electron density in the mid-latitude ionosphere and generates a negative ionospheric storm effect (Prölss, 1977, 1980, 1995; Buonsanto, 1999). These variations are believed to arise from the interaction between seasonal and storm induced winds which support each other in summer and in winter they are out of phase (Prölss, 1995). Furthermore, in winter, the equatorwards winds are weaker which reduces the possibility of composition disturbance zone to move equatorwards and highlighting the P ionospheric storm effects downwelling (Fuller-Rowell et al., 1994). As this is a statistical study that combined storms of different strengths over an extended period of time (2001-2015), it is not possible to isolate different physical mechanism(s) responsible for each class of ionospheric storm effect over individual locations during each storm period.

In order to understand the local time dependence, the main phase onset time has been used to define the start of geomagnetic storm (Prölss, 1993b). The beginning of the growth phase of the magnetospheric ring current which is indicated by a decrease of Dst index was used as a reference time. The Universal Time (UT) times were converted to Local Times (LT) for all stations by using the following expression:

$$\text{LT} = \text{UT} + \frac{\theta}{15°}, \tag{6.2}$$

where θ is the longitude of the station considered. The time occurrence of ionospheric storm effects were separated into three local times as morning (05:00 - 09:00 LT), daytime (09:00 - 18:00 LT) and nighttime (18:00 - 05:00 LT) (Adeniyi, 1986; Prölss, 1995).
The N ionospheric storm effects at mid-latitudes are usually observed following the geomagnetic storm which occurred during the preceding night. However, P ionospheric storm effects are generally associated with geomagnetic storms occurring in the local daytime (e.g. Appleton and Piggott, 1952; Matsushita, 1959; Prölss, 1993b, 1995; Mendillo, 2006). Figure 6.11 shows the local time dependence of ionospheric storm effects during CME and CIR-driven storms over the (a) southern (TDOU) and (b) northern (HALY) hemispheres mid-latitude stations.

Figure 6.11: Local time distribution of P, N, PN, NP and NS ionospheric storm effects over the (a) southern hemisphere, TDOU (23.08°S, 30.38°E; 33.92°S, geomagnetic), South Africa and (b) northern hemisphere, HALY (29.14°N, 36.10°E; 21.83°N, geomagnetic), Saudi Arabia during CME- and CIR-driven storms.

The P ionospheric storm effects were mainly observed following the geomagnetic storm main phase onset time that occurred in daytime (09:00 - 18:00 LT) and nighttime (18:00 - 05:00 LT) during both CME- and CIR-driven storms at TDOU and HALY. The daytime P ionospheric storm effects could be partly due to Traveling Atmospheric Disturbances (TADs), because during the night there is lack of ionization production preventing the formation of P ionospheric storm effects (Prölss, 1993b, 1995) and PPEF. The nighttime P ionospheric storm effects can be explained by Fuller-Rowell et al. (1994) suggestion that if a P ionospheric storm effect is generated by the wind before dusk, it will persist into the nightside.

The N ionospheric storms were mostly seen during the morning and nighttime main phase onset over both TDOU and HALY stations during CME-driven storms. This could be attributed to zonal transport of neutral composition changes by advection (the transfer of heat or matter by the flow of a fluid horizontally in the atmosphere) towards mid-latitude during the night and which subsequently rotate into the day sector (Prölss, 1993b, 1995).

6.2.2 Low latitudes ionospheric responses

The effects of CME- and CIR-driven storms on low latitude ionosphere have been studied using the southern hemisphere, Mbarara, MBAR (0.60°S, 30.74°E; 10.22°S, geomagnetic) and northern hemisphere, Sheba, SHEB (15.85°N, 39.05°E; 7.36°N, geomagnetic) stations. The ionospheric storm effects observed from the low latitude regions can be explained by electrodynamic effects (PPEF and DDEF) and mechanical effects (such as thermospheric composition changes and storm induced equatorward neutral wind effect) (Prölss, 1995; Buonsanto, 1999; Mendillo, 2006; Chakraborty et al., 2015).

Figure 6.12 shows the distribution of ionospheric storm effects over low-latitude stations, MBAR in the southern hemisphere and SHEB in the northern hemisphere. MBAR and SHEB stations are located within EIA latitude region.
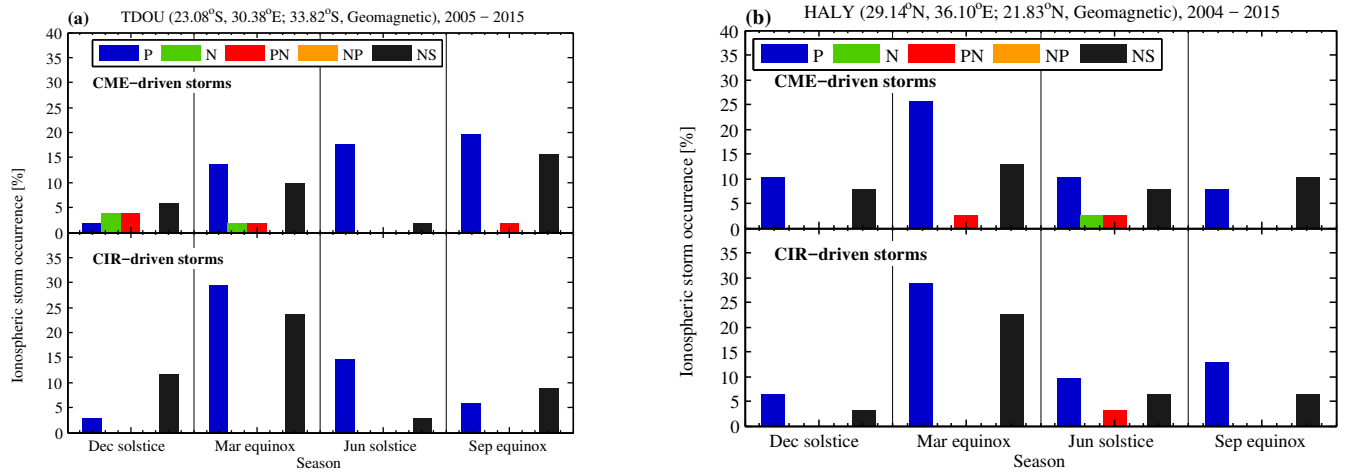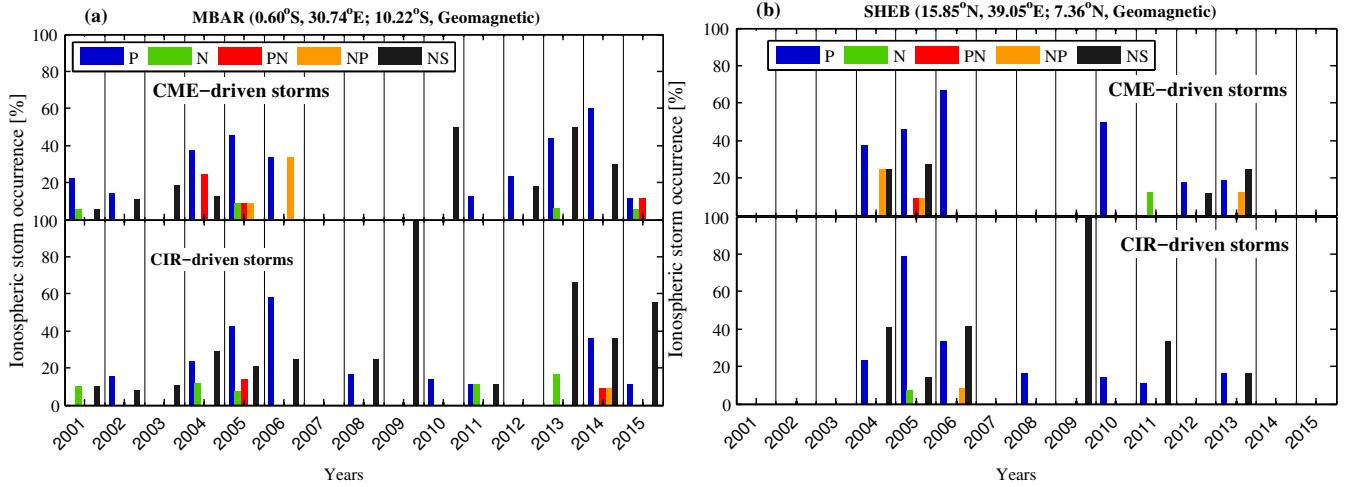
Figure 6.12: The annual distribution of positive (P), negative (N), positive-negative (PN), negative-positive (NP) and not-significant (NS) ionospheric storm effects occurrence over the (a) Southern hemisphere, MBAR (0.60°S, 30.74°E; 10.22°S, geomagnetic), Uganda and (b) Northern hemisphere, SHEB (15.85°N, 39.05°E; 7.36°N, geomagnetic), Eritrea.

Table 6.3: Low latitude ionospheric responses.

GNNS Location	Geom. Lat	Ionospheric storm effects (%)									
		CME-driven storms					CIR-driven storms				
		P	N	PN	NP	NS	P	N	PN	NP	NS
MBAR, Uganda	10.22°S	52.86	5.71	7.14	2.86	31.43	38.36	8.22	4.11	1.37	47.95
SHEB, Eritrea	7.36°N	48.57	2.86	2.86	14.29	31.43	53.33	2.22	0	2.22	42.22

Table 6.3 shows the statistical analysis of ionospheric storm effects over low latitude stations (MBAR and SHEB). Unlike the mid-latitude stations, NP ionospheric storm effects were observed during both CME- and CIR-driven storms. The NP ionospheric storm effects over the northern hemisphere station (SHEB) were more compared to the southern hemisphere station (MBAR). The N ionospheric storm effects usually accompany the positive ionospheric storm effects at low latitude F-region during geomagnetic storms (Matsushita, 1959; Adeniyi et al., 2014) and could be attributed to the strong fountain effect resulting from a large equatorwards winds (Kane, 1981; Huang et al., 1989; Gao et al., 2008; Adekoya and Adebesin, 2014). There are more NP ionospheric storm effects over SHEB probably because the disturbance electric field behave oppositely to background quiet day pattern. The disturbance electric fields result in the depression of EIA hump, acting as southward movement of northern equatorial hump. P or N ionospheric storms will be observed at south or north side of the hump (Blanc and Richmond, 1980; Gao et al., 2008).

P ionospheric storm effects were more prevalent over low latitude stations, which is in accordance with the previous studies (e.g., Adeniyi, 1986; Prölss, 1995; Adewale et al., 2011b; Vijaya Lekshmi et al., 2011). The P ionospheric storm effects can occur either due to the daytime eastward PPEFs or the mechanical effects of storm time equatorward neutral winds and surges alone. In the former case, taking the changes of the winds and PPEFs, the strength of the P ionospheric storm effects is centered at ±20° to ±30° magnetic latitudes (Kelley et al., 2003; Balan et al.,

2010; Vijaya Lekshmi et al., 2011). The P ionospheric storm effects are mostly attributed to changes in neutral composition (e.g. Prölss, 1995; Buonsanto, 1999; Crowley and Meier, 2008; Habarulema et al., 2013b). As explained by Prölss (1995), the high latitude heating which induce large scale thermospheric circulation results in transporting enhanced atomic oxygen density towards the low latitudes. Then this increased oxygen densities will affect both ionisation and diffusion, leading to positive ionospheric storm effect (Prölss, 1995; Liou et al., 2005; Mendillo, 2006; Bagiya et al., 2011). For example, the P ionospheric storm effects for 06 - 11 November 2004 and 16 - 20 March 2015 storm periods over the African low latitudes were due to changes in neutral composition (e.g Habarulema et al., 2013b; Astafyeva et al., 2015; Olwendo et al., 2017).

Figure 6.13: The seasonal distribution of positive (P), negative (N), positive-negative (PN), negative-positive (NP) and not-significant (NS) ionospheric storm effects occurrence over the (a) Southern hemisphere, MBAR (0.60°S, 30.74°E; 10.22°S, geomagnetic), Uganda and (b) Northern hemisphere, SHEB (15.85°N, 39.05°E; 7.36°N, geomagnetic), Eritrea.

Figures 6.13 (a) and (b) illustrate the seasonal variation of ionospheric storm effects over MBAR and SHEB. P ionospheric storm effects are prevalent in all seasons (e.g. Matsushita, 1959, 1963; Prölss, 1977; Adewale et al., 2011b) during both CME- and CIR- driven storms. Most P ionospheric storm were observed in June solstice and September equinox over the southern (MBAR) and northern (SHEB) hemispheres station during CME-driven storms. During CIR-driven storms most P ionospheric storm effects were observed in June solstice and March equinox over MBAR and SHEB stations respectively. The prominent P ionospheric storm effects during June solstice (winter) and equinoxes (March and September) could be due to downwelling of thermospheric gas (Fuller-Rowell et al., 1994), which is mainly caused by storm induced thermospheric winds and may cause the increase of ionisation at low latitudes without significant changes in O/N_2 (e.g. Fuller-Rowell et al., 1994; Danilov, 2001; Yizengaw et al., 2005).

N ionospheric storm effects were observed in December solstice (summer), March equinox, and June solstice during CME-driven storms while, during CIR-driven storms they were observed in all season over MBAR station. Over SHEB station, N ionospheric storm effects were observed in March equinox and December solstice during CME- and CIR-driven storms respectively. The negative ionospheric storm effects in summer could be due to the dynamic background thermospheric circulation and storm induced circulations reinforcing each other and their directed

equatorwards through the day (Yizengaw et al., 2005).

The NP ionospheric storm effects are equally distributed in September equinox and December solstice over MBAR, while for SHEB, they are mostly observed in June solstice. The N ionospheric storm effects could be attributed to neutral composition changes in summer hemisphere. The P ionospheric storm effects occurring during the recovery may be due to decreases in molecular mass caused by downwelling during storm (Fuller-Rowell et al., 1994). The PN ionospheric storm effects mainly occurred in December and June solstices respectively over MBAR and SHEB stations during CME-driven storms. Hence, PN ionospheric storm effects mainly occur in winter over low latitude stations.

During CIR-driven storms, the NS ionospheric storm effects were distributed throughout all seasons but most were observed in December solstice and March equinox over MBAR and SHEB stations.

Figure 6.14 illustrates the local time dependence of P (blue), N (green), PN (red), NP (yellow) and NS (black) ionospheric storm effects during CME- and CIR-driven storms over MBAR and SHEB stations. Most P ionospheric storm effects occurred at nighttime (18:00 - 05:00 LT) during CME- and CIR-driven storms over MBAR. During CME- and CIR-driven storms, $\sim 28\%$ and $\sim 25\%$ of P ionospheric storm effects occurred at nighttime respectively over MBAR. At SHEB, $\sim 34\%$ and $\sim 31\%$ P ionospheric storm effects were also observed at nighttime. A significant number of P ionospheric storm effects were also observed during the daytime over MBAR and SHEB during both CME- and CIR-driven storms. Few P ionospheric storm effects were observed in the morning times over both stations (MBAR and SHEB). The nighttime P ionospheric storm effects over MBAR and SHEB could be attributed to the plasmasphere that is compressed at nighttime due to convergence of equatorward disturbance winds from two sides of the equator and thus the electron density increases (Gao et al., 2008).

On the other hand, N ionospheric storm effects (6%) occurred mostly during CIR-driven storms in the nighttime over MBAR station. Also during CME- driven storms, N ionospheric storm effects seem to occur frequently during the nighttime and morning hours. PN ionospheric storm effects were more observed at morning and daytimes during CME-driven storm over MBAR and SHEB respectively. PN ionospheric storm effects have a tendency of occurring during the afternoon-evening main phase onsets of geomagnetic storm (Balan et al., 2010) which could be due to equatorward wind. Global-scale equatorward winds due to enhancement in particle and Joule heating, push ionospheric layers to greater heights and across pressure surfaces. Within this, fewer neutral composition molecular species are present and the ionosphere is slower to recombine and thus P ionospheric storm effects are observed (Prölss et al., 1991b; Fuller-Rowell et al., 1994). A significant number of NS ionospheric storm effects occurred at all times but mostly at nighttime over both stations during CME- and CIR-driven storms.

At low latitudes, geomagnetic storms with nighttime main phases in all seasons generally produce N ionospheric storm effects. The geomagnetic storms with daytime main phases in winter and equinox in general produce P ionospheric storm effects while in summer they produce PN ionospheric storm effects (Vijaya Lekshmi et al., 2011). The occurrence of P ionospheric storms in the morning and daytime local time are expected as the P ionospheric storms involve daytime production of ionization, which dominate over the chemical loss of ionization in the morning to noon local times (Balan et al., 2010; Vijaya Lekshmi et al., 2011).
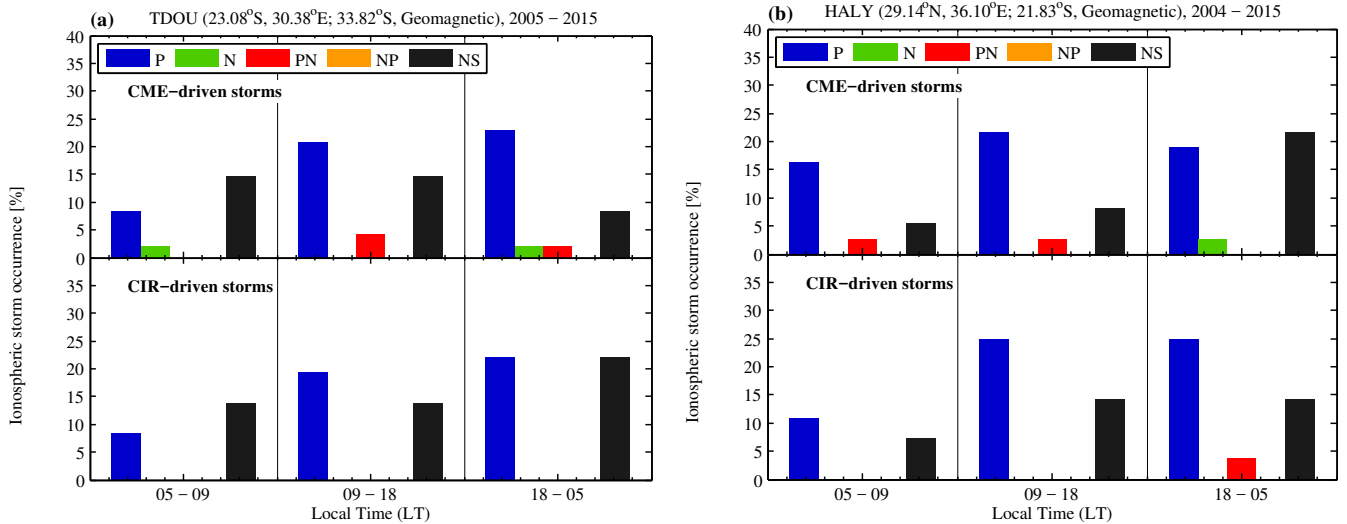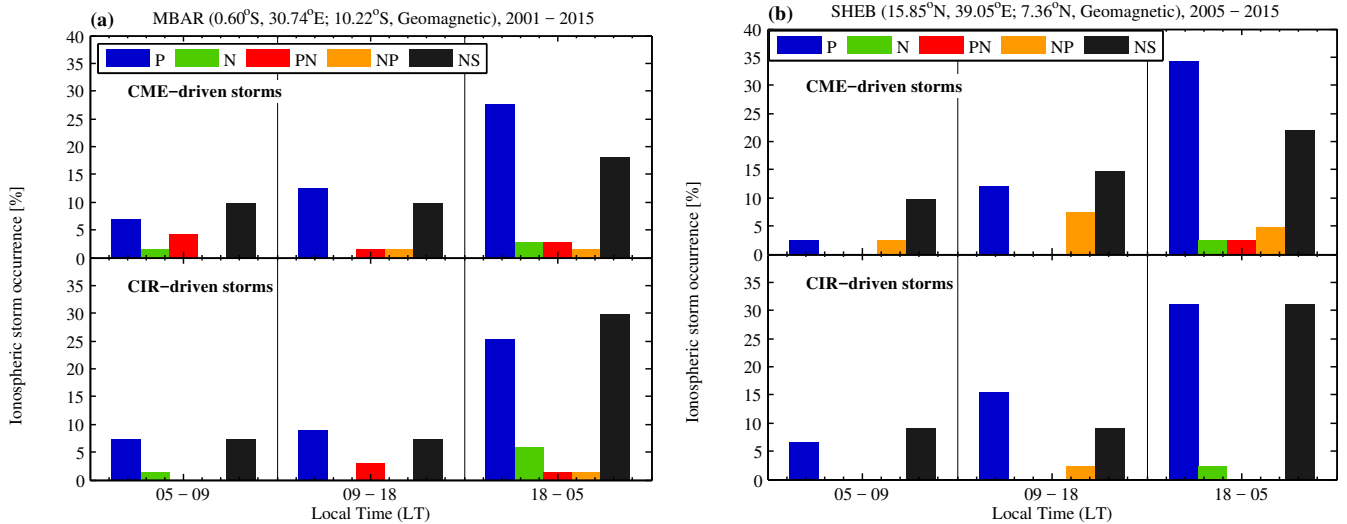
Figure 6.14: The local time distribution of P, N, PN, NP and NS ionospheric storm effects over the (a) southern hemisphere, MBAR (0.60°S, 30.74°E; 10.22°S, geomagnetic), Uganda and (b) northern hemisphere, Northern hemisphere, SHEB (15.85°N, 39.05°E; 7.36°N, geomagnetic), Eritrea during CME- and CIR-driven storms.

6.2.3 Equatorial latitude ionospheric responses

The features of the equatorial F2-region have been explained in terms of movement caused by $\mathbf{E} \times \mathbf{B}$ (Adeniyi, 1986; Buonsanto, 1999, and references therein). The $\mathbf{E} \times \mathbf{B}$ drift causes a force to act on ionization in the vertical direction. The direction of the electric field in the equatorial region is eastwards during the day-time and westwards at night (Balsley, 1973; Fejer et al., 1979b; Adeniyi, 1986). During the day-time, the $\mathbf{E} \times \mathbf{B}$ force is upwards. Ionisation diffuses along the magnetic field lines towards higher latitudes on both sides of the equator, thus causing a depletion of electron density around the equator. Collisional frequency decreases upwards, so that diffusion of electrons takes place more steadily as electrons drift to higher altitude (Kelley, 1989; Adeniyi, 1986). The $\mathbf{E} \times \mathbf{B}$ drifts are affected by PPEF of magnetospheric origin and long-lived DDEF from the disturbance neutral winds and storm-related changes in ionospheric conductivity (Fejer, 1997; Buonsanto, 1999).

Figure 6.15 shows the overall variation of ionospheric storm effects of ionospheric storm effects over the equatorial latitude station Nazret, NAZR (8.57°N, 39.29°E; 0.25°S, geomagnetic). NAZR has data starting from 2007 - 2015.
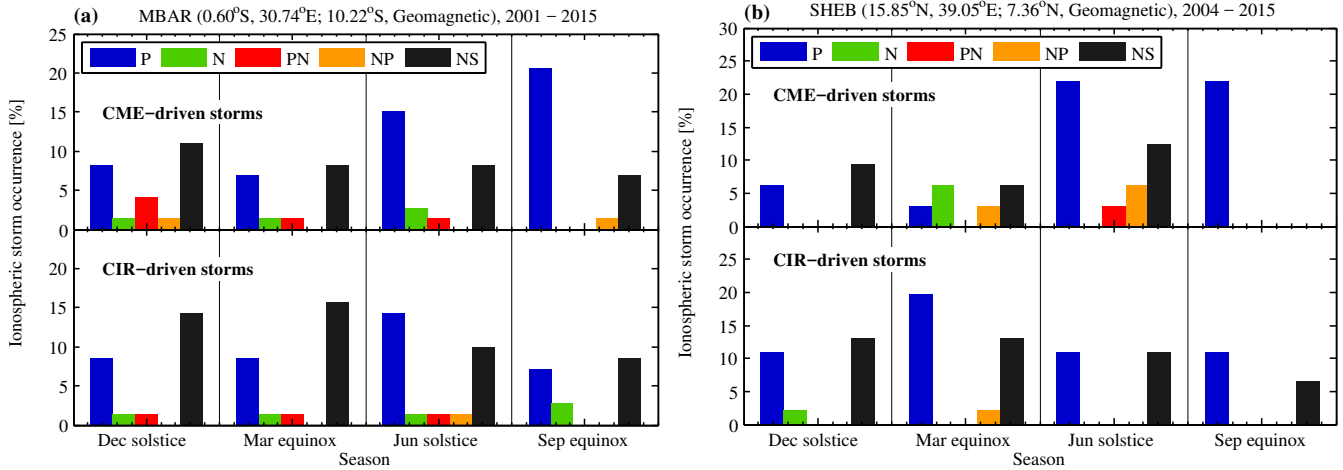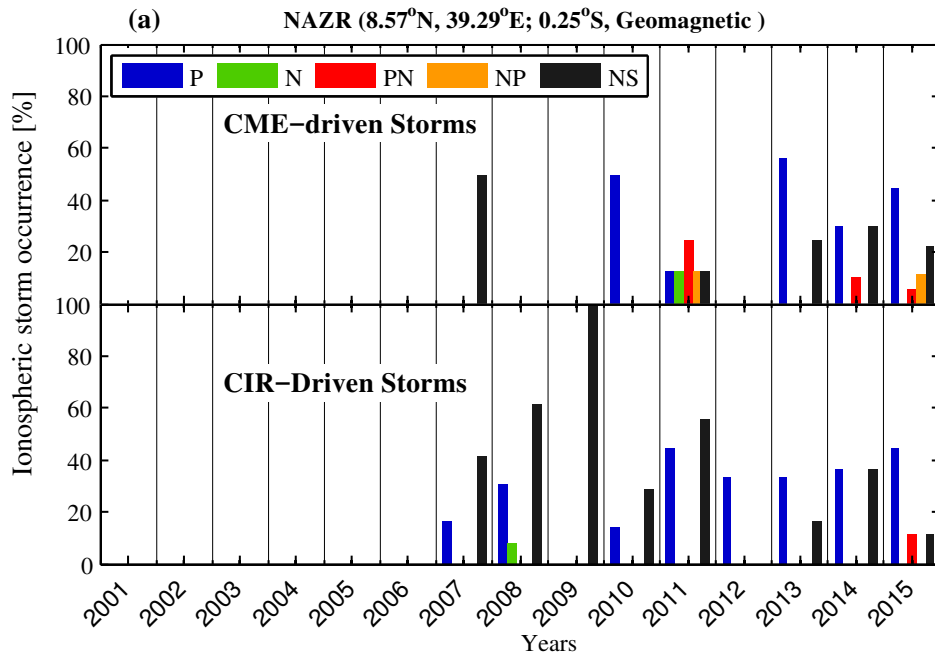
Figure 6.15: The annual distribution of positive (P), negative (N), positive-negative (PN), negative-positive (NP) and not-significant (NS) ionospheric storm occurrence over NAZR (8.57°N, 39.29°E; 0.25°S, geomagnetic).

Table 6.4: Equatorial latitude ionospheric responses.

GNNS Location	Geom. Lat	Ionospheric storm effects (%)									
		CME-driven storms					CIR-driven storms				
		P	N	PN	NP	NS	P	N	PN	NP	NS
NAZR, Ethiopia	0.25°S	51.16	2.38	12	9.5	30.23	43.14	2	2	0	52.92

Table 6.4 shows the statistics for the ionospheric storm effects over the equatorial station, NAZR. As expected, more P ionospheric storm effects were observed during CME-driven storms. During CIR-driven storms a significant number of NS ionospheric storm effects were observed. The NP ionospheric storm effects were also observed over the equatorial latitude. It is understood that the F-region in the equatorial latitude is highly influenced by electrodynamics even during quiet time periods (Buonsanto, 1999, and references therein). The zonal electric fields on the equatorial ionosphere control vertical plasma transport in the low-latitude ionosphere and drives the equatorial ionization anomalies and causes vertical drifts (Shume et al., 2009; Adeniyi et al., 2014). As reported extensively, dayside P ionospheric storm effects in equatorial regions are sometimes related to PPEF (Tsurutani et al., 2004; Mannucci et al., 2005; Huang et al., 2005a; Tsurutani et al., 2008a; Klimenko and Klimenko, 2012) and may depend on the strength of PPEF (Balan et al., 2010).
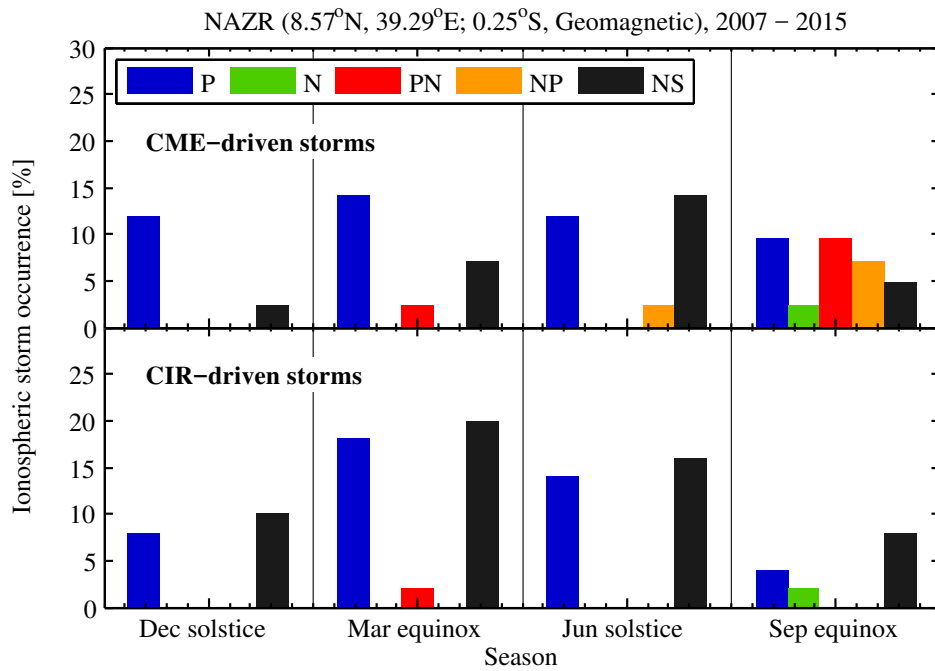
Figure 6.16: The seasonal variation of positive (P), negative (N), positive-negative (PN), negative-positive (NP) and not-significant (NS) ionospheric storm occurrence over NAZR (8.57°N, 39.29°E; 0.25°S, geomagnetic).

Figure 6.16 shows seasonal variation of ionospheric storm effects during CME- and CIR- driven storms over NAZR for the period 2007 - 2015. During CME-driven storms, a significant number of P ionospheric storm effects were distributed in all seasons with most observed in March equinox. N ionospheric storm effects were only observed in September equinox. In this study, over NAZR, PN and NP ionospheric storm effects mostly occurred during September equinox, which is in line with the findings by Adeniyi (1986) over the equatorial station, Ibadan (7.4°N, 3.9°E; 6°S, geom), Nigeria during a solar cycle period 1956-1966. During CIR-driven storms, NS and P ionospheric storm effects mainly occurred during March equinox. Few PN and N ionospheric storm effects were observed in March and September equinoxes respectively. Generally, the PN ionospheric storm effects are influenced by changes in fountain effects while N ionospheric storm effects could be due to disturbance dynamo electric fields (Fejer et al., 1983; Scherliess and Fejer, 1997). The ionospheric storm effects at equatorial and low latitudes are linked to magnetospheric inputs, such as PPEF, delayed effects, and composition changes (Mendillo, 2006). As stated before, it is not possible to pinpoint the physical mechanism responsible for the response in each storm period within the period of study analyzed. We however note that sometimes, there are a number of factors at play especially in low and equatorial latitude regions further complicating the full understanding of ionospheric storm effects causes.

Figure 6.17 shows the local time distribution of P (blue), N (green), PN (red), NP (yellow) and NS (black) ionospheric storm effects during CME- and CIR-driven storms over the equatorial station NAZR during the time interval 2007 - 2015. The morning time (05:00 - 09:00 LT), daytime (09:00 - 18:00 LT) as well as nighttime (18:00 - 05:00 LT) (Adeniyi, 1986; Prölss, 1995) were considered. P ionospheric storm effects were observed in the morning, daytime and nighttime during both CME- and CIR-driven storms over NAZR. The daytime P ionospheric storm effects could be due to electrodynamic effects of the equatorward winds which is explained by the daytime $\mathbf{E} \times \mathbf{B}$ drift (Balan et al., 2013) and PPEF (e.g. Basu et al., 2007; Tsurutani et al., 2004). N ionospheric storm

effects were observed at nighttime and daytime during CME- and CIR-driven storms respectively. PN ionospheric storm effects were observed at daytime during CIR- and CME-driven storms. Most NP ionospheric storm effects occurred following the daytime main phase onset time during CME-driven storms. The NS ionospheric storm effects mainly occurred at nighttime during CME- and CIR-driven storms respectively.
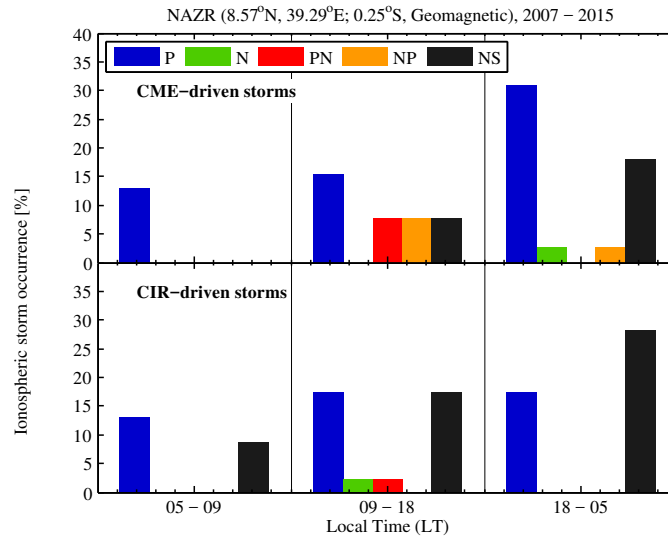
Figure 6.17: The ionospheric storm effects dependence on local time over NAZR (8.57°N, 39.29°E; 0.25°S, geomagnetic) during CME- and CIR-driven storms.

6.3 Summary

A statistical analysis of ionospheric storm effects due to CIR- and CME-driven storms were studied using GNSS TEC over the stations located within 30°E - 40°E geographic longitude in the southern and northern hemispheres (mid-, low and equatorial latitudes) in the African sector for the time interval 2001 - 2015. P ionospheric storm effects were more prevalent over mid-, low and equatorial latitude stations during both CME- and CIR-driven storms. Most P ionospheric storm effects were observed over the northern hemisphere station HALY during both CME- and CIR-driven storms. P ionospheric storm effects over mid-latitude stations occurred mostly during daytime following the main phase onset time. During disturbed conditions, there are a number of suggested mechanisms for P ionospheric storm effects including TIDs (e.g. Hines, 1960; Francis, 1974; Hunsucker, 1982; Hocke and Schlegel, 1996), expansion of the EIA towards mid-latitudes (e.g. Abdu, 1997; Abdu et al., 2008) and penetrating electric fields of magnetospheric origins (e.g. Fejer and Scherliess, 1995; Tsurutani et al., 2004, 2008a). In this study, the mechanisms for each storm period were not isolated because of the nature of the statistics considered. Over the southern (TDOU) and northern (HALY) hemisphere mid-latitude stations, N ionospheric storm effects were only observed during CME-driven storms and occurred mostly in summer. N ionospheric responses occurred following a morning and daytime main phase onset time of geomagnetic storm (Prölss, 1993b, 1995). N ionospheric storm effects are associated with neutral composition changes at the mid-latitudes (Prölss, 1980; Titheridge and Buonsanto, 1988; Prölss, 1995). N ionospheric storm effects were observed over the low latitude northern (SHEB) and southern (MBAR) hemisphere stations during both CME- and CIR-driven storms and they mainly occurred in March equinox and June solstice over SHEB and MBAR respectively for CME-driven storms. Over MBAR station, N ionospheric

storm effects also occur in December solstice and March equinox during CME-driven storms. During CIR-driven storms, N ionospheric storm effects occurred in all seasons in MBAR while at SHEB they only occur in December solstice. NP ionospheric storm effects were only observed over low and equatorial latitudes.

Chapter 7

Summary and future work

In this thesis, analyses of ionospheric storm effects due to four great geomagnetic storms (Dst ≤ -350 nT) of solar cycle 23 were examined. Global Navigation Satellite System (GNSS), Total Electron Content (TEC) and ionosonde critical frequency of F2 layer (foF2) data over southern (African sector) and northern hemispheres (European sector) mid-latitudes were used to study the ionospheric responses within 15°E - 40°E longitude and $\pm 31°$ - $\pm 46°$ geomagnetic latitude. This was done in order to simultaneously investigate the associated physical mechanisms of ionospheric responses in both hemispheres. Several authors have already investigated ionospheric response to great geomagnetic storms of solar cycle 23 (e.g. Mannucci et al., 2005, 2008, 2009; Tsurutani et al., 2004, 2005, 2007, 2008a; Basu et al., 2005; Lin et al., 2005; Sreehari and Nayar, 2006; Huang et al., 2007; Fejer et al., 2007; Zhao et al., 2008; Kelley et al., 2010; Habarulema et al., 2013b; Astafyeva et al., 2014). As an example, Basu et al. (2005) investigated the formation of ionospheric plasma density structures at middle and equatorial latitudes during the intense magnetic storms of March 30 - 31, 2001 and October 29 - 31, 2003. The solar flare of 28 October 2003 created intense day-side TEC increase never seen before (Tsurutani et al., 2005). The solar flare intensity was the highest EUV flare in recorded history. There was an enormous uplift of the ionosphere above CHAMP satellite ($\sim$ 400 km) due to the 30 October 2003 geomagnetic storm (Mannucci et al., 2005). The TEC increases at mid-latitude was $\sim 900\%$ (Mannucci et al., 2005). Tsurutani et al. (2007) showed oxygen ion uplift to over 850 km during 30 October 2003. The ion densities were higher than the neutral densities. They also derived the electric field to be 4 mV/m for the 30 October 2003 storm. The SAMI 2 model was used to show a match between the Tsurutani et al. (2005) CHAMP observational results and theory. Mannucci et al. (2008) analyzed the dayside ionospheric response to four great geomagnetic storms namely, 29 -30 October 2003, 20 November 2003 and 7 November 2004 over the low latitude ionosphere by superimposed epoch analysis. They reported the 20 November 2003 storm was unusual in that the TEC appeared $\sim$5 to 7 hours after the interplanetary Bz event. The penetration of electric field to the ionosphere was delayed an additional 6 hours while the other three followed quantitative expectations that significant TEC increase follow soon after significant Interplanetary Electric Field (IEF) (Mannucci et al., 2008). Fejer et al. (2007) studied equatorial ionospheric electric fields during the November 2004 magnetic storm. They observed the PPEF of about 3 mV/m over Jicamarca during the November 9, 2004 storm main phase, when large equatorial electrojet current and drift perturbations were also present in the pacific and Brazilian equatorial regions. Results reported in this thesis (Chapter 5) are different from the study of Mannucci et al. (2008) and the currently existing investigations about these storms in a sense that it focuses on mid-latitude changes in both southern (Africa) and northern (Europe) hemispheres, although

it also investigates possible contributions of low latitude changes to mid-latitude ionospheric responses. It was found that in all four great geomagnetic storm periods of solar cycle 23, Positive (P) and Negative (N) ionospheric storm effects either occur during the main or recovery phases in both hemispheres. Apart from the equinox 29 March - 02 April 2001 storm, the other three storm periods (27 - 31 October 2003, 18 - 23 November 2003 and 06 - 11 November 2004) occurred during winter and summer over northern and southern hemisphere mid-latitudes respectively. Seasonal effects were therefore predominant in determining the observed ionospheric storm effects in both hemispheres. On 31 March 2001 both decrease and increase in TEC were observed simultaneously between ~06:00 UT - 12:00 UT over both hemispheres. The decrease was observed at latitude from about 47°N - 50°N and 33°S - 38°S and increase was observed in other latitudes. Negative ionospheric effects were largely associated with neutral composition changes (Prölss, 1980; Titheridge and Buonsanto, 1988; Prölss, 1995) while P ionospheric storm effects were linked to low latitude changes related to the expansion of Equatorial Ionization Anomaly (EIA) (e.g. Abdu, 1997; Abdu et al., 2008; Katamzi and Habarulema, 2014a; Matamba et al., 2016).

For the 27 - 31 October 2003 storm period, P and N ionospheric storm effects were observed. On 29 October 2003, an increase in TEC was observed within ~2-3 hours after the sudden storm commencement over both hemispheres and the TEC increase that occurs almost simultaneously is due to Prompt Penetration Electric Field (PPEF) (Tsurutani et al., 2004, 2008a). The increase in TEC on 29 October 2003 was also attributed to expansion of EIA (e.g. Abdu, 1997; Lin et al., 2005). Large Scale Traveling Ionospheric Disturbances (LSTIDs) are also believed to have contributed to the increased electron density and hence TEC on 29 October 2003 (Borries et al., 2009; Katamzi and Habarulema, 2014a). Negative ionospheric storm effects on 30 - 31 October 2003 were mainly due to neutral composition changes. In addition, on 28 October 2003, an increase in TEC was due to large solar flare with previously determined intensity of X45±5 (Tsurutani et al., 2008a; Thomson et al., 2004).

For the 18 - 23 November 2003 storm period, P and N ionospheric storm effects were observed. On 20 November 2003, P ionospheric storm effects were observed over both hemispheres and it was attributed to PPEF, LSTIDs (Tsurutani et al., 2008a; Borries et al., 2009). P and N ionospheric storm effects were observed on 21 November 2003 over northern (winter) and southern (summer) hemisphere respectively indicating seasonal dependence of ionospheric storm (Prölss, 1977; Fuller-Rowell et al., 1996). P and N ionospheric storm effects were due to LSTIDs and neutral composition changes (Prölss, 1980, 1995).

For the storm period of 06 - 11 November 2004, N ionospheric storm effects were observed on 08 and 10 November 2004 over southern hemisphere and on 08 November 2004 over northern hemisphere. Negative ionospheric storm effects were attributed to neutral composition changes (Habarulema et al., 2013b) over both hemispheres. An increase in TEC was observed on 09 November 2004 over both hemispheres and it was partly due to LSTIDs and neutral composition changes (Sahai et al., 2009; Habarulema et al., 2013b). The most interesting result during this storm period is that the LSTIDs were observed on 10 November 2004 during N ionospheric storm effect over the southern hemisphere.

Furthermore, the statistical analyses of ionospheric storm effects due to Coronal Mass Ejections (CMEs)- and/or Corotating Interaction Regions (CIRs)-driven storms throughout the declining

phase of solar cycle 23 and the ascending, maximum and declining phases of solar cycle 24 over southern and northern hemispheres African mid, low and equatorial latitudes were studied (Matamba and Habarulema, 2017). Stations located within 30°E to 40°E geographic longitude over the southern and northern hemispheres in the African sector were considered. The overall statistics, seasonal and local time variation of ionospheric responses over mid, low and equatorial latitudes were studied. Previously, case studies of ionospheric storm effects over the African sector have been done during either CME- or CIR- driven storms (e.g., Prölss, 1980; Yizengaw et al., 2011; Amabayo et al., 2012; Katamzi and Habarulema, 2014a; Olwendo et al., 2017). Statistical analyses of ionospheric storm effects due to geomagnetic storms over mid- and low latitude in the African sector have been done separately in different latitude regions (e.g. Adeniyi, 1986; Adewale et al., 2011a; Adeniyi et al., 2014; Burešová et al., 2014; Matamba et al., 2015). In this thesis, a simultaneous analysis was performed over the African mid-, low and equatorial latitude regions, taking advantage of the existing long-term GNSS data from 2001 - 2015.

At mid-latitudes, $\sim 44\%$ and $\sim 60\%$ of P ionospheric storm effects were mainly observed during CME- and CIR-driven storms respectively. During disturbed conditions, there are a number of suggested mechanisms for P ionospheric storm effects including LSTIDs (e.g. Hines, 1960; Francis, 1974; Hunsucker, 1982; Hocke and Schlegel, 1996), expansion of the EIA towards mid-latitudes (e.g. Abdu, 1997; Abdu et al., 2008) and penetrating electric fields of magnetospheric origins (e.g. Fejer and Scherliess, 1995; Tsurutani et al., 2004, 2008a), although we are unable to isolate the mechanisms for each storm period due to the statistical nature of our study.

In mid-latitude, N ($\sim 5\%$) ionospheric storm effects were only observed during CME-driven storms over Thohoyandou, TDOU (23.08°S, 30.38°E; 33.92°S, geomagnetic), South Africa, in the southern hemisphere; and Halat Ammar, HALY (29.14°N, 36.10°E; 21.83°N, geomagnetic), Saudi Arabia, in the northern hemisphere stations following the nighttime and morning times onset of geomagnetic storms and mostly occurred in summer. N ionospheric storm effects are associated with neutral composition changes in the mid-latitudes (Prölss, 1977, 1980, 1995; Fuller-Rowell et al., 1996). The seasonal variations result from the interaction between seasonal and storm-induced winds. In winter, they are out of phase while in summer they support each other thus leading to observed seasonal changes of ionospheric storm effects (e.g. Prölss, 1995; Fuller-Rowell et al., 1996). During summer even moderate conditions may lead to N ionospheric storm effects over mid-latitude. During the nighttime, the background circulation is equatorward, which interacts with the storm induced circulation and the composition disturbance zone will move towards the lower latitudes and produce N ionospheric storm effects (Prölss, 1995; Fuller-Rowell et al., 1996).

PN ionospheric storm effects ($\sim 5\%$ and $\sim 2\%$) were observed during CME- and CIR-driven storms respectively over mid-latitude stations. PN ionospheric storm effects were mostly observed in summer and equinox season during CME-driven storms and during CIR-driven storms they mainly occurred in summer over HALY. The PN ionospheric storm effects could be due to local time dependence of ionospheric storm (Prölss, 1993b, 1995; Mendillo, 2006). P ionospheric storm effect will occur during the daytime initial phase and when the storm main phase occurs during the nighttime, delayed N ionospheric storm effect will be observed (Prölss, 1993b, 1995). Matsushita (1959) noted that PN ionospheric storm effects also have tendency of occurring over the mid-latitude regions. PN ionospheric storm effects can be explained by local time variation (Prölss, 1993b, 1995) where the delayed N ionospheric storm effect is observed the next morning after the

storm. This observation is in agreement with previous studies (e.g. Matsushita, 1959; Mendillo, 2006; Vijaya Lekshmi et al., 2011).

A significant number ($\sim 46\%$ and $\sim 38\%$) of NS ionospheric storm effects were observed during CME- and CIR-driven storms respectively. The NS ionospheric storm effects were observed in all seasons and at all local times considered in this study.

At low and equatorial latitudes, number of P ionospheric storm effects ($\sim 51\%$ and 46%) and ($\sim 51\%$ and 43%) were mainly observed during CME- and CIR-driven storms respectively. The low and equatorial latitudes are found to observe more P ionospheric storm effects during geomagnetic storms in all seasons (e.g. Prölss, 1977; Adeniyi, 1986). The equatorial $\mathbf{E} \times \mathbf{B}$ drifts drive the equatorial fountain effect, which dominates the electron density structure of the entire low latitudes (Buonsanto, 1999). These $\mathbf{E} \times \mathbf{B}$ drifts are influenced by PPEF and Disturbance Dynamo Electric Field (DDEF) from disturbance neutral winds and storm related changes in electric conductivity (Fejer, 1997; Buonsanto, 1999). The major physical mechanisms used to explain P ionospheric storm effects over the low and equatorial latitudes are storm time equatorward neutral winds and the daytime eastward PPEF (Tsurutani et al., 2004; Kikuchi et al., 2008; Balan et al., 2010, 2013; Adeniyi et al., 2014). The P ionospheric storm effects over low latitude are also suggested to be due to neutral composition changes (Titheridge and Buonsanto, 1988; Rishbeth, 1991; Prölss, 1995; Nayak et al., 2016). Over the African sector low and equatorial latitudes, increased TEC during some storm periods such as 09 November 2004 (Habarulema et al., 2013b), 17 March 2015 (Nayak et al., 2016; Nava et al., 2016; Olwendo et al., 2017) have been found to be due to increase in O/N2 ratio. Several other studies in other regions have made similar conclusions (Sahai et al., 2009; Nava et al., 2016; Nayak et al., 2016).

Over low and equatorial latitudes, few N ionospheric storm effects were observed during both CME- and CIR-driven storms. At low latitudes most N ionospheric storm effects (5%) were observed during CIR-driven storm while during CME-driven storms, only 4% were observed. Over the equatorial latitude most N ionospheric storm effects (4%) were observed during CME-driven storms and 2% occurred during CIR driven storms.

NP ionospheric storm effects were observed mostly over equatorial and low latitude stations during CME-driven storms and also during CIR-driven storm at low latitude. Matsushita (1959) noted the NP ionospheric storms having tendency of occurring most in low and equatorial latitudes with no seasonal effects.

A significant number of NS ionospheric storm effects ($\sim 45\%$ and $\sim 53\%$) were observed during CIR-driven storms over low and equatorial latitude respectively. For CME-driven storms, $\sim 31\%$ and $\sim 30\%$ of NS were observed over low and equatorial latitudes respectively. In this study, the mechanisms were not isolated due to the nature of the statistics considered.

7.1 Future work

The statistical studies focused on ionospheric storm effects caused by CIR- and/or CME- driven storms. The storm periods were categorized based on Dst≤ -30 nT and Kp ≥ 3 which limit some weak geomagnetic storms of Dst ≤ -25 nT (Tsurutani et al., 1995a, 2006a). For future work the following is recommended:

- The responses of the ionosphere during the main and recovery phases of the geomagnetic storm should be statistical analysed separately.

111

- The single, double and triple peak geomagnetic storms should be grouped and studied separately in order to study their drivers. For example Mannucci et al. (2008) studied ionospheric response to four intense geomagnetic storms, of the 2001 - 2005 period near solar maximum and declining phase of solar cycle 23 by superposed epoch analysis. They used common time of epoch when the interplanetary electric field first reaches 10mV/v. They superposed the single peak Dst index to study the PPEF.

- The responses of high latitudes regions must be statistically studied and compared with the mid, low, and equatorial latitude stations.

- The driving mechanisms of the ionospheric storm effects due to CIR- and CME-driven storms need to be studied and compared during high and low solar activities.

- The ionospheric storm effects should also be analyzed during events as High-Intensity Long-Duration Continuous AE Activity (HILDCAAs) (Tsurutani and Gonzalez, 1987) during the recovery phase of CIR-driven storms in details.

- The correlation of the P ionospheric storm effects and scintillation processes should be investigated. At equatorial and low latitude regions scintillation are associated with to the occurrence of equatorial irregularities or plasma bubbles. At mid-latitudes it would be possible to analyze Very High Frequency (VHF) scintillations possibly associated to plasma irregularities or the occurrence of MSTIDs, coming from middle latitudes. For this study it would be possible to compare to Digisonde data.

- Investigation of the relationship between particles precipitation and the ionospheric storms in mid latitudes.

This study was restricted to ionospheric storms over one longitudinal sector. This is because Europe has a dense GNSS receiver network that can be used to map the ionosphere (Borries et al., 2009). However, the African GNSS network is dense in the southern, eastern and western regions and is sparse in the northern and central regions (Isioye et al., 2015). In order to comprehensively study the ionospheric storms over different longitudes within the African sector, more GNSS receivers and other instrumentation such as ionosondes are needed. Chartier et al. (2014) studied ionospheric imaging in Africa and concluded that African ionospheric images can be made significantly more accurate if additional receivers are used.

Aviation, communication and navigation rely on radio frequency transmission that can be impacted by strong ionospheric perturbations (e.g. Kamide and Chian, 2007; Arbesser-Rastburg and Jakowski, 2007; Moldwin, 2008). Monitoring and forecasting of space weather associated ionospheric disturbances are essential for the mitigation of space weather impacts (Arbesser-Rastburg and Jakowski, 2007; Moldwin, 2008; Borries et al., 2009).

Statistical analyses of storm-time ionospheric response may assist in creating long-term databases that will be used in developing regional space weather models for accurate specification of ionospheric variability during CME and CIR driven storms.

References

Aarons, J. (2012), *Solar System Radio Astronomy: Lectures presented at the NATO Advanced Study Institute of the National Observatory of Athens: Cape Sounion August 2–15, 1964*, Springer Science & Business Media.

Abdu, M. A. (1997), 'Major phenomena of the equatorial ionosphere-thermosphere system under disturbed conditions', *Journal of Atmospheric and Solar-Terrestrial Physics* **59**(13), 1505–1519.

Abdu, M., De Paula, E., Batista, I., Reinisch, B., Matsuoka, M., Camargo, P., Veliz, O., Denardini, C., Sobral, J., Kherani, E. et al. (2008), 'Abnormal evening vertical plasma drift and effects on ESF and EIA over Brazil-South Atlantic sector during the 30 October 2003 superstorm', *Journal of Geophysical Research* **113**(A7).

Adekoya, B. and Adebesin, B. (2014), 'Hemispheric, seasonal and latitudinal dependence of storm-time ionosphere during low solar activity period', *Advances in Space Research* **54**(11), 2184–2193.

Adeniyi, J. (1986), 'Magnetic storm effects on the morphology of the equatorial F2-layer', *Journal of atmospheric and terrestrial physics* **48**(8), 695–702.

Adeniyi, J., Doherty, P., Oladipo, O. and Bolaji, O. (2014), 'Magnetic storm effects on the variation of TEC over Ilorin an equatorial station', *Radio Science* **49**(12), 1245–1253.

Adewale, A. O., Oyeyemi, E. O., Adeloye, A. B., Ngwira, C. M. and Athieno, R. (2011*a*), 'Responses of equatorial F region to different geomagnetic storms observed by GPS in the African sector', *Journal of Geophysical Research* **116**(A12), A12319.

Adewale, A. O., Oyeyemi, E. O., Adeloye, A. B., Ngwira, C. M. and Athieno, R. (2011*b*), 'Responses of equatorial F region to different geomagnetic storms observed by GPS in the African sector', *Journal of Geophysical Research* **116**(A12), A12319.

Afraimovich, E. L., Kosogorov, E. A., Leonovich, L. A., Perevalova, N. P. and Pirog, O. M. (2000), 'Observation of large-scale traveling ionospheric disturbances of auroral origin by global GPS networks', *Earth, planets and space* **52**(10), 669–674.

Akasofu, S.-I. (2007), *Exploring the Secrets of the Aurora*, Astrophysics and Space Science Library, 2nd edn, Springer.

Alves, M. V.& Echer, E. . G. W. D. (2006), 'Geoeffectiveness of corotating interaction regions as measured by Dst index', *Journal of Geophysical Research* **111**, A07S05.

Amabayo, E. B., McKinnell, L. A. and Cilliers, P. J. (2012), 'Ionospheric response over South Africa to the geomagnetic storm of 11–13 April 2001', *Journal of Atmospheric and Solar-Terrestrial Physics* **84–85**, 62–74.

Amabayo, E. B. and Pierre, J. C. (2013), 'Multi-station observation of ionospheric irregularities over South Africa during strong geomagnetic storms', *Advances in Space Research* **51**(5), 754–771.

Anderson, D., Anghel, A., Chau, J. and Veliz, O. (2004), 'Daytime vertical E X B drift velocities inferred from ground-based magnetometer observations at low latitudes', *Space Weather* **2**(11).

Anderson, D., Anghel, A., Yumoto, K., Ishitsuka, M. and Kudeki, E. (2002), 'Estimating daytime vertical E×B drift velocities in the equatorial F-region using ground-based magnetometer observations', *Geophysical Research Letters* **29**(12).

Andrioli, V. F., Echer, E., Savian, J. F. and Schuch, N. J. (2007), 'Positive and negative sudden impulses caused by fast forward and reverse interplanetary shocks', *Revista Brasileira de Geofísica* **25**, 175–179.

Appleton, E. and Piggott, W. (1952), 'The morphology of storms in the F2 layer of the ionosphere I. Some statistical relationships', *Journal of Atmospheric and Terrestrial Physics* **2**(4), 236–252.

Appleton, E. V. (1946), 'Two anomalies in the ionosphere', *Nature* **157**(3995), 691–691.

Appleton, E. V. and Barnett, M. (1926), 'On wireless interference phenomena between ground waves and waves deviated by the upper atmosphere', *Proceedings of the Royal Society of London. Series A, Containing Papers of a Mathematical and Physical Character* **113**(764), 450–458.

Arbesser-Rastburg, B. and Jakowski, N. (2007), *Effects on satellite navigation*, Springer Berlin Heidelberg, Berlin, Heidelberg, pp. 383–402.

Astafyeva, E., Yasyukevich, Y., Maksikov, A. and Zhivetiev, I. (2014), 'Geomagnetic storms, superstorms, and their impacts on GPS-based navigation systems', *Space Weather* **12**(7), 508–525.

Astafyeva, E., Zakharenkova, I. and Förster, M. (2015), 'Ionospheric response to the 2015 St. Patrick's Day storm: A global multi-instrumental overview', *Journal of Geophysical Research* **120**(10), 9023–9037.

Bagiya, M. S., Iyer, K., Joshi, H., Thampi, S. V., Tsugawa, T., Ravindran, S., Sridharan, R. and Pathan, B. (2011), 'Low-latitude ionospheric-thermospheric response to storm time electrodynamical coupling between high and low latitudes', *Journal of Geophysical Research* **116**(A1).

Baker, D., Daly, E., Daglis, I., Kappenman, J. G. and Panasyuk, M. (2004), 'Effects of space weather on technology infrastructure', *Space Weather* **2**(2).

Balan, N., Otsuka, Y., Nishioka, M., Liu, J. and Bailey, G. (2013), 'Physical mechanisms of the ionospheric storms at equatorial and higher latitudes during the recovery phase of geomagnetic storms', *Journal of Geophysical Research* **118**(5), 2660–2669.

Balan, N., Shiokawa, K., Otsuka, Y., Kikuchi, T., Vijaya Lekshmi, D., Kawamura, S., Yamamoto, M. and Bailey, G. J. (2010), 'A physical mechanism of positive ionospheric storms at low latitudes and midlatitudes', *Journal of Geophysical Research* **115**(A2), A02304.

Balogh, A., Gosling, J., Jokipii, J., Kallenbach, R. and Kunow, H. (2013), *Corotating Interaction Regions: Proceedings of an ISSI Workshop 6–13 June 1998, Bern, Switzerland*, Vol. 7, Springer Science & Business Media.

Balsley, B. (1973), 'Electric fields in the equatorial ionosphere: A review of techniques and measurements', *Journal of Atmospheric and Terrestrial Physics* **35**(6), 1035–1044.

Bartels, J., Heck, N. H. and Johnston, H. F. (1939), 'The three-hour-range index measuring geomagnetic activity', *Journal of Geophysical Research* **44**(4), 411–454.

Basu, S., Basu, S., Groves, K. M., MacKenzie, E., Keskinen, M. and Rich, F. (2005), 'Near-simultaneous plasma structuring in the midlatitude and equatorial ionosphere during magnetic superstorms', *Geophysical Research Letters* **32**(12).

Basu, S., Basu, S., Rich, F., Groves, K., MacKenzie, E., Coker, C., Sahai, Y., Fagundes, P. and Becker-Guedes, F. (2007), 'Response of the equatorial ionosphere at dusk to penetration electric fields during intense magnetic storms', *Journal of Geophysical Research* **112**(A8).

Basu, S., Basu, S., Valladares, C., Yeh, H.-C., Su, S.-Y., MacKenzie, E., Sultan, P., Aarons, J., Rich, F., Doherty, P. et al. (2001), 'Ionospheric effects of major magnetic storms during the International Space Weather Period of September and October 1999: GPS observations, VHF/UHF scintillations, and in situ density structures at middle and equatorial latitudes', *Journal of Geophysical Research* **106**(A12), 30389–30413.

Batista, I. S., Paula, E. d., Abdu, M., Trivedi, N. and Greenspan, M. (1991), 'Ionospheric effects of the March 13, 1989, magnetic storm at low and equatorial latitudes', *Journal of Geophysical Research* **96**(A8), 13943–13952.

Bauske, R. and Prölss, G. (1997), 'Modeling the ionospheric response to traveling atmospheric disturbances', *Journal of Geophysical Research* **102**(A7), 14555–14562.

Benacquista, R., Rochel, S. and Rolland, G. (2017), 'Understanding the variability of magnetic storms caused by ICMEs', **35**(1), 147.

Benkova, N. and Zevakina, R. (1970), 'Ionospheric disturbances (Planetary distribution of F region disturbances and related vertical electron concentration using satellite and ground data)'.

Bilitza, D., Altadill, D., Zhang, Y., Mertens, C., Truhlik, V., Richards, P., McKinnell, L.-A. and Reinisch, B. (2014), 'The International Reference Ionosphere 2012–a model of international collaboration', *Journal of Space Weather and Space Climate* **4**, A07.

Bilitza, D., McKinnell, L.-A., Reinisch, B. and Fuller-Rowell, T. (2011), 'The international reference ionosphere today and in the future', *Journal of Geodesy* **85**(12), 909–920.

Biswas, S. (2000), *Cosmic Perspectives in Space Physics*, Astrophysics and Space Science Library 242, 1 edn, Springer Netherlands.

Blanc, M. and Richmond, A. (1980), 'The ionospheric disturbance dynamo', *Journal of Geophysical Research* **85**(A4), 1669–1686.

Blanch, E., Altadill, D., Boška, J., Burešová, D. and Hernández-Pajares, M. (2005), November 2003 event: effects on the Earth's ionosphere observed from ground-based ionosonde and GPS data, *in* ' Annales Geophysicae', Vol. 23, Copernicus GmbH, pp. 3027–3034.

Bond, P. (2012), *Exploring the solar system*, John Wiley & Sons.

Borovsky, J. E. and Denton, M. H. (2006), 'Differences between CME-driven storms and CIR-driven storms', *Journal of Geophysical Research* **111**(A7), A07S08.

Borries, C., Berdermann, J., Jakowski, N. and Wilken, V. (2015), 'Ionospheric storms—A challenge for empirical forecast of the total electron content', *Journal of Geophysical Research* **120**(4), 3175–3186.

Borries, C., Jakowski, N. and Wilken, V. (2009), Storm induced large scale TIDs observed in GPS derived TEC, *in* 'Annales geophysicae', Vol. 27, Copernicus GmbH, pp. 1605–1612.

Boteler, D. (1994), 'Geomagnetically induced currents: present knowledge and future research', *IEEE Transactions on Power Delivery* **9**(1), 50–58.

Brekke, A. (1997), *Physics of the upper polar atmosphere*, John Wiley and Sons, Chichester.

Bruinsma, S. L. and Forbes, J. M. (2009), 'Properties of Traveling Atmospheric Disturbances (TADs) inferred from CHAMP accelerometer observations', *Advances in Space Research* **43**(3), 369–376.

Bruno, Zolesi & Ljiljana, R. C. (2014), *Ionospheric Prediction and Forecasting*, Springer.

Buonsanto, M. (1999), 'Ionospheric storms — a review', *Space Science Reviews* **88**(3-4), 563–601.

Buonsanto, M., Foster, J., Galasso, A., Sipler, D. and Holt, J. (1990), 'Neutral winds and thermosphere/ionosphere coupling and energetics during the geomagnetic disturbances of March 6–10, 1989', *Journal of Geophysical Research* **95**(A12), 21033–21050.

Burešová, D. and Laštovička, J. (2007), 'Pre-storm enhancements of foF2 above Europe', *Advances in Space Research* **39**(8), 1298–1303.

Burešová, D., Lastovicka, J., Hejda, P. and Bochnicek, J. (2014), 'Ionospheric disturbances under low solar activity conditions', *Advances in Space Research* **54**(2), 185–196.

Burns, A. G., Killeen, T., Carignan, G. and Roble, R. (1995), 'Large enhancements in the O/N2 ratio in the evening sector of the winter hemisphere during geomagnetic storms', *Journal of Geophysical Research* **100**(A8), 14661–14671.

Cai, H., Yin, F., Ma, S., Xu, J. and Liu, Y. (2012), 'Simultaneous observations of large-scale traveling ionospheric disturbances on the nightside and dayside middle latitude', **30**(12), 1709.

Campbell, W. H. (1978), 'Induction of auroral zone electric currents within the Alaska pipeline', *pure and applied geophysics* **116**(6), 1143–1173.

Case, N. and Wild, J. (2012), 'A statistical comparison of solar wind propagation delays derived from multi-spacecraft techniques', *Journal of Geophysical Research* **117**(A2).

Chakraborty, M., Kumar, S., De, B. K. and Guha, A. (2015), 'Effects of geomagnetic storm on low latitude ionospheric total electron content: A case study from indian sector', *Journal of Earth System Science* **124**(5), 1115–1126.

Chandra, S. and Herman, J. (1969), 'F-region ionization and heating during magnetic storms', *Planetary and Space Science* **17**(5), 841–851.

Chapman, S. (1969), 'Physics of the Earth in space: A program of research, 1968–1975: National Academy of Sciences-National Research Council, Washington DC, October 1968. v+ 109 pp.'.

Chartier, A. T., Kinrade, J., Mitchell, C. N., Rose, J. A. R., Jackson, D. R., Cilliers, P., Habarulema, J.-B., Katamzi, Z., Mckinnell, L.-A., Matamba, T., Opperman, B., Ssessanga, N., Giday, N. M., Tyalimpi, V., Franceschi, G. D., Romano, V., Scotto, C., Notarpietro, R., Dovis, F., Avenant, E., Wonnacott, R., Oyeyemi, E., Mahrous, A., Tsidu, G. M., Lekamisy, H., Olwendo, J. O., Sibanda, P., Gogie, T. K., Rabiu, B., Jong, K. D. and Adewale, A. (2014), 'Ionospheric imaging in Africa', *Radio Science* **49**(1), 19–27. 2013RS005238.

Chen, G.-M., Xu, J., Wang, W. and Burns, A. G. (2014), 'A comparison of the effects of CIR-and CME-induced geomagnetic activity on thermospheric densities and spacecraft orbits: Statistical studies', *Journal of Geophysical Research* **119**(9), 7928–7939.

Crowley, G. and Meier, R. (2008), 'Disturbed O/N2 ratios and their transport to middle and low latitudes', *Midlatitude Ionospheric Dynamics and Disturbances* pp. 221–234.

Daniell, R. E. and Strickland, D. J. (2001), 'Modeling negative ionospheric storm effects caused by thermospheric disturbances observed in satellite UV images', *Journal of Geophysical Research* **106**(A12), 30307–30313.

Danilov, A. (2001), 'F2-region response to geomagnetic disturbances', *Journal of Atmospheric and Solar-Terrestrial Physics* **63**(5), 441–449.

Danilov, A. and Lastovicka, J. (2001), 'Effects of geomagnetic storms on the ionosphere and atmosphere', *International Journal of Geomagnetism and Aeronomy* **2**(3), 209–224.

Dashora, N. and Pandey, R. (2007), 'Variations in the total electron content near the crest of the equatorial ionization anomaly during the November 2004 geomagnetic storm', *Earth Planets Space* **59**(2), 127–131.

Data Solar Geophysical (2012), 'Users guide to the preliminary report and forecast of solar geophysical data August 2012'.

Davies, K. (1990), *Ionospheric radio*, Peter Peregrinus, London.

Davies, K. and Hartmann, G. K. (1997), 'Studying the ionosphere with the Global Positioning System', *Radio Science* **32**(4), 1695–1703.

Ding, F., Wan, W., Liu, L., Afraimovich, E., Voeykov, S. and Perevalova, N. (2008), 'A statistical study of large-scale traveling ionospheric disturbances observed by GPS TEC during major magnetic storms over the years 2003–2005', *Journal of Geophysical Research* **113**(A3).

Ding, F., Wan, W., Ning, B. and Wang, M. (2007), 'Large-scale traveling ionospheric disturbances observed by GPS total electron content during the magnetic storm of 29–30 October 2003', *Journal of Geophysical Research* **112**, A06309.

Ding, F., Wan, W., Ning, B., Zhao, B., Li, Q., Wang, Y., Hu, L., Zhang, R. and Xiong, B. (2013), Observations of poleward-propagating large-scale traveling ionospheric disturbances in southern China, *in* 'Annales Geophysicae', Vol. 31, Copernicus GmbH, pp. 377–385.

Echer, E., Gonzalez, W. and Tsurutani, B. (2008), 'Interplanetary conditions leading to superintense geomagnetic storms (Dst≤- 250 nT) during solar cycle 23', *Geophysical Research Letters* **35**(6), L06S03.

Echer, E., Tsurutani, B. T. and Guarnieri, F. L. (2009), 'Solar and interplanetary origins of the November 2004 superstorms', *Advances in Space Research* **44**(5), 615–620.

Echer, E., Tsurutani, B. T. and Guarnieri, F. L. (2010), 'Interplanetary origins of November 2004 superstorms', *Journal of Atmospheric and Terrestrial Physics* **72**(4), 280–284.

El-Rabbany, A. (2002), *Introduction to GPS: the global positioning system*, Artech house.

Elliott, H., McComas, D., Schwadron, N., Gosling, J., Skoug, R., Gloeckler, G. and Zurbuchen, T. (2005), 'An improved expected temperature formula for identifying interplanetary coronal mass ejections', *Journal of Geophysical Research* **110**(A4).

Farrell, J. and Barth, M. (1998), *The global positioning system and inertial navigation*, McGraw-Hill, New York.

Fejer, B. (1997), 'The electrodynamics of the low-latitude ionosphere: Recent results and future challenges', *Journal of Atmospheric and Solar-Terrestrial Physics* **59**(13), 1465 – 1482. The Ninth International Symposium on Equatorial Aeronomy.

Fejer, B. G., Farley, D., Woodman, R. and Calderon, C. (1979a), 'Dependence of equatorial f region vertical drifts on season and solar cycle', *Journal of Geophysical Research* **84**(A10), 5792–5796.

Fejer, B. G., Gonzales, C., Farley, D., Kelley, M. and Woodman, R. (1979b), 'Equatorial electric fields during magnetically disturbed conditions 1. The effect of the interplanetary magnetic field', *Journal of Geophysical Research* **84**, 5797–5802.

Fejer, B. G., Jensen, J., Kikuchi, T., Abdu, M. and Chau, J. (2007), 'Equatorial ionospheric electric fields during the November 2004 magnetic storm', *Journal of Geophysical Research* **112**(A10).

Fejer, B. G., Larsen, M. and Farley, D. (1983), 'Equatorial disturbance dynamo electric fields', *Geophysical research letters* **10**(7), 537–540.

Fejer, B. G. and Scherliess, L. (1995), 'Time dependent response of equatorial ionospheric electric fields to magnetospheric disturbances', *Geophysical research letters* **22**(7), 851–854.

Francis, S. H. (1974), 'A theory of medium-scale traveling ionospheric disturbances', *Journal of Geophysical Research* **79**(34), 5245–5260.

Fuller-Rowell, T., Codrescu, M., Maruyama, N., Fredrizzi, M., Araujo-Pradere, E., Sazykin, S. and Bust, G. (2007), 'Observed and modeled thermosphere and ionosphere response to superstorms', *Radio Science* **42**(4).

Fuller-Rowell, T., Codrescu, M., Moffett, R. and Quegan, S. (1994), 'Response of the thermosphere and ionosphere to geomagnetic storms', *Journal of Geophysical Research* **99**(A3), 3893–3914.

Fuller-Rowell, T. J., Codrescu, M. V., Rishbeth, H., Moffett, R. J. and Quegan, S. (1996), 'On the seasonal response of the thermosphere and ionosphere to geomagnetic storms', *Journal of Geophysical Research* **101**(A2), 2343–2353.

Fuller-Rowell, T. J., Codrescu, M. V., Roble, R. G. and Richmond, A. D. (1997), How does the thermosphere and ionosphere react to a geomagnetic storm?, *in* B. Tsurutani, W. Gonzalez, Y. Kamide and J. Arballo, eds, '*Magnetic Storms*', American Geophysical Union, Washington D.C., pp. 203–225.

Gao, Q., Liu, L.-B., Zhao, B.-Q., Wan, W.-X., Zhang, M.-L. and Ming, B.-Q. (2008), 'Statistical study of the storm effects in middle latitude ionosphere in the East Asian sector', *Chinese Journal of Geophysics* **51**(3), 435–443.

Georges, T. (1968), 'HF Doppler studies of traveling ionospheric disturbances', *Journal of Atmospheric and Terrestrial Physics* **30**(5), 735IN5737–736IN8746.

Gombosi, T. I. (1998), *Physics of the space environment*, Cambridge atmospheric and space science series, Cambridge University Press.

Gonzalez, W. D., Echer, E., Clua-Gonzalez, A. L. and Tsurutani, B. T. (2007), 'Interplanetary origin of intense geomagnetic storms (Dst < 100 nT) during solar cycle 23', *Geophysical Research Letters* **34**(6), L06101. L06101.

Gonzalez, W. D., Echer, E., Tsurutani, B. T., de Gonzalez, A. L. C. and Dal Lago, A. (2011), 'Interplanetary origin of intense, superintense and extreme geomagnetic storms', *Space Science Reviews* **158**(1), 69–89.

Gonzalez, W. D. and Tsurutani, B. T. (1987), 'Criteria of interplanetary parameters causing intense magnetic storms (Dst<-100 nT)', *Planetary and Space Science* **35**(9), 1101–1109.

Gonzalez, W. D. and Tsurutani, B. T. (1992), *Terrestrial response to eruptive solar flares: Geomagnetic storms*, Vol. 399, Springer Berlin Heidelberg, Berlin, Heidelberg, pp. 277–286.

Gonzalez, W. D., Tsurutani, B. T. and Clúa de Gonzalez, A. L. (1999), 'Interplanetary origin of geomagnetic storms', *Space Science Reviews* **88**(3), 529–562.

Gonzalez, W., Guarnieri, F. and Yumoto, K. (2005), 'Global dayside ionospheric response to interplanetary electric fields: Plasma uplift and increases in total electron content', *Multiscale Coupling of Sun-Earth Processes* pp. 157–171.

Gonzalez, W., Joselyn, J., Kamide, Y., Kroehl, H., Rostoker, G., Tsurutani, B. and Vasyliunas, V. (1994), 'What is a geomagnetic storm?', *Journal of Geophysical Research* **99**(A4), 5771–5792.

Goodman, J. M. (2006), *Space weather & telecommunications*, Vol. 782, Springer Science & Business Media.

Gopalswamy, N. (2004), A global picture of CMEs in the inner heliosphere, *in* 'The sun and the heliosphere as an integrated system', Springer, pp. 201–251.

Gopalswamy, N. (2009), 'The CME link to geomagnetic storms', *Proceedings of the International Astronomical Union* **5**(S264), 326–335.

Gopalswamy, N., Barbieri, L., Lu, G., Plunkett, S. and Skoug, R. (2005), 'Introduction to the special section: Violent Sun-Earth connection events of October–November 2003', *Geophysical Research Letters* **32**(3).

Gopalswamy, N., Mewaldt, R. A. and Torsti, J. (2006), *Solar eruptions and energetic particles*, Vol. IUGG Volumes of *Geophysical Monograph series 165*, American Geophysical Union.

Gosling, J. T., McComas, D. J., Phillips, J. L. and Bame, S. J. (1991), 'Geomagnetic activity associated with earth passage of interplanetary shock disturbances and coronal mass ejections', *Journal of Geophysical Research* **96**(A5), 7831–7839.

Gps.gov (2017), 'Official U.S. government information about the Global Positioning System (GPS) and related topics', `https://www.gps.gov/systems/gps/control/`. (Accessed 2017-10-15).

Gubbins, D. and Herrero-Bervera, E. (2007), *Encyclopedia of geomagnetism and paleomagnetism*, Springer Science.

Gupta, M., Mishra, V. and Mishra, A. (2007), 'Solar activity parameters and their interrelationship: Continuous decrease in flare activity from solar cycles 20 to 23', *Journal of Geophysical Research* **112**(A5).

Habarulema, J. B., Katamzi, Z. T. and McKinnell, L.-A. (2013a), 'Estimating the propagation characteristics of large-scale traveling ionospheric disturbances using ground-based and satellite data', *Journal of Geophysical Research* **118**(12), 7768–7782.

Habarulema, J. B., Katamzi, Z. T., Sibanda, P. and Matamba, T. M. (2017), 'Assessing ionospheric response during some strong storms in solar cycle 24 using various data sources', *Journal of Geophysical Research* **122**(1), 1064–1082.

Habarulema, J. B., Katamzi, Z. T. and Yizengaw, E. (2015), 'First observations of poleward large-scale traveling ionospheric disturbances over the African sector during geomagnetic storm conditions', *Journal of Geophysical Research* **120**(8), 6914–6929.

Habarulema, J. B., McKinnell, L. A., Burešová, D., Zhang, Y., Seemala, G., Ngwira, C. M., Chum, J. and Opperman, B. (2013b), 'A comparative study of TEC response for the South African equatorial and mid-latitudes during storm conditions', *Journal of Atmospheric and Solar-Terrestrial Physics* **102**, 105–114.

Hajkowicz, L. and Hunsucker, R. (1987), 'A simultaneous observation of large-scale periodic tids in both hemispheres following an onset of auroral disturbances', *Planetary and Space Science* **35**(6), 785 – 791.

Häkkinen, L. V. T., Pulkkinen, T. I., Pirjola, R. J., Nevanlinna, H., Tanskanen, E. I. and Turner, N. E. (2003), 'Seasonal and diurnal variation of geomagnetic activity: Revised Dst versus external drivers', *Journal of Geophysical Research* **108**(A2).

Hanslmeier, A. (2002), *The Sun and Space Weather*, Astrophysics and Space Science Library, 1 edn, Springer.

Hanslmeier, A. (2008), *The Sun and Space Weather*, Astrophysics and Space Science Library, 2nd edn, Springer.

Hanson, W. B. and Moffett, R. J. (1966), 'Ionization transport effects in the equatorial F region', *Journal of Geophysical Research* **71**(23), 5559–5572.

Hargreaves, J. K. (1992), *The solar-terrestrial environment: an introduction to geospace-the science of the terrestrial upper atmosphere, ionosphere, and magnetosphere*, Cambridge University Press.

Hasan, S. (2003), Magnetic flux tubes and activity on the sun, *in* 'Lectures on Solar Physics', Springer, pp. 173–201.

Heikkila, W. J. (2011), *Earth's Magnetosphere: Formed by the Low-latitude Boundary Layer*, Elsevier.

Heisler, L. (1958), 'Anomalies in ionosonde records due to traveling ionospheric disturbances', *Australian Journal of Physics* **11**(1), 79–90.

Hines, C. O. (1960), 'Internal atmospheric gravity waves at ionospheric heights', *Canadian Journal of Physics* **38**(11), 1441–1481.

Ho, T. S. and Lee, S. B. (2004), *The Oxford Guide to Financial Modeling: Applications for Capital Markets, Corporate Finance, Risk Management and Financial Institutions*, Oxford university press.

Hocke, K. and Schlegel, K. (1996), 'A review of atmospheric gravity waves and travelling ionospheric disturbances: 1982–1995', *Annales Geophysicae* **14**(9), 917.

Hofmann-Wellenhof, B., Lichtenegger, H. and Collins, J. (1994), *Global Positioning System Theory and Practice*, 3rd edn, Springer Verlag, Vienna.

Hofmann-Wellenhof, B., Lichtenegger, H. and Collins, J. (1997), *GPS theory and practice*, 4th edn, Springer Verlag, Vienna.

Howard, T. (2013), *Space weather and coronal mass ejections*, Springer, Boulder, Colorado, USA.

Howard, T. (2014), *Space weather and coronal mass ejections*, Springer, Boulder, Colorado, USA.

Huang, C.-S., Foster, J. C. and Kelley, M. C. (2005a), 'Long-duration penetration of the interplanetary electric field to the low-latitude ionosphere during the main phase of magnetic storms', *Journal of Geophysical Research* **110**(A11), A11309.

Huang, C.-S., Foster, J., Goncharenko, L., Erickson, P., Rideout, W. and Coster, A. (2005b), 'A strong positive phase of ionospheric storms observed by the Millstone Hill incoherent scatter radar and global GPS network', *Journal of Geophysical Research* **110**(A6).

Huang, C.-S., Sazykin, S., Chau, J. L., Maruyama, N. and Kelley, M. C. (2007), 'Penetration electric fields: Efficiency and characteristic time scale', *Journal of Atmospheric and Terrestrial Physics* **69**(10), 1135–1146.

Huang, Y.-N., Cheng, K. and Chen, S.-W. (1989), 'On the equatorial anomaly of the ionospheric total electron content near the northern anomaly crest region', *Journal of Geophysical Research* **94**(A10), 13515–13525.

Hunsucker, P. R. D. (1991), *Radio Techniques for Probing the Terrestrial Ionosphere*, Physics and Chemistry in Space 22, 1 edn, Springer-Verlag Berlin Heidelberg.

Hunsucker, R. D. (1980), E and F region predictions for communication purposes at high latitudes, *in* 'Exploration of the Polar Upper Atmosphere', Springer, pp. 481–494.

Hunsucker, R. D. (1982), 'Atmospheric gravity waves generated in the high-latitude ionosphere: A review', *Reviews of Geophysics* **20**(2), 293–315.

Hunsucker, R. D. and Hargreaves, J. K. (2003), *The high-latitude ionosphere and its effects on radio propagation*, Cambridge University Press, Cambridge.

Huttunen, K. E. J., Koskinen, H. E. and Schwenn, R. (2002), 'Variability of magnetospheric storms driven by different solar wind perturbations', *Journal of Geophysical Research* **107**(A7).

Isioye, O. A., Combrinck, L., Botai, J. O. and Munghemezulu, C. (2015), 'The potential for observing African weather with GNSS remote sensing', *Advances in Meteorology* **2015**.

Jahoda, F. and Sawyer, G. (1971), 11. optical refractivity of plasmas, *in* R. H. Lovberg and H. R. Griem, eds, 'Plasma Physics', Vol. 9, Part B of *Methods in Experimental Physics*, Academic Press, pp. 1 – 48.

Jakowski, N., Heise, S., Wehrenpfennig, A., Schlüter, S. and Reimer, R. (2002), 'GPS/GLONASS-based TEC measurements as a contributor for space weather forecast', *Journal of Atmospheric and Solar-Terrestrial Physics* **64**(5), 729–735.

Joselyn, J. and Tsurutani, B. (1990), 'Geomagnetic sudden impulses and storm sudden commencements: A note on terminology', *Eos. Trans. AGU* **71**(47), 1808–1809.

Joseph, O. O., Yamazak, Y., Cilliers, P., Baki, P., Ngwira, C. M. and Mito, C. (2015), 'A study on the response of the Equatorial Ionization Anomaly over the East Africa sector during the geomagnetic storm of November 13, 2012', *Advances in Space Research* **55**(12), 2863–2872.

Kallenrode, M.-B. (2004), *Space Physics: An Introduction to Plasmas and Particles in the Heliosphere and Magnetospheres*, Advanced Texts in Physics, enlarged 3rd edn, Springer.

Kamide, Y., Baumjohann, W., Daglis, I., Gonzalez, W., Grande, M., Joselyn, J., McPherron, R., Phillips, J., Reeves, E., Rostoker, G. et al. (1998), 'Current understanding of magnetic storms: Storm-substorm relationships', *Journal of Geophysical Research* **103**(A8), 17705–17728.

Kamide, Y. and Chian, C. A. (2007), An overview of the solar-terrestrial environment , *in* Y. Kamide and A.-L. Chian, eds, '*Handbook of the solar-terrestrial environment*', Springer Verlag, Berlin, pp. 2–22.

Kane, R. (1981), 'Storm effects of ionospheric total electron content (TEC) at low latitudes', *Journal of Geomagnetism and Geoelectricity* **33**(7), 399–409.

Kaplan, E. D. and Hegarty, C. J. (2006), *Understanding GPS principles and applications*, 2nd edn, Artech House, Boston.

Katamzi, Z. T. and Habarulema, J. B. (2014*a*), 'Traveling ionospheric disturbances observed at South African mid-latitudes during the 29–31 October 2003 geomagnetically disturbed period', *Advances in Space Research* **53**(1), 48–62.

Katamzi, Z. T. and Habarulema, J. B. (2014*b*), 'Traveling ionospheric disturbances observed at South African midlatitudes during the 29–31 October 2003 geomagnetically disturbed period', *Advances in Space Research* **53**(1), 48–62.

Kelley, M. C., ed. (1989), *The Earth's Ionosphere: Plasma Physics and Electrodynamics*, Vol. 43 of *International Geophysics 43*, Academic Press, Elsevier.

Kelley, M. C., Ilma, R. R., Nicolls, M., Erickson, P., Goncharenko, L., Chau, J. L., Aponte, N. and Kozyra, J. U. (2010), 'Spectacular low-and mid-latitude electrical fields and neutral winds during a superstorm', *Journal of Atmospheric and Terrestrial Physics* **72**(4), 285–291.

Kelley, M. C., Makela, J. J., Chau, J. L. and Nicolls, M. J. (2003), 'Penetration of the solar wind electric field into the magnetosphere/ionosphere system', *Geophysical Research Letters* **30**(4).

Kelley, M. C., Wong, V. K., Aponte, N., Coker, C., Mannucci, A. J. and Komjathy, A. (2009), 'Comparison of COSMIC occultation-based electron density profiles and TIP observations with Arecibo incoherent scatter radar data', *Radio Science* **44**(4), RS4011. RS4011.

Kelley, M., Fejer, B. G. and Gonzales, C. (1979), 'An explanation for anomalous equatorial ionospheric electric fields associated with a northward turning of the interplanetary magnetic field', *Geophysical Research Letters* **6**(4), 301–304.

Kikuchi, T., Hashimoto, K. K. and Nozaki, K. (2008), 'Penetration of magnetospheric electric fields to the equator during a geomagnetic storm', *Journal of Geophysical Research* **113**(A6).

Kikuchi, T., Lühr, H., Schlegel, K., Tachihara, H., Shinohara, M. and Kitamura, T.-I. (2000), 'Penetration of auroral electric fields to the equator during a substorm', *Journal of Geophysical Research* **105**(A10), 23251–23261.

Kivelson, M. G. and Russell, C. T. (1995), *Introduction to space physics*, Cambridge Atmospheric and Space Science Series, Cambridge University Press.

Klimenko, M. and Klimenko, V. (2012), 'Disturbance dynamo, prompt penetration electric field and over-shielding in the Earth's ionosphere during geomagnetic storm', *Journal of Atmospheric and Solar-Terrestrial Physics* **90**, 146–155.

Kuai, J., Liu, L., Liu, J., Zhao, B., Chen, Y., Le, H. and Wan, W. (2015), 'The long-duration positive storm effects in the equatorial ionosphere over Jicamarca', *Journal of Geophysical Research* **120**(2), 1311–1324. 2014JA020552.

Kutner, M. L. (2003), *Astronomy: a physical perpective*, Cambridge University Press, Cambridge.

Lang, K. R. (2008), *The Sun from space* , Astronomy and Astrophysics Library, 2nd ed. edn, Springer.

Lanzerotti, L. J. (2007), 'Space weather effects on communications', *Space weather-physics and effects. Springer, Praxis Publishing, Chichester* pp. 247–268.

Lastovicka, J. (2002*a*), 'Monitoring and forecasting of ionospheric space weather—effects of geomagnetic storms', *Journal of Atmospheric and Solar-Terrestrial Physics* **64**(5), 697–705.

Lastovicka, J. (2002b), 'Monitoring and forecasting of ionospheric space weather—effects of geomagnetic storms', *Journal of Atmospheric and Terrestrial Physics* **64**.

LDI (2015), 'Background to Ionospheric Sounding', `http://www.digisonde.com/instrument-description.htm`. (Accessed 2017-10-20).

Lei, J., Liu, L., Wan, W. and Zhang, S.-R. (2005), 'Variations of electron density based on long-term incoherent scatter radar and ionosonde measurements over Millstone Hill', *Radio science* **40**(2).

Leitinger, R., Ladreiter, H.-P. and Kirchengast, G. (1997), 'Ionosphere tomography with data from satellite reception of Global Navigation Satellite System signals and ground reception of Navy Navigation Satellite System signals', *Radio Science* **32**(4), 1657–1669.

Lin, C., Richmond, A., Heelis, R., Bailey, G., Lu, G., Liu, J., Yeh, H. and Su, S.-Y. (2005), 'Theoretical study of the low-and midlatitude ionospheric electron density enhancement during the October 2003 superstorm: Relative importance of the neutral wind and the electric field', *Journal of Geophysical Research* **110**(A12).

Liou, K., Newell, P. T., Anderson, B. J., Zanetti, L. and Meng, C.-I. (2005), 'Neutral composition effects on ionospheric storms at middle and low latitudes', *Journal of Geophysical Research* **110**(A5), A05309.

Loewe, C. A. and Prölss, G. W. (1997), 'Classification and mean behavior of magnetic storms', *Journal of Geophysical Research* **102**(A7), 14209 – 14213.

Lugaz, N., Farrugia, C., Huang, C.-L. and Spence, H. E. (2015), 'Extreme geomagnetic disturbances due to shocks within CMEs', *Geophysical Research Letters* **42**(12), 4694–4701.

Lukianova, R. (2003), 'Magnetospheric response to sudden changes in solar wind dynamic pressure inferred from polar cap index', *Journal of Geophysical Research* **108**(A12).

Mandea, M. and Korte, M. (2010), *Geomagnetic observations and models*, Vol. 5, Springer.

Mannucci, A. J., Tsurutani, B. T., Kelley, M. C., Iijima, B. A. and Komjathy, A. (2009), 'Local time dependence of the prompt ionospheric response for the 7, 9, and 10 November 2004 superstorms', *Journal of Geophysical Research* **114**(A10).

Mannucci, A., Tsurutani, B., Abdu, M., Gonzalez, W., Komjathy, A., Echer, E., Iijima, B., Crowley, G. and Anderson, D. (2008), 'Superposed epoch analysis of the dayside ionospheric response to four intense geomagnetic storms', *Journal of Geophysical Research* **113**(A3).

Mannucci, A., Tsurutani, B., Iijima, B., Komjathy, A., Saito, A., Gonzalez, W., Guarnieri, F., Kozyra, J. and Skoug, R. (2005), 'Dayside global ionospheric response to the major interplanetary events of October 29–30, 2003 "Halloween Storms"', *Geophysical Research Letters* **32**(12), L12S02.

Maris, H. B. (1932), 'Seasonal Variations in Magnetic Storms', *Physical Review* **39**, 504–514.

Maruyama, T. and Nakamura, M. (2007), 'Conditions for intense ionospheric storms expanding to lower midlatitudes', *Journal of Geophysical Research* **112**(A5), A05310.

Matamba, M. T., Habarulema, J. B. and Burešová, D. (2016), 'Midlatitude ionospheric changes to four great geomagnetic storms of solar cycle 23 in Southern and Northern Hemispheres', *Space Weather* **14**(12), 1155–1171. 2016SW001516.

Matamba, T. M. and Habarulema, J. B. (2017), 'Ionospheric response to CME and CIR- driven geomagnetic storms along 30°E - 40°E over the African sector from 2001 - 2015', *Space Weather* p. Under review.

Matamba, T. M., Habarulema, J. B. and McKinnell, L.-A. (2015), 'Statistical analysis of the ionospheric response during geomagnetic storm conditions over South Africa using ionosonde and GPS data', *Space Weather* **13**(9), 536–547.

Matsushita, S. (1959), 'A study of the morphology of ionospheric storms', *Journal of Geophysical Research* **64**(3), 305–321.

Matsushita, S. (1962), 'On geomagnetic sudden commencements, sudden impulses, and storm durations', *Journal of Geophysical Research* **67**(10), 3753–3777.

Matsushita, S. (1963), 'Equatorial ionospheric variations during geomagnetic storms', *Journal of Geophysical Research* **68**(9), 2595–2601.

Mavromichalaki, H., Vassilaki, A. and Marmatsouri, E. (1988), 'A catalogue of high-speed solar-wind streams: Further evidence of their relationship to Ap-index', *Solar physics* **115**(2), 345–365.

Mayaud, P. (1980), 'Derivation, meaning and use of geomagnetic indices', *Geophys. Monograph* **22**.

Mayr, H. and Trinks, H. (1977), 'Spherical asymmetry in thermospheric magnetic storms', *Planetary and Space Science* **25**(7), 607 – 613.

Mayr, H. and Volland, H. (1972), 'Magnetic storm effects in the neutral composition', *Planetary and Space Science* **20**.

McNamara, L. F. (1991), *The ionosphere: communications, surveillance and direction finding*, Kriger Publishing, Malabar FL.

Mendillo, M. (2006), 'Storms in the ionosphere: Patterns and processes for total electron content', *Reviews of Geophysics* **44**(4).

Mendillo, M., Narvaez, C. and Marusiak, A. G. (2013), 'Are ionospheric storms the same during different solar cycles?', *Journal of Geophysical Research* **118**(10), 6795–6805.

Misra, P. and Enge, P. (2006), *Global positioning system: signals, measurements, and performance*, 2nd edn, Ganga-Jamurna Press, Lincoln VA.

Moldwin, M. (2008), *An introduction to space weather*, Cambridge University Press, Cambridge.

Mullan, D. J. (2009), *Physics of the Sun: A First Course*, Pure and Applied Physics, 1 edn, Chapman and Hall/CRC.

Nava, B., Rodríguez-Zuluaga, J., Alazo-Cuartas, K., Kashcheyev, A., Migoya-Orué, Y., Radicella, S., Amory-Mazaudier, C. and Fleury, R. (2016), 'Middle-and low-latitude ionosphere response to 2015 St. Patrick's Day geomagnetic storm', *Journal of Geophysical Research* **121**(4), 3421–3438.

Nayak, C., Tsai, L.-C., Su, S.-Y., Galkin, I., Tan, A. T. K., Nofri, E. and Jamjareegulgarn, P. (2016), 'Peculiar features of the low-latitude and mid-latitude ionospheric response to the St. Patrick's Day geomagnetic storm of 17 March 2015', *Journal of Geophysical Research* **121**(8), 7941–7960.

Ngwira, C. M. (2011), An analysis of ionospheric response to geomagnetic disturbances over South Africa and Antarctica, PhD thesis, Rhodes University, Grahamstown, South Africa.

Ngwira, C. M., McKinnell, L. A., Cilliers, P. J. and Yizengaw, E. (2012), 'An investigation of ionospheric disturbances over South Africa during the magnetic storm on 15 May 2005', *Advances in Space Research* **49**, 327–335.

Ngwira, C. M., McKinnell, L. A., Cilliers, P. J. and Yizengaw, E. (2012a), 'An investigation of ionospheric disturbances over South Africa during the magnetic storm on 15 May 2005', *Advances in Space Research* **49**, 327–335.

Ngwira, C. M., Pulkkinen, A., McKinnell, L.-A. and Cilliers, P. J. (2008), 'Improved modeling of geomagnetically induced currents in the south african power network', *Space Weather* **6**(11), S11004. S11004.

Ngwira, C. M., Seemala, G. K. and Habarulema, J. B. (2013), 'Simultaneous observations of ionospheric irregularities in the African low-latitude region', *Journal of Atmospheric and Terrestrial Physics* **97**, 50–57.

Ngwira, C., McKinnell, L., Cilliers, P. J. and Coster, A. (2012b), 'Ionospheric observations during the geomagnetic storm events on 24-27 July 2004: long-duration positive storm effects ', *Journal of Geophysical Research* **117**(A9), A00L02.

Nicolls, M. J. and Heinselman, C. J. (2007), 'Three-dimensional measurements of traveling ionospheric disturbances with the Poker Flat Incoherent Scatter Radar', *Geophysical Research Letters* **34**(21), L21104. L21104.

Nicolls, M. J., Kelley, M. C., Coster, A. J., González, S. A. and Makela, J. J. (2004), 'Imaging the structure of a large-scale TID using ISR and TEC data', *Geophysical Research Letters* **31**(9).

Nishida, A. and Cahill, L. J. (1964), 'Sudden impulses in the magnetosphere observed by Explorer 12', *Journal of Geophysical Research* **69**(11), 2243–2255.

Obara, T. (2002), 'The magnetosphere', *Journal of the communications Research Laboratory* **49**(3), 61–74.

Olwendo, O., Cesaroni, C., Yamazaki, Y. and Cilliers, P. (2017), 'Equatorial ionospheric disturbances over the East African sector during the 2015 St. Patrick's day storm', *Advances in Space Research* **60**(8), 1817–1826.

Paouris, E. and Mavromichalaki, H. (2017), 'Interplanetary Coronal Mass Ejections Resulting from Earth-Directed CMEs Using SOHO and ACE Combined Data During Solar Cycle 23', *Solar Physics* **292**(2), 30.

Parkinson, W. B., Spilker, J. J., Enge, p. and Axelrad, P. (1996), *Global positioning system: theory and applications*, Vol. 1, 5 edn, American Institute of Aeronautics and Astronautics, Michigan.

Pfaff, R. F. (2012), 'The near-Earth plasma environment', *Space science reviews* **168**(1-4), 23–112.

Picone, J., Hedin, A., Drob, D. P. and Aikin, A. (2002), 'NRLMSISE-00 empirical model of the atmosphere: Statistical comparisons and scientific issues', *Journal of Geophysical Research* **107**(A12).

Pirjola, R. (2000), 'Geomagnetically induced currents during magnetic storms', *IEEE Transactions on Plasma Science* **28**(6), 1867–1873.

Pirjola, R., Kauristie, K., Lappalainen, H., Viljanen, A. and Pulkkinen, A. (2005), 'Space weather risk', *Space Weather* **3**(2), S02A02. S02A02.

Pirjola, R., Pulkkinen, A. and Viljanen, A. (2003), 'Studies of space weather effects on the finnish natural gas pipeline and on the finnish high-voltage power system', *Advances in Space Research* **31**(4), 795–805.

Priest, E. R. (1988), *Dynamics and structure of quiescent solar prominences*, Vol. 150, Springer Science & Business Media.

Prölss, G. (1976), 'On explaining the negative phase of ionospheric storms', *Planetary and Space Science* **24**(6), 607–609.

Prölss, G. (1977), 'Seasonal variation of atmospheric-ionospheric disturbances', *Journal of Geophysical Research* **82**(10), 1635–1640.

Prölss, G. (1981), 'Latitudinal structure and extension of the polar atmospheric disturbance', *Journal of Geophysical Research* **86**(A4), 2385–2396.

Prölss, G. (1993*a*), 'Common origin of positive ionospheric storms at middle latitudes and the geomagnetic activity effect at low latitudes', *Journal of Geophysical Research* **98**(A4), 5981–5991.

Prölss, G. (2008), Ionospheric storms at mid-latitude: a short review, *in* P. Kintner, A. Coster, T. Fuller-Rowell, A. Mannucci, M. Mendillo and R. Heelis, eds, '*Midlatitude ionospheric dynamics and disturbances*', American Geophysical Union, Washington, DC, pp. 9 –24.

Prölss, G., Brace, L., Mayr, H., Carignan, G., Killeen, T. and Klobuchar, J. (1991*a*), 'Ionospheric storm effects at subauroral latitudes: A case study', *Journal of Geophysical Research* **96**(A2), 1275–1288.

Prölss, G. and Fricke, K. (1976), 'Neutral composition changes during a period of increasing magnetic activity', *Planetary and Space Science* **24**(1), 61–67.

Prölss, G. and Jung, M. (1978), 'Travelling atmospheric disturbances as a possible explanation for daytime positive storm effects of moderate duration at middle latitudes', *Journal of Atmospheric and Terrestrial Physics* **40**(12), 1351–1354.

Prölss, G., Roemer, M. and Slowey, J. (1988), 'Dissipation of solar wind energy in the earth's upper atmosphere: The geomagnetic activity effect', *Advances in space research* **8**(5-6), 215–261.

Prölss, G. W. (1980), 'Magnetic storm associated perturbations of the upper atmosphere: recent results obtained by satellite-borne gas analyzers', *Reviews of Geophysics* **18**(1), 183–202.

Prölss, G. W. (1993b), 'On explaining the local time variation of the ionospheric storm effects', *Annales Geophysicae* **11**, 1–9.

Prölss, G. W. (1995), Ionospheric F-region storms, *in* H. Volland, ed., '*Handbook of the atmospheric electrodynamics*', Vol. 2, CRC Press, Bonn, chapter 8, pp. 195–248.

Prölss, G. W. (1997), Magnetic storm associated perturbations of the upper atmosphere, *in* B. T. Tsurutani, W. D. Gonzalez, Y. Kamide and J. K. Arballo, eds, 'Magnetic storms', American Geophysical Union, Washington, D. C., pp. 227–241.

Prölss, G. W. (2004), *Physics of the Earth's space environment: an introduction*, Springer, Berlin.

Prölss, G. W., Brace, L. H., Mayr, H. G., Carignan, G. R., Killeen, T. L. and Klobuchar, J. A. (1991b), 'Ionospheric storm effects at subauroral latitudes: a case study', *Journal of Geophysical Research* **96**(A2), 1275–1288.

Prölss, G. W., von Zahn, U. and Raitt, W. J. (1975), 'Neutral atmospheric composition, plasma density, and electron temperature at F region heights', *Journal of Geophysical Research* **80**(25), 3715–3718.

Prölss, G. and Zahn, U. (1974), 'Esro 4 Gas Analyzer results 2. Direct measurements of changes in the neutral composition during an ionospheric storm', *Journal of Geophysical Research* **79**(16), 2535–2539.

Prölss, G. and Roemer, M. (1987), 'Thermospheric storms', *Advances in Space Research* **7**(10), 223 – 235.

Pulkkinen, A. et al. (2003), 'Geomagnetic induction during highly disturbed space weather conditions: Studies of ground effects'.

Rastogi, R. (1975), 'On the simultaneous existence of eastward and westward flowing equatorial electrojet currents', *Proceedings Mathematical Sciences* **81**(2), 80–92.

Rastogi, R., Chandra, H., Das, A., Sridharan, R., Reinisch, B. and Ahmed, K. (2012), 'Effects of a magnetic cloud simultaneously observed on the equatorial ionosphere in midday and midnight sectors', *Earth, planets and space* **64**(4), 353–360.

Rees, M. H. (1989), *Physics and Chemistry of the Upper Atmosphere*, Cambridge Atmospheric and Space Science Series, 1 edn, Cambridge University Press.

Richardson, I. (2006), 'The formation of CIRs at stream-stream interfaces and resultant geomagnetic activity', *Recurrent magnetic storms: Corotating solar wind streams* pp. 45–58.

Richardson, I. and Cane, H. (2010), 'Near-Earth interplanetary coronal mass ejections during solar cycle 23 (1996–2009): Catalog and summary of properties', *Solar Physics* **264**(1), 189–237.

Richardson, I. G. (2004), 'Energetic particles and corotating interaction regions in the solar wind', *Space Science Reviews* **111**(3-4), 267–376.

Rishbeth, H. (1991), 'F-region storms and thermospheric dynamics', *Journal of geomagnetism and geoelectricity* **43**(Supplement1), 513–524.

Rishbeth, H., Fuller-Rowell, T. J. and Rodger, A. S. (1987), 'F-layer storms and thermospheric composition', *Physica Scripta* **36**(2), 327.

Rishbeth, H. and Garriott, O. K. (1969), *Introduction to Ionospheric Physics*, International Geophysics 14, Academic Press.

Russell, C. T. and McPherron, R. L. (1973), 'Semiannual variation of geomagnetic activity', *Journal of Geophysical Research* **78**(1), 92–108.

Sahai, Y., Becker-Guedes, F., Fagundes, P., de Jesus, R., de Abreu, A., Paxton, L., Goncharenko, L., Brunini, C., Gende, M., Ferreira, A. et al. (2009), 'Effects observed in the Latin American sector ionospheric F region during the intense geomagnetic disturbances in the early part of November 2004', *Journal of Geophysical Research* **114**, A00A19.

Sastri, J. H. (1988), 'Equatorial electric-fields of ionospheric disturbance dynamo orgin', *Annales Geophysicae* **6**(6), 635–642.

Scherliess, L. and Fejer, B. G. (1997), 'Storm time dependence of equatorial disturbance dynamo zonal electric fields', *Journal of Geophysical Research* **102**(A11), 24037–24046.

Schunk, R. and Nagy, A. F. (2009), *Ionospheres: physics, plasma physics and chemistry*, 2nd edn, Cambridge University Press, Cambridge.

Seaton, M. (1956), 'A possible explanation of the drop in F-region critical densities accompanying major ionospheric storms', *Journal of Atmospheric and Terrestrial Physics* **8**(1–2), 122–124.

Seemala, G. K. (2011), GPS-TEC analysis application , Technical report, Institute for Scientific Research, U.S.A.

Seemala, G. K. and Valladares, C. E. (2011), 'Statistics of total electron content depletions observed over the South American continent for the year 2008', *Radio Science* **46**(5), RS5019.

Shume, E. B., de Paula, E. R., Maus, S., Hysell, D. L., Rodrigues, F. S. and Bekele, A. (2009), 'Equatorial zonal electric fields inferred from a 3-D electrostatic potential model and ground-based magnetic field measurements', *Journal of Geophysical Research* **114**(A6), A06305. A06305.

Sizun, H. and de Fornel, P. (2005), *Radio wave propagation for telecommunication applications*, Springer.

Sreehari, C. and Nayar, S. P. (2006), Penetration of interplanetary electric field to the equatorial F region during the magnetic storm on November 20, 2003, *in* N. Gopalswamy and A. Bhattacharyya, eds, 'Proceedings of ILWS workshop', Vol. 24.

Stauning, P. (2013), 'The Polar Cap index: A critical review of methods and a new approach', *Journal of Geophysical Research* **118**(8), 5021–5038.

Stix, M. (2004), *The Sun: An introduction*, 2ed. edn, Springer.

Strang, G. and Borre, K. (1997), *Linear algebra, geodesy, and GPS*, Siam.

Sugiura, M. (1963), 'Hourly values of equatorial Dst for the IGY'.

Sugiura, M. and Kamei, T. (1991), 'Equatorial Dst index 1957–1986, IAGA Bull., 40, ISGI Pub', *Office, Saint-Maur-des-Fossess, France* .

Tanaka, T. (1981), 'Severe ionospheric disturbances caused by the sudden response of evening sub-equatorial ionospheres to geomagnetic storms', *Journal of Geophysical Research* **86**(A13), 11335–11349.

Tandberg-Hanssen, E. (1974), *Solar Prominences*, Geophysics and Astrophysics Monographs 12, 1 edn, Springer Netherlands.

Tandberg-Hanssen, E. and Emslie, A. G. (1988), *The physics of solar flares*, Cambridge Astrophysics, 1 edn, Cambridge University Press.

Tesema, F., Damtie, B. and Nigussie, M. (2015), 'The response of the ionosphere to intense geomagnetic storms in 2012 using GPS-TEC data from East Africa longitudinal sector', *Journal of Atmospheric and Terrestrial Physics* **135**, 143–151.

Thomson, N. R., Rodger, C. J. and Dowden, R. L. (2004), 'Ionosphere gives size of greatest solar flare', *Geophysical research letters* **31**(6), L06803.

Titheridge, J. and Buonsanto, M. (1988), 'A comparison of northern and southern hemisphere TEC storm behaviour', *Journal of atmospheric and terrestrial physics* **50**(9), 763–780.

Troshichev, O., Dmitrieva, N. and Kuznetsov, B. (1979), 'Polar cap magnetic activity as a signature of substorm development', *Planetary and Space Science* **27**(3), 217–221.

Tsagouri, I., Belehaki, A., Moraitis, G. and Mavromichalaki, H. (2000), 'Positive and negative ionospheric disturbances at middle latitudes during geomagnetic storms', *Geophysical Research Letters* **27**(21), 3579–3582.

Tsugawa, T., Saito, A. and Otsuka, Y. (2004), 'A statistical study of large-scale traveling ionospheric disturbances using the GPS network in Japan', *Journal of Geophysical Research* **109**(A6), A06302.

Tsugawa, T., Zhang, S.-R., Coster, A., Otsuka, Y., Sato, J., Saito, A., Zhang, Y. and Paxton, L. (2007), 'Summer-winter hemispheric asymmetry of the sudden increase in ionospheric total electron content and of the O/N2 ratio: Solar activity dependence', *Journal of Geophysical Research* **112**(A8), A08301.

Tsurutani, B., Judge, D., Guarnieri, F., Gangopadhyay, P., Jones, A., Nuttall, J., Zambon, G., Didkovsky, L., Mannucci, A., Iijima, B., Meier, R., Immel, T., Woods, T., Prasad, S., Floyd, L., Huba, J., Solomon, S., Straus, P. and Viereck, R. (2005), 'The October 28, 2003 extreme EUV solar flare and resultant extreme ionospheric effects: Comparison to other Halloween events and the Bastille Day event', *Geophysical Research Letters* **32**(3), L03S09.

Tsurutani, B., Lakhina, G., Verkhoglyadova, O., Gonzalez, W., Echer, E. and Guarnieri, F. (2011), 'A review of interplanetary discontinuities and their geomagnetic effects', *Journal of Atmospheric and Terrestrial Physics* **73**(1), 5–19.

Tsurutani, B., Mannucci, A., Iijima, B., Abdu, M. A., Sobral, J. H. A., Gonzalez, W., Guarnieri, F., Tsuda, T., Saito, A., Yumoto, K. et al. (2004), 'Global dayside ionospheric uplift and enhancement associated with interplanetary electric fields', *Journal of Geophysical Research* **109**, A08302.

Tsurutani, B. T., Echer, E., Guarnieri, F. L. and Kozyra, J. (2008b), 'Cawses november 7–8, 2004, superstorm: Complex solar and interplanetary features in the post-solar maximum phase', *Geophysical Research Letters* **35**(6), L06S05.

Tsurutani, B. T. and Gonzalez, W. D. (1987), 'The cause of high-intensity long-duration continuous AE activity (HILDCAAs): Interplanetary Alfvén wave trains', *Planetary and Space Science* **35**(4), 405–412.

Tsurutani, B. T., Gonzalez, W. D., Gonzalez, A. L. C., Guarnieri, F. L., Gopalswamy, N., Grande, M., Kamide, Y., Kasahara, Y., Lu, G., Mann, I., McPherron, R., Soraas, F. and Vasyliunas, V. (2006b), 'Corotating solar wind streams and recurrent geomagnetic activity: A review', *Journal of Geophysical Research* **111**(A7), A07S01.

Tsurutani, B. T., Gonzalez, W. D., Gonzalez, A. L. C., Tang, F., Arballo, J. K. and Okada, M. (1995b), 'Interplanetary origin of geomagnetic activity in the declining phase of the solar cycle', *Journal of Geophysical Research* **100**(A11), 21717–21733.

Tsurutani, B. T., Gonzalez, W. D., Thang, F., Akasofu, S. I. and Smith, E. J. (1988), 'Origin of interplanetary southward magnetic fields responsible for major magnetic storms near solar maximum (1978 - 1979) ', *Journal of Geophysical Research* **93**(A8), 8519–8531.

Tsurutani, B. T., Ho, C. M., Arballo, J. K., Goldstein, B. E. and Balogh, A. (1995a), 'Large amplitude IMF fluctuations in corotating interaction regions: Ulysses at mid-latitudes', *Geophysical Research Letters* **22**(23), 3397–3400.

Tsurutani, B. T., McPherron, R. L., Gonzalez, W. D., Lu, G., Gopalswamy, N. and Guarnieri, F. L. (2006a), 'Magnetic storms caused by corotating solar wind streams', *Recurrent Magnetic Storms: Corotating Solar Wind Streams* pp. 1–17.

Tsurutani, B., Verkhoglyadova, O., Mannucci, A., Araki, T., Sato, A., Tsuda, T. and Yumoto, K. (2007), 'Oxygen ion uplift and satellite drag effects during the 30 October 2003 daytime superfountain event', *Annales Geophysicae* **25**(3), 569–574.

Tsurutani, B., Verkhoglyadova, O., Mannucci, A., Saito, A., Araki, T., Yumoto, K., Tsuda, T., Abdu, M., Sobral, J., Gonzalez, W. et al. (2008a), 'Prompt Penetration Electric Fields (PPEFs) and their ionospheric effects during the great magnetic storm of 30–31 October 2003', *Journal of Geophysical Research* **113**, A05311.

Valladares, C. E. and Hei, M. A. (2012), 'Measurement of the characteristics of TIDs using small and regional networks of GPS receivers during the campaign of 17–30 July of 2008', *International Journal of Geophysics* **2012**, Article ID 548784.

Vanzandt, T. E. (1967), The Neutral Atmosphere and the Quiet Ionosphere, *in* S. Matsushita and W. H. Campbell, eds, 'Physics of Geomagnetic Phenomena', p. 509.

Vijaya Lekshmi, D., Balan, N., Tulasi Ram, S. and Liu, J. Y. (2011), 'Statistics of geomagnetic storms and ionospheric storms at low and mid latitudes in two solar cycles', *Journal of Geophysical Research* **116**(A11), A11328.

Viljanen, A. and Pirjola, R. (1994), 'Geomagnetically induced currents in the finnish high-voltage power system', *Surveys in Geophysics* **15**(4), 383–408.

Wand, I. C. (1967), An investigation into the ionospheric effects of solar flares., PhD thesis, Physics and Astronomy.

Wang, W., Lei, J., Burns, A. G., Solomon, S. C., Wiltberger, M., Xu, J., Zhang, Y., Paxton, L. and Coster, A. (2010), 'Ionospheric response to the initial phase of geomagnetic storms: Common features', *Journal of Geophysical Research* **115**, A07321.

Wanninger, L. (1995), 'Monitoring ionospheric disturbances using the IGS network', *SPECIAL TOPICS AND NEW DIRECTIONS* **57**.

White, R. (1970), *Space Physics*, Gordon and Breach, New York.

Woodman, R. and Hagfors, T. (1969), 'Methods for the measurement of vertical ionospheric motions near the magnetic equator by incoherent scattering', *Journal of Geophysical Research* **74**(5), 1205–1212.

Wright Jr, J., Lennon, T., Corell, R., Ostenso, N., Huntress Jr, W., Devine, J., Crowley, P. and Harrison, J. (1995), 'National space weather program, strategic plan', *Rep. FCM-P30-1995* .

Xu, G. and Xu, Y. (2016), *GPS: theory, algorithms and applications*, Springer.

Xystouris, G., Sigala, E. and Mavromichalaki, H. (2014), 'A Complete Catalogue of High-Speed Solar Wind Streams during Solar Cycle 23', *Solar physics* **289**(3), 995–1012.

Yizengaw, E. (2004), 'The southern hemisphere and equatorial region ionization response for a 22 september 1999 severe magnetic storm', *Annales Geophysicae* **22**(8), 2765–2773.

Yizengaw, E., Moldwin, M., Dyson, P. and Immel, T. (2005), 'Southern Hemisphere ionosphere and plasmasphere response to the interplanetary shock event of 29–31 October 2003', *Journal of Geophysical Research* **110**, A09S30.

Yizengaw, E., Moldwin, M., Komjathy, A. and Mannucci, A. (2006), 'Unusual topside ionospheric density response to the November 2003 superstorm', *Journal of Geophysical Research* **111**(A2), A02308.

Yizengaw, E., Moldwin, M., Mebrahtu, A., Damtie, B., Zesta, E., Valladares, C. and Doherty, P. (2011), 'Comparison of storm time equatorial ionospheric electrodynamics in the African and American sectors', *Journal of Atmospheric and Terrestrial Physics* **73**(1), 156–163.

Yizengaw, E., Moldwin, M., Zesta, E., Biouele, C., Damtie, B., Mebrahtu, A., Rabiu, B., Valladares, C. and Stoneback, R. A. (2014), The longitudinal variability of equatorial electrojet and vertical drift velocity in the African and American sectors, *in* 'Annales Geophysicae', Vol. 32, Copernicus Gesellschaft Mbh.

Zhang, D., Mo, X., Cai, L., Zhang, W., Feng, M., Hao, Y. and Xiao, Z. (2011), 'Impact factor for the ionospheric total electron content response to solar flare irradiation', *Journal of Geophysical Research* **116**, A04311.

Zhang, D. and Xiao, Z. (2003), 'Study of the ionospheric total electron content response to the great flare on 15 April 2001 using the International GPS Service network for the whole sunlit hemisphere', *Journal of Geophysical Research* **108**(A8), 1330.

Zhang, D. and Xiao, Z. (2005), 'Study of ionospheric response to the 4B flare on 28 October 2003 using International GPS Service network data', *Journal of Geophysical Research* **110**, A03307.

Zhang, D., Xiao, Z., Igarashi, K. and Ma, G. (2002), 'GPS-derived ionospheric total electron content response to a solar flare that occurred on 14 July 2000', *Radio Science* **37**(5), 1086.

Zhang, Y., Paxton, L. J., Morrison, D., Wolven, B., Kil, H., Meng, C.-I., Mende, S. B. and Immel, T. J. (2004), 'O/N2 changes during 1–4 October 2002 storms: IMAGE SI-13 and TIMED/GUVI observations', *Journal of Geophysical Research* **109**(A10), A10308.

Zhao, B., Wan, W., Liu, L. and Ren, Z. (2009), Characteristics of the ionospheric total electron content of the equatorial ionization anomaly in the Asian-Australian region during 1996–2004, *in* 'Annales Geophysicae', Vol. 27, Copernicus GmbH, pp. 3861–3873.

Zhao, B., Wan, W., Tschu, K., Igarashi, K., Kikuchi, T., Nozaki, K., Watari, S., Li, G., Paxton, L., Liu, L. et al. (2008), 'Ionosphere disturbances observed throughout Southeast Asia of the superstorm of 20–22 November 2003', *Journal of Geophysical Research* **113**, A00A04.